



<https://theses.gla.ac.uk/>

Theses Digitisation:

<https://www.gla.ac.uk/myglasgow/research/enlighten/theses/digitisation/>

This is a digitised version of the original print thesis.

Copyright and moral rights for this work are retained by the author

A copy can be downloaded for personal non-commercial research or study, without prior permission or charge

This work cannot be reproduced or quoted extensively from without first obtaining permission in writing from the author

The content must not be changed in any way or sold commercially in any format or medium without the formal permission of the author

When referring to this work, full bibliographic details including the author, title, awarding institution and date of the thesis must be given

Enlighten: Theses

<https://theses.gla.ac.uk/>
research-enlighten@glasgow.ac.uk

LIGHT INDUCED AC LOSS IN AMORPHOUS SILICON

MICHAEL JAMES ANDERSON

Ph.D

THE UNIVERSITY OF GLASGOW

DEPARTMENT OF PHYSICS AND ASTRONOMY

MAY 1989

© Michael James Anderson 1989

ProQuest Number: 10999380

All rights reserved

INFORMATION TO ALL USERS

The quality of this reproduction is dependent upon the quality of the copy submitted.

In the unlikely event that the author did not send a complete manuscript and there are missing pages, these will be noted. Also, if material had to be removed, a note will indicate the deletion.



ProQuest 10999380

Published by ProQuest LLC (2018). Copyright of the Dissertation is held by the Author.

All rights reserved.

This work is protected against unauthorized copying under Title 17, United States Code
Microform Edition © ProQuest LLC.

ProQuest LLC.
789 East Eisenhower Parkway
P.O. Box 1346
Ann Arbor, MI 48106 – 1346

"Boring ... libellous ... an error a page"

Robert Maxwell

Declaration

The work presented in this thesis is that of the author except where explicitly mentioned in the text when an appropriate reference is given.

Some of the results presented in this thesis have already been published (K. Shimakawa, A.R. Long, M.J. Anderson and O. Imagawa, Journal of Non-Crystalline Solids 97 and 98 623 (1987)) and A.R. Long, M.J. Anderson, K. Shimakawa and O. Imagawa, Journal of Non-Crystalline Solids 32, L1199-L1204 (1988)) but no part has been submitted previously for a degree at this or any other university.

TABLE OF CONTENTS

	Page
Acknowledgements	(i)
Abstract	(ii)
Chapter 1 Introduction	1
Chapter 2	3
2.1 The Density of States	3
2.2 The Notation Used in Discussing the Frequency Dependent Loss	4
2.3 Sputtered Amorphous Materials	5
(a) DC Conductivity	5
(b) Hopping in Deep States	5
2.4 AC Conductivity in Sputtered Material	8
(a) Sputtered a-Si and a-Ge	8
(i) Electron Transfer by Tunnelling	10
(ii) The Extended Pair Approximation (EPA)	11
(iii) Polaron Tunnelling	12
(iv) Effect of Intersite Correlation on Ac Loss	12
(v) Atomic Tunnelling	13
(vi) Correlated Barrier Hopping	14
(vii) Experimental Review of Sputtered Material	15
2.5 Glow Discharge Materials	16
(a) (i) Conductivity	16
(b) (i) Extended State Conduction	16
(ii) Hopping in Band-Tails	18

		Page
2.6	AC Conductivity in Glow Discharge Material	19
	Inhomogeneous Model	
2.7	Chalcogenides	22
	(i) DC Conductivity	22
	(ii) AC Conductivity	22
 Chapter 3		
3.1	Light Induced Changes in Amorphous Semiconductors	24
	(a) The Staebler-Wronski Effect	24
	(b) Photoluminescence	27
	(c) Light Induced Electron Spin Resonance (LESR)	30
	(d) DC Photoconductivity	33
	(e) Transient Photoconductivity	35
3.2	Recombination in Amorphous Silicon	37
3.3	The Effect of Infra-Red Radiation on Induced Changes	39
	(a) Photoconductivity	39
	(b) Photoluminescence	41
	(c) The Effect of IR on LESR Measurements	43
3.4	Optically Induced AC Loss	45
3.5	Summary	46
 Chapter 4		
4.1	Sample Geometry	48
4.2	Sample Preparation	49
	(a) Thermal Evaporation	49

		Page
	(b) RF Sputtering	50
	(c) Glow Discharge Decomposition	51
4.3	Preparation Details	52
	Sputtered Sample	52
	Glow Discharge Sample	53
4.4	Sample Cooling and Cryostat Design	53
	Cryostats	54
	Long Term Helium Dewar	55
	Low Temperature Inserts	55
4.5	High Temperature Sample Holder	56
4.6	Relative Importance of Coding Techniques	57
4.7	Sample Mounting	58
4.8	Temperature Measurement and Control	59
4.9	Sample Illumination	62
	(a) Illumination Through ITO Bottom Electrodes	63
4.10	Intensity Calibration	63
4.11	Transmittance and Reflection Measurements	66
4.12	AC Measurements	67
	(a) Manual AC Bridge	68
	(b) Computer Controlled System	69
4.13	Computer Programmes for AC Measurements	70
4.14	DC Measurements	71
4.15	Sample Thickness Measurements	72
Chapter 5		
5.1	Sample Characteristics	74
5.2	Corrections to the Measured Conductivity	74
5.3	Dark Conductivity	77

		Page
5.4	Magnetron Sputtered a-Si	78
5.5	a-Si:H Samples	80
5.6	DC Conductivity	82
5.7	Frequency Dependent Conductivity in Glow Discharge Samples	84
5.8	Inhomogeneous Model Applied to a-Si:H	85
5.9	Method of Contact Evaporation	87
5.10	The Effect of the Electrode Material on the Dark Characteristics	88
5.11	Electrode Requirements for Optical Experiments	89
5.12	Arsenic Selenide Sample	90
(a)	Temperature Dependence of the Conductivity	90
(b)	DC Conductivity	90
(c)	Frequency Dependent Effects	91
5.13	Models for the Observed Behaviour of σ_{tot} with T and ω	91
 Chapter 6		
6.1	General Description of the Optical Response	94
(a)	Glow Discharge Material	94
(b)	Sputtered Material	95
6.2	Preparation of the Dark State	95
6.3	Magnitude of Errors in Capacitance Measurements	96
6.4	Intensity Dependence of $\Delta\epsilon$	99
(a)	Sputtered Material	99
(b)	Glow Discharge Samples	99

		Page
6.5	Magnitude of $\Delta\epsilon$	100
(a)	Dependence of $\Delta\epsilon$ on Sample Material	100
	As ₂ Se ₃ Sputtered a-Si Sample	101
	Glow Discharge Samples	101
(b)	Effect of Electrode Material on $\Delta\epsilon_1$ for Glow Discharge Material	102
6.6	Temperature Dependence of $\Delta\epsilon_1$	103
6.7	The Effect of Increasing Temperature at a Constant Level of Illumination	105
6.8	The Frequency Dependence of the Optical Response	105
6.9	The Decay to the Dark State	106
(a)	Sputtered Samples	106
(b)	Glow Discharge Material	107
6.10	Contact Effects	108
6.11	The Thickness Dependence of the Response in Sputtered a-Si	108
6.12	Effect of Different Wavelengths on $\Delta\epsilon_1$	109
6.13	DC Photoconductivity	110
Chapter 7		
7.1	General Mechanism for the Optically Induced AC Loss in a-Si and a-Si:H	111
7.2(a)	Sputtered a-Si and a-Si:H	112
(b)	Applications of the Rate Equation in Sputtered Material	114
(c)	Inadequacies of the Simple Model	116
(d)	The Reduced Rate of Increase of $\Delta\epsilon$ with Increasing Intensity	117

		Page
	(e) The Temperature Dependence of $\Delta\epsilon_1/\epsilon_1$	118
7.3	Glow Discharge a-Si:H	119
	(a) Comparison of the Optical Effect in Glow Discharge Material with the Response in Sputtered Samples	119
	(b) Mechanism Responsible for the Optically Induced Loss in Glow Discharge Material	119
	(c) The Integrating Response at Low Intensities	122
	(d) Recombination	123
	(e) Analysis of the Dark Decay	124
	(f) Fitting Procedure	126
	(g) The Detection of Carriers Trapped in the Band Tails	127
7.3(a)	The Temperature Dependence of $\Delta\epsilon_1$ in Glow Discharge Samples	128
	(b) The Effect of Increasing Temperature at a Constant Level of Illumination	128
	(c) Other Analysis Problems	129
7.5	Other Relevant Experiments	130
	(a) Comparisons with LESR Measurements	130
	(b) DC Photoconductivity and Low Temperature Drift Mobility	131
	(c) Transient Photoconductivity	132

		Page
7.6(a)	D Sample	133
(b)	Metallic Diffusion in a-Si and a-Si:H Samples	133
(c)	As ₂ Se ₃ Sample	134
Chapter 8	Summary and Conclusions	135
References		140

Acknowledgements

I would like to thank the following people who helped throughout the course of this project.

Firstly, my supervisor Dr. A.R. Long for his help and encouragement and the members of the Solid State Physics Group for many interesting and stimulating discussions.

I am also grateful to the technical staff of Mr. D. McDonald and Mr. A. Young for their help.

Finally I thank Mrs. I. Anderson for typing the thesis and the SERC for the provision of a research studentship.

Abstract

Light-induced AC losses have been observed in sputtered a-Si, a-Si:H and a-Ge. The aim of this work was to investigate the effect of light on the ac loss in sputtered a-Si and glow discharge a-Si:H and compare the results with previous research.

The glow discharge a-Si:H showed an optical response which was intensity dependent. At intensity greater than $\sim 1 \mu\text{Wcm}^{-2}$ the response was rapid and reached a saturation value within minutes. At lower illuminating intensities an integrating response was observed in which saturation values may not be reached for many hours. The intensity dependence of the optically induced loss is similar to that observed in sputtered a-Si, although the illuminating intensities used to create a similar magnitude of response are around 2 orders of magnitude loss in sputtered material. A power law relation is found in which $\Delta\epsilon \propto I^A$ where $A \approx 0.2$ in glow discharge samples and $A \approx 0.25$ in sputtered a-Si.

The induced loss in sputtered a-Si has been attributed to optically excited carriers becoming trapped in defect states within the band gap where they respond to the ac measuring field. Evidence is found from the frequency and temperature dependences of the dark and optically induced losses to show that band-tail states are responsible for trapping carriers and hence for the induced ac loss, in glow discharge a-Si:H. The mechanism postulated to account for the light induced ac loss involves the excitation of carriers by the applied light. Carriers thermalise rapidly through the extended states and subsequently become trapped in the band-tails. They can now recombine by tunnelling through the band-tails until they recombine with an excess hole via defect states.

The dark decay towards equilibrium is accounted for by considering trapped carriers recombining, by tunnelling, leading to a greater spacing between the remaining carriers. This then leads to a reduced response which decays slowly with time. The temperature dependence of these decays was also investigated and it was found that the decays were faster as the temperature was increased from 4.2K to 60K. A model involving the physical principle described above was used to obtain parameters to quantify the rate of decay.

CHAPTER 1

Introduction

The aim of this work was to investigate optically induced ac loss in amorphous materials. The materials investigated were amorphous silicon prepared by RF magnetron sputtering (a-Si), hydrogenated amorphous silicon prepared by the glow discharge decomposition of silane (a-Si:H) both doped n-type and undoped and amorphous arsenic selenide prepared by thermal evaporation.

The term ac loss is used to denote energy loss within the amorphous material. When an external ac field is applied energy is required to polarise the medium but it is recovered during the next half cycle (this gives the real part of the polarizability). Energy loss occurs, in the form of heat generated, due to the imaginary part of the polarizability.

In this thesis the term "dark loss" is used to denote the ac conductivity when a sample is measured in the absence of any applied illumination. This was studied in order to obtain information about the conduction mechanisms in amorphous materials. This enabled samples to be characterized so that comparisons with previous research could be made. Both the dark and the optically induced ac losses are interpreted in terms of a variety of appropriate models.

A review of the mechanisms generally recognised as leading to ac loss and dc conductivity in amorphous materials is given in Chapter 2.

The next chapter deals with light-induced phenomena. A review of the Staebler-Wronski effect, photoluminescence, dc and time dependent photoconductivity, light-induced electron spin resonance and previous studies of optically induced ac loss is presented.

Chapter 4 explains the experimental procedures and techniques used in cooling samples, the illumination of samples and data measuring techniques.

The results presented in Chapter 5 show the dark data, concentrating on the frequency and temperature dependence of the dark loss. Some of the models discussed in Chapter 2 are applied to explain the results obtained.

Chapter 6 deals with the optical results covering the increase of capacitance and conductance under illumination and its decay with time when the illumination is removed.

In Chapter 7 analysis of the results presented in Chapter 6 is carried out. The results are explained using models specially developed for this purpose. Finally, a comparison is made with light-induced electron spin resonance experiments and with steady state and time dependent photoconductivity data.

A summary of the results and conclusions are discussed in Chapter 8, along with the possible application to detecting low intensity optical radiation. Ideas for future work and further research are also discussed.

CHAPTER 2

In the following chapter the general features of ac and dc transport in amorphous semiconductors are reviewed. Theoretical models are considered and their relevance to conduction mechanisms in a-Ge, a-Si, a-Si:H and a-As₂Se₃ are discussed.

2.1 The Density of States

The density of states as a function of energy generally assumed for an amorphous semiconductor is shown in diagram 2.1.

The energies E_c and E_v are known as the mobility edges and the states above and below, in energy, are respectively referred to as extended states. In extended states, the wavefunctions extend over large regions of space. At energies between E_v and E_c states also exist. These are known as localized states and differ from extended states in that the wave functions are centred at a particular point and decay exponentially away from this point. These states can also trap carriers which can remain for a considerable time.

The density and nature of the states with the band gap (equivalent to $E_c - E_v$) determine the mechanism of electron transport within the material. Structural disorder such as bond angle and bond length fluctuations give rise to localized states just below E_c and above E_v . These are band-tail states and are of considerable importance for conductance mechanisms, especially in a-Si:H prepared by glow discharge. States close to the mid-gap i.e. deep states, occur mainly as a result of structural defects within the amorphous material.

In a-Si, the density of deep states is high ($\sim 10^{18} \text{ cm}^{-3} \text{ eV}^{-1}$, see later sections) and these dominate electron transport. Glow

discharge a-Si:H has a much lower density of mid-gap states (typically two orders of magnitude lower) and transport occurs in band-tail states or by band conduction, depending upon the temperature. These transport mechanisms are discussed in more detail in later sections.

2.2 The Notation Used in Discussing the Frequency Dependent Loss

The frequency dependent loss measurements consist of measuring the conductance (which gives the conductivity, σ_1) and the capacitance (which is used to calculate the dielectric constant, ϵ_1 , when geometrical factors are taken into account). The ac response is generally expressed in terms of the real and imaginary parts of the conductivity i.e.

$$\hat{\epsilon} = \epsilon_1 + i\epsilon_2 \quad (2.1)$$

$$\text{and } \tilde{\sigma} = \sigma_1 + i\sigma_2 \quad (2.2)$$

In equations (1) and (2) σ_1 and σ_2 are related by $\sigma_2 = \omega(\epsilon_1 - \epsilon_\infty)\epsilon_0$ and $\epsilon_2 = \frac{(\sigma_1 - \sigma_1(0))}{\omega\epsilon_0}$. The quantity ϵ_∞ is due to atomic polarisation

and is discussed in the next paragraph. The Kramers-Kronig relations enable the real part of the conductivity to be calculated if the imaginary part is known, since they are dependent on each other, and vice-versa.

The capacitance which is measured consists of two components and can be expressed as $C = C_{ac}(\omega, T) + C_\infty$ where C_∞ is frequency independent and due to high frequency atomic and dipolar vibrational transitions. In real data C_∞ can be estimated from the high frequency capacitance (i.e. - at around 10^5 Hz). Another technique used to isolate the frequency dependent portion of the capacitance is to plot $-dC/d\ln\nu$

against n on a logarithmic scale. The physical basis for this procedure is discussed in more detail in section 2.6.

2.3 Sputtered Amorphous Materials

(a-Si, a-Ge, a-Si:H)

2.3(a) DC Conductivity

The dominant dc conduction mechanism in this type of material is widely believed to be transport in deep states. The following section deals with these mechanisms in detail.

2.3(b) Hopping in Deep States

If a high density ($10^{18} \text{ eV}^{-1} \text{ cm}^{-3}$) of defect states exists close to the Fermi level then electron transport will take place between localized states by phonon assisted hopping. This will be due to carriers tunnelling from one localised state to the other with the energy difference ($\hbar\omega_0$) being taken up by the exchange of phonons with the lattice.

Mott (1969) proposed a mechanism for nearest-neighbour hopping between two localised sites. One site was filled and was slightly below E_F and the other empty and just above E_F . They are separated by a distance R and have an energy difference of W . In order to calculate the hopping transition rate, ν , some factors must be taken into account.

If the energy difference, W , is less than the energy of a phonon of energy $\hbar\omega_0$ then hopping can proceed by a process involving one phonon. Should W be greater than $\hbar\omega_0$ then several phonons are necessary for electron transfer between the two sites.

If electron transfer takes place by tunnelling then overlapping of the wavefunctions must be considered. Assuming that each state is

exponentially localized this leads to a factor of $\exp(-2\alpha R)$ where α^{-1} is the localization length.

The frequency of the number of hopping attempts is also important. This depends on both electron-phonon coupling and the phonon density of states. The attempt frequency is represented as ν_0 .

By putting these factors together the hopping transition rate, as calculated by Mott, is

$$\nu = \nu_0 \exp(-2\alpha R - W/k_B T). \quad (2.3)$$

The conductivity is then found using the Einstein relation involving the carrier mobility and the diffusion constant

$$\text{i.e.} \quad \mu = \frac{eD}{k_B T} \quad (2.4)$$

where

$$D = \frac{\nu R^2}{6} \quad (2.5)$$

The conductivity is thus

$$\sigma = n e \mu \quad (2.6)$$

where n = the number of electrons hopping.

$$\text{i.e.} \quad \sigma = \frac{ne^2 \nu R^2}{6k_B T} \exp(-2\alpha R - W/k_B T) \quad (2.7)$$

Mott (1969) proposed that, at low temperatures, nearest neighbour hopping is energetically unfavourable and that tunnelling to a more distant site would be more favourable if this had a smaller energy separation than a site which was closer in space. By optimising the factor $(2\alpha R + W/k_B T)$ to take the variable range nature

of the hopping process into account, Mott showed that

$$\sigma = \sigma_0 \exp\left(\frac{T_0}{T}\right)^{\frac{1}{4}} \quad (2.8)$$

Where σ_0 is of the form $[N(E_F)T]^p$ with $|p| \leq 1$.

Other researchers have obtained a similar form to 2.3 for variable range hopping. Ambegaokar et al (1971) used percolation theory to derive 2.8 with different constants. Ambegaokar et al proposed that the amorphous material could be modelled as a network of resistors. The resistors represent the paths between a pair of states and therefore there is a wide range of values of the resistances in the network.

In determining the conductance necessary for the percolation current through the network Ambegaokar et al found that it was not the very large or low conductances that were responsible for the ~~conductance~~ of the percolation path. The conductances which contributed were those greater than the critical conductance, which is defined as the largest conductance for which there is a connected path through the network. By evaluating the critical conductance Ambegaokar et al were able to show that

$$\sigma_0 = \sigma_0 \exp\left(-\frac{A}{T^{\frac{1}{4}}}\right) \quad (2.9)$$

$$\text{where } A = \frac{4 \alpha^3 \eta_c}{k_B N(E_F)}$$

α^{-1} = localization length of the wavefunction.

$\eta_c \approx \text{constant} \approx 4$.

$N(E_F)$ = density of states near the Fermi level.

Equation 2.9 is of the "Mott $T^{-\frac{1}{4}}$ " form.

This form of hopping has been found to dominate the dc conductivity in materials with a high density of defect states around the Fermi level. Diagram 2.2 shows data for a-Si (Long et al 1988, and it can be seen that $\sigma \propto T^{-\frac{1}{4}}$ for a range of samples of differing thicknesses over a temperature range of ~50K to ~360K.

2.4 AC Conductivity in Sputtered Material

AC conductivity in amorphous materials has been studied for a number of years. Various mechanisms have been proposed by various authors to explain the data obtained for sputtered a-Ge, a-Si, glow discharge a-Si:H and a-As₂Se₃. These mechanisms are now reviewed and their relevance to the materials studied in this thesis are discussed.

2.4(a) Sputtered a-Si and a-Ge

The log σ_{ac} vs log T plots for these materials can be divided into high and low temperature regions, as shown in diagram 2.4. The ac conductivity changes with frequency (diagram 2.5) and is found to obey the following empirical expression (Long 1982)

$$\sigma \propto \omega^s T^n \quad (2.10)$$

where s (~1) and n are hardly temperature dependent. One of the earliest techniques used to account for the ac conductivity was the pair approximation (Pollak and Geballe 1961).

If a pair of sites are separated in energy by Δ_{12} and by R_{12} in space electrons can transfer between them. By calculating the probability of these states being occupied and by considering their average polarizability, α , under the application of a small oscillating field the ac conductivity can be calculated. The pair approximation predicts that the imaginary part of the polarizability will be at a

maximum when $\omega = 1/\tau$ since

$$\alpha = \frac{e^2 \Gamma_{12}^2}{4kT} \frac{1}{\cosh^2(\Delta_{12}/2kT)} \frac{1}{(1+i\omega\tau)}, \text{ which is of standard Debye form} \quad (2.11)$$

where ω = frequency of the applied ac field

τ = the effective relaxation time

$$= \frac{\tau_0}{2} \left[\cosh \left(\frac{\Delta}{2kT} \right) \right]^{-1} \times \text{tunnelling term} \quad (2.12)$$

The $\cosh^2(\Delta_{12}/2kT)$ factor in 2.11 ensures that loss will only occur at pair separation $\leq kT$.

Miller and Abrahams (1960) found an alternative expression for the relaxation time

$$\tau = \frac{1}{B|\Delta|_{12}} \tanh \left(\frac{\Delta_{12}}{2kT} \right) \times \text{tunnelling term} \quad (2.13)$$

when B is a parameter which contains details of the interaction between the states. This is valid for single phonon transitions at low T.

As $\Delta_{12} \rightarrow 0$ (2.13) will not hold due to quantum mechanical splitting of the states caused by electron transfer between them.

The pair approximation applies to a single isolated pair of localized states. In a real amorphous system the pair approximation will only be applicable under certain circumstances. The closest states randomly distributed in space will have the shortest relaxation times and will therefore respond at the highest frequencies. They are also not likely to be closely coupled to neighbouring states. Thus the pair approximation should give a good description of the system at high frequencies.

At lower frequencies interactions between neighbouring states

will take place since the separation between contributing states will increase.

(i) Electron Transfer by Tunnelling

The following mechanism has been proposed to account for the strong temperature dependence of the ac conductivity in the high temperature regime. Above ~100K, in sputtered a-Ge and a-Si, the dc conductivity can be fitted to the Mott $T^{-\frac{1}{4}}$ law. The ac conductivity is likely to involve electron transport between states close to the Fermi level, in the same manner as in the mechanism responsible for the dc conductivity i.e. tunnelling between states close to the Fermi level (see also section 2.3).

The conductivity is calculated from the polarizability, the relaxation time and from the distribution of the sites in space. This gives (Long 1982) the following expression for σ_1 the real part of the conductivity).

$$\sigma_1 = \frac{\pi^4}{12} \frac{e^2 g_0^2 kT}{2} \omega R_\omega^4 \quad (2.14)$$

where g_0 = the density of states

α = decay length of the wavefunction

R_ω = the separation of states of the pair for which $\omega\tau = 1$ and the contribution to the loss is a maximum.

This can be expressed in the empirical form.

$$\text{i.e. } \sigma_1 \propto \omega^s T^n \quad (2.15)$$

$$\text{where } s = 1 + \frac{4}{\ln(\omega\tau_0)} \quad (2.16)$$

The conductivity data is therefore predicted to follow a power law, which is observed experimentally (see section 2.4(a)(ii)). The value of s , i.e. the gradient of a $\log \sigma_1$ vs $\log \omega$ plot, is predicted

to be less than one and independent of temperature. Experimental results (section 2.4(vii) for sputtered a-Ge and a-Si shows that s is actually temperature dependent).

(ii) The Extended Pair Approximation (EPA)

The extended pair approximation was first proposed by Summerfield and Butcher (1982) to account for the fact that a dc limit is reached in the conductivity at low frequencies. The pair approximation (PA) (section 2.3(i)) is only valid at high frequencies and takes no account of a continuous percolation path through the material. The EPA is a better approximation than the PA. Transport of carriers may proceed by any appropriate mechanism in either approximation scheme, though the EPA has been most commonly applied to hopping transport.

The EPA model uses the equivalent circuit proposed by Miller and Abrahams (1960) as a starting point. By extending this model Summerfield and Butcher considered the effect of neighbouring states on the response of a pair of states. The response of the complete network could then be obtained. The results from the EPA model tend towards those of the pair approximation at high frequencies and account for the dc limit, at low frequencies, being reached. It is predicted that a peak will be found, known as a loss peak, (see section 2.6 for an explanation of a loss peak) in a plot of $\ln \left(\frac{d\epsilon_1}{d \ln \nu} \right)$ vs $\ln \nu$ or in $(\sigma_1 - \sigma_0)$ vs $\ln \nu$. Such peaks are seen in data obtained by Long et al (1983, 1985, 1988 for a-Ge, a-Si and a-Si:H (prepared by RF sputtering)). The peak denotes the transition to frequency dependent behaviour and cannot be accounted for by the pair approximation.

EPA fits have also been applied to the frequency dependent conductivity data for sputtered materials (Long et al 1985, 1988). The EPA calculations agree closely with the experimental results (see

diagram 2.6, from Long et al 1988).

The low temperature (i.e. below 30K) data for the temperature dependence of the conductivity in a-Si or a-Ge cannot be explained using a simple tunnelling mechanism alone. A mechanism involving charge transfer within clusters, rather than between clusters (the basis of the explanation of the high temperature loss) is likely to be responsible. Mechanisms for charge transfer at low temperatures are now discussed.

(iii) Polaron Tunnelling

Electron self-trapping at a defect site leads to a distortion of the surrounding lattice. The energy of the system is lowered by an amount W_p which is known as the "polaron" binding energy. Since thermal energy is necessary to produce distortions in the lattice for electrons to tunnel from site to site the tunnelling rates will be reduced, especially at low temperatures. This has a significant effect on the predicted frequency and temperature exponents.

(iv) Effect of Intersite Correlation on AC loss

Interactions between the electrons on the sites of the pairs contributing to the ac conductivity have not yet been taken into account. The effect of Coulomb repulsion between an electron on one site of the pair is to raise the energy of a neighbouring site. This has the effect of decreasing the probability of it being occupied. The ac loss is therefore going to be greater when electrons transfer between sites.

If the energy of interaction, E_{12} , between the sites is much less than kT then intersite correlation effects can be disregarded, and the ac loss measurements will not be influenced. Should E_{12} become of the

order of kT or greater, then the effect must be considered. To establish at what point E_{12} becomes important calculations were performed by Pollak (1971) and Efros (1981). Site separations of 50\AA were considered and a dielectric constant of ~ 12 was used. Using the equation for the energy due to electrostatic repulsion, $\frac{e^2}{4\pi\epsilon\epsilon_0 R_{12}}$, E_{12}/k was found. From this T was estimated to be around 280K. This implies that all measurements below room temperature are likely to be affected.

Long (1982) calculated the effect of intersite correlation on the polarizability and thus on σ . It is found that σ is increased by factor of around $\frac{E_{12}}{kT}$. This means that n is reduced by 1 and the value of s will also change slightly. This calculation follows and reproduces Efros.

(v) Atomic Tunnelling

Although electronic mechanisms are responsible for the ac losses in amorphous silicon and germanium (prepared by methods outlined in Chapter 4), a variation of the atomic tunnelling model involving electronic processes has been used to account for the low temperature data in a-Ge (Long, Hogg, Holland, Balkan and Ferrier 1985). The atomic tunnelling model is now briefly discussed.

The polarization, p , of a pair of atomic sites can be calculated and from knowing the relaxation time, Long (1982) developed the ac conductivity σ_1 , following the treatment of Frossatiet et al (1977)

$$\text{i.e. } \sigma_1 = A \omega \tanh \left(\frac{\Delta_0}{2kT} \right) \quad (2.17)$$

where Δ_0 = the energy width over which values of the site separation energy, Δ , may be found.

The form of equation 2.18 predicts that the conductivity is both frequency and temperature dependent.

The atomic tunnelling model has been applied to chalcogenides such as As_2Se_3 in section 2.7.

(vi) Correlated Barrier Hopping

Correlated barrier hopping (CBH) describes electron transport between two sites via an activated hopping mechanism. The sites are separated by a potential barrier over which the electron must hop. The barrier height is reduced by the coulomb interaction between the two sites. Pike (1972) showed that for the height of this barrier, W is correlated with the site separation R , i.e.

$$W = W_m - \frac{e^2}{\pi\epsilon\epsilon_0 R_{12}} \quad (2.18)$$

where W_m = the barrier height at infinite site separation.

The ac conductivity may be calculated for the case of a single electron or pairs of electrons hopping over the barrier. The results are found to be of the form

$$\sigma_1 = A N^2 e^2 \omega \left(\frac{R^4}{dW} \frac{dR}{d\omega} \right)_{\text{opt}} \quad \text{if } \Delta_0 \ll kT \quad (2.19)$$

$$\text{or } \sigma_1 = B(kT)^2 \omega^2 \left(\frac{R^4}{dW} \frac{dR}{d\omega} \right)_{\text{opt}} \quad \text{if } \Delta_0 \gg kT \quad (2.20)$$

where N = the number of states distributed over an energy interval Δ_0 .

The expressions differ in the two cases (i.e. one or two electrons) by a factor contained in A or B .

By writing the expressions in the form of a power law, $\sigma_1 \propto \omega^{sT^n}$, s (and n) can be found.

$$\text{i.e. } s = 1 - \frac{6kT}{\omega_m + kT \ln(\omega \tau_{oh})} \quad (2.21)$$

where τ_{oh} is the relaxation time at zero energy separation of the two sites.

The parameter s is thus predicted to decrease from 1 as the temperature increases.

(vii) Experimental Review in Sputtered Material

The conductivity vs temperature data can be divided into two regimes in sputtered materials. These are the high and low temperature regimes shown in diagram 2.4.

None of the electron transfer mechanisms outlined in the previous sections could successfully account for the experimental ac losses observed at low temperatures in sputtered material. For example, the tunnelling model alone predicts a tunnelling distance of ~20nm for electrons. Experimentally, this distance was observed to be ~1nm in field dependence experiments (Long, Hogg, Holland, Balkan and Ferrier 1985). This is a more likely figure since small angle scattering measurements show that voids of ~1nm are present in a-Si and a-Ge. Long et al then proposed a model involving electron tunnelling between states associated with this void structure with some degree of lattice rearrangement (see Chapter 5 for more detail).

The high temperature regime has been explained by the variable range hopping mechanism discussed in section 2.3.

The frequency dependent conductivity data shown in diagram 2.5, has been analysed using the EPA model (Summerfield and Butcher, 1982). This has been successful in a-Ge and a-Si (Long, McMillan, Balkan and Summerfield 1988 - see diagram 2.6) data. The loss peaks and scaling

to higher temperatures as the dc conductivity falls (Summerfield and Butcher 1985, Long, Hogg and Balkan 1983) can be fitted using this model.

2.5 Glow Discharge Materials

(a) DC Conductivity

In a-Si:H prepared by the glow discharge decomposition of SiH_4 gas the density of gap states is lower than in sputtered material. The dominating dc conduction mechanisms are different as a result and are now discussed.

2.5(b)(i) Extended State Conduction

This process involves the activation of electrons (or holes) to the conduction (or valence) band. Mott and Davis (1979) found the following form for the conductivity.

$$\sigma = \sigma_{\min} \exp \left(-\frac{E_c - E_F}{kT} \right). \quad (2.22)$$

The factor σ_{\min} is of the order of Mott's maximum metallic conductivity (Mott and Davis (1979)). In practice this model is somewhat oversimplified because the fermi level shifts with respect to the conduction band edge as the temperature is changed. The quantity ΔE_σ , obtained by plotting a graph of $\log \sigma$ vs $1/T$ is not the true activation energy which is defined as $\Delta E_\sigma = E_c - E_F(T)$. The position of the fermi level can be approximated by linear relation according to

$$E_F(T) \approx E_F^*(0) - \gamma_F T. \quad (2.23)$$

Rewriting the conductivity σ , and using the above expression we obtain

$$\sigma = \sigma_0 \exp(-\Delta E_\sigma^*/kT) \quad (2.24)$$

where $\sigma_0^* = \sigma_{\min} \exp(-\gamma_F^*/k)$

and $E_\sigma^* = E_c - E_F^*(0)$

The shift in the Fermi level therefore gives rise to a difference in the value of ΔE_σ^* and ΔE_c . This is calculated to be $-\gamma_F^*T$ according to the above analysis.

Similar analysis of the thermopower (this quantity determines the voltage produced when a temperature gradient occurs over a sample) yields a similar result.

$$\text{i.e. } \frac{q}{k} S = E_\sigma^*/kT + A^* \quad (2.25)$$

where q = the charge on a carrier,

s = the thermopower

$A^* = A + \gamma_F^*/k$ and A is a constant.

Thus the observed thermopower activation energy differs from the true value. Overhof and Beyer (1981) considered the function

$$Q(T) = \ln \sigma(T) + eS(T)/k$$

$$\text{where } \sigma(T) = \sigma_0 \exp\left(\frac{-(E_c - E_F)}{kT}\right)$$

$$\text{and } \frac{q}{k} S = \left(\frac{E_c - E_F}{k_B T}\right) + A$$

Such a function cancels effects due to the statistical shift in the Fermi level or changes in E_c or A due to temperature changes or doping. A linear relation

$$Q(T) = \text{const} - (E_\sigma - E_\sigma^0)kT \quad (2.26)$$

is found by Overhof and Beyer

This apparent difference in dc conductivity and thermopower activation energies is attributed to the modulation of E_c by long range potential fluctuations due to inhomogeneities within the amorphous material. A model involving inhomogeneous regions has also been used by Long (1989) to account for the frequency dependence of the total conductivity in a-Si:H (see section 2.6 and Chapter 5).

The statistical shift of the Fermi level also leads to the Meyer Neldel rule which states that the pre-exponential factor is an exponential function of the experimental activation energy.

$$\text{i.e. } \ln \sigma_0^* = \text{constant} + \frac{E^*}{E_{\text{MNR}}} \quad \text{where } E_{\text{MNR}} = 0.043 \text{ eV}$$

Conductivity involving the extended states is the dominant mechanism at high temperatures (greater than 300K) in As_2Se_3 (Edmond 1966 see also data in Mott and Davis 1979). Extended state conduction is also observed in glow-discharge a-Si:H at temperatures around 250K to 350K (Le Comber and Spear 1970), see diagram 2.3. At lower temperatures some measurements suggest the conduction mechanism changes to one involving hopping in the band-tail states. This accounts for the change in activation energy observed and is discussed in the next section.

2.5(b)(ii) Hopping in Band-Tails

In section 2.5(a) localized states within the band-gap were not considered as being involved in the conduction process. Activated hopping can also occur among carriers moving in band-tail states. Mott and Davis (1979) showed, that, for carrier hopping between nearest-neighbours,

$$\sigma = \sigma_1 \exp \left(- \frac{E_A - E_F + \omega_1}{k_B T} \right) \quad (2.27)$$

E_A is the energy at the bottom of the band-tail, (see diagram 2.1),

and σ_1 is a pre-exponential factor which is expected to be smaller than σ_{\min} . This is due to the lower density of states near E_A in comparison with E_C and the lower carrier mobility in the band-tails. The quantity ω_1 is the activation energy for the hopping mechanism responsible for conduction in the tail-states.

This process is likely to be significant at lower temperatures than the mechanism discussed in the previous section.

2.6 AC Conductivity in Glow Discharge Material

The ac conductivity of glow discharge a-Si:H has been studied by Shimakawa et al (1987) and again two temperature regimes were found (see diagram 2.8). The low temperature loss is thought to arise from the polarisation of electrons within active centres close to the fermi level, as in sputtered material. The models presented so far have, however, been unable to account for the high temperature ac loss. A model (Long 1989) is now described to explain the high temperature ac loss in glow discharge a-Si:H.

Inhomogeneous Model

Effective medium methods have been used by various researchers to account for the conduction properties of amorphous materials. Such a model involves one material into which regions of another material are found. This is then modelled as an effective medium and the response can be calculated. This was carried out on a macroscopic scale by Bruggeman (1936). The model used in the analysis by authors such as Overhof and Beyer (1981,1983) and Long (1989) are applied on a microscopic scale. In such a model a pair state, for example, is surrounded by other states and the response of the effective medium is calculated.

An example of an effective medium is the EPA used by Summerfield

and Butcher (1982,3) to analyse the frequency dependent conductivities a-Ge and a-Si. Other authors (e.g. Bryksin 1980 and Movaghar et al 1980) used effective medium methods to explain the ac response at intermediate frequencies.

Long (1984) used a model proposed by Overhof and Beyer (1981,1983) as a starting point for his calculations. The Overhof and Beyer model considers a-Si:H as having mobility edges which vary in energy with respect to the Fermi level. This model has been successful in explaining properties such as the differences in the activation energies for dc conductivity and thermopower.

Long proposed that a-Si:H can be considered as having spherical high conductivity regions within a background material.

These regions give rise to a randomly varying potential fluctuation between points in the sample. Long considered the case in which the conduction band mobility edge is lowered, with respect to E_F , as a result of this variation. The conductivity can be written as

$$\sigma = \sigma_b \exp(\Delta E/kT). \quad (2.28)$$

where σ_b = the conductivity of the background material

and ΔE = the amount by which the mobility edge is lowered

by the high conductivity region. It is assumed that each region is large enough for a conductivity to be defined for each one.

By calculations by Bruggeman (1936) and Springett (1973) and by assuming an exponential distribution of high conductivity regions Long explained some features of the frequency dependent conductivity data. The distribution assumed is

$$C(\Delta E) = (C_0/kT_0) \exp(-\Delta E/kT_0) \quad (2.29)$$

with $\Delta E > 0$. C_0 ranges from 0.17 to 0.4 in Long's calculations.

The empirical result (Shimakawa et al 1987),

$$s \approx 1-T/T_0 \quad (2.30)$$

where $T_0 \sim 400K$, for a-Si:H

is predicted by this model using the exponentially distributed inhomogeneities (see also Chapter 5).

One feature predicted by the above analysis is the loss peak observed in the $\log - \left(\frac{d\epsilon_1}{d\ln\nu} \right)$ vs $\log \nu$ data. The maxima in such curves are loss peaks.

They are due to the polarisation of the high conductivity regions due to an applied field. As the frequency of this field is reduced more regions can respond thus the measured capacitance rises. When the frequency reaches a sufficiently low value then all the regions will respond and the capacitance will reach a constant value. The numerical differentiation procedure used in calculating $-\frac{d\epsilon_1}{d\ln\nu}$ will give rise to the shape observed on the graphs of $\log \left(-\frac{d\epsilon_1}{d\ln\nu} \right)$ vs $\log \nu$. The existence of loss peaks imply that the ac and dc conduction mechanisms are related.

Other distributions have also been considered by Long, such as double sided exponential and Gaussian distributions. The double-sided distribution gives similar shaped curves to equation 2.8, although broader loss peaks are observed. The rate at which conductance increases with frequency is influenced by the distribution of high conductivity regions. A particular case is the Gaussian, in which the conductivity

saturates at high frequencies. This is consistent with a T/T_0 value greater than 0.2, corresponding to a low density of high conductivity regions. It will differ from an exponential distribution in these cases.

2.7 Chalcogenides

(i) DC Conductivity

In chalcogenide material, both in bulk and thin film form the dc conductivity is activated and follows a $1/T$ law. The processes responsible have been discussed in section 2.5a.

(ii) AC Conductivity

High and low temperature regimes have been identified Elliott (1987) for ac conductivity in chalcogenides.

The process responsible for the low temperature loss (shown in diagram 2.7) is thought to be atomic tunnelling. Such a model gives rise to a weakly temperature dependent ac loss at low temperatures. The frequency dependence of the conductivity is predicted to be linear with $s \sim 1$. Such behaviour is observed experimentally (see Long 1982, Elliott 1987) in chalcogenides.

At intermediate temperatures (around 100K to 300K in As_2Se_3 : materials such as AsTe shows similar effects at lower temperatures) bipolaron transport, which involves the correlated hopping of electron pairs over a potential barrier, is thought to be responsible for the loss (Long 1982, Elliott 1984). At higher temperatures (i.e. 300K in As_2Se_3) σ_{tot} (where $\sigma_{tot} = \sigma_{dc} + \sigma_{ac}$) becomes strongly temperature dependent. This is also due to correlated barrier hopping involving bipolarons. As the dc limit is reached bipolarons may be involved in the hopping (Shimakawa 1982).

These mechanisms give rise to a strongly temperature dependent conductivity, and a temperature dependent value of the frequency exponent s . This parameter is predicted to decrease, as discussed in section 2.4(a)(vi) where correlated barrier hopping is discussed in more detail.

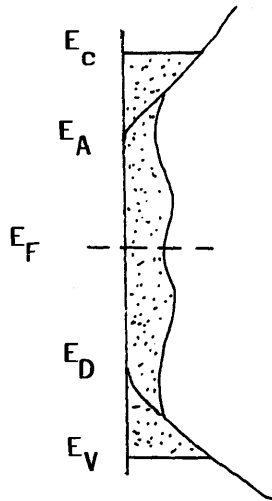


Diagram 2.1

Model showing the density of states in an amorphous material such as a-Si:H.

E_C is the conduction band edge

E_A is the bottom of the conduction band-tail

E_F is the Fermi level

E_D is the top of the valence band-tail

E_V is the valence band edge

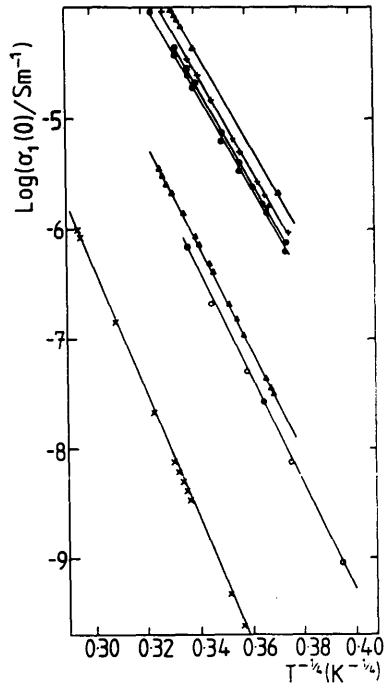


Diagram 2.2

DC conductivities of various a-Si samples Long et al 1988).

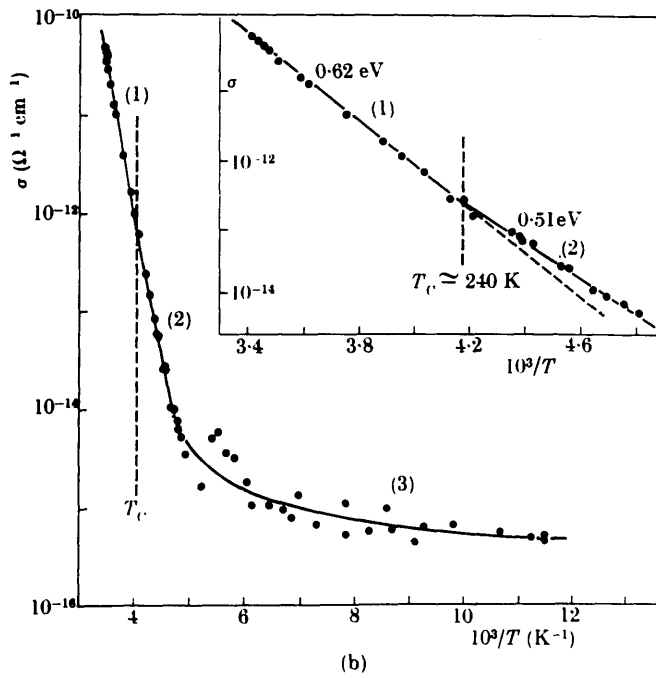


Diagram 2.3

The temperature dependence of glow discharge a-Si:H deposited at 500K (Le Comber and Spear 1970).

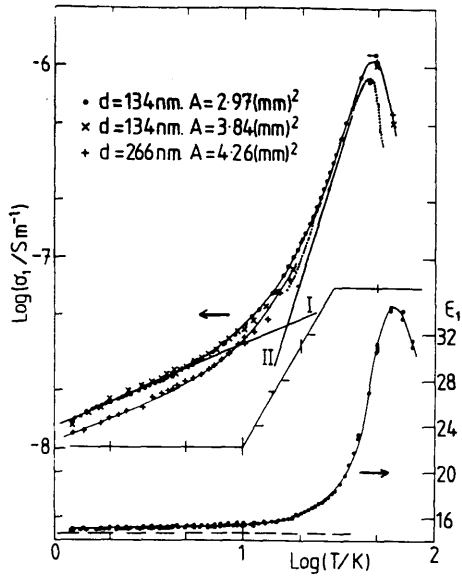


Diagram 2.4

The temperature dependence of G and C of an a-Ge sample measured at 3kHz. The high (I) and low (II) temperature regions indicated. An EPA fit is shown by the dashed line (Long 1981).

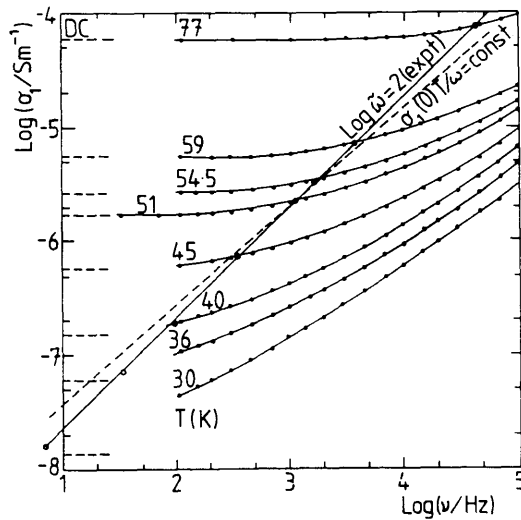


Diagram 2.5

The frequency dependence of the conductivity for an a-Si sample. The broken lines show the measured dc values. The locus of points at a scaled frequency of 100 is compared with an EPA fit, which suggests that $\sigma_1(0)T(\omega) = \text{constant}$. (Long et al 1988).

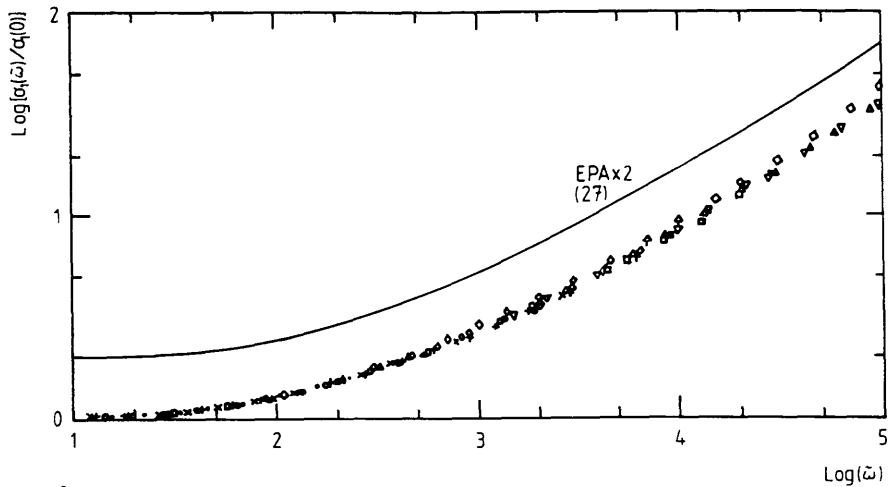


Diagram 2.6

The EPA fit to data for $(T_0/T)^{1/4} = 27$. The fit is offset vertically by a factor of two (Long et al 1988).

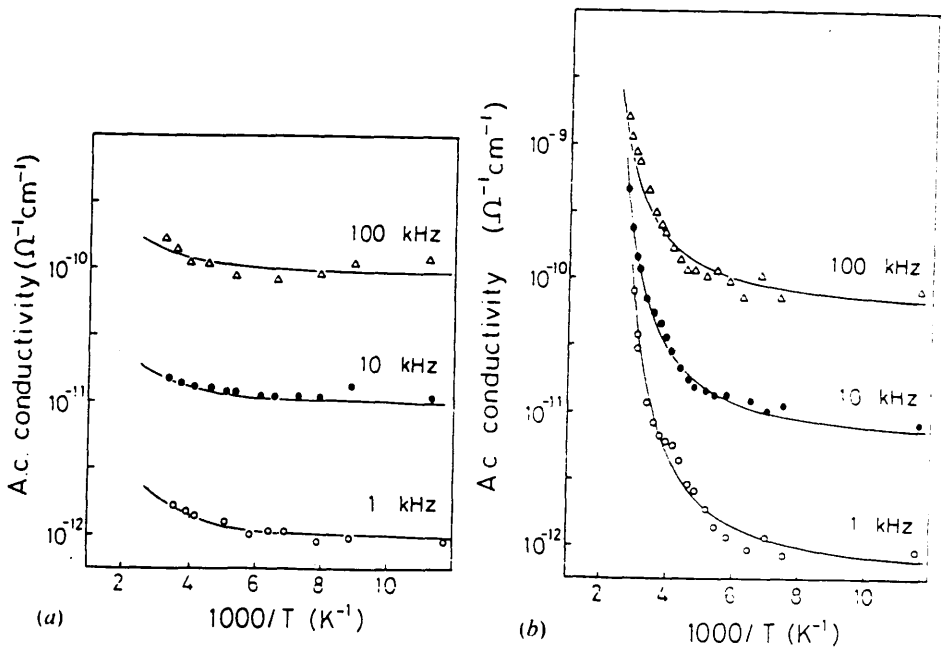


Diagram 2.7

Temperature dependence of σ_{ac} to illustrate the HTR and LTR in As_2Se_3 and is Ag doped As_2Se_3 (Hirata et al 1983).

CHAPTER 3

3.1 Light-Induced Changes in Amorphous Semiconductors

A number of optically induced changes have been studied in amorphous semiconductors. The work discussed in this chapter concentrates on experiments which involve the production of long-lived and metastable states by illumination. Such effects include the Staebler-Wronski effect, some luminescence effects, light-induced electron spin resonance (LESR) and some low temperature persistent photoconductivity phenomena. This chapter concentrates on the effects which have been observed in a-Si:H.

3.1(a) The Staebler-Wronski Effect

Staebler and Wronski (1977) illuminated doped and undoped a-Si:H films with light of wavelength between 600 and 900nm. Intensities of $100\text{-}200\text{mWcm}^{-2}$ were used. Under illumination it was observed that both the dark conductivity and the photoconductivity decreased with time. If the light was applied for around 4 hours, the dark conductivity decreased rapidly at first and the saturated decay rate was found to be dependent upon the illuminating intensity i.e. higher intensities produced a faster decay. Each value to which the dark conductivity decayed was found to be stable, to within a factor of 2, for days if the illumination was interrupted.

The light induced change was found to be completely reversible. If the sample was annealed at around 150°C it would return to its original state. The annealing temperature determined the rate at which the reverse process occurred.

The temperature dependence of the dark conductivity follows the Meyer-Neldel Rule. This is rewritten as

$$\sigma = \sigma_0 \exp(-E_a/kT) \quad (3.1)$$

where $\sigma_0 = C \exp(DE_A)$ (3.2)

E_a = the activation energy

k = Boltzmann's constant

T = temperature

and C, D are constants.

The value of E_a can be changed by doping the sample or by exposing it to light. The subsequent shift in the fermi level (and therefore of E_a) is responsible for the change in σ_0 and the change in the temperature dependent conductivity, $\sigma(T)$. Staebler and Wronski showed that the changes were a property of the bulk of the material. The changes in conductivity are due to a decrease in the number of free carriers and are consistent with a change in the density or occupation of deep-gap states. If the Fermi level is lowered towards the middle of the energy gap by the light then the activation energy increases and the conductivity falls. It is thought that new gap states are generated by the light. Similar changes in the activation energy and movement in the Fermi level have been observed by creating new gap states by other means such as the bombardment or deposition of the a-Si:H films at low substrate temperatures.

A mechanism to explain how new gap states could be created has been proposed by Staebler and Wronski (1980). They state that the photoconductivity change is not a direct absorption process since the same Staebler-Wronski change is observed irrespective of the

photoconductivity per absorbed photon. Experiments were performed with light of wavelengths from 600nm to 900nm in order to show a correlation between photoconductivity and the Staebler-Wronski effect. It is likely that after recombination or trapping at a localized defect, sufficient energy is released to create a local bond reorientation or displacement. Hydrogen which saturates dangling bonds in a-Si:H is likely to be involved. Thermal energy can then be supplied in the annealing process which would then cause relaxation of the displaced configuration and thus a return towards the pre-illuminated state. Further evidence of this mechanism can be seen when the activation energy for the annealing process is compared with the diffusion energy of hydrogen in a-Si:H. Staebler and Wronski (1980) obtain a value of 1.5eV.

A second model was also proposed by Staebler and Wronski (1980). Here electrons are optically excited to states which are in poor communication with the extended states. These electrons are trapped and no longer take part in the balance which establishes thermodynamic equilibrium. The Fermi level will drop as a result of the bulk being deprived of free carriers. A fall in the number of available free carriers will thus cause the dark conductivity to decrease. The fall in the photoconductivity can be explained by an increase in the recombination cross-sections. This will be caused by ionization of some defects by the transfer of charge or by the fall in the Fermi level.

The annealing process in this model is due to electrons being excited from their traps. An activation energy of ~1.5eV and the fact that these centres must be within 0.2 or 0.3eV of the mobility

edge, otherwise the centres would be lower than the Fermi-level and would not be thermally annealed, is consistent with the concept of the centres being in poor communication with the extended states. According to Steabler and Wronski this is because the centres are surrounded by a strong repulsive barrier which must be overcome if they are to be emptied by annealing.

Other models have been proposed to explain the metastable states obtained under illumination. Dersch et al (1981) explained these states by considering weak Si-Si bonds which break. Hydrogen atoms are transferred to these bonds from clusters of Si-H bonds at the internal surface of voids in the a-Si:H bulk. Elliot (1979) suggested that excitons generated by the light become self-trapped and produce D^+D^- pairs. Their Coulomb interaction and a "soft" lattice, near weak bonds stabilizes the charged dangling bonds. The metastable states created by the light could result from two neutral configurations of a single dangling bond, as suggested by Wantelet et al (1981).

In a recent review Fritzsche (1985) favoured the model in which new dangling bond states are created by the incident light. As the activation energy, E_A , increases as the illuminating time increases the Fermi level moves towards mid-gap. Fritzsche found that the rate at which this change occurs could be explained by the shape of the density of states within the gap.

3.1(b) Photoluminescence

Luminescence has been observed in a range of amorphous materials e.g. a-Si:H, a-As₂S₃ and a-Si:O:H. Experiments consist of illuminating the material under study with either constant radiation or with short pulses of light. Light is subsequently emitted from the material and

its wavelength and intensity can be measured. These experiments can be divided into those which study the luminescence intensity as a function of wavelength and those which measure the time dependence of the luminescence intensity. The spectral dependence of the luminescence intensity is shown in diagram 3.13(1). A peak is observed around the middle of the range of luminescence intensities. Street (1980) and Tsang and Street (1979) observed that the peak energy shifts to lower values, with time, after exposure to short-pulses of light. Initially, the peak energy decreases rapidly in ~ 100 n seconds which is attributed to a thermalisation process involving non-radiative transitions through band-tail states. A further decrease is found after $\sim 10^{-4}$ seconds has elapsed. This is due to carriers recombining by non-radiative transitions involving tunnelling.

The radiative processes responsible for the luminescence effect can now be considered. Electron-hole pairs are created by incident illumination and the resulting carriers are subsequently trapped in band-tail states or states due to structural defects such as dangling bonds. Recombination can then occur in principle by one of several mechanisms, all of which explain why the emitted radiation has a range of wavelengths at lower energies than the incident light. One mechanism is that excited electrons will thermalize down through the gap until radiative recombination takes place with a hole in a valence band-tail state. Another possibility considers electrons recombining with defect states emitting photons, and forming a band deep in the gap.

It is assumed that electron-lattice coupling is negligible in these two models. If this is strong then energy levels change as electrons are excited. This means that an electron excited from (1) (see diagram

3.1) to the conduction band can recombine at this same centre, but at a different energy (2). This gives a difference in excitation and luminescence energies (Stokes shift).

The position of luminescence peak is found to be temperature dependent and is explained by Street (1981) and Kosarev et al (1987). It is found, by Street, that the luminescence intensity increases in the range $10\text{K} < T < 50\text{K}$. At temperatures from 50K upwards the luminescence intensity decreases. Such effects are observed to be independent of the excitation wavelength and dependent on the intensity (see diagram 3.3).

The low temperature luminescence intensity is due to radiative transitions within the band-tails (Street 1981). Recombination can then take place by a geminate ^{process} (i.e. one in which an electron-hole pair generated in one event later recombine) unless the density of optically induced carriers is sufficiently high for a non-geminate process (i.e. a process in which the overlap between electron-hole pairs is such that recombination can take place with neighbouring electron-hole pairs). As the temperature increases to $\sim 50\text{K}$ (Tsang and Street 1979) the luminescence intensity also increases. This implies that the number ^{of} radiative transitions divided by the number of non-radiative transitions is increasing. Tsang and Street observed that their luminescence decay data showed that the decay times, i.e. without illumination, decreased with increasing temperature. This implies that the number of radiative transitions is increasing with inverse temperature.

Above 80K electron-hole pairs begin to diffuse apart rapidly in band-tail states. The increased thermal energy now supplied prevents

carriers being trapped in the band-tails. The dominating recombination mechanism is now non-radiative and is via defect states. The luminescence intensity therefore decreases as non-radiative recombination becomes more dominant.

The presence of dangling bonds, due to defect states, within the band gap also influence the luminescence intensity. Carriers recombine by non-radiative tunnelling via these states. It follows that materials with the highest density of defect states will have the lowest photoluminescence efficiency. Materials containing high densities of dangling bonds (e.g. a-Si) do not show a luminescence signal (Street 1987).

3.1(c) Light Induced Electron Spin Resonance (LESR)

LESR has been used to study recombination mechanisms in a-Si:H (Street and Biegelsen 1982, Carius and Fuhs 1982).

At low temperatures and under illumination a rise in the ESR signal is observed (Street and Biegelsen 1982, Carius and Fuhs 1982). Removal of the light causes the signal to drop, initially at a fast rate followed by a slow decay towards the equilibrium value.

The LESR signal is made up from the superposition of resonances and signals due to charge trapped in band-tail states and in states due to dangling bonds. The ESR technique only detects states which are paramagnetic (i.e. states in which the total spin of the system is not zero). Resonance occurs when the frequency of an oscillating magnetic field, applied at right angles to a static magnetic field, fulfils the conditions necessary for transitions between split energy levels due to the static field.

Street and Biegelsen (1982) and Carius and Fuhs (1985) studied

the LESR and luminescence data in a-Si:H. At low temperatures the recombination takes place radiatively and is geminate. This is a monomolecular process in which the separation of electrons and holes is less than the distance between the electron-hole pairs. As the density of electron hole pairs increases so that the inter-pair separation becomes comparable to the intra-pair separation the system can convert to bimolecular recombination. This means that carrier lifetimes will be shorter.

In LESR experiments evidence is available to show that the recombination takes place by a bimolecular process. This is different from the monomolecular process taking place in luminescence processes although these are performed at the same time by Street et al.

The plot of \log (excitation intensity) against \log (number of induced spins) is close to linear with a gradient of around 0.2 (see diagram 3.4). Such behaviour cannot be explained by a geminate process as a linear relation would be expected if this was the case.

Applying 1 sec pulses of light of varying intensity provides further evidence for the bimolecular recombination process. Diagram 3.4 shows that the decays observed when the light is removed span several orders of magnitude in time. The decays are shorter for low intensity pulses indicating that carrier lifetimes are increasing with intensity, which is expected in a bimolecular process. This implies that a broad distribution of carrier lifetimes is involved which is indicative of a tunnelling process.

The experiment using pulsed light, (of 20msec duration) applied every 12.5 sec, can be used to differentiate between distant pair and geminate recombination. In a distant pair recombination

process, a small number of electron-hole pairs are created by the first light pulse. These are widely separated. For times less than the time between pulses, luminescence is negligible, therefore the creation of induced spins is 100% efficient. More pulses increase the density of excited carriers and the degree of radiative recombination increases, as the average separation of electrons and holes decreases. An equilibrium situation is eventually reached. In a geminate process, if the electron-hole separations are such that recombination takes place before the next pulse arrives, then the same distribution of carriers is obtained after each pulse arrives. This predicts that a low density of induced spins and a high luminescence efficiency will be found, no matter how many pulses of light are incident on the sample.

The results obtained by Street et al (1982) show that this is indeed the case, thus suggesting a geminate recombination process.

Street and Biegelsen postulated a mechanism to explain recombination in luminescence and LESR experiments. Electrons are excited to band-tail states and thermalize by several short tunnelling transitions. The intra-pair radial distribution function of carriers before recombination is

$$G(r) = \sqrt{\pi/2\bar{r}^3} r^2 \exp(-r^2/\bar{r}^2) \quad (3.3)$$

where \bar{r} = average intra-pair separation $\sim 50\text{\AA}$.

$G(r)$ can be written as $G(\ln\tau)$ from equation 3.3 and knowing $\tau(r)$ (Diagram 3.5a shows plots of these quantities against the density of carriers. 3.5b shows the distribution after several pulses. The one pulse graph shows the carrier distribution when all carriers within

a radius R_x have recombined. The fraction of carriers remaining are longer lived and the number of these metastable states steadily increases. When these carriers reach a sufficiently high density recombination can take place between non-geminate pairs and a bimolecular process occurs. As the light continues to excite carriers the carrier distribution moves towards shorter lifetimes at a higher degree of excitation. This means that recombination is a mixture of a geminate process between short lived states and a non-geminate bimolecular regime of long-lived states. LESR is dominated by bimolecular behaviour since it measures the number of trapped carriers which are paramagnetic. The luminescence measurements are due to carriers recombining radiatively and are attributed to the faster geminate process.

Other work with LESR has been used to identify carrier types (Carius and Fuhs, 1985). They showed that the spin density of trapped holes in p-type material was larger than that of electrons and dangling bonds. The electron and dangling bond signal decayed more rapidly than that of holes. (See also section 3.3.)

IR radiation has the effect of quenching the LESR signal and will be discussed more fully in section 3.3.

3.1(d) DC Photoconductivity

Light exposure has been shown to increase the dc conductivity of a-Si:H samples. This is a different effect from the Staebler-Wronski effect discussed earlier (section 3.1(a)). The Staebler-Wronski effect involves the production of metastable states by the light. The dc photoconductivity discussed in this section decays to zero at long enough times without any need for annealing the

material. The division between the two effects is not sharp and a transition region is likely to exist.

Photoconductivity experiments involve illuminating the a-Si:H material with either short probes or continuous light. The intensity and temperature dependence of any optically induced changes in conductivity are then measured.

The intensity dependence of the dc photoconductivity is generally observed to obey the following law (Staebler and Wronski 1980, Hoheisel, Carius and Fuhs 1983 and Huang et al, 1983, for example).

$$\sigma_{\text{dcph}} \propto I^\gamma \quad (3.4)$$

The temperature dependence of this relation was investigated by Huang et al. It was found that γ varies from about 0.65 at -94°C to ~ 0.75 at around 100°C .

The measured photoconductivity is due to the incident light creating electron-hole pairs which contribute to the current. Recombination mechanisms will influence the dependence of the photoconductivity. At high ($\sim 250\text{K}$) temperatures recombination is thermally activated and the $\ln(\text{photocurrent}) \propto 1/T$. At lower temperatures carriers become trapped and the photocurrent will depend on the *trap* limited drift mobility. This is the more important regime as far as we are concerned and will now be considered in detail.

Experiments were performed by Spear et al (1986, 1987) and by Hoheisel et al (1984) to measure the low temperature photoconductivity in a-Si:H. Their discussion concerned the product $\eta \mu_e \tau_a$ where η is defined as the photogeneration efficiency, μ_e is the electron drift mobility and τ_a is the carrier lifetime within the light-absorbing

region of the sample. The photocurrent is obtained from the photoconductivity which is written as

$$\sigma_{ph} = e G \tau_a \mu_e \quad (3.5)$$

G is a quantity dependent on the light intensity absorbed by the silicon in a thickness, d , and $G \propto \eta I$. Both researchers found that the $\eta \mu_e \tau_a$ product rises by 4 orders of magnitude between 80K and room temp. Below 80K the value of $\eta \mu_e \tau_a$ tends to an almost constant value of $10^{-11} \text{ cm}^2 \text{ V}^{-1}$ (see diagram 3.2).

Hoheisel^{et al} interpreted their results by saying that carriers only contribute to the photocurrent during thermalization and are subsequently trapped in localized states within the band-tails. Spear et al suggest that another mechanism is responsible for the observed data. If the $\eta_c \mu_e \tau_a$ product is calculated from Hoheisel's results then $\eta_{pc} \approx 1$. This is unrealistic if the efficient low temperature luminescence process is considered. Both Hoheisel et al and Spear et al found strong anti-correlation between η_{pc} and η_{pL} i.e. at low T (below ~90K) $\eta_{pc} \sim 1$ and $\eta_{pL} \sim 10^{-1}$. Spear et al attribute transport through band-tail states as the major contributing mechanism to the photocurrent.

3.1(e) Transient Photoconductivity

Transient photoconductivity measurements have been used by several researchers (e.g. Orenstein and Kastner 1981, Huang et al 1983) to provide evidence for recombination mechanisms and states within the band gap. The experiments consist of exposing samples to short pulses of light (generally of the order of 100 p seconds up to a few n seconds). A power law dependence of the photocurrent decay is found

which follows $I_{pc} \propto t^{-s}$. At temperatures greater than 100K, $s = 1 - T/T_0$ (where T = the temperature and T_0 ranges from 300K to 1000K). Below 100K the value of s tends to one.

Huang et al used the multi-trapping model to interpret their results. The optically induced carriers are excited to extended states and then thermalise in a broad distribution of localised tail states. Huang et al then obtained a diagram (diagram 3.10) showing the density of states within the band-gap. This was accomplished by converting the time scale to an energy scale using $E = E_c - kT \ln(v_0 t)$ where v_0 = the escape frequency associated with the traps and E_c is the conduction band edge.

Monroe (1985) (and similar calculations performed by Movaghar et al (1986), and Grinewald et al (1986, 1987)) analysed the photocurrent decays using a model in which carriers become trapped in band-tail states after excitation and thermalisation. After trapping carriers can either hop down in energy (this is important for shallow states) or are activated to shallow states and subsequently hop down in energy (this is important for deep states). Monroe predicts that initially hopping down from shallow states will be responsible for the photocurrent decay, giving rise to a 1/time dependence with a logarithmic connection. As time progresses carriers will move to deeper energies and the recombination process will become slower. Thermal energy supplied to the sample should therefore excite carriers as described at the start of this paragraph and therefore increase the decay rate of the photocurrent. This mechanism is discussed again in Chapter 7 and its application to the optically induced ac loss data is considered. It is concluded that the temperature dependence of

the $\Delta\epsilon_1$ decays does not support Monroe's idea.

3.2 Recombination in Amorphous Silicon

Several carrier recombination mechanisms are possible in a-Si or a-Si:H. The dominating mechanism is dependent on structural properties (e.g. the concentration of defect states within the band gap) and experimental conditions (e.g. temperature and degree of illumination used to excite carriers). Diagram 3.9 shows the various recombination mechanisms identified by Street (1981).

Recombination mechanisms have been divided into radiative and non-radiative processes. Two radiative processes can take place, and these give rise to luminescence in a-Si:H. One mechanism is when carriers at the band edges recombine directly. The process causes photons with an energy comparable to the band gap to be emitted, although they cannot of course have a greater energy than the exciting photons. This process is most likely to occur at low temperatures in samples with a low density of defect states. Radiative recombination can take place at lower energies, via defect states. This occurs after carriers have become trapped in defects after having undergone tunnelling or thermalisation. This will occur if the defect density is sufficiently high and is more likely to take place at higher temperatures if carriers are thermally excited out of band-tail traps to defects.

Non-radiative recombination can also occur by more than one process. The major recombination mechanism at low temperatures is tunnelling to defect clusters. The electrons trapped in these clusters will then recombine with a trapped hole at a later stage. This is likely to be the major recombination in sputtered a-silicon samples

which have a high defect density.

At higher temperatures trapped carriers can recombine by a thermally activated diffusion mechanism. These carriers can be subsequently trapped in defect states and recombine by tunnelling.

At high excitation (above 10^{20} photons absorbed/cm³s¹) intensities two other recombination mechanisms are relevant. These are both non-radiative processes. Luminescence data (Street and Biegelsen 1982) shows a decrease in luminescence under pulsed illumination at high intensities. This cannot be explained by geminate or distant pair models. The LESR signal increases and appears to quench the luminescence. This is thought to be due to Auger recombination.

Such a process takes place when the excited carrier density is sufficiently high (greater than 2×10^{18} cm⁻³ - Street 1981) for non geminate recombination to take place, at high illuminating intensities. Auger recombination is non-radiative and involves three particles in overlapping electron hole pairs. Two possible mechanisms are illustrated systematically in diagram 3.8. The rate of this transition is sufficiently large, at high intensities, to dominate over radiative transitions, thus leading to a fall in luminescence.

The second process evident at high levels of illumination is recombination involving surface states. Evidence of such an effect is available (Shah et al 1980) from experiments using different wavelengths of light. Luminescence decays were studied at a constant illumination intensity. It was found that the decays increased in length with increasing photon energies incident on the sample of a-Si:H. This could be explained by carriers being excited by a

larger energy and diffusing further apart. The increased separation of the electron and hole results in a longer decay time which decreases the decay rate in luminescence. However evidence is available to indicate that surface recombination occur in Si:H. Experiments performed on samples of differing thickness show the initial luminescence decay is independent of thickness. The excitation density is also unaffected by thickness so that the initial decay is not a bulk property. It is probable that surface recombination takes place in defect or impurity states at the a-Si:H surface.

3.3 The Effect of Infra-Red Radiation on Optically Induced Changes

The photoexcited carriers which are trapped in band-tail states, at low temperatures, can recombine radiatively or non-radiatively. Luminescence is observed as a result of the radiative recombination of trapped carriers recombining with carriers trapped in the other band-tail. Non-radiative recombination proceeds by carriers tunnelling to defect states and recombining. These mechanisms are illustrated in diagrams 3.6 and 3.9.

3.3(a) Photoconductivity

Photocurrent transients have been studied by Fuhs (1985). A dual beam experiment, where a-Si:H films can be illuminated by both visible and IR radiation, was carried out. It was found that the photocurrent transient changed when IR radiation ($h\nu < 0.7\text{eV}$) was applied and removed from the a-Si:H film. The change consisted of a short enhancement followed by quenching at 130K. At 30K the photocurrent increased until a steady value is reached. This can be seen in diagram 3.7.

The observed IR quenching effect is thought to be due to

recombination rates being increased by the excitation of trapped carriers by the IR radiation. It is possible to explain the results using the recombination mechanism in diagram 3.6. Carriers are generated and after thermalization are trapped in band tail states. These carriers are either re-emitted to recombine radiatively or through defect states due to dangling bonds. The band tail electrons tunnel to neutral dangling bonds (D^0) to form a D^- state. Recombination then proceeds by a transition from the D^- state to a hole trapped in the valence band tail. If the mobility of trapped holes is increased then the recombination rate can be increased.

In doped films, enhancement of the photocurrent is observed in both n and p-type films under 50K. At 50K quenching is found in n-type films, but quenching is not seen until 130K in p-type films. The quenching effect vanishes (at 130K in n-type and 250K in p-type) at higher temperatures as a result of the thermal clearing of trapped carriers competing with the IR effect. A trap depth of 0.11eV for electrons in n-type material and 0.27eV for holes in p-type films can be obtained from these temperatures.

The temperature dependence of the quenching effect in n-type films vanishing at 150K is easily explained by the following idea. Traps are cleared by exciting the trapped carriers by supplying thermal energy. The fact that quenching is observed in p-type films at temperatures up to 250K is inconsistent with a trap depth of 0.11eV or 0.27eV. The spectral dependence of photocurrent quenching begins at 0.5eV or 0.6eV. This implies that transitions from D^- states, rather than shallow traps, are excited by IR radiation. In p-type samples this leads to an increase in the number of D^0 states

This will encourage more electrons to tunnel from band-tail states to D^0 states therefore the recombination rate will increase.

In n-type films electrons are excited from D^- states when the IR is applied. This would explain the observed initial enhancement. The tunnelling rate is strongly dependent on the concentration of D^0 states. An increase in their number carries the recombination rate to increase. This would account for the subsequent decrease in the photocurrent seen a short time after the application of IR radiation to the sample.

Further evidence to support the idea of IR quenching being due to the mechanisms described come from spin dependent photoconductivity result. These show that the tunnelling process of band-tail electron to D^0 states is important. Here it is suggested (Dersch et al 1983) that the direct capture of electrons at D^0 states competes with the tunnelling process as temperature increases. This occurs at a higher temperature in p-type than in n-type samples because there are fewer free and fewer trapped electrons in p-type films. It is likely that the decrease of the IR quenching effect with increasing temperature is due to the same process and not as a result of optical excitation directly competing with thermal excitation.

IR quenching ceases to be seen when the direct capture of electrons at D' states becomes significant. Thermal quenching is caused by the direct capture of thermally activated holes at D^- or D^0 states.

3.3(b) Photoluminescence

Quenching of the photoluminescence (PL) effect by IR radiation in a-Si:H has been observed below 100K. It has been seen in both doped

and undoped materials, although the quenching effect is larger in p-type films (Fuhs 1985).

A graph of luminescence intensity plotted against energy shifts to a lower energy and ceases to be a symmetric shape when both visible (1.92eV and $h\nu < 0.7\text{eV}$) and IR radiation are applied. Diagram 3.13 illustrates this and it can also be seen that the quenching effect is smaller at lower photon energies.

A similar effect can be obtained by applying a high electric field up to the films or by heating, which supplies thermal energy. The thermal effect is due to electrons being activated from band-tail states. The demarcation level is moved to a lower energy as electrons tunnel to D^0 states resulting in non-radiative recombination. Increasing diffusion of carriers due to higher temperatures in the higher band-tail states could also cause the same shift in the spectral dependence.

The IR quenching mechanism will work in a similar way, leading to the observed change in the spectral dependence of the luminescence intensity.

As the wavelength of the IR radiation is reduced a cut-off at $2.5\mu\text{m}$ is found in the PL quenching. This is similar to the cut-off seen in photoconductivity quenching and is probably due to the same processes. Trapped holes are excited and transferred to defects thus increasing non-radiative recombination.

If photoexcited holes (Varmozis et al 1984) are trapped at -0.5eV above the edge of the valence band then they will be strongly localized and have low recombination rates. These holes can move to shallow traps if they are excited by IR radiation. Here they are less

localized and electrons can recombine with them directly. This leads to an enhanced luminescence intensity. Within a few milliseconds more D^0 starts will be produced by tunnelling functions. Non-radiative recombination will thus be speeded-up to allow delocalized electron-hole pairs to interact with dangling bonds. Such a transient has been observed by Fuhs (1985).

3.3(c) The Effect of IR on LESR Measurements

The recombination of non-equilibrium carriers trapped after illumination of a-Si:H at low temperature have been studied using LESR. In experiments by Carius and Fuhs (Caruis and Fuhs 1985, Fuhs 1985) IR radiation was applied to the sample a short time after the visible illumination was removed. The slow decay can be seen (diagram 3.11) to be quenched by IR illumination. The photoconductivity and photoluminescence exhibit a transient response (see diagram 3.11) first increasing in magnitude and then decaying.

As in photoconductivity and photoluminescence measurements the LESR signal decreases under IR illumination because of trapped carriers being excited into higher states and then recombining in a similar manner.

Under illumination electrons are excited to dangling bond states, creating D^0 and D^- states. The rate of this transition is governed by the time taken for the tunnelling of band tail holes to D^0 and D^- states.

IR excitation quenches the LESR signal due to holes more strongly than that due to the electron-dangling bond signal in p-type material. These samples have a high density of trapped holes thus showing a larger LESR signal compared with the signal due to dangling bonds

containing trapped electrons. In order for charge neutrality to be maintained additional negative charge is needed in the conduction band tail and in the D^- states.

The decay mechanisms can be studied by varying the time at which the IR beam is applied after the removal of visible illumination. By plotting the logarithmic derivative of the peak value against \log (time) it is possible to obtain more information from the LESR, PL and PC decays. The three measurements show a similar form of decay (see diagrams 3.11a and (3.12) and it can be observed that decay times of the LESR signal are longer in p-type than in n-type material. The PC transient decays are independent of sample-type and fall on the same line as the lower LESR values for p-type material. The PL data is close to the LESR values for n-type samples.

A wide range of tunnelling distances would indicate that the lifetimes of trapped carriers is also widely distributed. This gives rise to the observed form of the decay. A calculation performed by Biegelsen et al (1983) and Boulitrop (1984) assumes a rectangular distribution of tunnelling distances. Some lines have been fitted to data taken by Fuhs (1985). These are shown in diagram 3.12 and can be seen to be a reasonable fit. It has also been assumed that tunnelling takes place between a trapped carrier and a dangling bond state. The radii of the band tail electrons and holes are calculated to be 10\AA and 8\AA respectively.

As temperature is increased it is found that the long decay is independent of temperature up to 65K. As temperature increases above 80K the decay is much faster. This can be explained by considering that recombination proceeds by tunnelling at low temperatures. At

higher temperatures thermal energy gives electrons and holes greater mobility and allows them to diffuse to defect states.

3.4 Optically Induced AC Loss

At low temperatures, Long and Holland (1985) discovered that if a-Si or a-Si:H, prepared by RF sputtering, is illuminated by visible light a change in capacitance and conductance is observed. Both C and G show a fast rise to an equilibrium value under illumination. As the intensity increases, the magnitude of the response increases. High and low intensity regimes were identified as $\Delta\epsilon_1 \propto I^{\frac{1}{2}}$ at low I and $\Delta\epsilon_1 \propto I^{\frac{1}{4}}$ at high I (see Chapters 6 and 7).

When the light was removed an initial fast decay, followed by a slow decay lasting many hours was found. A rate equation model was proposed to explain the effects observed in sputtered material and is successful in explaining the low intensity regime and the proportionality to $1/t$ found at intermediate times in the decay.

Holland (Ph.D thesis 1987) found that the magnitude of the optically induced response was dependent upon sample material. The largest ΔC values were observed in pure a-Si (both magnetron and conventionally sputtered materials showed a similar site of change in capacitance) and in a-Ge. Hydrogenated material proved to have a lower response, at high intensities, which increased with decreasing hydrogen content. This is attributed to the number of defect states present in the band gap. If hydrogen is introduced during sample preparation it has the effect of saturating dangling bonds and leading to a lower defect density. Under illumination these states trap carriers and contribute to the ac loss.

At low intensities in the $I^{\frac{1}{2}}$ region Holland observed that the optically induced change was higher in samples containing hydrogen

than in pure a-Si samples. Such behaviour is explained by considering that electrons are strongly self-trapped in this region (see Chapters 6 and 7 where $I^{\frac{1}{2}}$ region is described in detail). Evidence is available (Holland Ph.D. thesis 1987) to suggest that increasing the hydrogen content increases the energy scale of the self trapping. As states further from the Fermi-level are filled by increasing the illuminating intensity, and generating more carriers, transition to the $I^{\frac{1}{4}}$ region is observed. In heavily hydrogenated sample this transition will occur at a lower intensity than than is found in pure a-Si samples. This is due to there being fewer mid-gap states because of the hydrogen-saturated dangling bonds. These states will therefore be filled more quickly in hydrogenated material.

The optically induced ac loss in a-Si and a-Si:H (prepared by sputtering and glow discharge) is analysed in detail in Chapter 7.

3.5 Summary

The thesis generally describes measurements carried out below 100K in amorphous materials. In a-Si:H and a-Si a division in the conduction mechanism is found (see Chapters 5,6 and 7). Many light-induced properties have been discussed in this chapter, notably photoluminescence, transient photoconductivity, drift mobility and LESR. The Staebler-Wronski effect is less relevant since high light intensities are used to produce structural changes leading to metastable states being formed. These are only reversible by annealing samples at temperatures of around 150°C).

The low temperature region (i.e. below ~100K) is characterised by a strong luminescence signal, a low constant photoconductivity and

a long lived LESR signal. These effects have been shown to be influenced by IR quenching. The study of such effects provide information on both conduction and recombination mechanisms which have been discussed in the preceeding chapter.

The AC loss technique used by Long and Holland (1985) is a useful method of detecting carriers trapped in defect states. It is known that carriers are trapped in band tail states in a-Si:H and the purpose of this thesis was to find out if these carriers can be detected using the ac loss technique and then to obtain information on the properties of a-Si:H. These are discussed in detail in subsequent chapters (5,6,7 and 8).

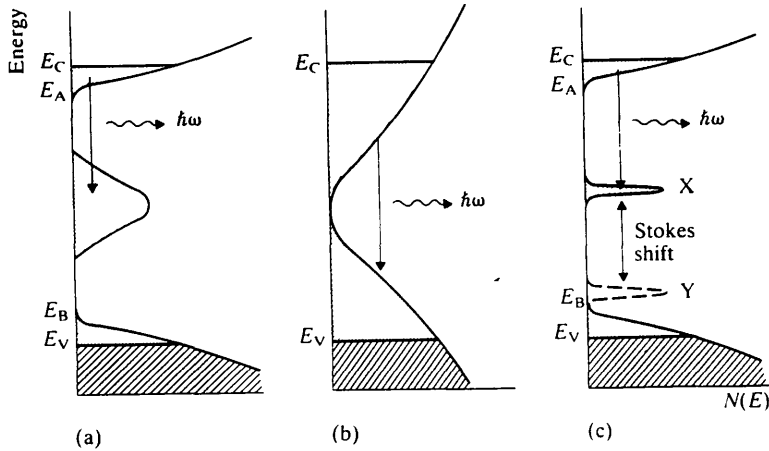


Diagram 3.1

Possible radiative recombination channels which give rise to a luminescent energy much less than the excitation energy: (a) and (b) assume no electron-phonon coupling and (c) assumes strong electron-phonon coupling (Street 1976).

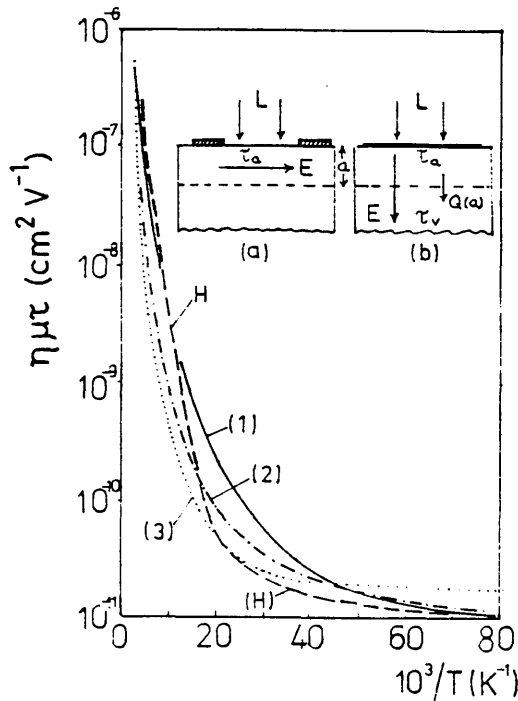


Diagram 3.2

The $\eta\mu\tau$ product determined from steady-state photoconductivity measurements on undoped a-Si plotted as a function of $10^3/T$. Curve H: results of Hoheisel *et al.* (1984) using coplanar electrodes; curves (1)–(3): present results on junction and Schottky barrier specimens. Inset: (a) coplanar electrodes: τ_a is the lifetime within the absorption depth a . (b) sandwich electrodes: τ_v , volume lifetime in i region. Curve (1) —, p^+i-n^- (1.84 μm); curve (2) - - - - - Cr $i-n^-$ (0.7 μm) and curve (3) p^+i-n^- (1.3 μm).

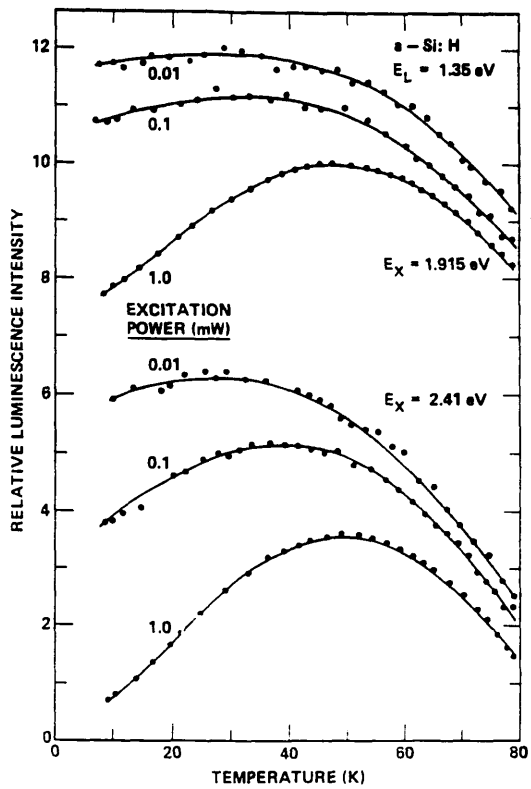


Diagram 3.3

Temperature dependence of the luminescence intensity in the range 0–80 K for various incident excitation powers and wavelengths as shown. The data are normalized such that the maximum intensity is 10 units of the vertical scale, and the different curves have offset zeros. The illumination spot diameter is 2 mm.

(Street 1981).

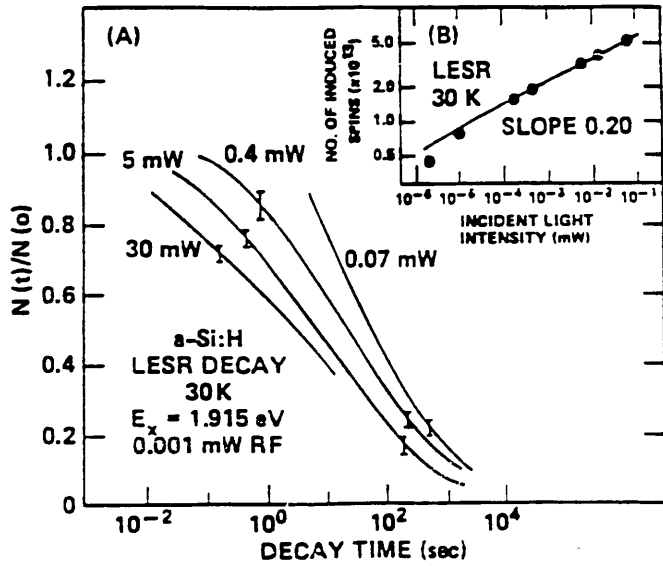


Diagram 3. 4

- (A) LESR decay in a-Si:H at different illumination intensities. Steady state conditions were attained before removal of the pulse.
- (B) Dependence of the equilibrium values reached, in an LESR experiment, plotted against the incident light intensity (Street and Biegelsen 1982).

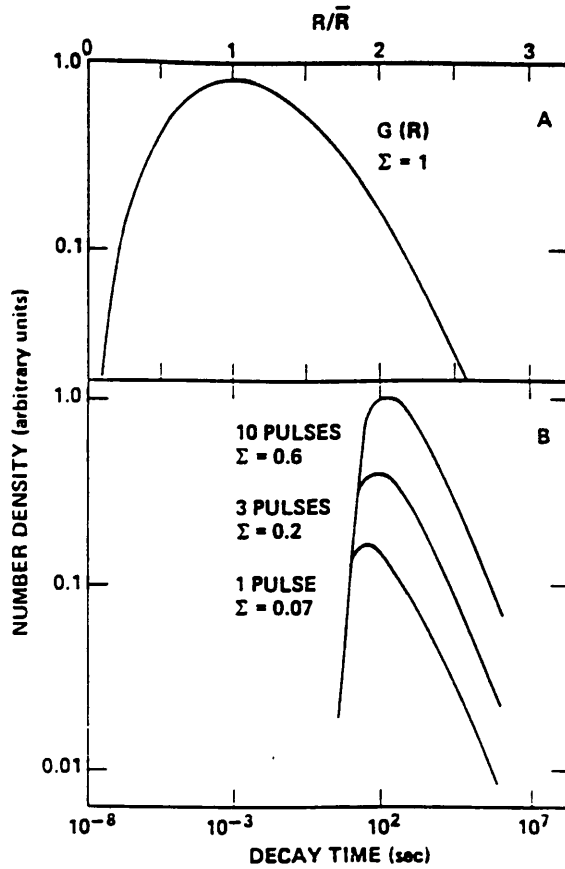


Diagram 3. 5

- (A) Model distribution of the pair separation of geminate electron-hole pairs.
- (B) The remaining distribution just before the 2nd, 4th and 11th pulse.
(Street and Biegelsen 1982)

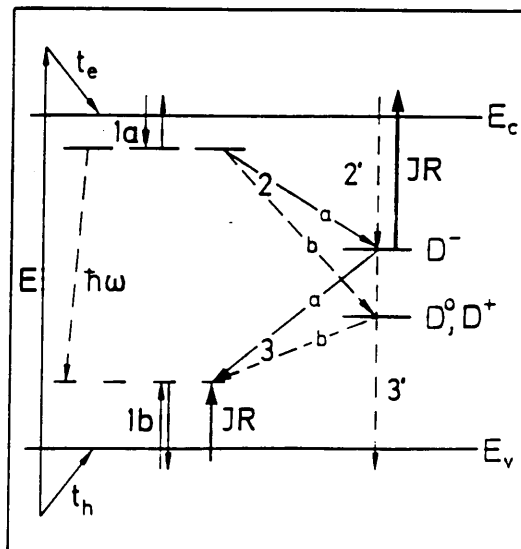


Diagram 3.6

Dersch et al (1983) - recombination mechanism. See text for details.

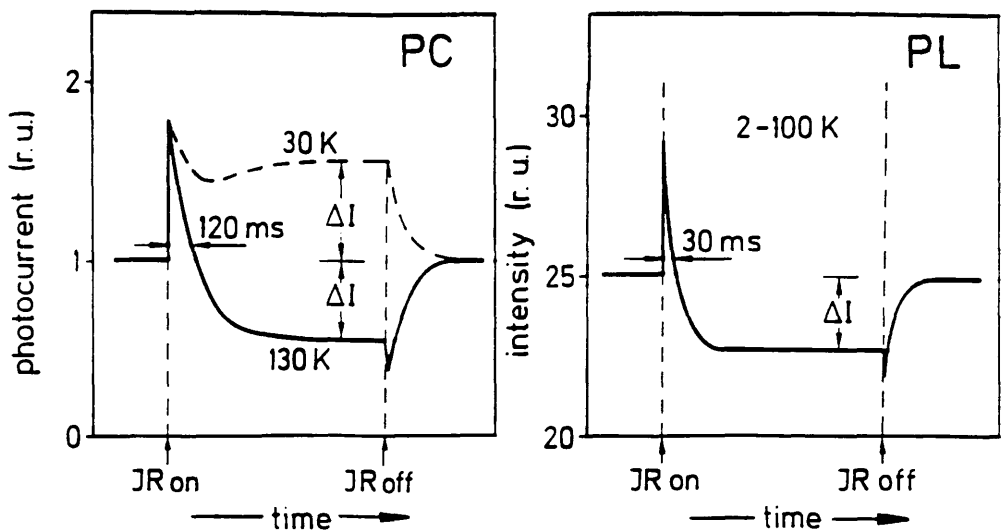


Diagram 3.7

Transient behaviour of the photoconductivity and the photoluminescence in a dual beam experiment. (Carius and Fuhs 1984).

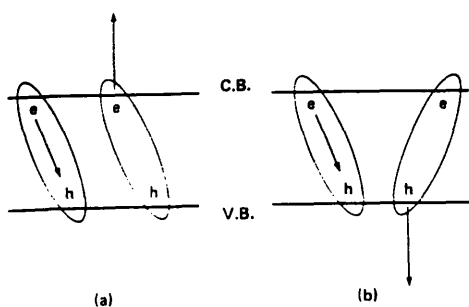


Diagram 3.8

Schematic diagram to illustrate two possible Auger recombination processes for two neighbouring electron-hole pairs. The ovals denote geminate pairs.

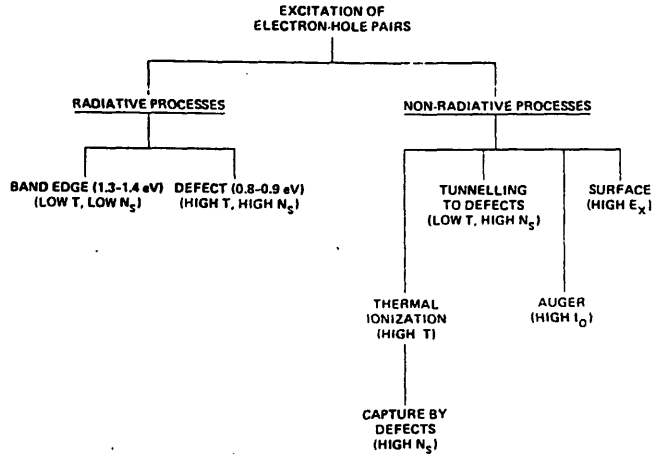


Diagram 3.9

Diagram showing the radiative and non-radiative recombination mechanisms identified by Street (1981).

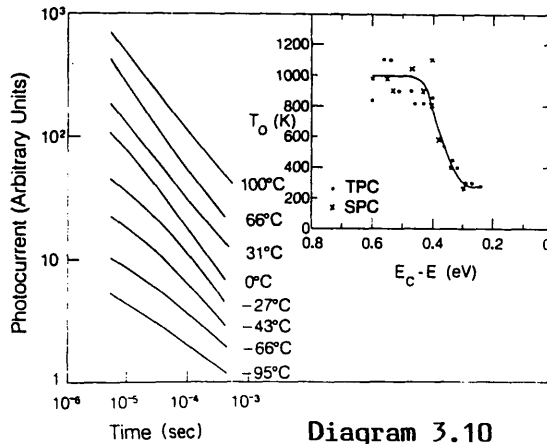


Diagram 3.10

Dependence of photocurrent on time at different temperatures. The inset shows T_0 as a function of energy away from the conduction-band edge as obtained from the transient and steady-state photoconductivity data.

Huang et al 1983.

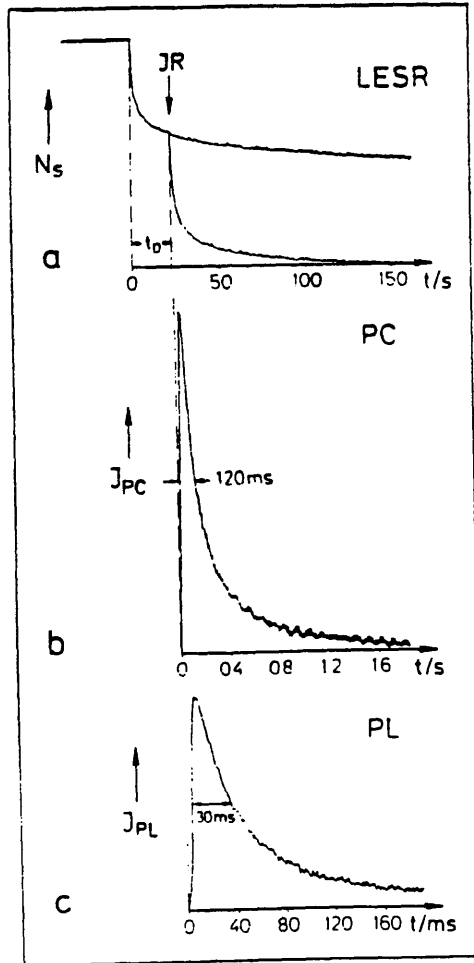


Diagram 3.11

Transients of (a) LESR, (b) Photocurrent and (c) photoluminescence at 15K. The plots are exposed to an IR beam (of energy $<0.7\text{eV}$). The same light intensities are used in (b) and (c), but that in (a) was much lower. (Carius and Fuhs 1984).

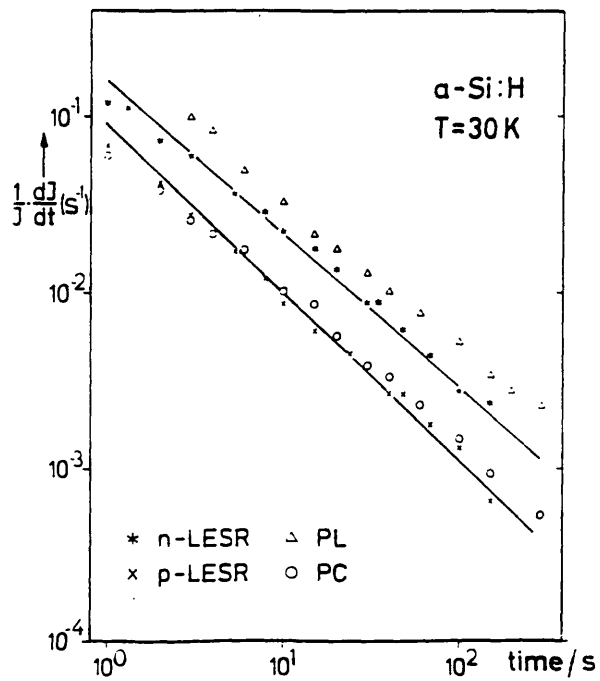


Diagram 3.12

The LESR decays for n and p type a-Si:H at 30K. The full lines are calculated (Carius and Fuhs 1984).

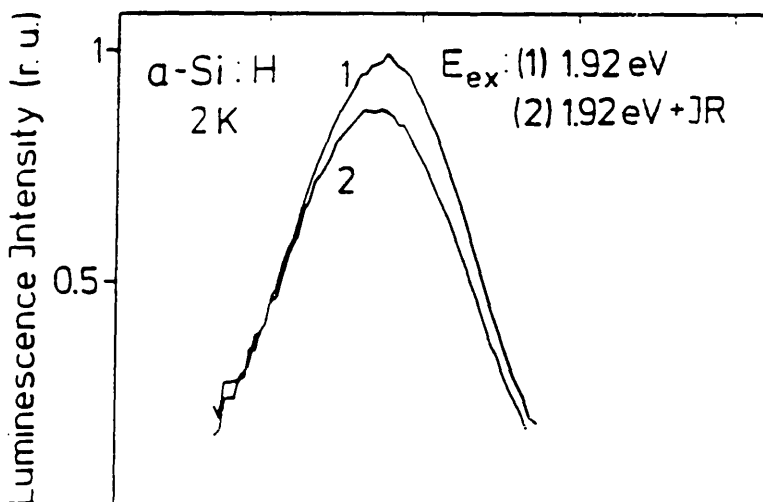


Diagram 3.13

Luminescence spectre for single (1) and dual (2) beam measurements (Fuhs 1985).

CHAPTER 4

In order to study the optical properties of amorphous silicon it was necessary to prepare samples in thin film form. In this chapter sample geometry (section 4.1), preparation details (4.2 and 4.3), and methods of cooling to low temperatures (section 4.4 to 4.5) are discussed. Sample mounting procedures (4.7) and details of the optical techniques (4.9 to 4.11) are dealt with, as well as temperature control (4.8) and the techniques used for measurements (4.12 to 4.14) are described in detail.

4.1 Sample Geometry

The thin film amorphous silicon samples studied using the ac bridge technique were prepared in sandwich form. This involves the sequential deposition of a bottom electrode, on a glass substrate, followed by the a-Si film. Finally, a top electrode is deposited on the a-Si. Coplanar electrode configurations (see diagrams 4.1a and b) are less suitable for measurement with an ac bridge due to their lower conductance. Moreover capacitance measurements are affected by edge effects to a greater degree than with sandwich samples.

Contact effects, due to the metal-semiconductor interface, are the major problem with sandwich samples. It is unlikely that the electronic properties of a-Si are determined by charge carriers at the metal-Si interface because of the high density of states in the energy-gap (see section 5.9 for details of contact diffusion and how the data is affected). This is evident from the ac and dc conductances being independent of sample thickness. For example, in a-Si sample MA4 the ac conductance at a 2kHz measuring frequency is $1.25 \times 10^{-9} \times \text{Scm}^{-1}$ for either the thick or thin junction at 10K.

The formation of any barrier at the interface is negligibly

small since the current-voltage characteristics are symmetrical at the measuring voltages used. It is therefore concluded that the electronic properties measured are determined by the bulk of the a-Si.

4.2 Sample Preparation

Samples were prepared using three techniques which are described below and particular details of each type of sample will be discussed in section 4.3.

4.2(a) Thermal Evaporation

This method relies on material being brought to its melting point and vaporised. This process is carried out in a vacuum chamber (usually a glass bell-jar) which has been pumped to around 10^{-6} Torr by a diffusion pump. Heating energy is supplied by passing a high dc current through a tungsten wire or molybdenum boat on which the material to be evaporated is placed. It is also possible to vaporise material by heating using electron-beam bombardment from an electron gun within the chamber. The substrate is clamped to a holder whose temperature can be varied by means of a heater.

In order to overcome the problem of inhomogeneous deposition of material "flash evaporation" can be used. This involves dropping powder onto a heated ribbon to vaporize it instantly.

The properties of evaporated films are dependent on a number of factors. These are

1. Substrate temperature
2. Substrate-source separation distance and orientation.
3. Base gas pressure in the vacuum chamber - usually kept as low as possible to eliminate impurities.
4. Impurities from the evaporation boat and from gases released from surfaces within the chamber.

5. Filament or boat temperature (the filament current can be monitored on an ammeter during evaporation).

Evaporation was useful for preparing As_2Se_3 samples. Thermal evaporation is only suitable for preparing a-Si under ultra-high vacuum conditions due to the a-Si's ability to gather oxygen strongly.

4.2(b) R.F. Sputtering

The sputtering process is carried out within a chamber which can be pumped to low pressures ($\sim 10^{-7}$ Torr) using a diffusion pump. Low pressure gas (either argon or a hydrogen-argon mixture at a pressure of around 5 m Torr) is allowed into the chamber.

A radio-frequency (RF) voltage of 13.56 MHz is applied between two electrodes, within the chamber, to create a plasma. The lower electrode (this set-up is used in the Glasgow system shown in diagram 4.3, but the electrodes can be reversed) is made from the material to be sputtered (target) and the upper electrode is metallic and generally earthed. The substrate (a glass slide) is attached to this electrode and its temperature can be varied by a heater.

An RF voltage is applied between the target and substrate. During positive half cycles, electrons are attracted to the substrate and during each negative half cycle ions are attracted to the target. The electrons' higher mobility ensures that a greater number reach the target than there are of ions reaching the substrate electrode. This results in a build-up of negative bias on the target. This negative voltage now causes a plasma sheath of around 5-10mm in thickness to be formed across the surface of the target. The dc voltage is now dropped across this plasma sheath causing ions to be accelerated across it. These ions bombard the surface of the target and material is ejected from the silicon. The ejected material is

then carried to the substrate resulting in a thin film of a-Si to be built-up. Typical current densities are of the order of $\sim 1 \text{ nAcm}^{-2}$. If the target is replaced by a permanent magnet (magnetron sputtering) the current density is increased (to around 40 mAcm^{-2}) and the deposition rate is greater. (See Elliott 1983).

Variables affecting the reproducibility of films and deposition rates are:

1. Sputtering gas pressure and flow rate.
2. Ratio of hydrogen to argon in sputtering gas.
3. RF power applied to the target.
4. Bias voltage of target or substrate.
5. Substrate-target separation.
6. Presence of permanent magnet around the target.

4.2(c) Glow Discharge Decomposition

As in the sputtering process, a plasma is formed between two electrodes (capacitive coupling) in a chamber containing low pressure silane (SiH_4). RF power (of around 14 MHz and 1-10W power) is applied between the electrodes (which may also be inductively coupled). Chemical decomposition of the SiH_4 gas (some extra hydrogen can be added) to smaller molecules then occurs, leading to the deposition of a-Si:H on a glass substrate (which may be heated). By introducing gases such as PH_3 and B_2H_6 into the chamber, along with the SiH_4 n or p-type doping can be achieved. Dopant atoms are incorporated into the structure of the a-Si:H.

Due to the presence of hydrogen in the SiH_4 gas it is only possible to produce hydrogenated amorphous silicon, therefore the sputtering process is required to make pure a-Si.

A number of factors influence the films formed in this method.

These are listed below.

1. Gas pressure and temperature (see section 4.3 for particular details of these quantities).
2. Argon - SiH_4 ratio within the chamber.
3. Gas flow rate and time within the chamber.
4. Shape of chamber and the position of the substrate relative to the plasma.
5. Applied RF power.
6. Substrate bias voltage.
7. Substrate temperature.
8. Whether the RF power is coupled to the plasma by the inductive or capacitive technique.

4.3 Preparation Details

Sputtered Sample

MA4 was produced by magnetron sputtering. The aluminium target used for contacts was presputtered for 15 min. in pure argon before deposition. Deposition times were around 45 min. in pure Ar. The Si films were deposited for $1\frac{1}{2}$ and for 3 hrs. (double thickness) after presputtering the target for 15 min. in pure argon. The argon flow rate into the sputtering chamber was at rate 10 (on a scale up to 50). The outward flow rate was measured on a Furness Capacitance micromanometer to be $0.05 \text{ Torr}\cdot\text{s}^{-1}$.

RF power was supplied at a rate of 100W with a dc voltage of 300 Volts during silicon deposition and $\sim 1.1\text{KV}$ during Al deposition. This sample was sputtered in pure Ar with no additional hydrogen.

The semi-transparent gold electrodes were evaporated without a break in the vacuum and Al tabs were deposited at the edges to

allow pressed indium contacts to be made.

Glow Discharge Samples

The glow discharge samples were a-Si:H deposited upon an ITO coated substrate. The $n^+ - i - n^+$ samples (K-type) were prepared in a 50% SiH_4 in H_2/Ar mixture at a chamber pressure of 0.25 Torr. Doping (in the n^+ layers) was carried out by the addition of 5000 ppm in volume of PH_3 . The substrate was held at 250°C and a power density of $0.06\text{W}/\text{cm}^2$ was used. S type ($n^+ - i$) samples were prepared in the same way.

Doped samples (n^+ , D-type) were prepared using identical conditions, apart from the gas mixture which contained 50% - SiH_4 without extra hydrogen. *The samples were prepared at Gifu University, Japan.*

4.4 Sample Cooling and Cryostat Design

Cooling samples from room temperature down to 1.2K requires the use of sophisticated cooling techniques. Two different methods were used in the course of the experimental work described.

The first technique involved cooling to 12K using a CII Cryogenics cryocooler (model number 215C). This machine uses a Gifford-McMahon cycle to cool to low temperatures. (See White - Experimental Techniques in Low Temperature Physics, Oxford 1968.) This cycle consists of four stages (refer to diagram 4.5). The first stage involves compressed helium gas flowing into the warm end of the cylinder when the piston is displaced towards the cold end. The piston then moves upwards (warm end in diag. 4.5) and the size of the cold volume is increased. Gas is displaced through the regenerator, towards the cold end, and more gas enters through the intake valve, which remains open, to equalize the gas pressure. The expansion phase, and third stage, occurs when the intake valve is

closed and the exhaust valve is slowly opened. The expansion causes the cold volume to be cooled and the final stage takes place as the piston moves downwards to displace the remaining cold gas. By repeating this cycle, cooling to around 12K can be achieved in the CII cryocooler.

Cooling from room temperature to 12K generally takes around 2 hrs, but if temperature and frequency dependent data are taken as cooling occurs, this time increases.

Cryostats

The other cooling technique involved passive cooling using liquid helium. A glass cryostat is contained within a stainless steel outer dewar as shown in diagram 4.6. An insert, onto which the sample is attached, is then placed into the glass container. Liquid nitrogen is contained by the stainless steel dewar. This surrounds the helium container and prevents rapid evaporation of liquid helium. Liquid helium in the glass cryostat is used for cooling to 4.2K. Lower temperatures can be obtained (down to 1.2K) by decreasing the He vapour pressure. This is achieved by pumping the cryostat as indicated in diagram 4.6. Similarly, if the cryostat contains liquid nitrogen it is possible to lower the vapour pressure and reach temperatures of ~50K.

To obtain temperatures above the boiling point of liquid helium a constantan wire heater, in good thermal contact with the sample is used. By passing a controlled current through this heater (see section 4.8) we can attain temperatures up to 40K. If the inner glass container contains liquid nitrogen it is possible to heat the sample to ~100K (see MA4 data - graph 5.3).

Long Term Helium Dewar

An Air Liquide 38 litre helium storage dewar was also used for cooling to 4.2K. This had the advantage of holding helium for long periods of time thus enabling week long experimental runs at 4.2K to be carried out. A specially designed insert was used with this dewar. This insert can be lowered directly into the dewar and contains the electrical connections to the sample, along with the Cu and Ge thermometers and fibre optic cable (see Holland Ph.D. thesis 1987, section 4.5).

Low Temperature Inserts

The low temperature inserts consisted of a brass top plate connected to a copper tail-piece by means of thin stainless steel and cupro-nickel tubes. Both these materials have high mechanical strength and low thermal conductivities. This reduces heat leakage to the environment surrounding the sample.

Electrical connection is made to the sample which is mounted on the copper tail-piece by feeding vinyl coated copper wires through several copper-nickel tubes. These tubes are carried through the helium bath therefore allowing the wires to be cooled. The wires are vacuum sealed at the cryostat head, by Araldite. The wires are then led into the copper can (see diagram 4.7). Stycast compound is used to vacuum seal the wires going into the can. Stycast is used for this purpose since its thermal contraction is similar to that of copper-nickel. This prevents the Stycast from splitting off the metal at low temperatures. The thermometer wires and heater wires are led into the copper can in other cupro-nickel tubes. Thermal earthing is achieved due to the wires being at helium temperatures outside the can by the Stycast seals. The wires are then attached to the sample

mounting platform on the tail-piece. They are thermally earthed to the copper platform by using Stycast. Interlead capacitances are minimized by feeding two sets of wires to the tail-piece in separate cupro-nickel tubes. By connecting the two sets of wires to different sides of the mounting platform (see diagram 4.8) connection can be made to the sample from different sets of wires. This will reduce the effect of a capacitance due to parallel wires running together over a distance of ~ 1 metre.

The copper vacuum can at the lower end of the insert encloses the copper tail-piece. This ensures that the sample is thermally decoupled from the liquid gas thus enabling the sample to be heated to temperatures greater than that of the refrigerant bath. The can was vacuum sealed by means of an indium ring and pumped to ~ 0.01 Torr before cooling. Cryopumping reduces this pressure further when liquid helium is introduced into the system.

The pumping tube is used for evacuating the can. To minimise the effects of room temperature radiation causing heating several radiation shields are put in the pumping tube.

The fibre optic cable was carried to the can by means of a thin stainless steel tube and sealed at the cryostat head, again by Araldite, after removing the cladding around the fibre. Sealing at the lower end was carried out by soldering around the tube at the point of entry to the can.

4.5 High Temperature Sample Holder

In order to study AC and DC conductance up to 440K a different sample holder was used (the maximum temperature found to be obtainable with the standard He insert was ~ 330 K due to limitations with the heater). The insert is similar in construction to a low temperature

insert, but it is not necessary to use stycast seals. Araldite seals were found to be leak tight at all the temperatures involved.

Temperatures were measured with a calibrated copper coil thermometer and cross checked with a thermocouple. Temperature stabilization was accomplished with an Oxford DTC2 automatic Temperature Control Unit. The sample can was evacuated in order to prevent oxidation of the sample at high temperature.

4.6 Relative Importance of Cooling Techniques

In order to study the optical properties of the a-Si or a-Si:H samples they must first be cooled to low temperatures. Different cooling techniques were appropriate to different types of samples. The majority of a-Si:H samples were cooled in the CTI cryocooler. This enabled samples to be cooled easily and allowed the selection of any temperature above the base temperature of 12K to be straightforward (see section 4.8). As chapter 6 explains in detail, temperatures of 50K must be obtained. This is not possible with the helium cryostats due to limitations in the heater current and the rate of helium boil off will be substantially increased at this temperature (especially during long runs of 90000 seconds). It is possible, however, to transfer inserts from the liquid helium to a nitrogen bath to achieve a temperature of 77K, but this is time-consuming when compared with the convenience of the CTI Cryocooler.

The fact that any temperature from 12.5K to room temperature can be selected also eliminates the need for separate measurements to be taken from 50K to 100K using liquid N₂, and from 1.2K to 30K, using liquid He. The temperature dependent and frequency dependent data can therefore be taken in a "clean sweep" down to base without

breaks in measurement.

Liquid helium was mainly used for cooling samples below 12K. Experiments were performed on both pure a-Si and a-Si:H. The a-Si samples did not require heating to 50K to return them to this dark state, therefore it was not necessary to use the CTI Cryocooler. Optical runs could be performed with a good degree of temperature stability at 4.2K on both a-Si and a-Si:H samples, especially for K12 and D2 in the long-term dewar.

4.7 Sample Mounting

Samples were mounted on the copper tail-pieces of the inserts. In some cases the samples were raised by means of copper blocks or thin sheeting to allow illumination through the bottom electrode.

The glass slides were glued to the copper by means of a 50/50 mixture of Bostik No 1 adhesive and acetone. This enabled good thermal contact between the sample and the mounting stage to be made. The adhesive is also flexible down to low temperatures and allows the differential thermal expansion between the glass substrate and copper block to be accommodated.

Electrical connection was made by attaching wires to the sample electrodes. These wires were stuck down by Electrodag (a conducting paint with a high silver content) or by pressed indium contacts (MA4 only). Pressed indium contacts are preferable to Electrodag contacts because of their greater mechanical strength. This means that the wires are less likely to become detached by thermal contraction or by vibration during the cooling process. Unfortunately, pressed indium contacts are unsuitable for use with ITO backed samples as the a-Si film can be damaged or punctured during the mounting procedure.

These contacts influence the apparent conductance of the samples by offering a resistance in series with the a-Si. This is explained in greater detail in section 5.2.

4.8 Temperature Measurement and Control

Temperatures were measured using sensors whose resistance varied with temperature. A constant current was applied to all the sensors used and the voltage was measured. This was accomplished by temperature control units (TCUs) which will be discussed later.

To measure temperatures above 50K, a calibrated copper coil thermometer was used. Below 50K, the resistance becomes too invariant with temperature to be of practical use due to the current limitations imposed by the TCU. Using this thermometer it was possible to measure temperatures up to room temperature. Copper coil thermometers and other sensors were attached to the copper tail-piece of the insert in good thermal contact with the sample.

A second sensor was also attached to the inserts, also in close thermal contact with the sample. This was a germanium thermometer which was capable of measuring temperatures from 1.2K up to 40K. Above 40K a loss in sensitivity rendered the diode unsuitable for use at higher temperatures.

The silicon diode used in the CTI Cryocooler could measure temperatures from 12K up to room temperature. This differs from the Ge thermometer in being a p-n junction device with non-linear I-V characteristics (the Ge thermometer is a linear resistive element). At a constant sense current of 10 μ A the voltage drop across the diode will increase from 0.4V to 2.0V over a temperature range from room temperature down to 10K.

The TCU, which controlled the temperature, works by applying a constant current to the sensor and the voltage can be measured, thus determining temperature. To select a temperature above the boiling point of a liquid gas the voltage signal must be monitored, amplified and compared with a reference signal which corresponds to a preset temperature. This process now enables a controlled output current through a constantan wire heater to be produced. Automatic operation ensures that the temperature is monitored constantly, enabling the heater output to be controlled precisely.

Two such devices were used in the course of this work. These were a Lakeshore Cryotronics Inc Cryogenic TCU (Model DTC-500SP) and a home-built TCU. Although the Lakeshore TCU contains more sophisticated electronics, both controllers operate on the principle described above. The block diagram (diag. 4.9) shows the Lakeshore TCU and it contains the following stages.

1. A constant current source to supply the thermometers.
2. The voltage across the thermometers is fed through an amplifier. This creates a positive current through the $3M\Omega$ resistor into the current summing amplifier.
3. The digital set point (present temperature) is converted to an analogue voltage by a DAC. The resulting negative voltage is applied to a string of resistors and the current generated is fed into a summing amplifier to balance the thermometer current. When a balance is achieved the digital set point is the actual temperature measured by the sensor.
4. The error signal is measured on a null meter and can be integrated. The output signal is then added to the existing controller output. This enables the overall output to change until no error remains.

The temperature is now at the required point with no offset in the set point.

5. A heater is supplied by a current controlled by the size of the error signal measured on the null meter and by the set point.

During an optical experiment it is necessary to maintain a stable temperature for ~ 90000 secs. It is therefore important to measure any temperature fluctuations and investigate their effect on the data obtained.

By measuring the temperature (recorded automatically using the IEEE interfaced voltmeter and QL computer) over time periods of ~ 90000 seconds it was possible to estimate the temperature drift. This involved comparing the measured voltage with the temperature calibration graph for the germanium thermometer. Graph 4.10 shows that the temperature is remarkably stable with a drift corresponding to better than 0.005K until the helium begins to boil off. This occurs at 20000 seconds. The effect on ~~some~~ results can be seen by examining graph (6.6) which shows the capacitance data plotted against time. Temperature fluctuations of 0.005K would imply that capacitance changes due to this are negligible. A noticeable peak is observed at 70000 seconds which corresponds to the helium evaporating and a temperature rise of $\sim 1\text{K}$. Refilling the cryostat cooled the sample to 4.2K and thus achieved a steady temperature.

The CTI Cryocooler, in conjunction with the TCU, maintains a stable temperature remarkably well. The temperature drift at low temperatures (less than 50K) was measured to be less than 0.01K over a period of several days. Such a change in temperature corresponds to a capacitance change of around 0.005pF (for sample K11 - other samples have a similar temperature dependence). Such a change in

capacitance does not have a significant effect on the optical results.

Short term temperature fluctuations are easily recognized on the capacitance versus time graphs. These changes can be seen as small oscillations (about 5×10^{-4} pF in magnitude and occurring over a few hundred seconds). The fluctuations in temperature are therefore negligible since most capacitance changes under illumination are of the order of 0.01pF to several pF.

In order to measure temperature drift and temperature fluctuations it was necessary to calibrate the offset shown on the null meter. This was achieved by noting the offset which corresponds to a known temperature change. By keeping the gain control at the setting it was at during an experiment, the temperature changes observed could be compared with the values obtained from the calibrated offset.

4.9 Sample Illumination

The main source of light for sample illumination was a 2mW Coherent He-Ne laser ($\lambda = 633$ nm). A water cooled tungsten-halogen lamp in conjunction with a PRT MC1-04 monochromator was used to provide illumination at wavelengths between 500 nm and 1 μ m.

The optical bench set-up consisted of a linear arrangement of a light source, filter holder and fibre holder mounted on X-Y movement stands as shown in diagram 4.11. A 3m fibre optic cable was used to collect the light in both methods of illumination. The narrow laser output beam was defocused in order to ensure straightforward alignment with the fibre and to minimise the risk of a slight vibration causing misalignment.

Illumination intensity control was accomplished by using pre-calibrated neutral density filters and by varying the laser to fibre

distance. At low intensities it was necessary to shield the optical bench assembly from ambient room light.

Samples with transparent top electrodes could be illuminated directly from the fibre output in the CTI Cryocooler as shown in diagram 4.12. In the standard helium insert the light output from the fibre was reflected from a front Al coated mirror onto the sample. (See diagram 4.13.)

4.9(a) Illumination through ITO bottom electrodes

Since ITO is semi-transparent, it is possible to illuminate a junction through the ITO back electrode. This was achieved by raising the sample on copper blocks and reflecting the light from the fibre from a front aluminised mirror, positioned between the blocks, and onto the sample from below. The mirror was angled to allow higher illuminating intensities to be available. This method was useful in the CTI cryocooler and standard He-inserts, but in the long term He dewar a different arrangement was used. This is due to the small size of the mounting block and surrounding can (less than 50 mm external diameter in order to enter the neck of the dewar which is 50 mm in diameter). The sample was angled and attached to thin Cu sheeting as illustrated in diagram 4.14. Thermal earthing was achieved by fastening the sheeting to the copper tail-piece and coating with a Bostik-acetone mixture. Higher illuminating intensities could be obtained using this technique as the fibre to sample distance is small (~1-2 mm here as opposed to 7 mm when a mirror is used).

4.10 Intensity Calibration

To measure the intensity of light falling on the a-Si sample the system must be calibrated. This involved measuring the light

intensity at the end of the 3m fibre before connecting it to the cryostat fibre. Intensity measurements were made with a Photodyne 88XLA light meter. After attaching the 3m fibre to the cryostat fibre a second intensity measurement is carried out at a pre-measured distance. This distance is of the order of 2 mm - 10 mm, similar to that of the junction-fibre separation.

In order to obtain the actual light intensity absorbed by the junctions a number of corrections must be made. These are:

1. If the junction-fibre separation differs from the photodyne-fibre distance the intensity must be corrected using the inverse square law. The factor is calculated to be

$$\frac{(\text{cryostat fibre-photodyne distance})^2}{(\text{cryostat fibre - junction distance})^2}.$$

2. The junction was not normally in the centre of the cone of light output from the fibre. The intensity profile of I vs ϕ is shown in diagram 4.15. ϕ is the angle between the line of the cone centre and the line from the junction to the fibre output. (See diagram 4.16a.) As ϕ changes from 0° (the junction is at the cone centre) to 90° the intensity incident on the junction decreases. By measuring the horizontal distance, d , between the cone centre and the junction, and by measuring f_1 the fibre to glass distance, ϕ can be calculated. The light intensity on the junction can therefore be found from 4.15. The reduction factor ranges from 0 at $\phi = 90^\circ$ to 1 when $\phi = 0^\circ$. A correction term to account for variations in the fibre or mirror angle is also made and this factor is less than 1.

The diode sensing element on the Photodyne meter has a finite size of 0.42 cm^2 . Because of this, the intensity indicated on

the meter is an average reading corresponding to the centre and less intense outer regions of the cone of light. To account for the higher central intensity a factor of $1/x$ must be used to correct the meter reading. A typical value is 0.95 and x approaches 1 as the fibre-junction distance decreases.

3. A factor must be introduced to account for the reflectance and transmittance of light by the semi-transparent electrodes and the a-Si film.

Measuring the light intensity transmitted through the glass and ITO combination gives rise to a factor which reduces the initial intensity by $T_{g/ITO}$. The light intensity onto the junction is further reduced by reflection from the ITO/Si boundary. A quantity, $T_{g/ITO}R_{Si}$, is subtracted from the intensity incident on the silicon. The initial light intensity must now be corrected by a factor $T_{g/ITO} (1-R_{Si})$.

Light from multiple reflections within the films is neglected due to the small values of R_g and R_{ITO} (typically < 5%).

Secondary reflections from the Al top electrode are also neglected due to the low transmittance of the silicon films ($T_{Si} \sim$ a few %).

4. The aluminium mirrors used were not 100% reflective. A factor of 0.9 (equal to R_{AL} at 633nm) was incorporated to account for this. R_{AL} vs wavelength is plotted on graph 4.17a.
5. A final correction factor caused by the increasing loss from the fibres at low temperatures must also be taken into account. In order to calculate the factor an experiment involving cooling the fibres was performed. A fibre was led into the CTI Cryocoder

and its output directed at a second fibre (the one which illuminates the junctions). By shining light into this fibre and then measuring the output it is possible to calculate the loss at low temperatures. Cooling the system showed that below room temperature the light output was reduced and reached a steady value at 150K. Factors of 0.64 at 500 nm, 0.76 at 633 nm and 0.81 at 800 nm were found (see graph 4.17b). This factor is of importance for all optical experiments.

A similar experiment performed by passing a fibre through liquid nitrogen showed no change in light output intensity, but if the fibre was led through liquid helium a drop was observed (reduction factor of 0.81 was found at 633 nm). The fact that a decreased output was observed below 150K in the CTI system can be explained. The system has a first cooling stage onto which a second is attached. The sample is fixed to the second stage and its temperature can be changed by using a heater. The first cooling stage remains close to the base temperature, when the sample is heated. Since the fibres are in contact with the first cold stage, they are at a low temperature and thus the amount of light output is reduced. As the thermometers are on the second cold stage they record the sample temperature rather than the 1st cold station temperature.

The factor must therefore be included at all helium temperature experiments and when the CTI system was employed.

4.11 Transmittance and Reflection Measurements

Transmittance and reflectance measurements were obtained for the a-Si and the electrode material. Measurements were carried out by means

of a monochromator, which allowed the variation of wavelengths, and reflected and transmitted intensities were measured using a photomultiplier. These intensities were then compared with the reflectance of aluminium and the transmittance of air respectively. A range of wavelengths, from 500 nm to 1.5 nm could be obtained using this equipment.

Absolute errors in intensity measurements are rather high (~15-20%). Distances, e.g. of junction position with respect to the centre of light cone, mirror junction distance and mirror-fibre, can only be estimated to ± 0.25 mm. When these distances are substituted into the inverse-square law formula and when they are taken into account for determining junction positions they contribute the main sources of error into the intensity measurements. Errors due to correction factors 2.5 contribute errors of a few percent each, but are small in comparison with the distance errors of around 4% to 8% and the 10% error in calculating intensities from graph 4-15.

Intensity errors between the different intensities used during an optical run are small. Contributions to this error are due to the calibrations of the neutral density filters. Errors are minimised by calibrating the various filter combinations and using these combinations for each experiment. An estimated error of around 2% is attributed to filter calibrations.

4.12 AC Measurements

Capacitance and conductance can be measured to a high degree of accuracy using an ac bridge. The ac bridge used is described in section 4.12a.

4.12a Manual AC Bridge

A transformer ratio bridge (a General Radio Capacitance Bridge type 1615A) was used for measuring capacitance and conductance. This ac bridge uses a null method in which the unknown's (a-Si sample sandwiched between electrodes) capacitance is balanced against six calibrated variable capacitors. The sample's conductance is compared to the variable impedances in the transformer ratio arms of the bridge. The design is shown schematically in diagram 4.18. The ratio arms and variable capacitances are shown and when the detector is reading a zero current the bridge is balanced and the capacitance and conductance of the sample can be read from the front panel of the bridge.

The transformer ratio design ensures extremely accurate measurements can be made. In the frequency range up to 30kHz, the absolute capacitance error is better than 0.02%. Between 30kHz and 100kHz the accuracy drops to around 0.5%. Absolute measurements of conductance are correct to within 1% at audio frequencies. During the course of an optical experiment (on sample S2) it was necessary to measure small changes in capacitance. Using the General Radio bridge, it was possible to detect changes of 0.001pF in ~25pF. This implies a relative accuracy of $\sim 4 \times 10^{-3}\%$. Relative conductance errors were higher, being of the order of ~1% at 2KHz.

The signal frequencies ranged from 11Hz up to 100KHz and were supplied using a Levell oscillator. Capacitance and conductance values were generally several hundred picofarads and down to 10^{-10} S respectively at mid-frequency values (see section 5.7 for details of the frequency dependence of C and G). The General Radio bridge was most useful for measuring frequency dependent data due to the

wide frequency range available and its high degree of accuracy in measuring C and G.

4.12b Computer Controlled System

In order to enable the measurement of long capacitance decays (typically 1-3 days - see chapter 6) it was essential to use a computer controlled measuring system. A Hewlett Packard 4274A LCR meter was used for this purpose. This bridge had twelve inbuilt measuring frequencies ranging from 100Hz to 100KHz. Signal voltages from 1mV up to 5V could be applied, although measurements were generally taken at a 100mV measuring signal. Stray conductances and capacitances of the test leads were offset by the meter and all data was measured in the high resolution mode. This enabled ten data points to be averaged before the result was displayed by the meter.

Control of the system was performed by a Sinclair QL computer interfaced to the LCR bridge by an CST (Cambridge Systems Technology) IEEE interface. A Solatron 7150 digital voltmeter was also available for automatic temperature recording, in conjunction with the Glasgow University built TCU. This allowed a check to be made of temperature drift during a long experimental run.

The programmes developed by Holland (Ph.D. thesis 1987) were used for the experiments. Points could be taken each second (or every 20 seconds which is useful for measuring the response of C or G when illumination is applied or removed). A facility for taking data points every 1, 3 or 10 minutes was also available. These were more useful for measurements over a long time scale. Points taken in this way were the averages of up to 20 measured points. This has the effect of increasing measurement resolution and allows changes of 0.0085% to be detected (equivalent to 0.05pF in 600 pF).

An extension to the LCR programme enabled frequency sweeps to be carried out. When conductance values were relatively high, i.e. greater than 10^{-9} S at higher temperatures, frequency sweeps taken on the HP bridge were identical to those taken on the General Radio bridge.

As conductance values dropped, with decreasing frequency or temperature, the computer controlled system was measuring conductance to around $\pm 10\%$, (capacitance values were still accurate to 0.05pF in ~ 600 pF). At this point it became necessary to use the General Radio bridge. Conductance values are compared in graph 4.20 where it can be seen that the 2kHz values are consistent at all temperatures on both bridges. The 200Hz values are also compared. Measurements of conductance below 10^{-9} S was taken on the General Radio bridge on the lower frequencies.

Analysis of the data was carried out on the Sinclair QL using programmes described by Holland (Ph.D. thesis 1987, ; see section 4.13).

4.13 Computer Programmes for AC Measurements

The programme developed by Holland to control the bridge by means of the QL computer was written in basic. It allows data points to be taken every second, 20 sec., 1 min., 3 min. or every 10 min. A degree of averaging is carried out and the result is displayed on a monitor screen. The data collecting process may be interrupted at any time to allow a frequency sweep to be taken to allow the storage of the data on a disc or to change the frequency of data measurement.

Analysis programmes allow capacitance to be plotted against time and conductance data can be corrected for series resistance effects.

Frequency dependent data can be corrected for the conductance and series resistance can be fitted by the computer using a linear fitting routine.

The frequency sweep programme averages 20 points at each frequency supplied by the bridge and either outputs the data to a disc or printer.

The plotting programmes allow automatic or manual scale settings to be made on the axes and also allow functions of x or y to be plotted. This is extremely useful for plotting $\log(t)$ data (see Chapter 7).

4.14 DC Measurements

To measure dc conductances circuit 4.21 was set up. Here, a constant voltage is applied across the sample and the current is measured. The voltage drop across the picoammeter is less than 100 μV (Data from meter handbook) which is small in comparison with the measuring voltages used.

A computer controlled system consisting of a Keithley 230 programmable voltage source, and a Keithley 485 autoranging picometer. A Sinclair QL computer was employed to enable voltage sweeps to be taken. Programme details are shown in diagram 4.22, and are now discussed briefly. The voltage source is set up to produce a maximum and a minimum voltage (usually from +100mV to -100mV in 10mV steps). Twenty current readings are taken automatically for each voltage and the average current is calculated. The resulting I-V characteristics can now be output to a disc or printer. A graph can also be obtained by using a graph plotting programme.

It is necessary to take a voltage sweep in order to determine whether the I-V characteristics are linear. At high electric fields

(usually greater than $\sim 100\text{mV}$) carrier injection occurs and the resistance of the sample increases and becomes non-linear. The low-voltage linear region was used for calculated dc conductance and photoconductance values.

4.15 Sample Thickness Measurements

Sample thicknesses could be measured by two techniques. Both rely on optical interference and are briefly described.

The first method involved the use of a Varian Å-scope interferometer. Interference fringes are produced in an air wedge by light omitted by a sodium vapour lamp which is reflected from the silvered silicon sample (silvering increases the reflectance of the surface and enables the thickness measurement to be performed more easily) and then from a glass plate the beam shines through. Multiple reflections from the plate and sample produce the interference fringes. Since the sample is on a glass slide, a step exists at the point where the silicon borders onto the glass. If the step is under the beam from the sodium lamp a distance offset will be observed in the interference pattern. By measuring the offset and spacing it is straightforward to calculate the film thickness.

The second technique also relied on the interference of light, due to multiple reflections in a thin film. The transmittance of the a-Si sample was measured on SP Unicam 8000 spectrophotometer and interference fringes were observed in the high transmittance region at long wavelengths. To calculate d , the sample thickness, light is incident normal to the a-Si surface and is reflected from both the a-Si and the glass substrate. The light reflected from the substrate undergoes a 180° phase change since $n_{\text{Si}} > n_{\text{Glass}}$

(n = refractive index). The condition, therefore, for maximum reflected intensity is $2d = (m + \frac{1}{2}) \frac{\lambda}{n_{S_i}}$, where λ = wavelength, $m = 0, 1, 2, \dots$ and n_{S_i} = refractive index of a - S_i .

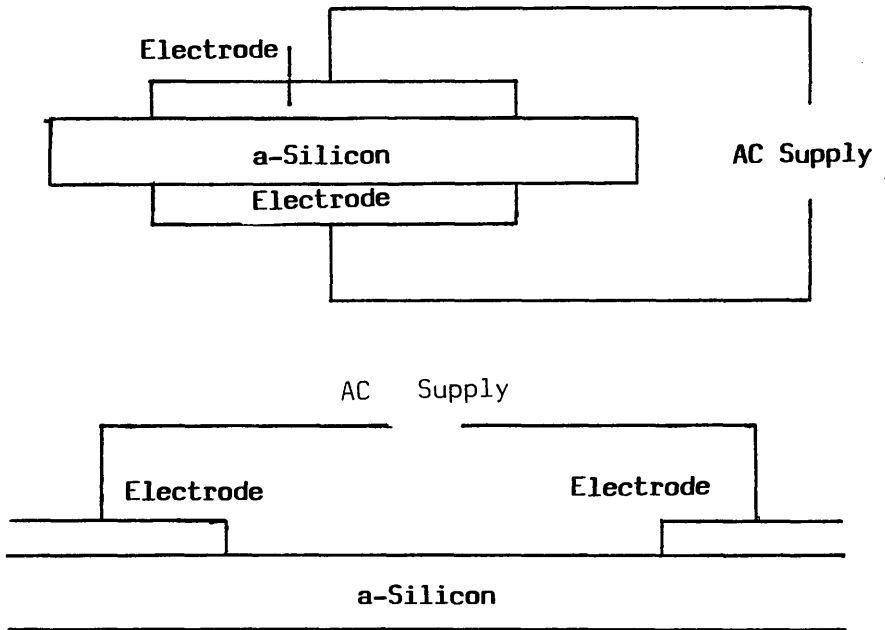


Diagram 4.1

- (a) Sandwich configuration
- and
- (b) Coplanar configuration of electrodes.

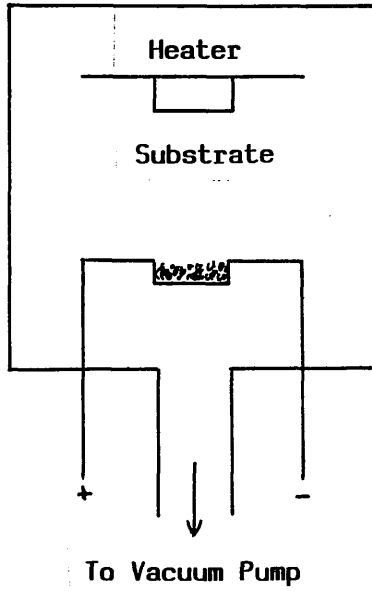


Diagram 4.2

Thermal evaporation unit.

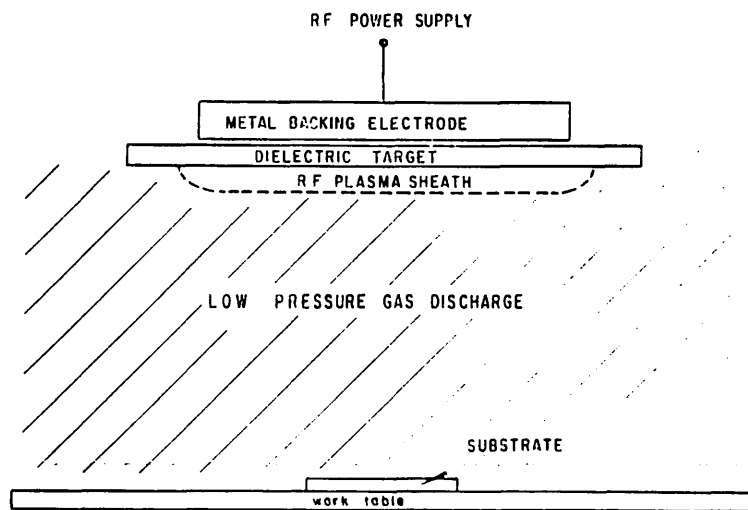


Diagram 4.3

RF Sputtering unit used for preparing MA4 -
a magnetron sputtered a-Si sample.

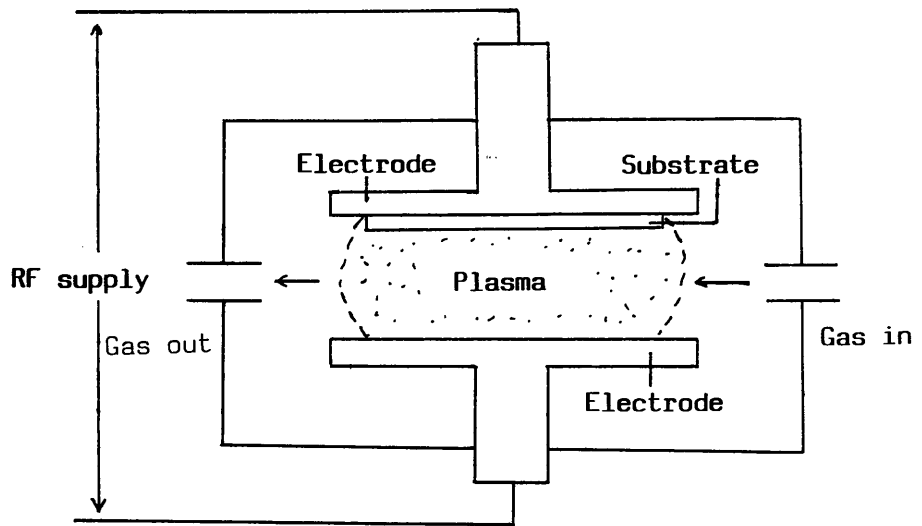


Diagram 4.4

Schematic diagram of a capacitively coupled glow discharge system. The gas inlet allows SiH_4 mixed with Ar, H_2 or PH_3 to be admitted to the chamber (Spear 1977).

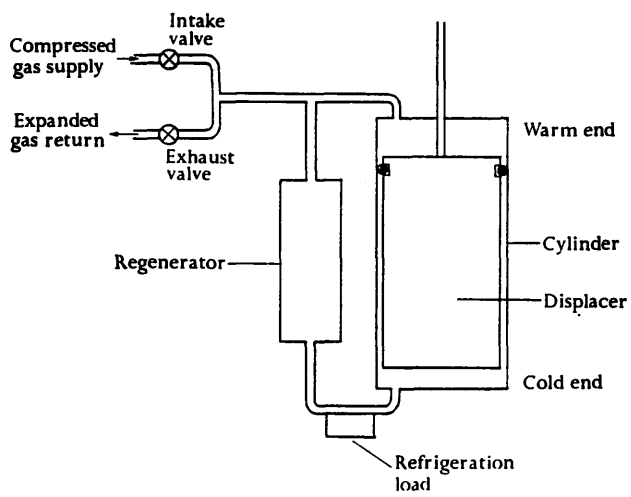


Diagram 4.5

A single stage version of the Gifford-McMahon refrigerator
(after McMahon 1960).

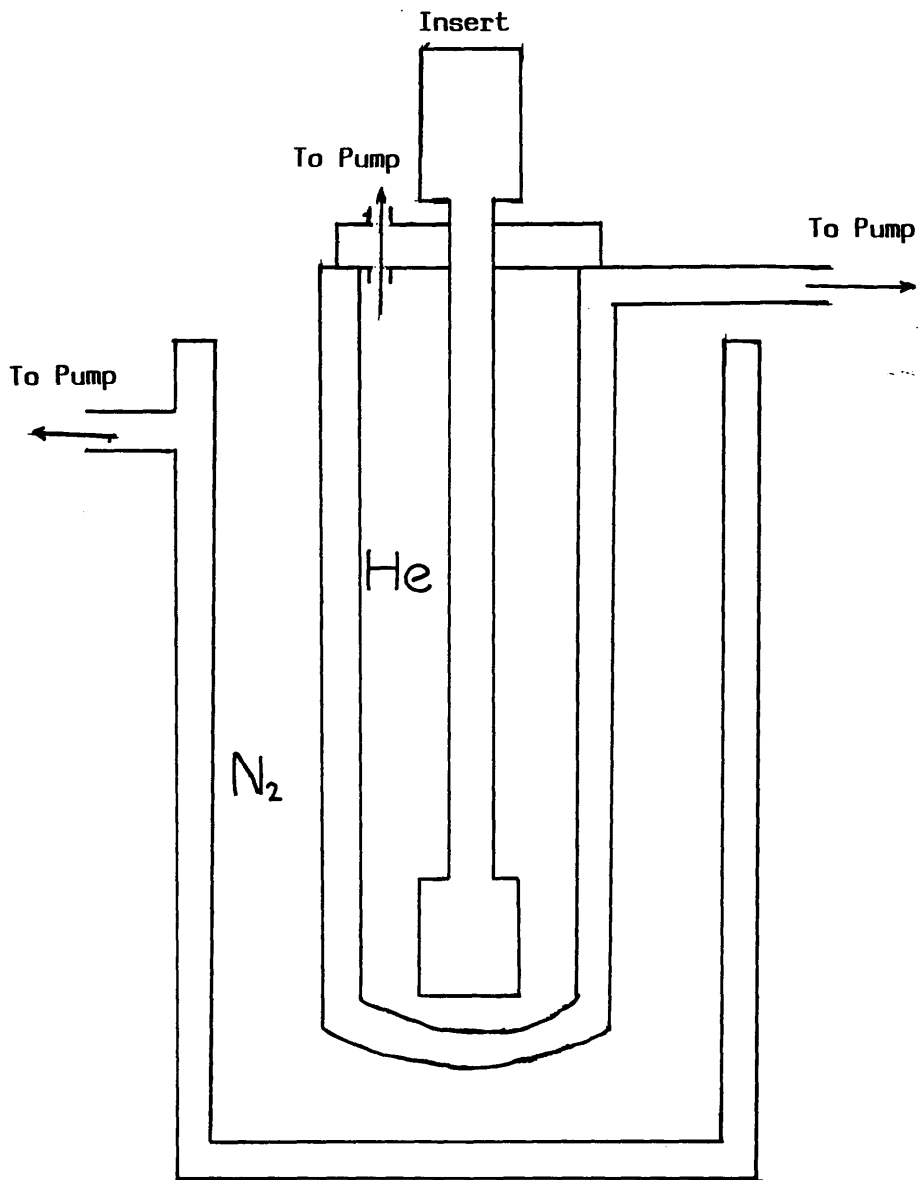


Diagram 4.6

Standard helium cryostat.

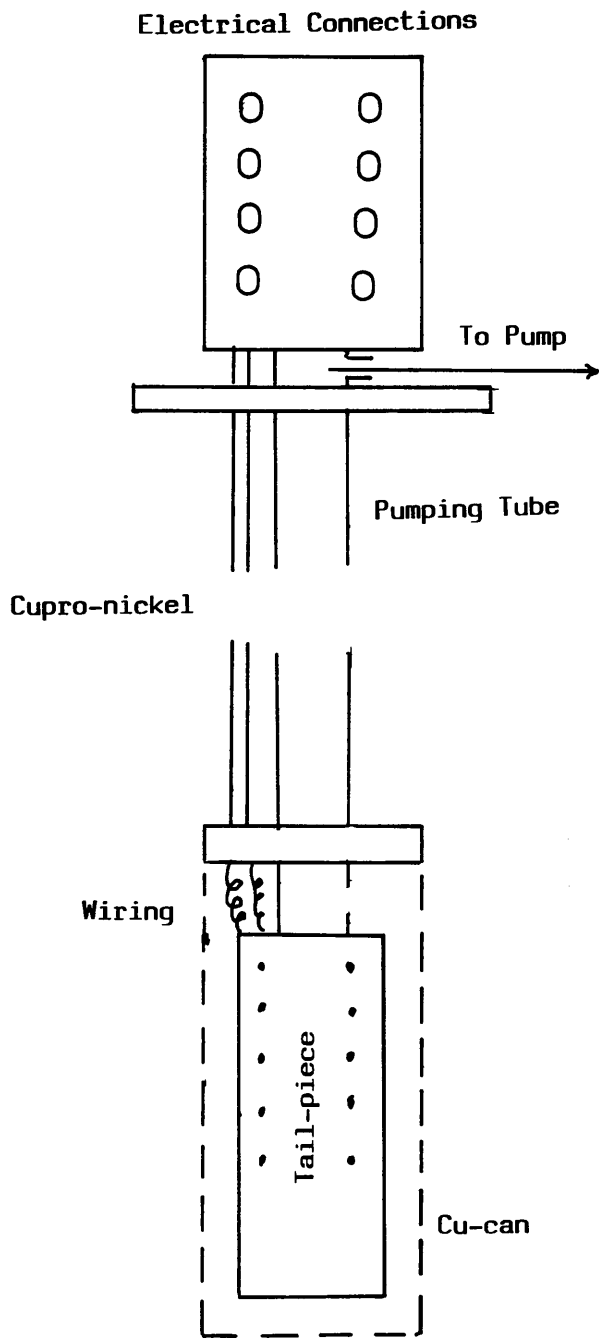


Diagram 4.7

Low temperature insert for use in cryostats.

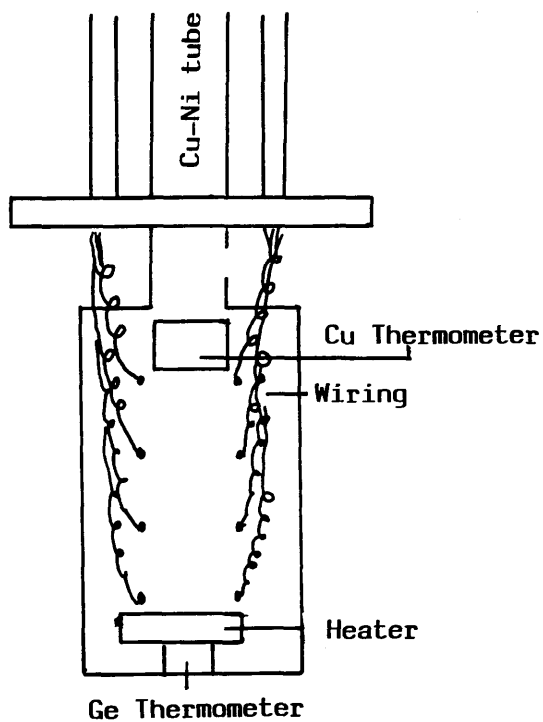


Diagram 4.8

Interlead capacitance can be reduced by using the above wiring system

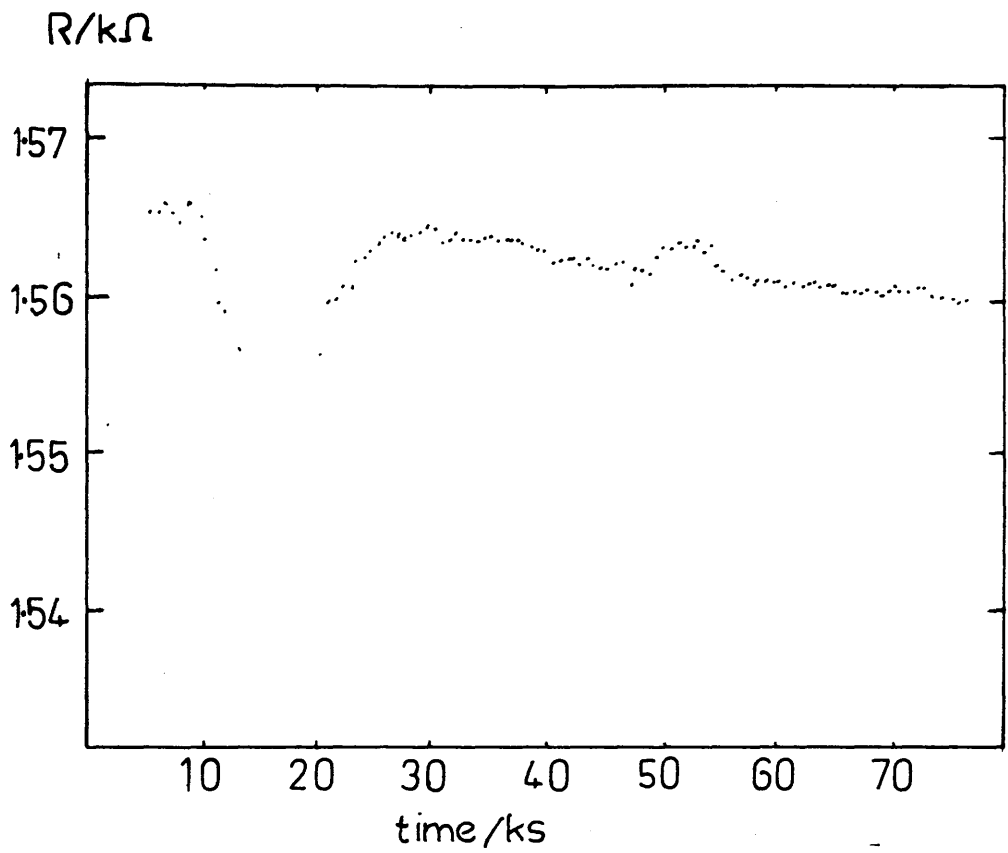


Diagram 4.10

Graph showing the variation in temperature when monitored continuously during an experiment using liquid helium.

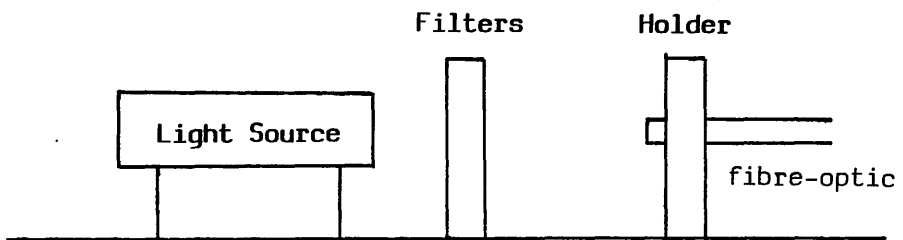


Diagram 4.11

Optical bench layout. The light source can be a laser or a white light focussed on the fibre-optic cable.

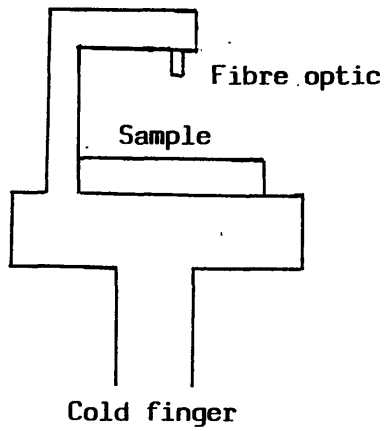


Diagram 4.12

Illumination technique employed in the cryocooler.

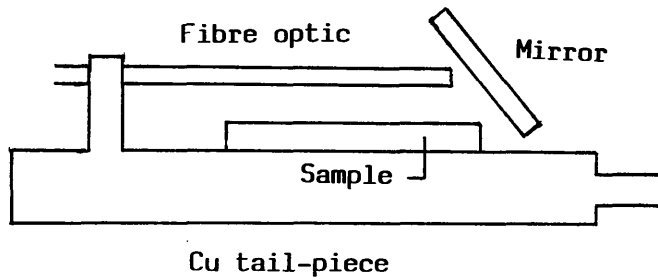


Diagram 4.13

Illuminating a sample using an Al-coated mirror in a helium insert.

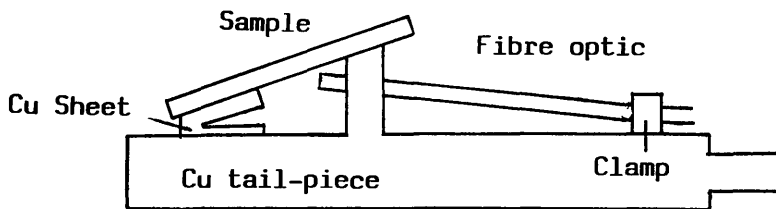


Diagram 4.14

Illumination through an ITO bottom contact in the long term He-dewar.

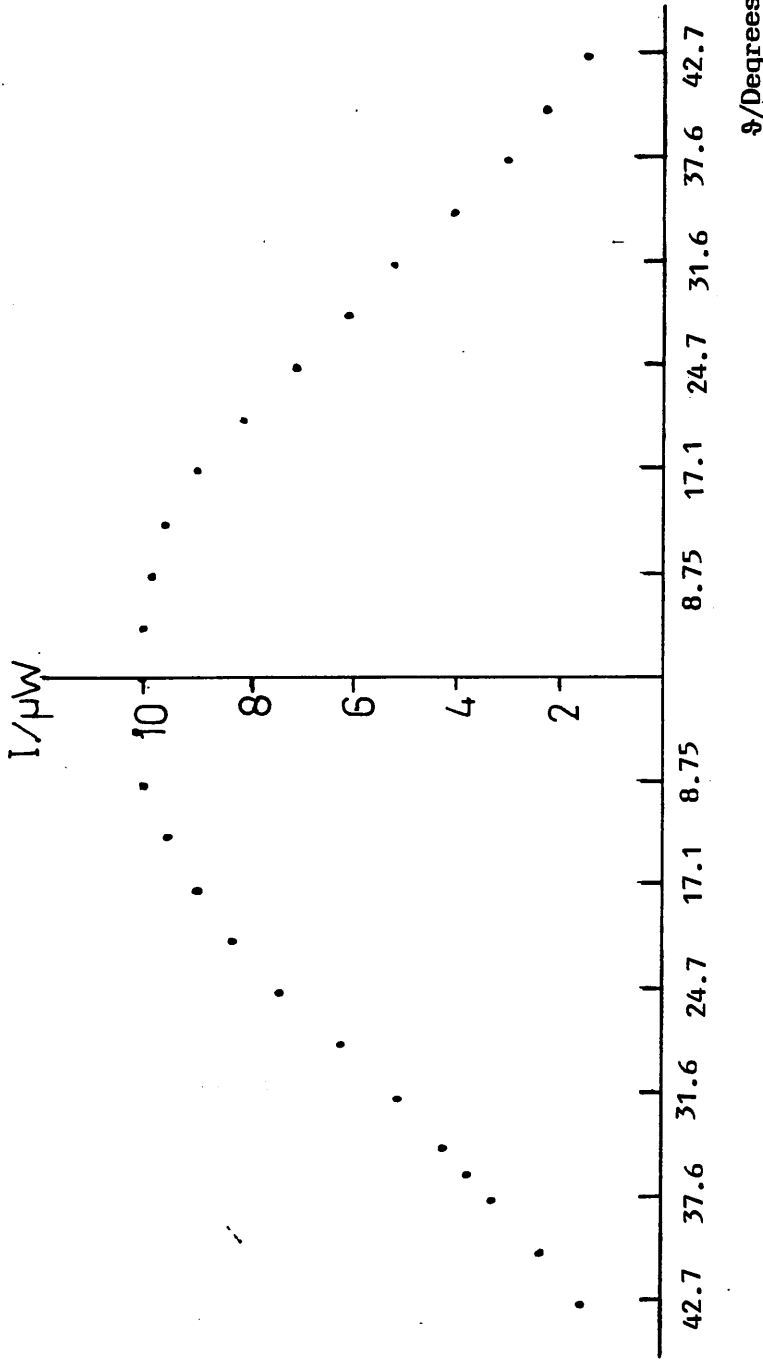


Diagram 4.15

The intensity profile with increasing distance from the centre of a junction.

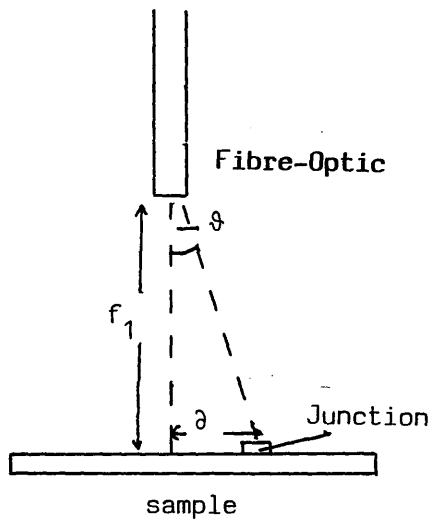


Diagram 4.16

Definitions of angles and distances used in intensity calibrations.

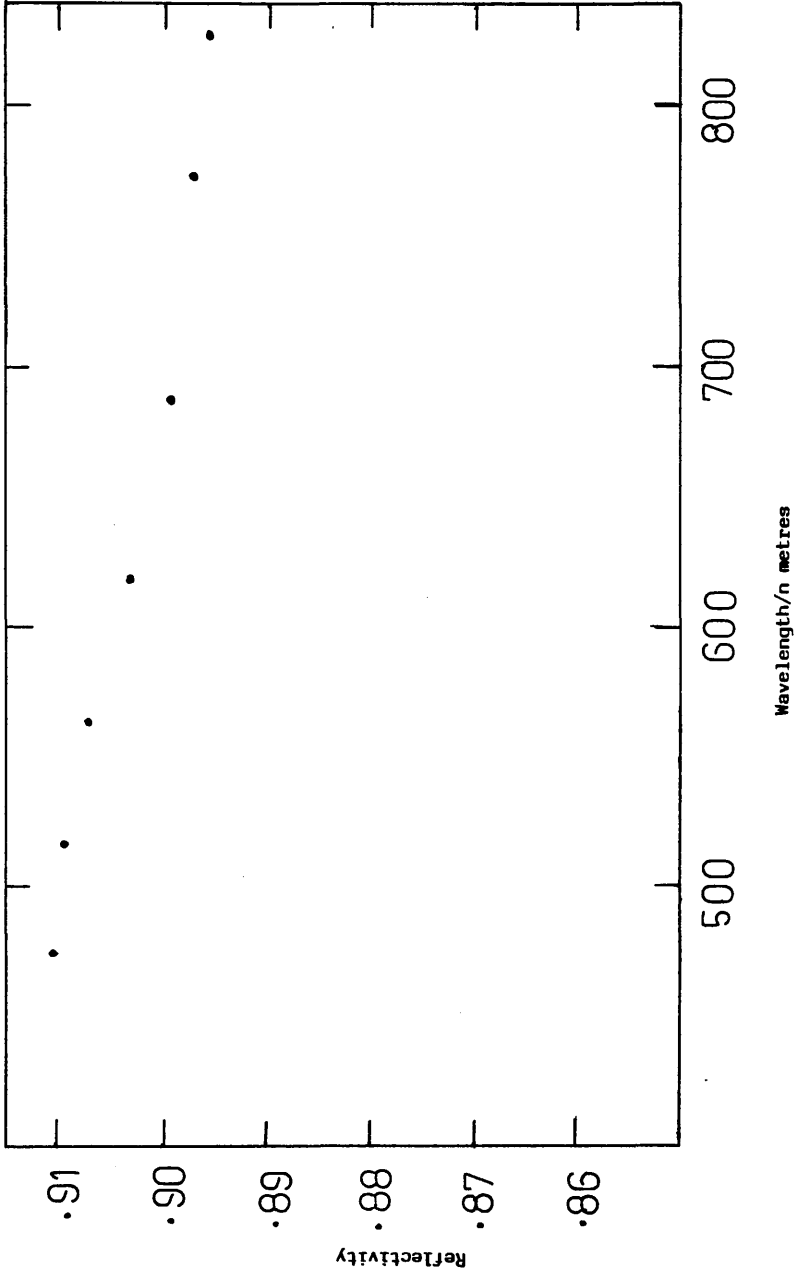
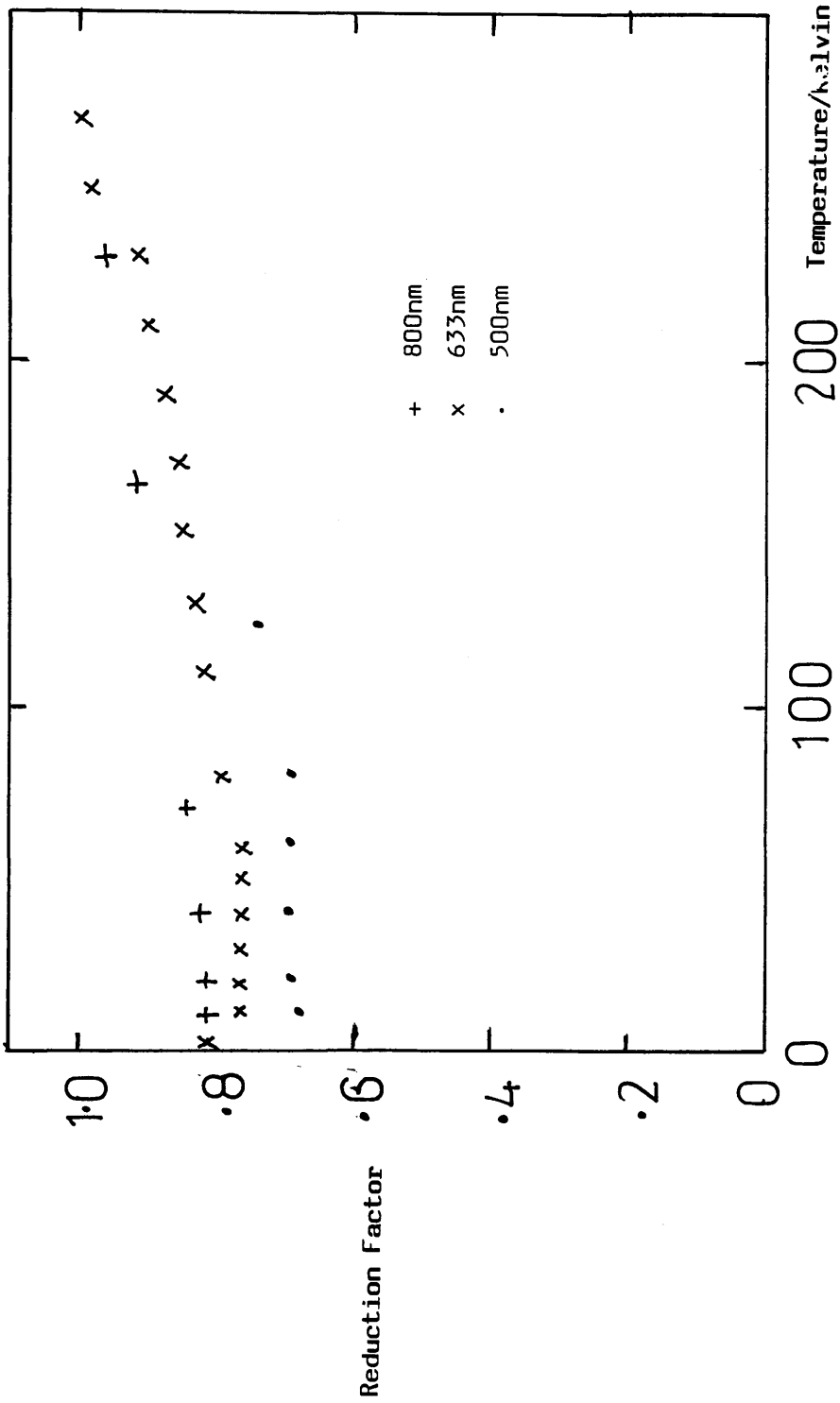


Diagram 4.17

(a) Graph showing the reflectance of Al versus wavelength.



Graph 4.17

(b) Graph showing the fibre reduction factor versus temperature.

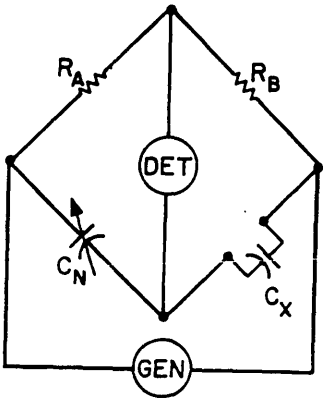


Diagram 4.18

The basic ratio ac bridge.

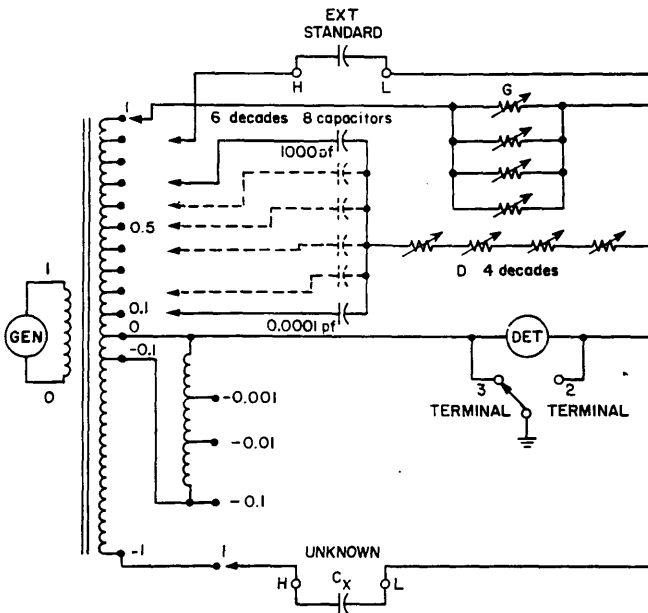
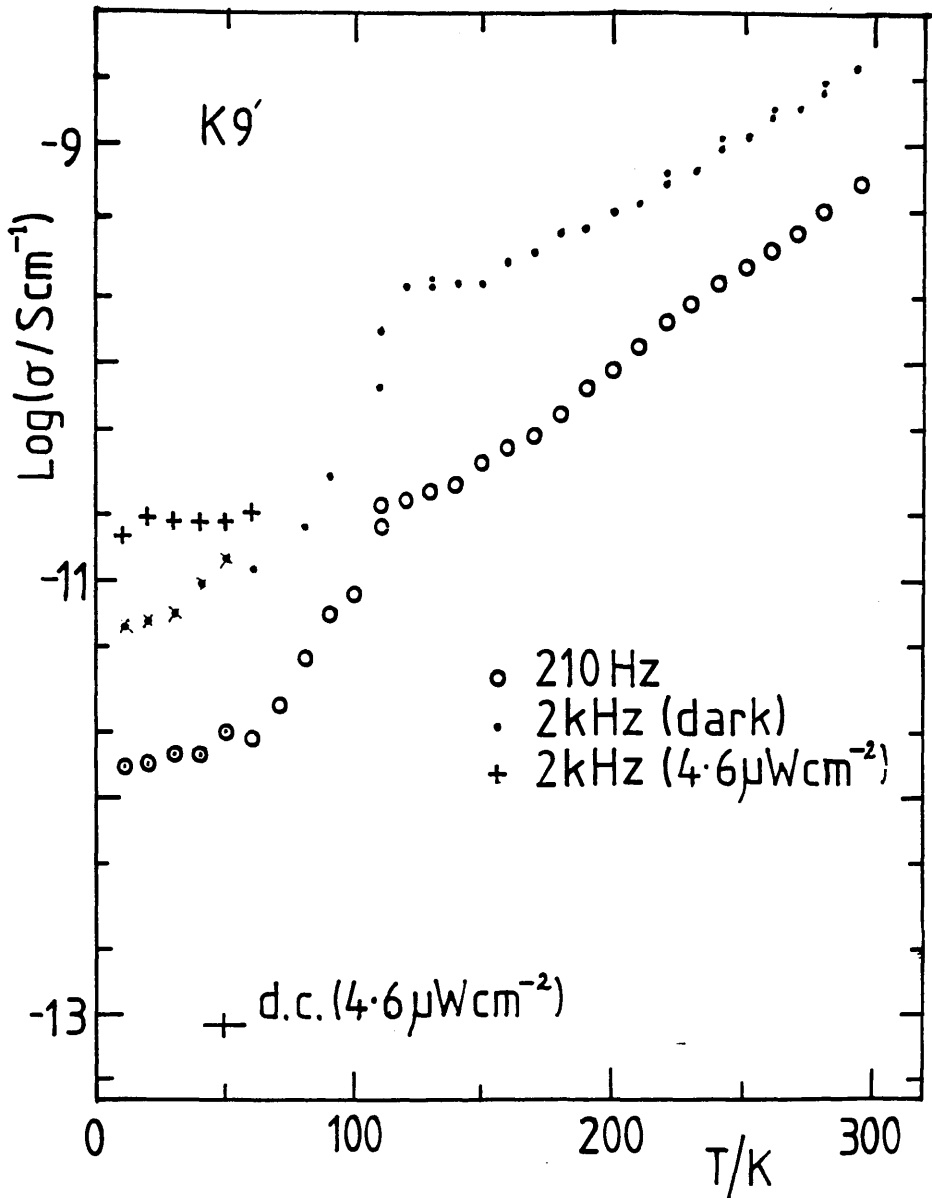


Diagram 4.19

Schematic diagram of the General Radio ac bridge.



The points \circ and \times were measured on both the General Radio Bridge and the LCR meter and plotted on the graph. The points \cdot and \cdot were measured only on the LCR meter.

Diagram 4.20

Diagram comparing points taken with the General Radio bridge and the computer controlled system.

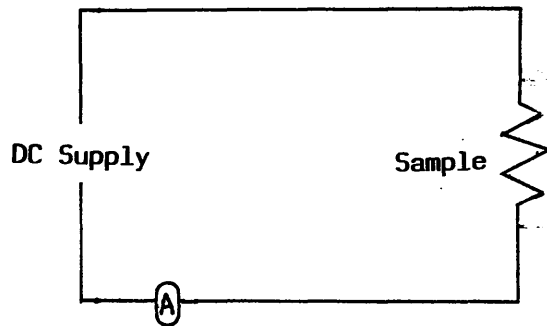


Diagram 4.21

DC measuring circuit.

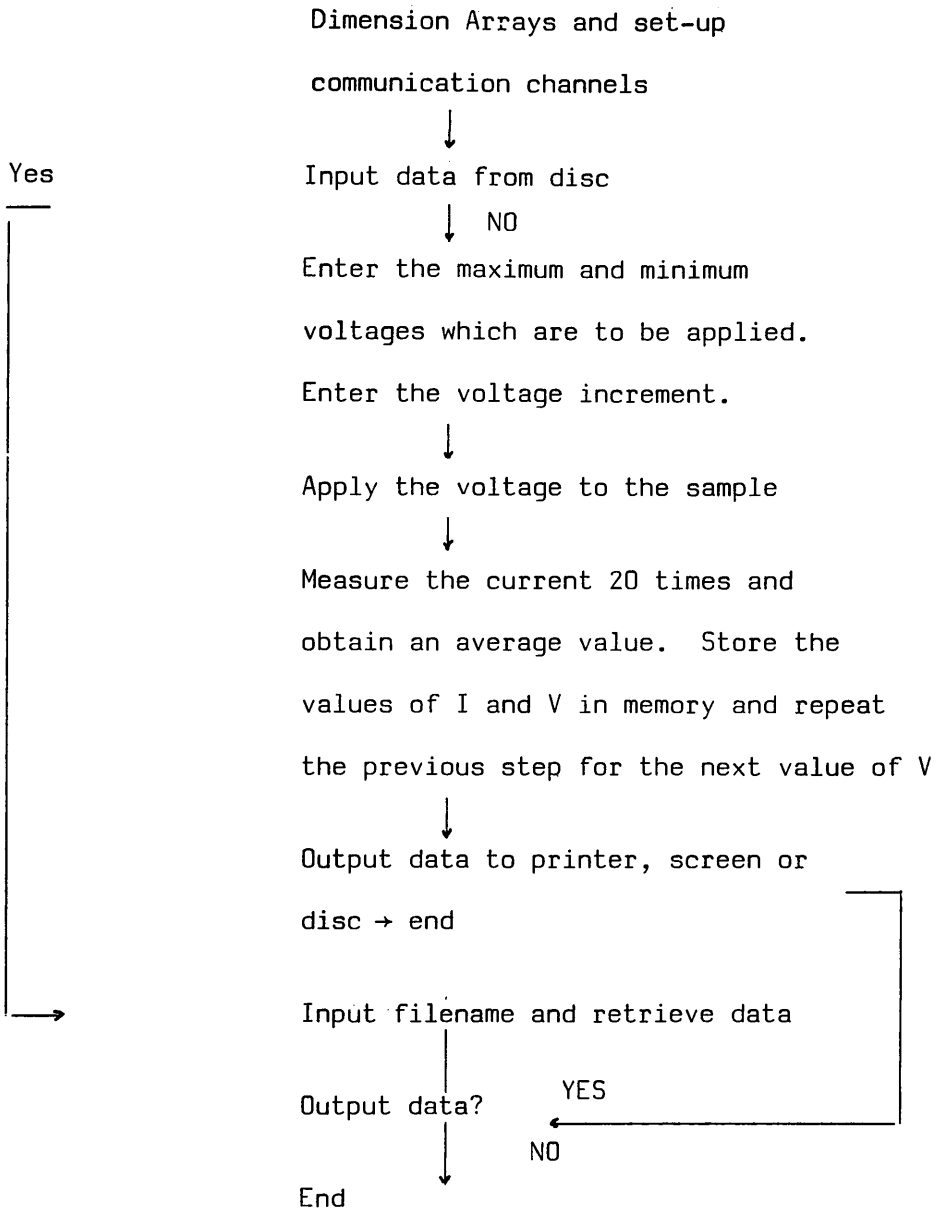


Diagram 4.22

Flow chart showing the details of the programme used for obtaining I-V characteristics.

CHAPTER 5

5.1 Sample Characteristics

Three different types of sample were studied in the course of this work. These were magnetron sputtered a-Si, glow discharge a-Si:H and evaporated a-As₂Se₃. In order to check that our samples showed characteristics similar to that seen in previous work (Long 1982, Long, McMillan, Balkan and Summerfield 1988) the samples were studied in the dark. This involved cooling the samples from room temperature down to liquid helium temperature and measuring their conductances (both dc and ac at selected frequencies) and capacitances, generally at 10K temperature intervals. Full frequency sweeps were taken over a more limited range of temperatures.

5.2 Corrections to the Measured Conductivity

The ac bridges measure the total conductivity of a sample. This can comprise of contributions from σ_{ac} , and σ_{dc} of the sample as well as a contribution from the measuring leads and sample electrodes.

Firstly, the lead and electrode resistances can be represented as a resistor in series with the sample (shown as a parallel combination of a resistor and capacitor in diagram 5.1). This is called the series resistance and is denoted by R_o . Under certain circumstances, R_o can be measured (Long and Balkan 1979, Long 1982) and is generally designed to be small compared with the sample resistance by using low resistance leads and thick electrodes.

Analysis of the equivalent circuit shown in diagram 5.1 yields the following equations for the effective values of the capacitance conductance.

$$C_{\text{eff}} = \frac{R_o^2 C}{(R_o + R)^2 + (\omega CR)^2 N_o^2} \quad (5.1)$$

$$G_{\text{eff}} = \frac{(R_o + R) + (\omega CR)^2 R_o}{(R_o + R)^2 + (\omega CR)^2 R_o^2} \quad (5.2)$$

If $R_o \ll R$ when, at low frequencies,

$$G_{\text{eff}} = \frac{1}{R} \text{ and } C_{\text{eff}} = C \quad (5.3)$$

As the frequency is increased the R_o term becomes significant and to first order

$$G_{\text{eff}} = G + \omega^2 C^2 R_o \quad (5.4)$$

Long et al (1979) and Long (1982) found that the high frequency (>20KHz) conductance values for a-Ge samples were higher than expected. By measuring N_o it was found that the slope of a G_{eff} vs $\log \omega$ plot was equivalent to the $\omega^2 C^2 R_o$ term at high frequencies. Subtracting this term from G_{eff} gives the true conductance, G , for the sample.

In the case of ITO backed samples we have only indirect measures of the series resistance. It is therefore necessary to estimate R_o from the gradient of a $\log G_{\text{eff}}$ vs $\log \omega$ plot at high frequencies. Assuming that $G_{\text{eff}} \approx \omega^2 C^2 R_o$ in this region a value for R_o can be

obtained. As an example, frequency dependent conductivity data for D1 is shown, both uncorrected (graph 5.2) and corrected (graph 5.17) for the effect of R_0 . An estimate of $R_0 \approx 190\Omega$ is obtained. The curves converge at high frequencies at all temperatures as shown on graph 5.2 implying that R_0 is independent of temperature. Other ITO samples behave in a similar manner, with the high frequency conductances tending to a common line. The values of R_0 range from $\sim 50\Omega$ up to $\sim 200\Omega$ depending upon the sample, but R_0 values are constant for a particular sample. Measurements on ITO films confirm that the conductances measured at high frequency are due to the ITO and not to the measuring leads as these contribute $<10\Omega$ to the series resistance.

The above procedure for series resistance corrections can thus be applied to other a-Si:H data. Since R_0 is not strongly temperature dependent (true for thin AL electrodes where boundary scattering predominates or for ITO electrodes) then the R_0 value can be used at higher temperatures.

A computer programme, developed by Holland (Ph.D. thesis 1987) was available to carry out the series resistance correction.

Assuming that $G_{\text{eff}} = A\omega^s + \omega^2 C^2 R_0$ at low temperatures then an estimate of R_0 can be fitted by the procedure described earlier. A line can then be fitted to the data and R_0 adjusted until the optimum fitted line is obtained. Such a procedure generally yields a value of $s \approx 1$ at low temperatures for a-Si:H. This is comparable to accepted values (Long 1982) of s .

A further division in the true conductivity can be made if ac and dc conduction mechanisms are independent of one another. i.e.

$$\sigma = \sigma_{dc} + \sigma_{ac} \quad (5.5)$$

Evidence of whether the ac and dc conduction mechanisms are due to the same processes can be obtained by considering the capacitance change with frequency. If the capacitance increases with decreasing frequency a saturation value of capacitance will be reached at low frequency. This is due to inhomogeneous regions or clusters within the medium (see Chapter 2 for more details) responding to the applied field. As the frequency decreases more of these regions can respond until all the regions are responding and thus the capacitance saturates at a low frequency if this type of response occurs then if $\log \left(\frac{-dC}{d \ln \nu} \right)$ is plotted against $\log \sigma$ then a peak will be observed. This is known as a loss peak and is found in materials where ac and dc conduction mechanisms are linked. Loss peaks have been observed in a-Ge, a-Si and a-Si:H (Long 1982, Long et al 1983 and Long et al 1985). In a-As₂Se₃ (see Section 5.12) no loss peaks were observed and the ac and dc conduction mechanisms are thought to be independent of one another (also Long 1982 and Elliott 1988).

5.3 Dark Conductivity

By studying the behaviour of the ac and dc conductance with frequency and temperature it is possible to obtain information about the underlying conduction mechanisms. This will be discussed in the next sections.

5.4 Magnetron Sputtered a-Si

The data showing how the dark conductivity changes with temperature is plotted on graph 5.3. It can be seen that the total conductivity is greater than $10^{-4} S$ above 100K (this value is comparable in magnitude with data obtained by Long et al (1988) on a-Si). As the temperature drops from 100K to around 25K the total conductance falls rapidly by around two orders of magnitude. The gradient has a value of about 6 between 40K and 100K. Below ~25K the total conductance changes less rapidly with temperature and a gradient of around 0.4 is found in this region.

The two junctions studied show total conductance values differing by a factor of two, to within 5%. Since the areas of both junctions agree to within 2% and the thicknesses differ by a factor of $2.00 \pm 2\%$ it is obvious that the total conductance scales with thickness. The total conductance is therefore a property of the bulk of the sample.

Conductance frequency sweeps, with ν varying from 100Hz to 100KHz have been plotted on diagram 5.4. The graph shows the total conductance varying with frequency at both high (>25K) and low (<25K) temperatures. The graph shows the ac conductance corrected for the series resistance effects (see Section 5.1) varying with frequency.

It can be seen that the total conductance tends towards the measured dc value as the frequency decreases. At temperatures under 10K the $\log G_{ac}$ vs $\log \omega$ graphs are linear. The gradient, s , is measured to around 1. As the temperature rises the gradient and

s decreases.

The log G vs log T graph (graph 5.3) can be divided into two temperature regimes in the manner described by Long (1985) for a-Ge data. The low temperature region occurs below ~20K and is attributed to electronic tunnelling processes within defects. In the high temperature regions (above ~40K) the ac loss is attributed to electrons hopping between defects (Long 1988).

The weak temperature dependence at low T has been analysed by analogy with the atomic tunnelling model (Long 1982, Long et al 1985). Here, the electronic processes responsible for the ac loss in amorphous silicon are compared to those which give rise to ac loss in bulk glasses. In bulk glasses the loss arises from relaxation processes within groups of atoms trapped in metastable states. This is analogous to the electronic tunnelling transitions within defect clusters in amorphous silicon. Long et al calculated the electron tunnelling distance using this model and found a value of ~20nm. This is much greater than the tunnelling distance of 1nm which is calculated from experimental field effect data. This implies that an additional mechanism is involved in producing the observed ac loss in amorphous silicon at low temperatures. It is likely that the ac loss is due to electrons tunnelling a distance of ~1nm with some atomic rearrangement also taking place.

Evidence for defects of 1nm in size, often called microvoids, has been obtained by using small angle scattering techniques (Craven et al 1985).

The ac loss in the high temperature regime is attributed to hopping between defect states (Long et al 1988).

5.5 a-Si:H Samples

The temperature dependence of the total conductivity of intrinsic a-Si:H sample can again be divided into two temperature regimes. In the three types of samples studied (see Chapter 4 for details of S, K and D samples) similar characteristics were found. Above 150K, in S and K samples, the conductance decreases rapidly with temperature. This can be seen on graphs 5.5 to 5.9 which show σ_{tot} vs T for the various samples studied. The total conductivity approaches the dc conductivity around room temperature. Below ~100K σ_{tot} is very weakly temperature dependent and is close to a constant value in all the samples studied, except when gold electrodes were used on sample S2. Here it can be seen (graph 5.11) that σ_{tot} is proportional to temperature below ~100K. This will be discussed in greater detail in section 5.10.

D1 shows similar behaviour, although the temperature range is different (see graph 5.10).

A peak is observed in the $\log \sigma_{tot}$ vs T graphs at around 150K at 2KHz in undoped samples. At 200Hz this peak shifts to 120K.

The peak is not due to intrinsic a-Si:H layer (denoted as i-layer) but is caused by the thin n^+ contact layers (Shimakawa et al 1987, Long et al 1987). If these n^+ layers are treated as a parallel combination of G_s and C_s in series with the i-layer (whose total conductance and capacitance are G_b and C_b respectively), as shown in the equivalent circuit (diagram 5.13) then

$$G_n = \frac{G_b G_s (G_b + G_s) + \omega^2 (G_s G_b^2 + G_b G_s^2)}{(G_b + G_s)^2 + \omega^2 (C_b + C_s)^2} \quad (5.6)$$

$$\text{and } C_m = \frac{(C_b G_s^2 + C_s G_b^2) + \omega^2 C_b C_s (C_b + C_s)}{(C_b + G_s)^2 + \omega^2 (C_b + C_s)^2} \quad (5.7)$$

At high temperatures G_s is large and $G_m = G_b$, $C_m = C_b$. As the temperature decreases G_s decreases and contributes to the value of G_m , giving

$$G_m = G_b + \omega^2 C_b^2 / G_s \quad (5.8)$$

As the temperature falls further, the loss angles in the n^+ layers become small (i.e. $\omega C_s G_s < 1$) and the equation 5.8 no longer holds. The capacitance of the n^+ contact layers will now begin to short out their contribution to G_m which then falls rapidly. The capacitance data shows analogous behaviour and it can be observed that it falls from C_b to the series combination of C_b and C_s (these are calculated from the measured film thickness). This further supports the above model for a series layer.

The *shoulder* observed in the $\log \sigma_{tot}$ vs T curve (graph 5.10) for sample D1 is likely to be due to an oxide layer and is discussed more fully in Section 5.17 which deals with the frequency dependence of σ_{tot} .

The $\log \sigma_{tot}$ can be divided into two regimes. In S and K (intrinsic samples) the conductivity increases rapidly above 100K, at 2KHz. This is attributed to the *movement* of carriers *within* inhomogeneous regions (see Chapter 2) in the a-Si:H bulk. D samples also show a rapid decrease in $\log \sigma_{tot}$ with decreasing temperature (illustrated in graph 5.10).

At low temperatures under $\sim 100\text{K}$, where σ_{tot} is almost independent of T a different process is thought to be responsible. The states responsible for the ac loss are deep states around the Fermi level. The low density of states in the band gap (approximately $10^{16} \text{eV}^{-1} \text{cm}^{-3}$ - obtained from space charge limited current techniques) can be compared with the values of $10^{18} \text{eV}^{-1} \text{cm}^{-3}$ for sputtered material. This implies that the ac conductivity will be smaller. For example, in MA4, $\sigma_{\text{tot}} = 2.53 \times 10^{-10} \text{Scm}^{-1}$ and in an a-Si:H sample, prepared using glow discharge, $\sigma_{\text{tot}} = 3.16 \times 10^{-12} \text{Scm}^{-1}$ at a temperature of 12.4K and at a measuring frequency of 2KHz . This observation is consistent with the observed density of states around the Fermi level. Since s decreases with temperature a correlated hopping mechanism (see Chapter 2) is probably responsible for the loss. Tunnelling models in which s is temperature independent and polaronic models where s increases with temperature or is not proportional can also be discounted, at least as a dominating mechanism.

5.6 DC Conductivity

The temperature dependence of the dc conductivity was measured at the same time as the ac conductivity. The dc data has been plotted on the same graphs as the ac data for samples K9' and D1, (graphs 5.8 and 5.6). It can be seen for K9' that the dc conductance is less than 10^{-12}S at the lowest temperatures. It was not feasible to measure these values at measuring voltages of 100mV with the equipment used (see Chapter 4). Voltages larger than 100mV may damage the sample or cause the data to be measured in the non-linear region of the I-V characteristics. This is plotted in graph 5.14.

The equivalent graph for D1 shows that σ_{dc} varies strongly with

temperature at high temperatures but reaches a steady value of 1.8×10^{-11} S below 70K. This may be due to a small leakage current through the sample.

Measurements of the dc conductivity of the intrinsic a-Si:H are complicated due to a variety of reasons. The first of these are problems caused by the n^+ contact layers. One of these, due to the series n^+ layer has already been discussed as far as its contribution to the measured ac conductivity is concerned. The n^+ layer lies on top of the intrinsic a-Si:H layer and makes contact with the ITO bottom electrode at the edges of the sample. This has the effect of introducing a resistance in parallel with that of the i-layer. At high temperatures, when the resistance of the n^+ -layer is low, this effectively shorts out the contribution to the dc conductivity from the i-layer. The magnitude of the total conductivity due to the n^+ -layer has been deduced from the measured conductivity, G_m , and from equation 5.8. This is indicated on the $\log G_m$ vs T plots for the various samples studied, calculating the activation energy from the \log (conductivity deduced for n^+ layer) against $1/T$ plots give a value of $E_a = (0.26 \pm 0.01)$ eV (for sample K11). This is identical to activation energy found from n^+ sample (D1) where $E_a = (0.23 \pm 0.01)$ eV.

A further complication arises from an oxide layer between the electrode-silicon interface. Such a layer can be treated as a series layer in the same manner as the n^+ layers.

The plateau observed in the $\log \sigma_{tot}$ vs $\log \omega$ plots (see Section 5.6 for details of the frequency dependence of σ_{tot} and graphs 5.17 to 5.19) is due to the oxide layer. The oxide barrier

dominates the low frequency capacitance (which is of the order of several nanofarads in D1 below a measuring frequency of ~22Hz) and the dc. conductance. The conductance of the plateau region is dominated by the bulk of the sample. The conductance on the plateau region is plotted on a $\log \sigma_p$ vs $1/T$ graph (graph 5.15). The activation energy for conduction across this layer has been calculated to be $E_a \approx (0.23 \pm 0.05)$ eV.

5.7 Frequency Dependent Conductivity in Glow Discharge Samples

At temperatures below ~50K, the frequency dependence of σ_{tot} is very similar for S, K and D samples. The graphs 5.17 to 5.19 show σ_{tot} vs (freq) plotted on log scales. It can be seen that a power law relation is obeyed with $\sigma_{tot} \propto \omega^s$. The value of s can be obtained from the gradient and is around one at the lowest temperatures (~12K). In sample D1 s varies from 1.00 ± 0.05 to 0.90 ± 0.05 between 12.4K and 70K. It can be seen that there is little variation in the $\log \sigma_{tot}$ vs $\log \omega$ plots between these temperatures (graph 5.17).

Values of s have been plotted against T for the various samples. Graph 5.20 shows this for S and K samples. At low temperatures, $s = 1.00 \pm 0.05$ and s decreases as temperature increases. The change is proportional to temperature and this behaviour has been noted by other researchers for glow-discharge a-Si:H (Shimakawa et al 1987, Long 1988).

The s vs T plot for D1 (graph 5.20) shows that s is constant and has a value of 1.00 ± 0.05 from 13.5K to 70K. Beyond 70K s decreases rapidly until 120K is reached.

5.8 Inhomogeneous Model Applied to a-Si:H

Long (1989) proposed a model involving high conductivity regions within a background material to account for the frequency dependent results in a-Si:H. This is discussed in Chapter 2 and the results are now applied to data from undoped and doped a-Si:H.

Assuming that the dc conductivity is simply activated gives

$$\sigma_b = \sigma_0 \exp(-E_0/k_B T) \quad (5.9)$$

and the absolute ac conductivity σ_m is calculated ^{(from 5.10).} The high frequency data in the $\log \sigma_{tot}$ vs $\log \omega$ plots can be seen to obey a power law, thus

$$\frac{\sigma_m}{\sigma_b} \approx C_0 (\omega \tau_b)^s \quad (5.10)$$

From observations on data by Long (1989),

$$s = 1 - \frac{T}{T_0}, \quad \text{empirically.} \quad (5.11)$$

and C_0 = the concentration of high conductivity regions

$\omega \tau_b$ = the reduced angular frequency.

The conductivity σ_m can be written as

$$\sigma_m = C_0 \sigma_0 \exp(-E_0/k_B T_0) (\omega \epsilon_b \epsilon_0 / \sigma_0)^{1-T/T_0} \quad (5.12)$$

By taking the logarithm of each side we obtain

$$\log \sigma_m = A + \log B \omega - \frac{T}{T_0} \log B \omega \quad (5.13)$$

where A and B are constants.

At a constant frequency $\log \sigma_m \propto T$, from 5.13. The solid lines shown in the $\log \sigma_{tot}$ against T plots are fitted using this equation. It can be seen that this only applies at high temperatures and when the dc conductivity is much less than the ac conductivity.

In fitting expression 5.12 to the conductivity data T_0 must be found. This can be taken as the temperature at which the 2kHz and 200Hz lines intersect. Since $T = T_0$ at this point equation 5.12 can now be simplified and gives

$$\log \sigma_m = \log C_0 \sigma_0 - E_0/k_B T_0 \quad (5.14)$$

Thus $C_0 \sigma_0$ can be found if E_0 is known. This is found using 5.9. The value of σ_0 can also be obtained from the gradients of the $\log \sigma_m$ vs T graphs. A comparison can then be made between the values obtained for σ_0 , if C_0 is estimated as around 0.1.

Long (1989) found that for an S-type sample that $C_0 \sigma_0 \approx 300 \text{ Sm}^{-1}$ with $C_0 \sim 0.1$ and also found $\sigma_0 \sim 10 \text{ Sm}^{-1}$ from the 2kHz gradient. Values have been calculated for various S and K samples and are shown in Table 5.21.

Although some samples fit the model well (e.g. Long 1989, Sample S1), others do not. For example, in K12 the 2kHz and 200Hz high temperature data run parallel to one another. This makes it impossible to estimate T_0 from their intersection. Similarly it is impossible to obtain a T_0 value for S3 with Cr electrodes using this technique.

S2, S3 (Al electrodes) and K9 give plausible results for σ_0 although discrepancies occur between σ_0 values calculated by the

two methods used.

A possible reason for the differences observed is due to the assumption made for the distribution of inhomogeneous regions, An exponential distribution is assumed, but there is no reason why another form (e.g. Gaussian distribution) cannot be used.

The models presented by both Long (1988) and Dyre (1987) derive that

$$s \approx 1 - T/T_0. \quad (5.15)$$

The samples manufactured using glow discharge techniques (a-Si:H) fit this relation (shown by K11 data). Previous results, on similar materials (Long 1988) show that these also have $s = 1 - T/T_0$.

Doped a-Si:H (sample D1) clearly does not follow this law, as shown on graph 5.20. Here, a plot of s vs T has a gradient which differs from the value predicted by 5.15. An alternative explanation is therefore necessary.

A possible reason is that the low due to deep states ($s \approx 1$) contributes to σ as the contribution due to inhomogeneous regions decreases. If this process occurs more rapidly (as T decreases) in D1 than in S or K samples then the effect would be for s to become closer to one at a higher temperature, which is observed in graph 5.20.

5.9 Method of Contact Evaporation

Contacts were evaporated using resistive heating within a vacuum chamber (base pressure $\sim 10^{-5}$ Torr). Aluminium electrodes were evaporated onto sample S3. The contacts prepared in this way were not satisfactory because of "jumps" occurring in the capacitance data, at arbitrary times, due to poor contact to certain parts of the sample.

By changing the evaporation system to a cleaner evaporator which can be pumped down to $\sim 6 \times 10^{-7}$ Torr, better contacts were obtained. Al contacts prepared in this system were free from discontinuities in the data.

It was suspected that the problems were caused by volatile impurities being trapped on the a-Si surface as the Al condenses on the sample. By eliminating the oxygen by decreasing the pressure this problem was solved.

5.10 The Effect of the Electrode Material on the Dark Characteristics

Experiments using semi-transparent gold electrodes on a-Si:H (sample S2) showed that a higher than usual loss was observed. Comparison with data obtained by Shimakawa et al (1987) show that the total conductivity is around one order of magnitude less, at low temperatures when aluminium electrodes are used. Further experiments with Al electrodes on this particular sample confirmed that the loss is indeed higher when using Au electrodes (graphs 5.5 and 5.11). Below $\sim 100\text{K}$ for S2 with Au electrodes, the conductivity is proportional to temperature. Such a result is predicted for uncorrelated hopping between states near the Fermi level (Austin and Mott 1969) but has virtually never been observed (Long 1982). This suggests that there has been a degree of diffusion into the A-Si:H by Au atoms.

Other materials, such as Cu-Ni and Cr, used for electrodes on a-Si:H also cause the low temperature conductivity to be enhanced due to metallic diffusion. This is shown in graphs 5.8 and 5.12 where the low temperature conductivity for samples K9 and S2 can be found. These values of low temperature conductivity are greater than those for the same samples when Al electrodes were used.

5.11 Electrode Requirements for Optical Experiments

In order to find suitable electrode materials used in optical experiments a number of factors must be considered. Ideally, at least one electrode should be semi-transparent to allow the illumination of the a-Si junctions. The electrode should have a low series resistance (preferably under 100Ω) so as not to contribute significantly to the high frequency loss. The material used should be unreactive to prevent oxidation and should not diffuse into the films and introduce paths of lower resistance.

The various materials described in the previous section are now considered for their suitability as electrodes. Aluminium electrodes of a suitable thickness are known to have an open granular structure and tend to deteriorate after a short length of time, presumably due to oxidation. Their optical properties, i.e. reflectance and transmittance, also change with time. The series resistance will also increase as the electrodes deteriorate.

Materials such as Au or Cr diffuse to such an extent as to mask the low temperature conductivity and are therefore unsuitable for studying optically induced loss. Cu-Ni electrodes diffuse to a lesser extent but are prone to deterioration.

The most useful contact material was found to be ITO. This is an oxide of indium and tin and is semi-transparent in thin film form. Although a high series resistance ($>100\Omega$) was observed in some samples using this material the ac loss was of the same order of magnitude in Al/a-Si:H/ITO samples as in Al/a-Si:H/Al samples. ITO is therefore not prone to diffusing into a-Si:H and the electrodes were not observed to deteriorate over periods of several weeks since the series resistance remained the same over this time.

5.12 Arsenic Selenide Sample

5.12(a) Temperature Dependence of the Conductivity

The total conductance of the arsenic selenide film was measured from 1.2K up to 420K. A log (conductance) vs log T plot was constructed and is shown in diagram 5.22. The graph shows that the conductance (σ_{tot} at 2kHz) increases slowly above 1.2K ~ 4K. The increase then becomes more rapid, with a gradient of ~0.5 until ~20K. Here the slope falls to around 0.25 until σ becomes constant between 150K and 200K. This behaviour continues up to 345K. At this temperature the value of σ_{tot} begins to increase by about an order of magnitude to ~420K with a slope, on a log σ_{tot} vs 1/T plot equivalent to the dc activation energy of 0.95 eV.

The low temperature σ data (up to 20K) is proportional to T^x . This behaviour is reminiscent of that observed in a-Si:H when Au electrodes are used, as was the case in this particular a-As₂Se₃ sample. Annealing the a-As₂Se₃ sample (at T > 350K over several hours) had the effect of reducing the room temperature conductivity by ~5% when the sample cooled back down to room temperature.

The temperature dependent data is similar to that found by Holland (Ph.D. Thesis 1987). This work involved the same type of measurement on a sputtered sample with Au top and bottom electrodes.

5.12(b) DC Conductivity

The plot of log σ_{dc} vs 1/T shown in graph 5.24 is linear at high temperature with an activation energy 0.95 eV obtained from its gradient. Mott and Davis (1979 edition p458) quoted a value of 0.905 eV for the activation energy (Edmond, T. 1966).

5.12(c) Frequency Dependent Effects

Frequency sweeps are shown in graph 5.23, along with some $\left(\frac{dG}{d\nu}\right)$ data.

The frequency data shows that the value of σ_{tot} approaches the dc conductivity value at low frequencies and higher temperatures. As the frequency increases, σ_{tot} also increases and is generally proportional to frequency, as the room temperature data shows. Here $s \sim 1.00 \pm 0.05$.

Plotting $\log\left(\frac{dG}{d\nu}\right)$ vs $\log \omega$ shows that no loss peaks are observed in the temperature range from 290K to 420K. The total conductivity changes from being strongly frequency dependent to dc behaviour at around 360K. It is in this region, i.e. the transition to non-dispersive behaviour, that loss peaks are found in a-Si:H (see Section 5.8).

5.13 Models for the Observed Behaviour of σ_{tot} with T and ω

It has been proposed that ac and dc conduction mechanisms are unrelated in chalcogenide materials (Long 1982, Elliott 1988). The dc conductivity is likely to be due to band conduction and the ac conductivity due to relaxation processes.

The low temperature ac conductivity has been attributed to an atomic tunnelling mechanism (Elliott 1988). In such a process tunnelling between atoms or groups of atoms trapped in metastable states will result in a range of relaxation rates. Calculating the ac conductivity (Long et al 1985), results in the following expression.

$$\sigma_1 \propto f \left[\ln \left(\frac{2kT}{B} \right) \right] \quad (5.16)$$

and

$$s = 1 + \frac{m}{\ln(2kT/\omega B)} \approx 1 \text{ at low } T. \quad (5.17)$$

where $B =$ a constant and f is a function of $\ln(2kT/B)$.

It is assumed that the dipole moment is independent of its tunnelling coupling parameter, and single phonon coupling is involved.

The atomic tunnelling model predicts that the ac conductivity will be weakly temperature dependent and that the frequency exponent s will be close to 1.

The low temperature data plotted on graph 5.22 shows a weak temperature dependence. The possibility of the proportionality of σ_{tot} to T^x below $\sim 10\text{K}$ being due to diffusion of the gold sample electrodes cannot be ruled out. (See Section 5.9 which deals with Au diffusion in a-Si:H.)

The value of s is found to be close to 1 for all temperatures up to room temperature. This again supports the idea that the loss is due to atomic tunnelling at low temperatures.

The ac and dc conduction mechanisms are unlikely to be related. Dc conductivity is probably due to the activation of carriers across the band gap, rather than by a variable-range hopping mechanism which obeys a $T^{-\frac{1}{4}}$ law. The As_2Se_3 dc data can be seen to obey a $1/T$ relation above room temperature. Further evidence for a band conduction mechanism can be obtained from the dc activation energy of $\sim 0.95\text{eV}$. If the Fermi-level lies close to the middle of the gap then the band gap $\approx 2 \times E_A \approx 1.9 \text{ eV}$. This is close to the value obtained by Shimakawa (1982) of 1.8eV . The absence of loss peaks in dG/dv curves also supports the idea of independent ac and dc mechanisms.

If a loss peak is found, the dc current is carried by percolation through a network of regions of differing conductivity which give the enhanced response at high frequencies. Such behaviour is expected to occur above $\sim 300\text{K}$ in the As_2Se_3 sample, but is not observed. The total conductivity can thus be written as

$$\sigma_{\text{tot}} = \sigma_{\text{ac}} + \sigma_{\text{dc}} \quad (5.18)$$

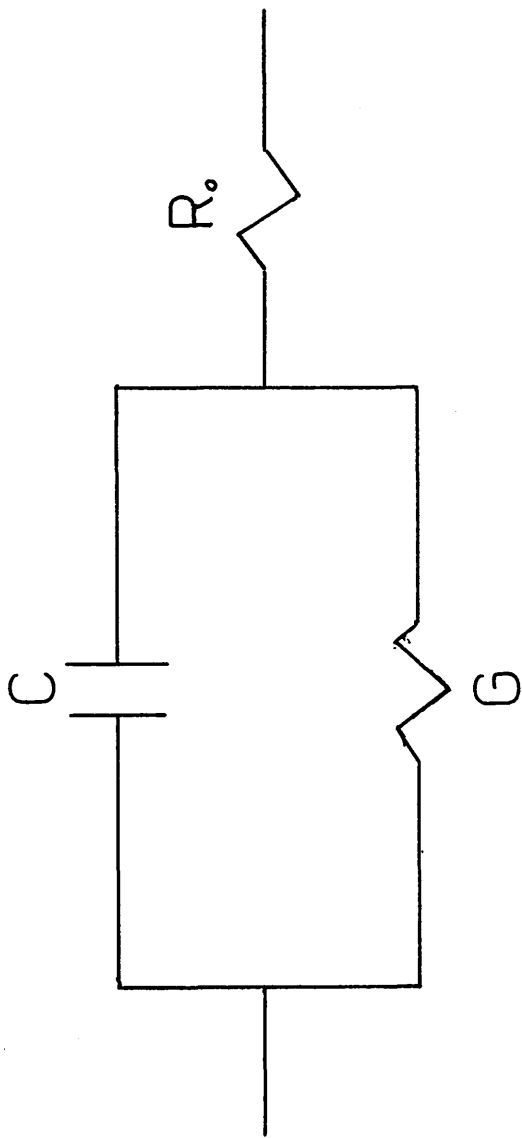
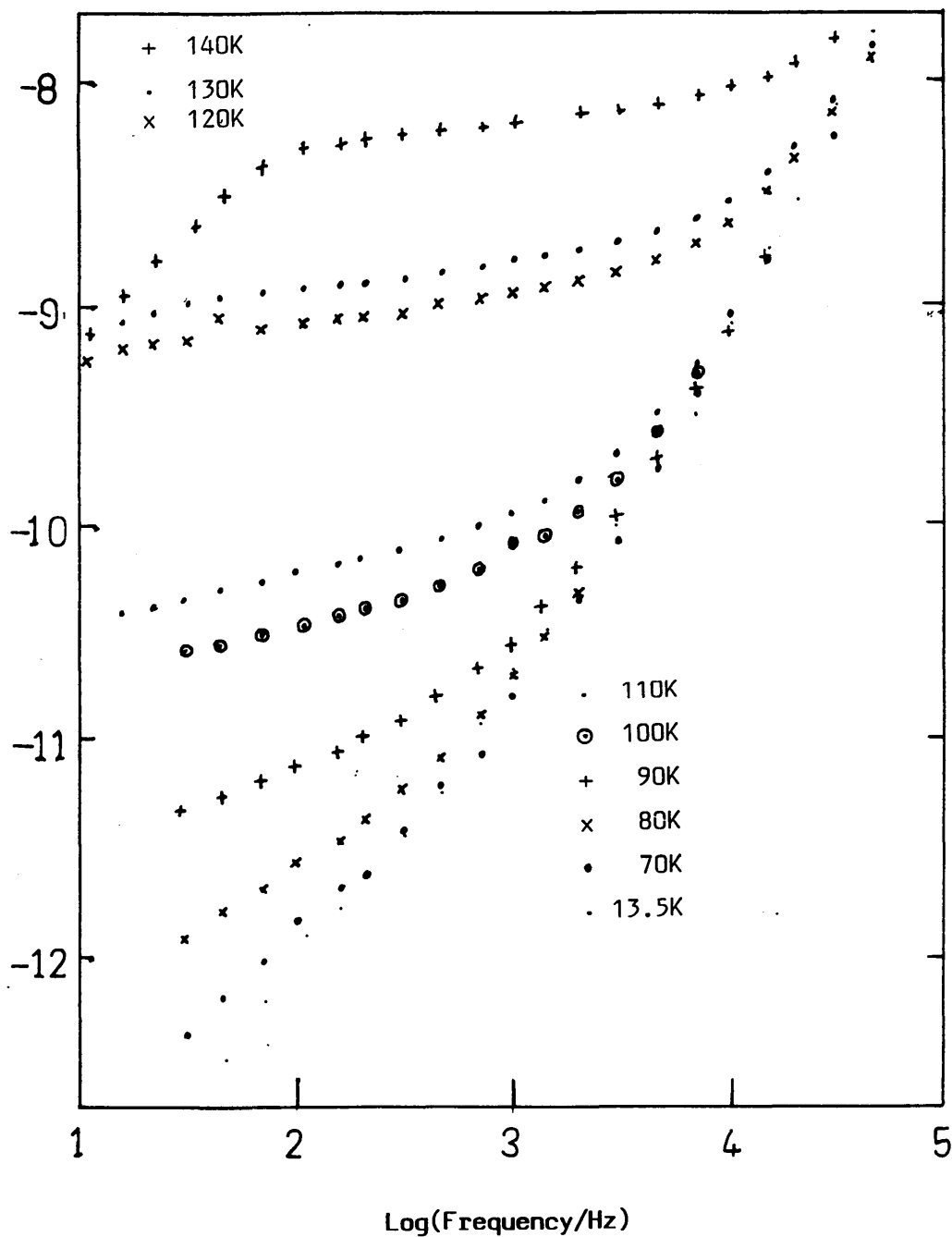


Diagram 5.1

The Equivalent circuit used to represent the sample (G,C) and the series resistance (R_o).

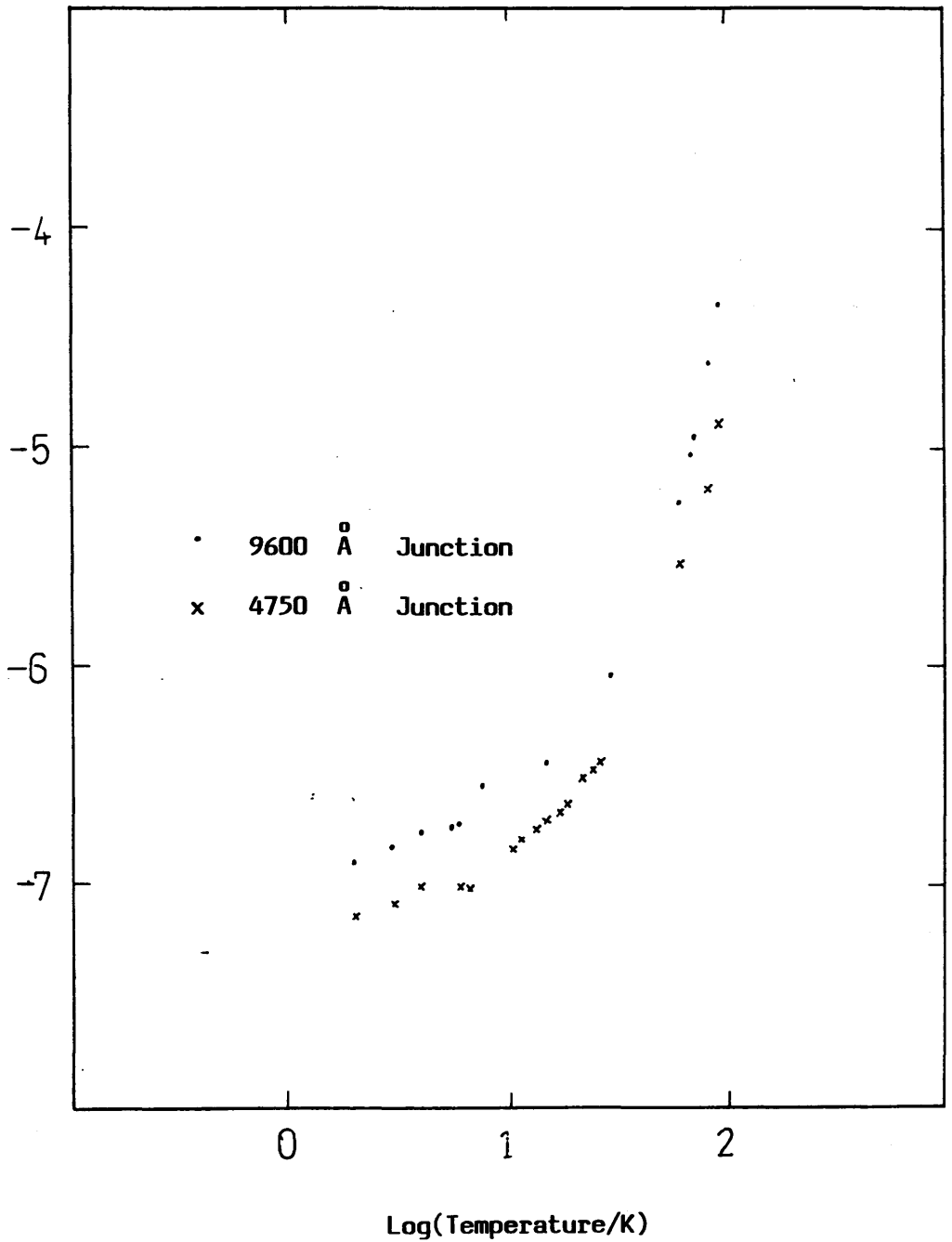
$\log(\text{conductance}/\text{Scm}^{-1})$



Graph 5.2

Frequency dependent conductivity for an n^+ sample, D1, uncorrected for series resistance. The appropriate temperatures at which each set of data was measured is indicated on the graph.

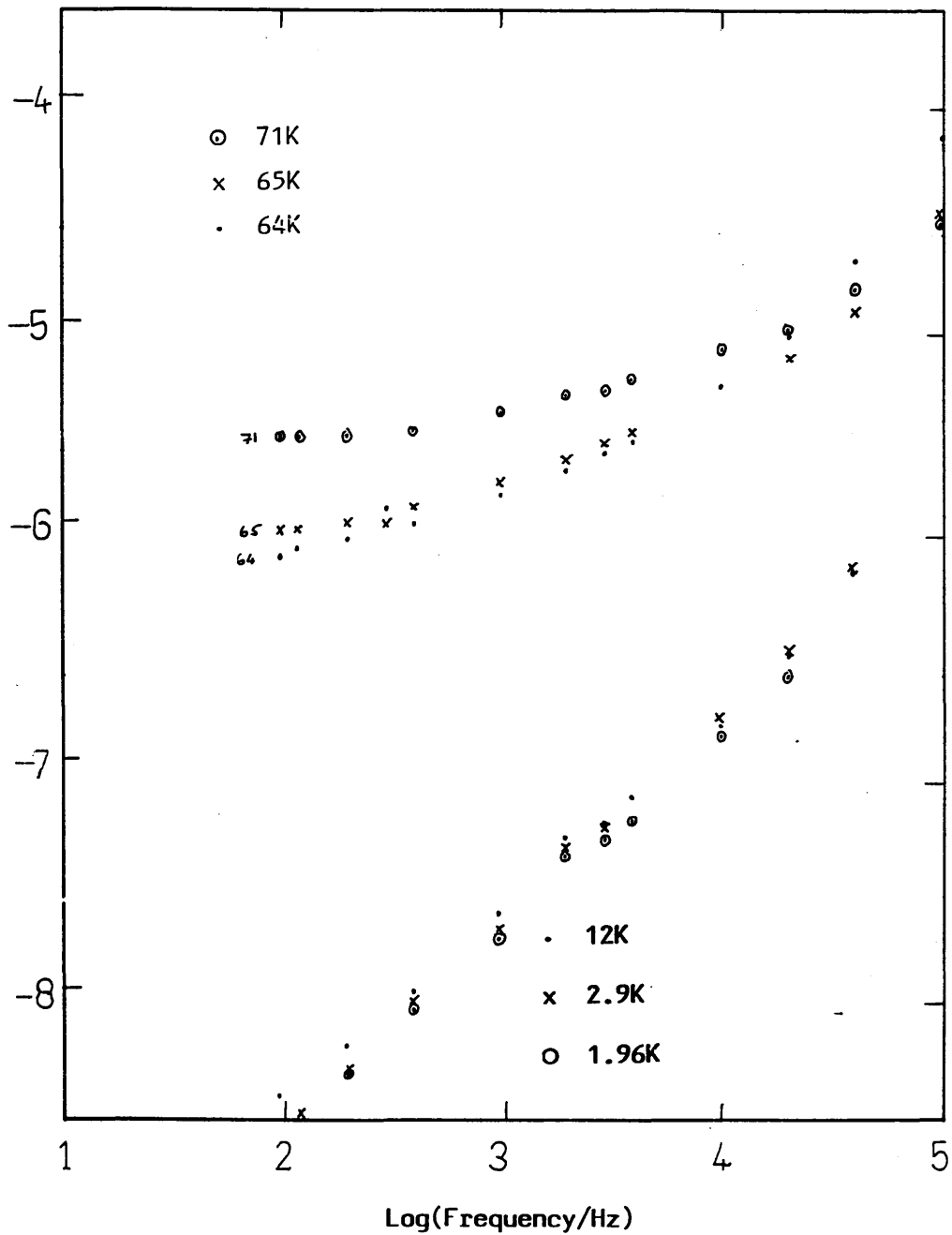
$\log(\text{conductance}/\text{Scm}^{-1})$



Graph 5.3

The temperature dependent conductivity for a magnetron sputtered a-Si sample, MA4. The data is corrected for series resistance. The crosses (x) indicate the thin junction and the dots (.) represent the thick junction.

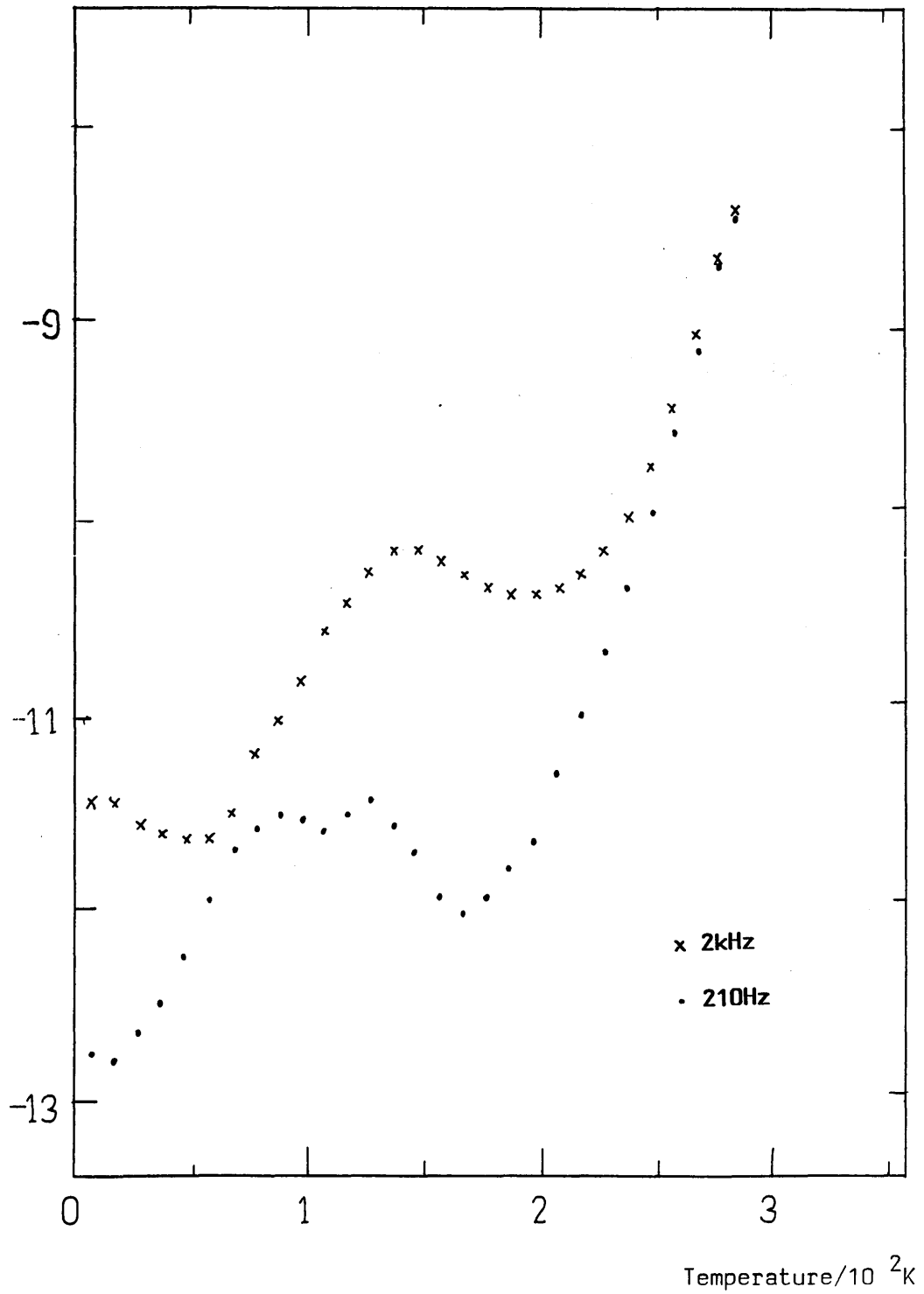
$\log(\text{conductance}/\text{Scm}^{-1})$



Graph 5.4

The frequency dependent conductivity, after correction for the series resistance, for MA4. The appropriate temperature for each set of data is marked on the graph.

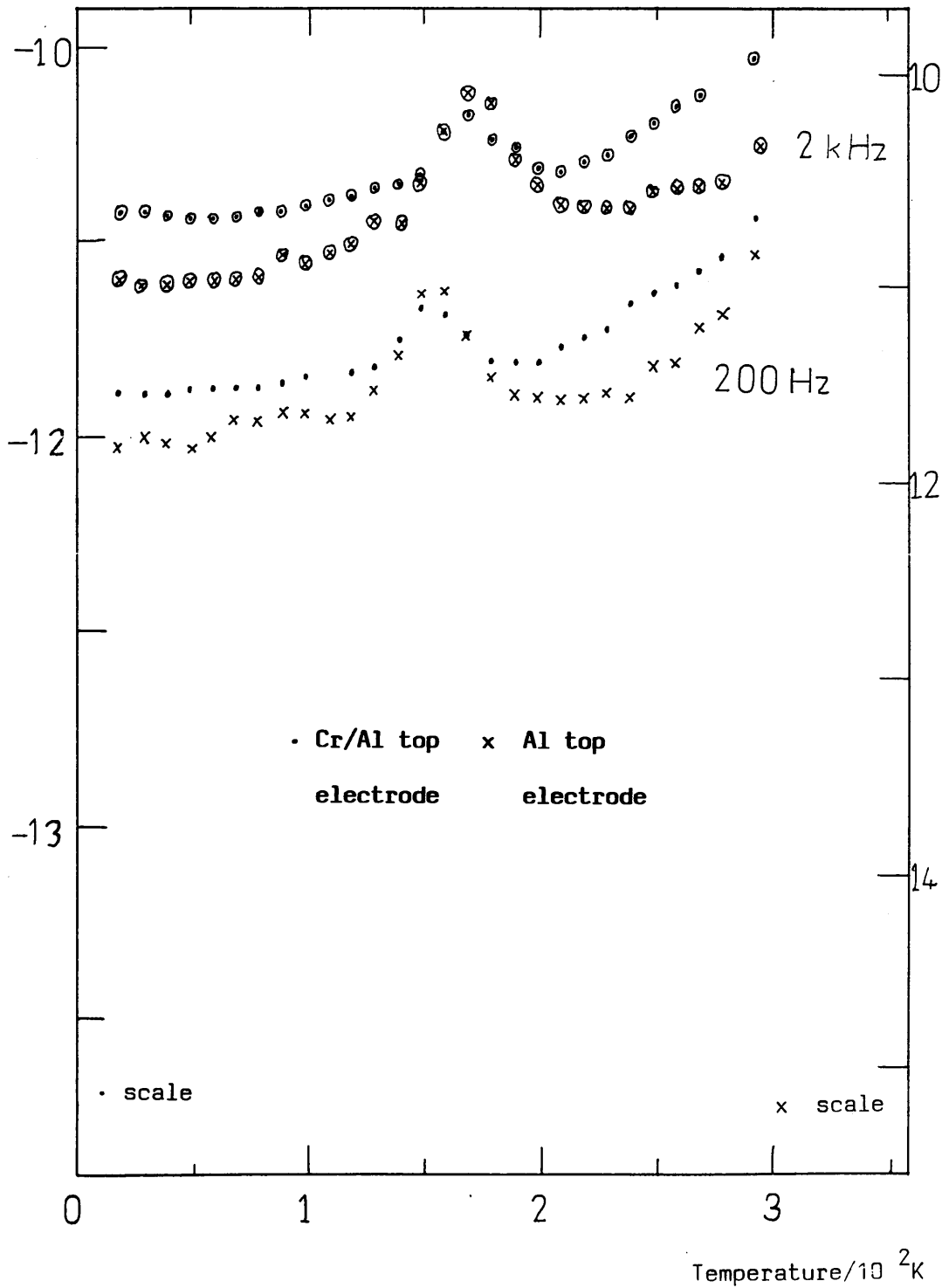
$\log(\text{conductance}/\text{Scm}^{-1})$



Graph 5.5

The temperature dependence of the conductivity for S2, an n^+i sample, with aluminium electrodes.

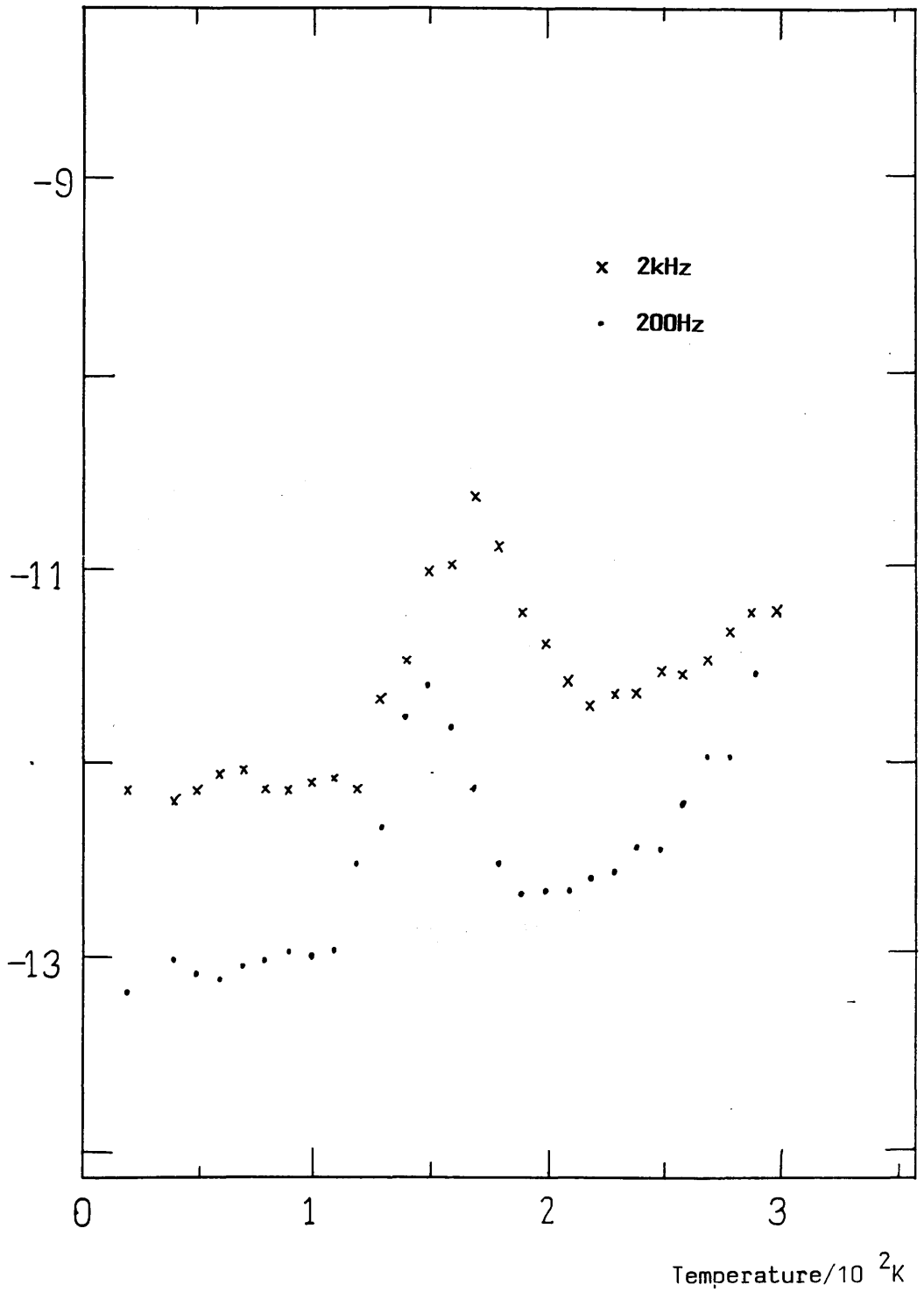
$\log(\text{conductance}/\text{Scm}^{-1})$



Graph 5.6

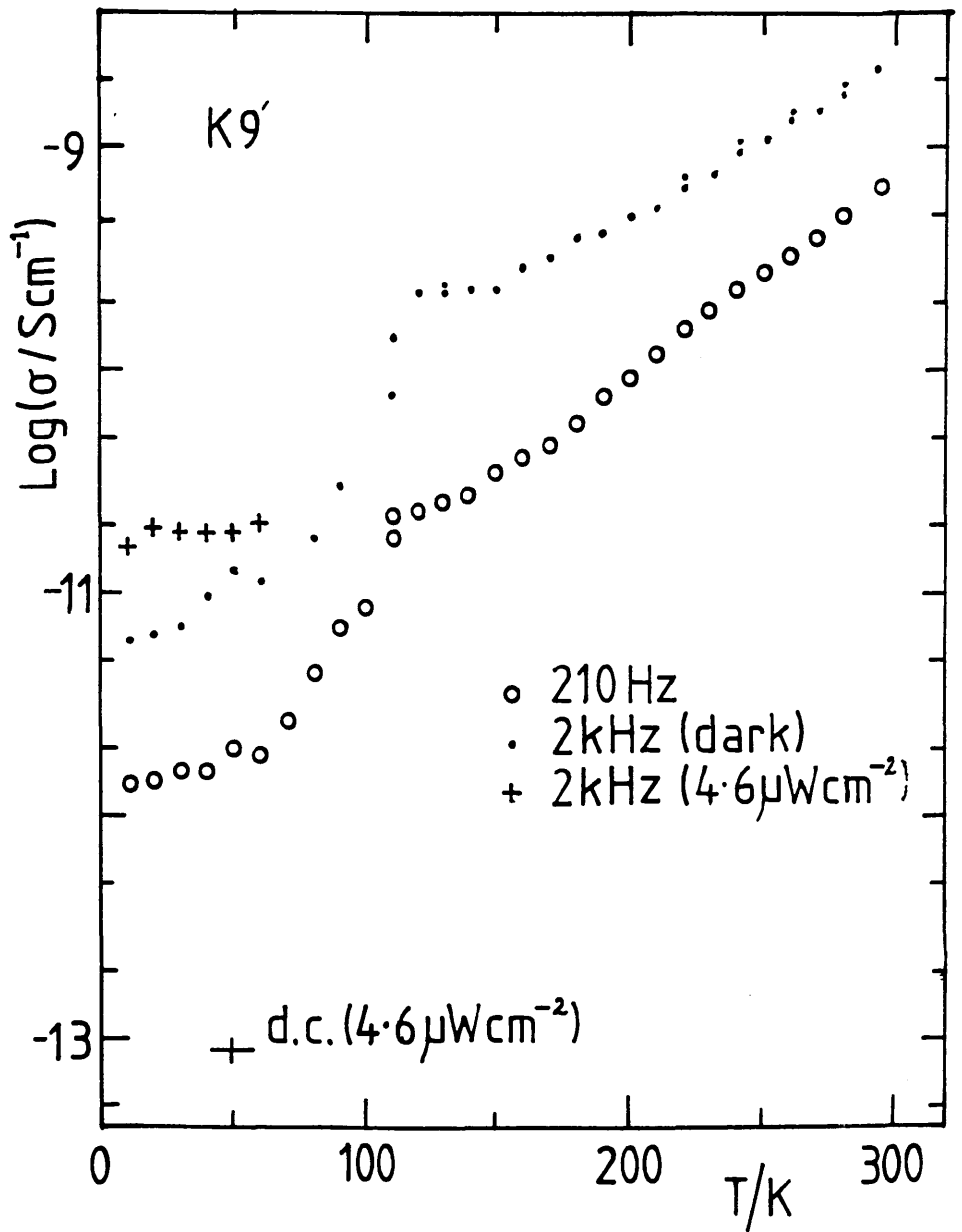
The temperature dependent conductivity for S3 at 2KHz and 200Hz. S3 is an $n^+ - i$ sample.

$\log(\text{conductance}/\text{Scm}^{-1})$



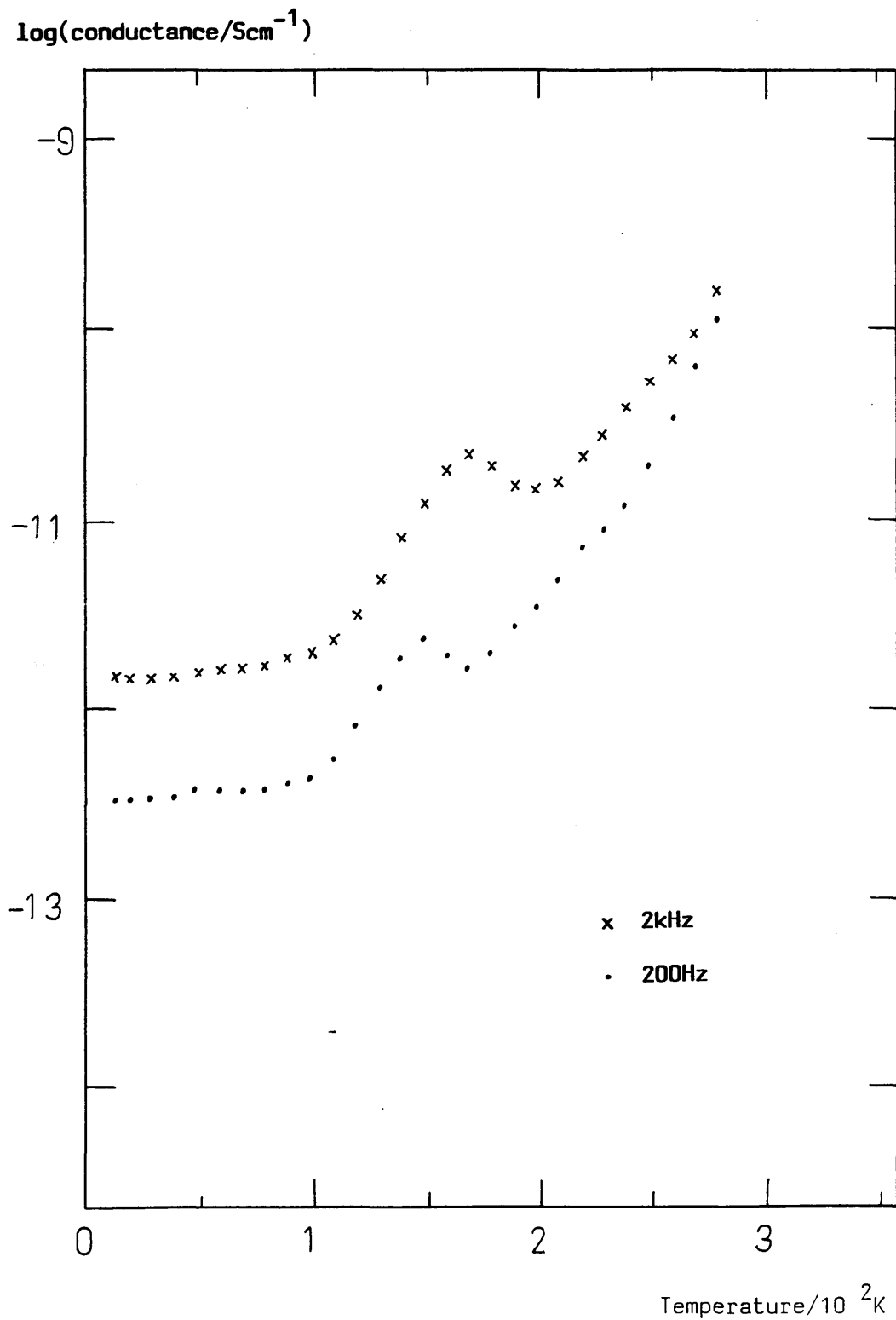
Graph 5.7

The dependence of the conductivity with temperature for an n^+i sample (S5).



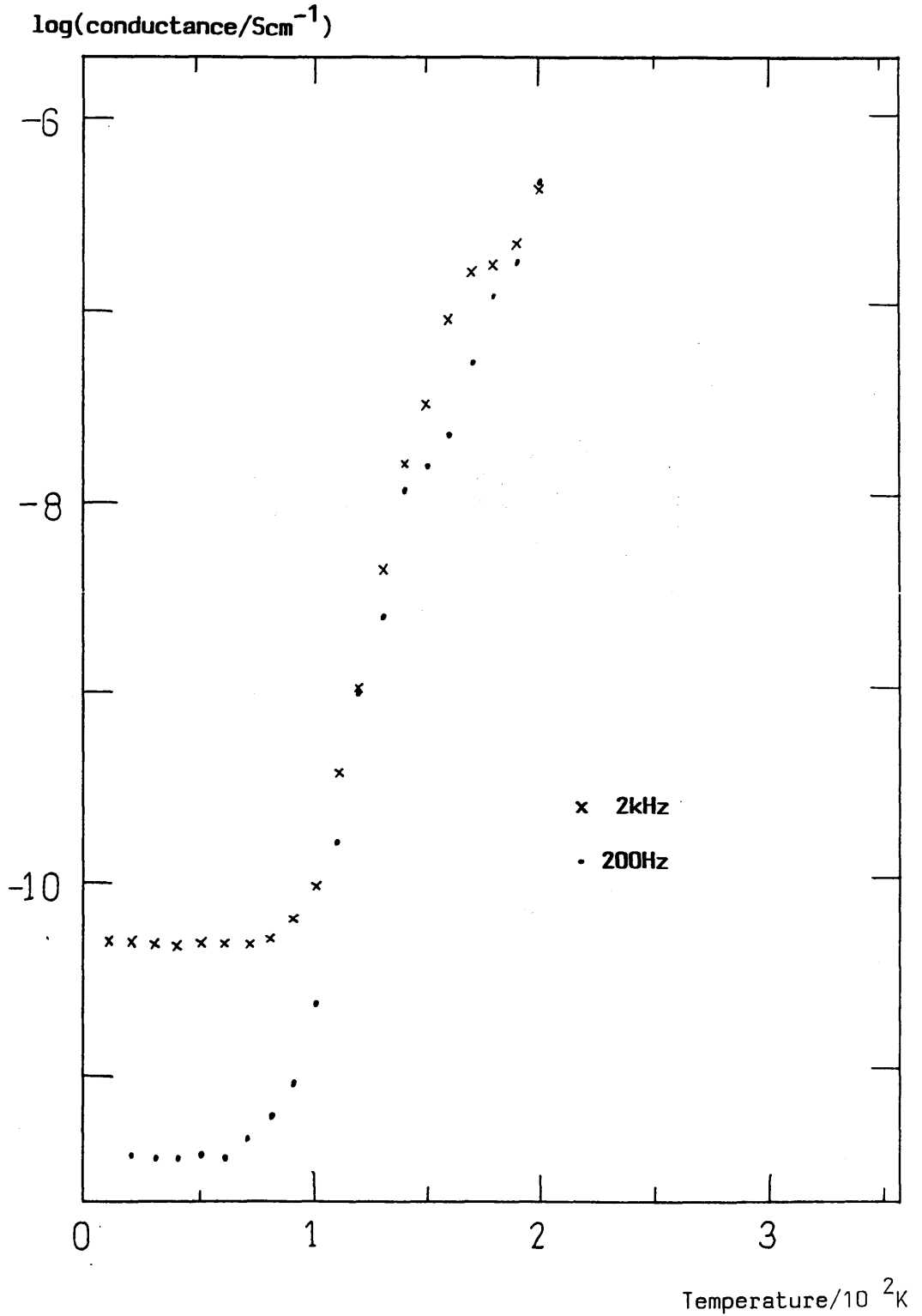
Graph 5.8

The temperature dependence of the conductivity for an n⁺-i-n⁺ sample (K9').



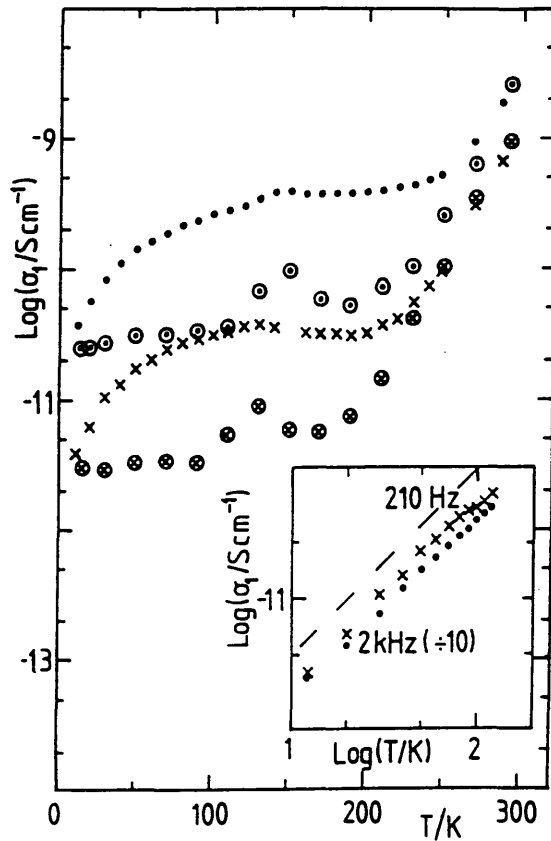
Graph 5.9

The temperature dependence of the conductivity for K11, an $n^+ - i - n^+$ sample.



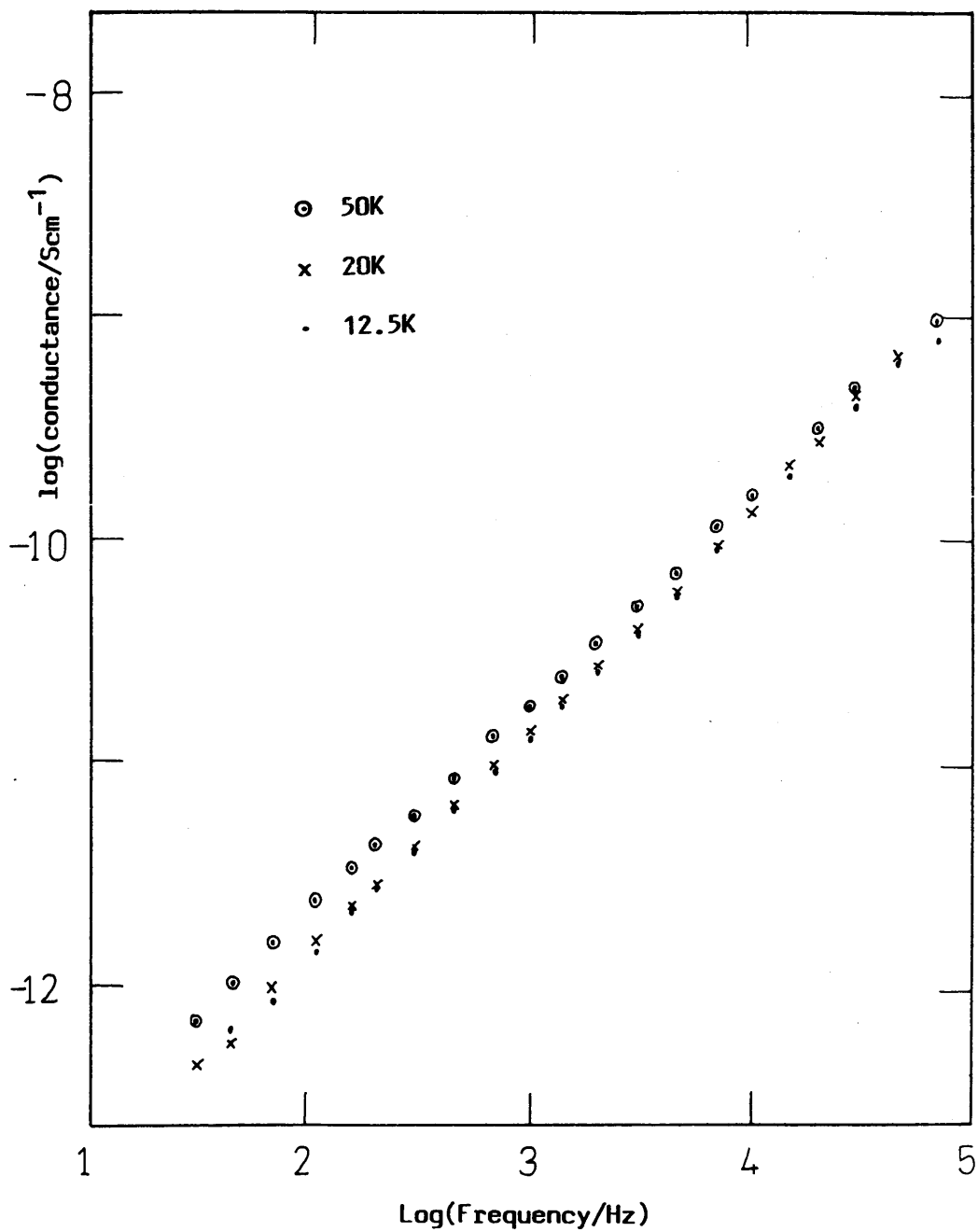
Graph 5.10

The dependence of the ac conductivity on temperature for D1₁ a doped (n⁺) sample.



Graph 5.11

The variation of the dark conductivity with temperature for an n^+i sample (S2) with Cu-Ni (ringed points) and Au (unringed points) electrodes. The inset shows that $\sigma_1 \propto T^n$ at low temperatures. The upper set of data on the main graph was taken using a 2kHz ac measuring field. The lower set was obtained by using a 210Hz field.



Graph 5.12

A graph of the frequency dependence of the total conductivity for an $n^+ - i - n^+$ sample (K11').

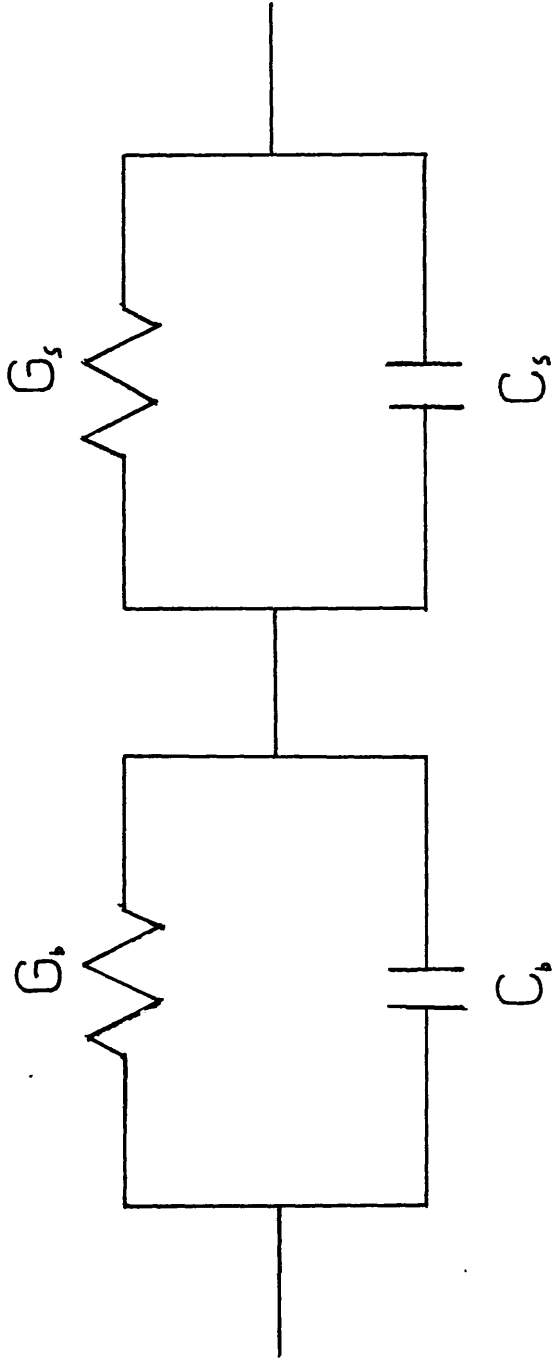
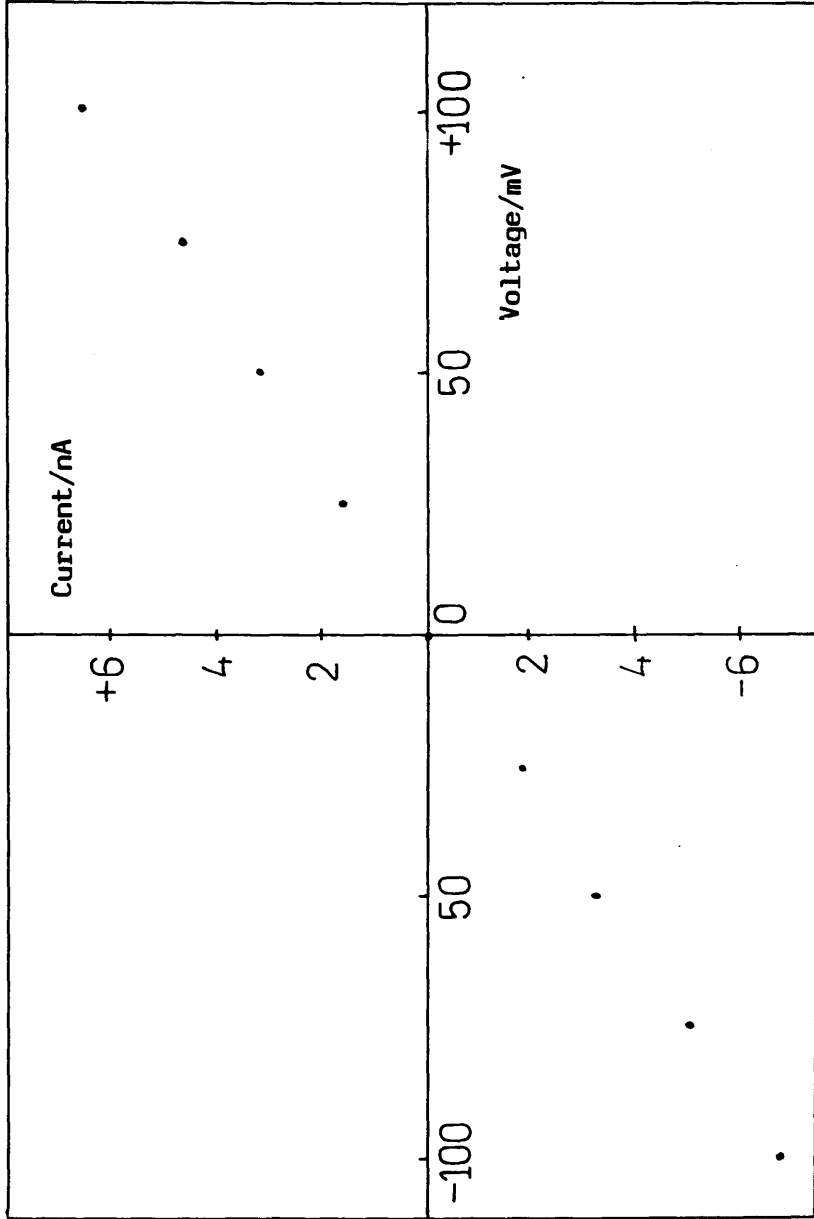


Diagram 5.13

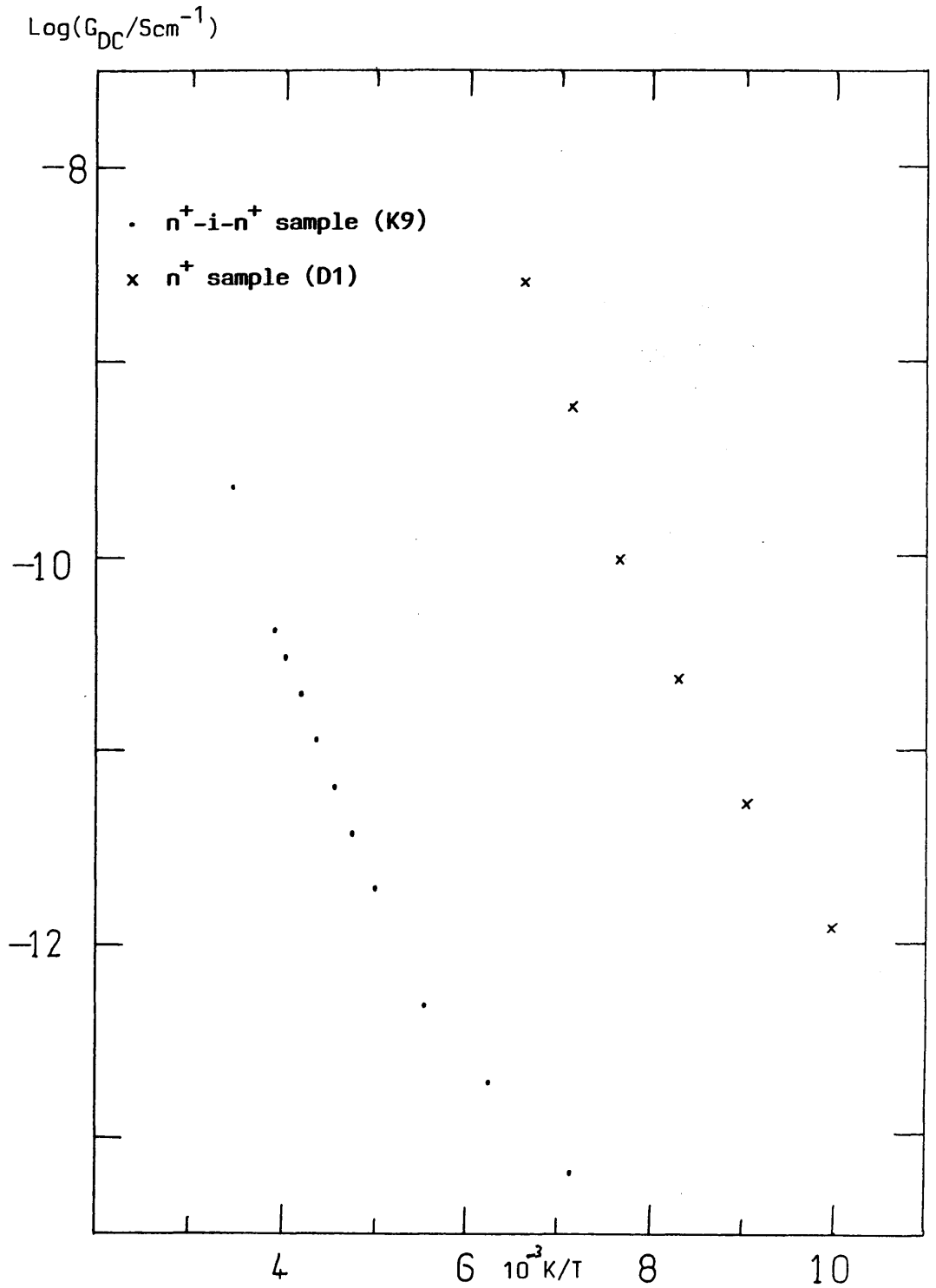
Equivalent circuit used to analyse the effect of a series layer.

G_b and C_b represent the sample and G_s and C_s represent the series layer.



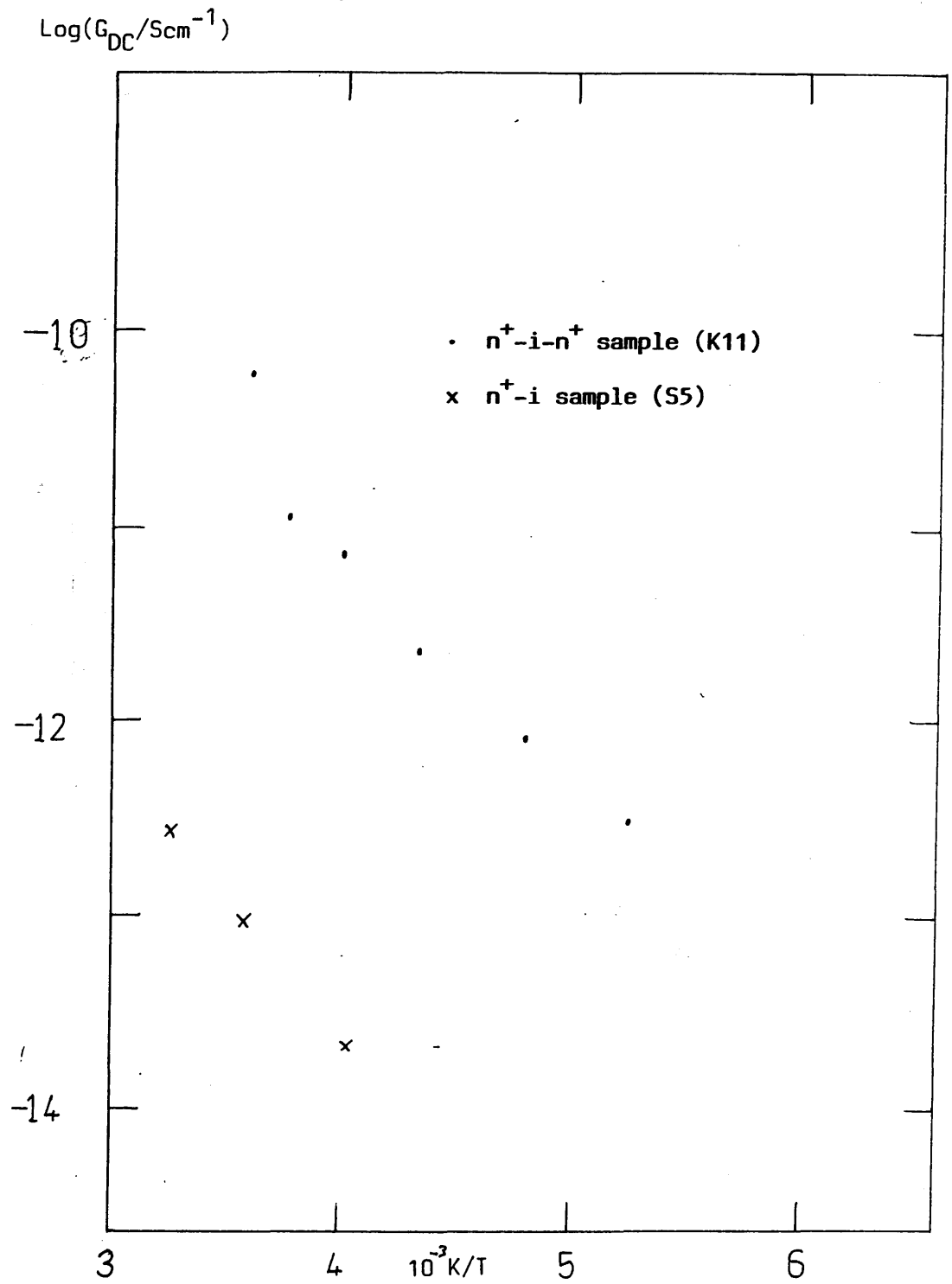
Graph 5.14

I-V characteristics for sample K9, ($n^+ - i - n^+$)
at room temperature.



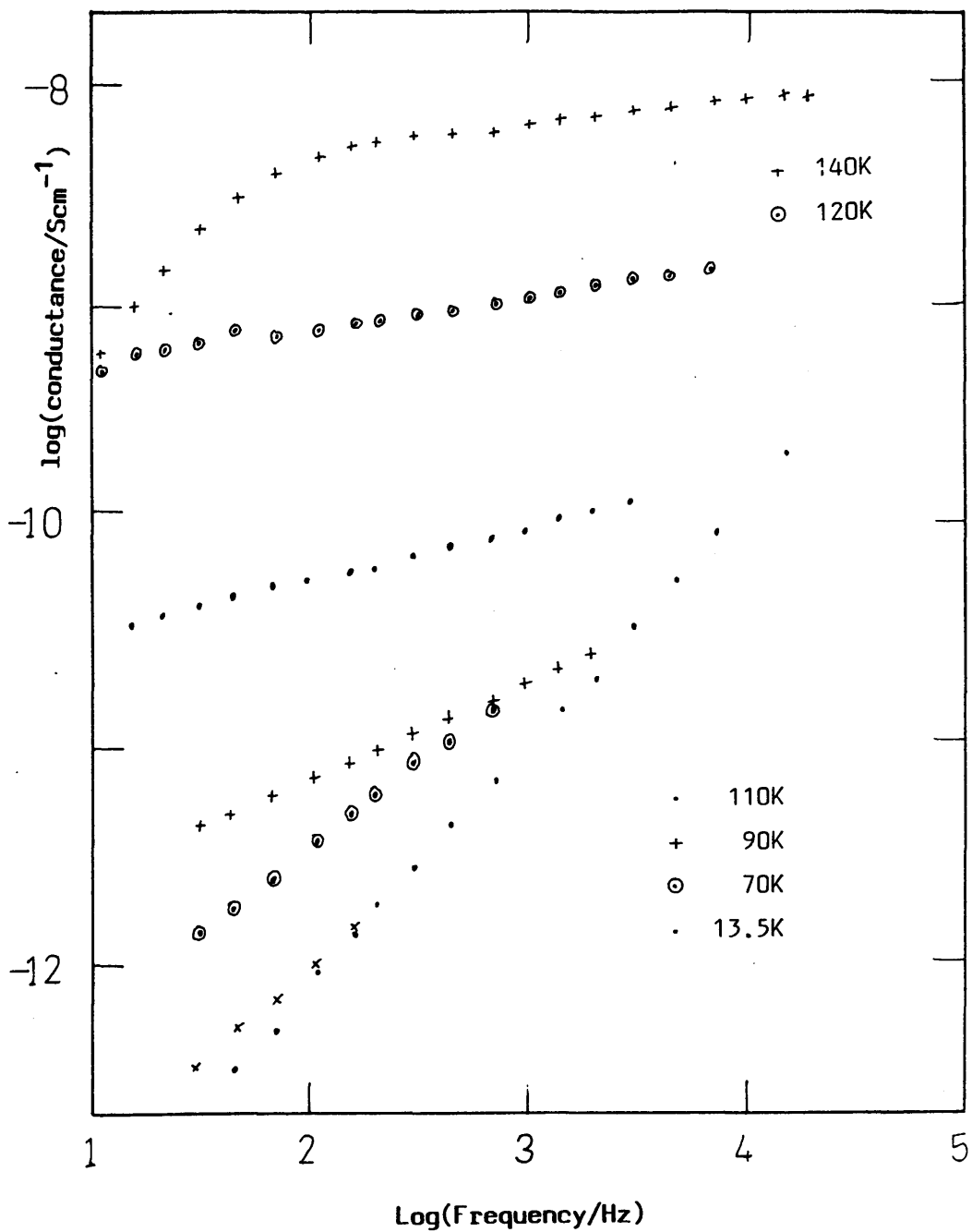
Graph 5.15

Plot of the logarithm of the dc conductivity versus $1/T$ for a doped (n^+ , D1) sample and an intrinsic sample ($n^+ - i - n^+$, K9').



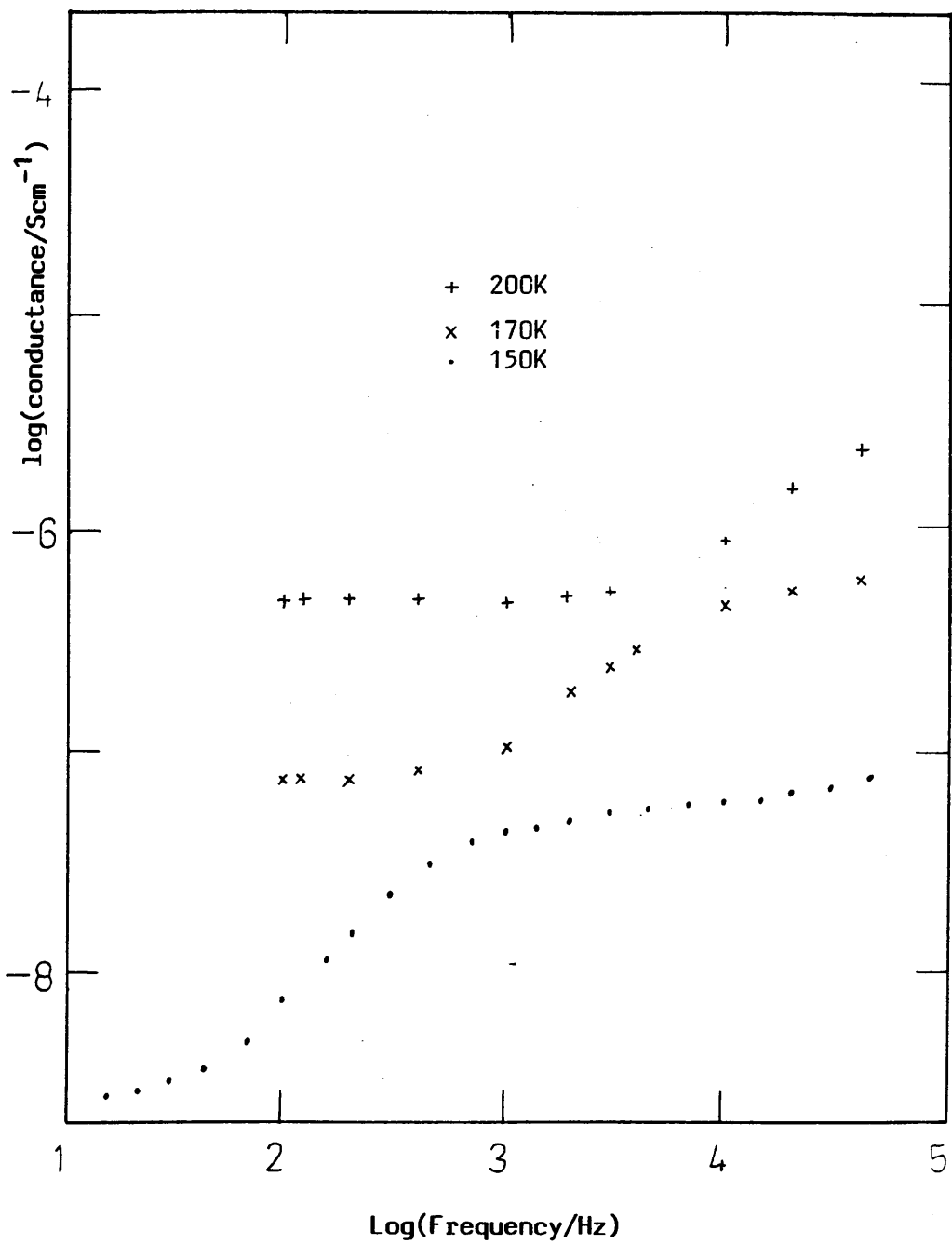
Graph 5.16

The logarithm of the dc conductivity plotted against $1/T$ for two samples.



Graph 5.17

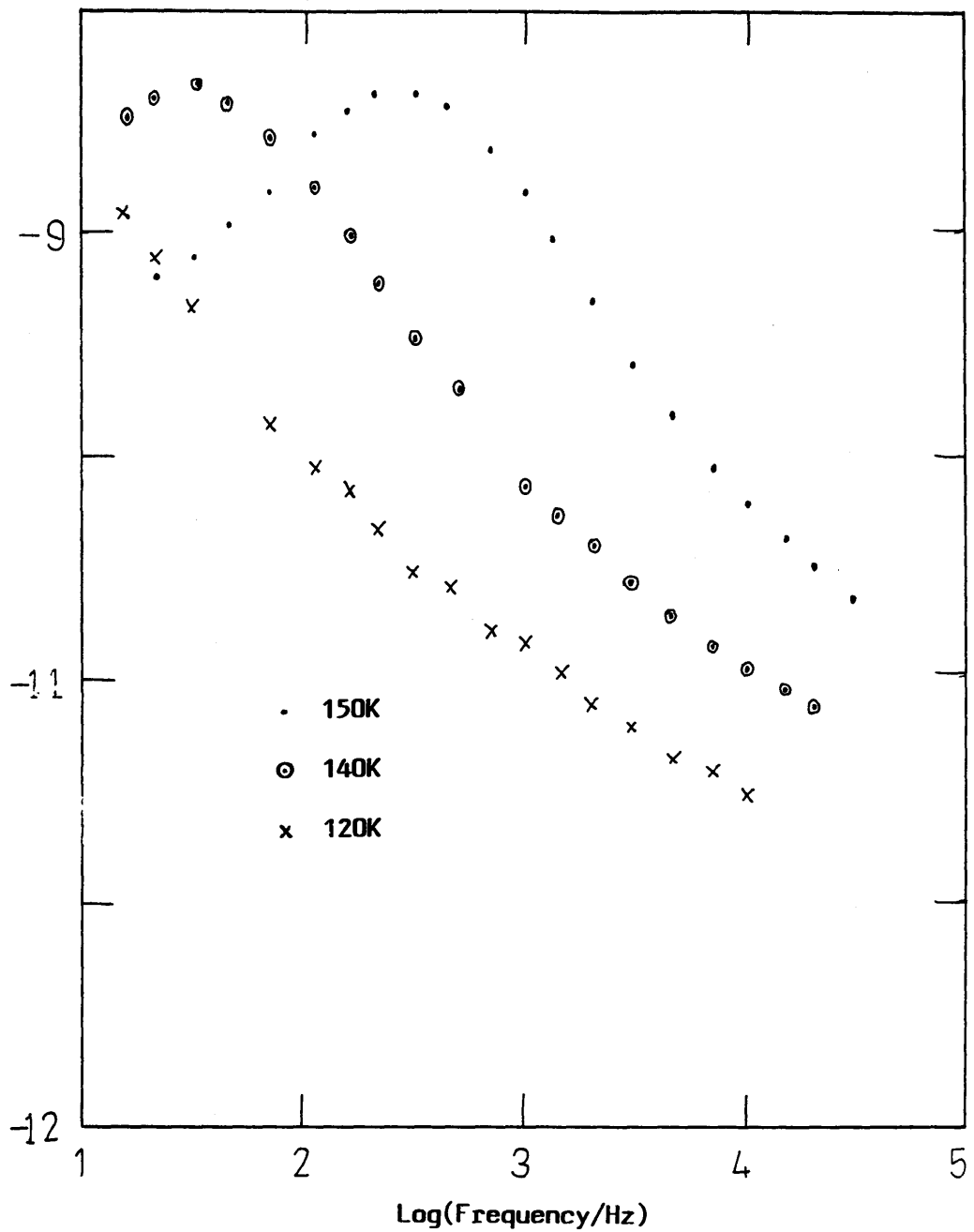
(a) The frequency dependence of the total conductivity for an n⁺ sample (D1).



Graph 5.18

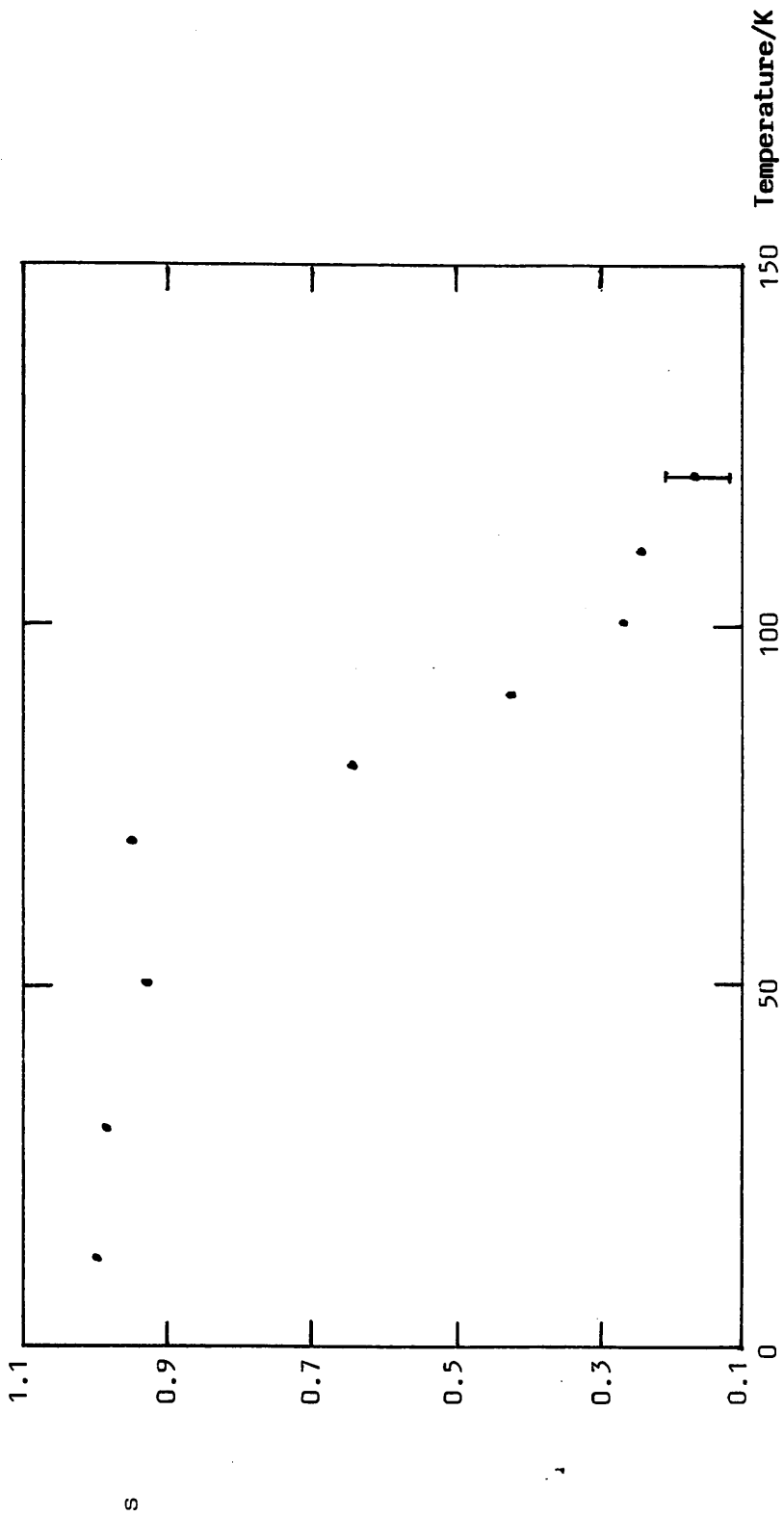
(b) The high temperature frequency dependence of the n^+ sample (D1).

$$-\left(\frac{dC}{d\ln\nu}\right)$$



Graph 5.19

(c) Loss peaks obtained from the capacitance and frequency data for a doped sample (D1, n⁺).



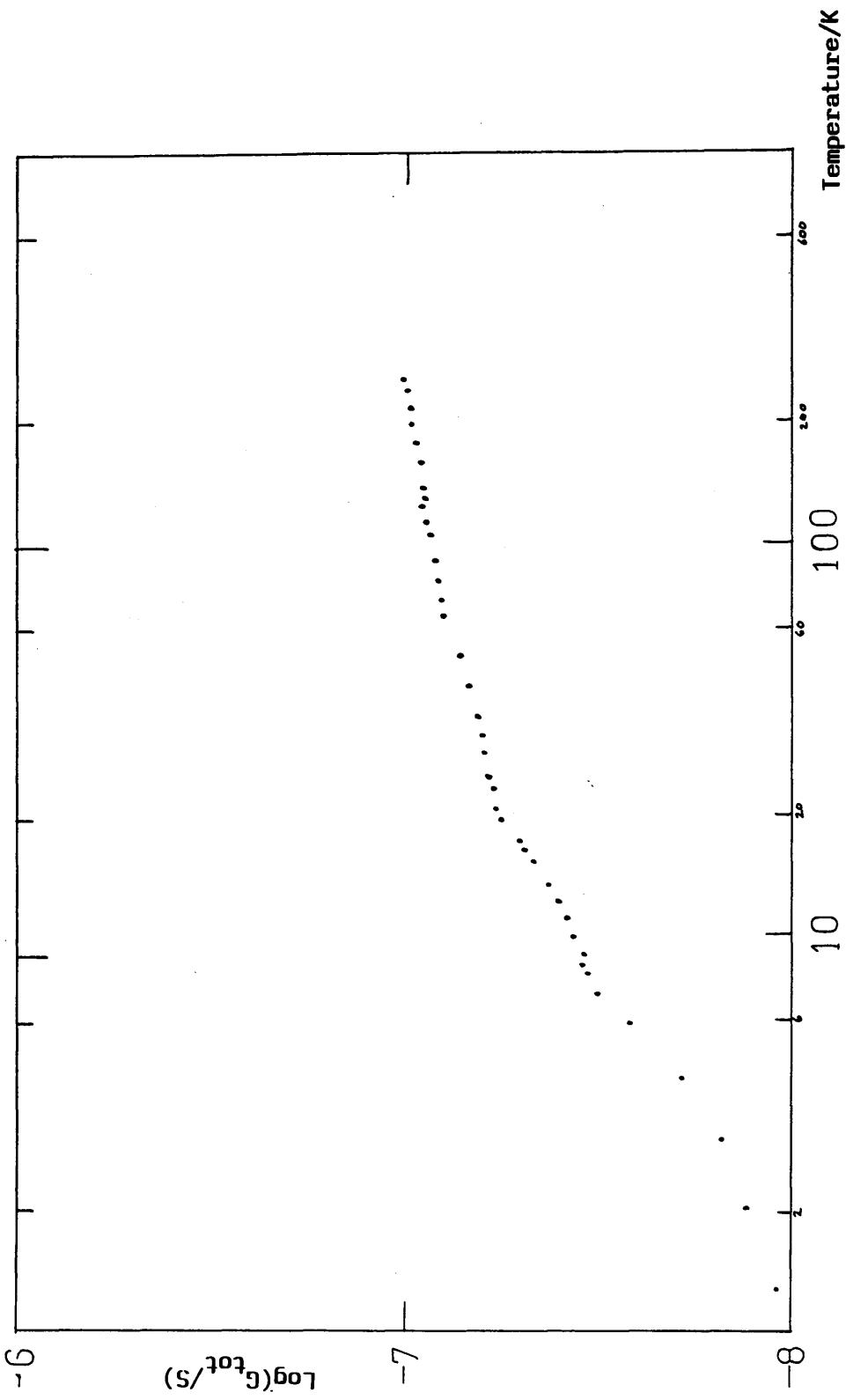
Graph 5.20

A plot of s vs T for an n^+ sample (D1).

Table 5.21

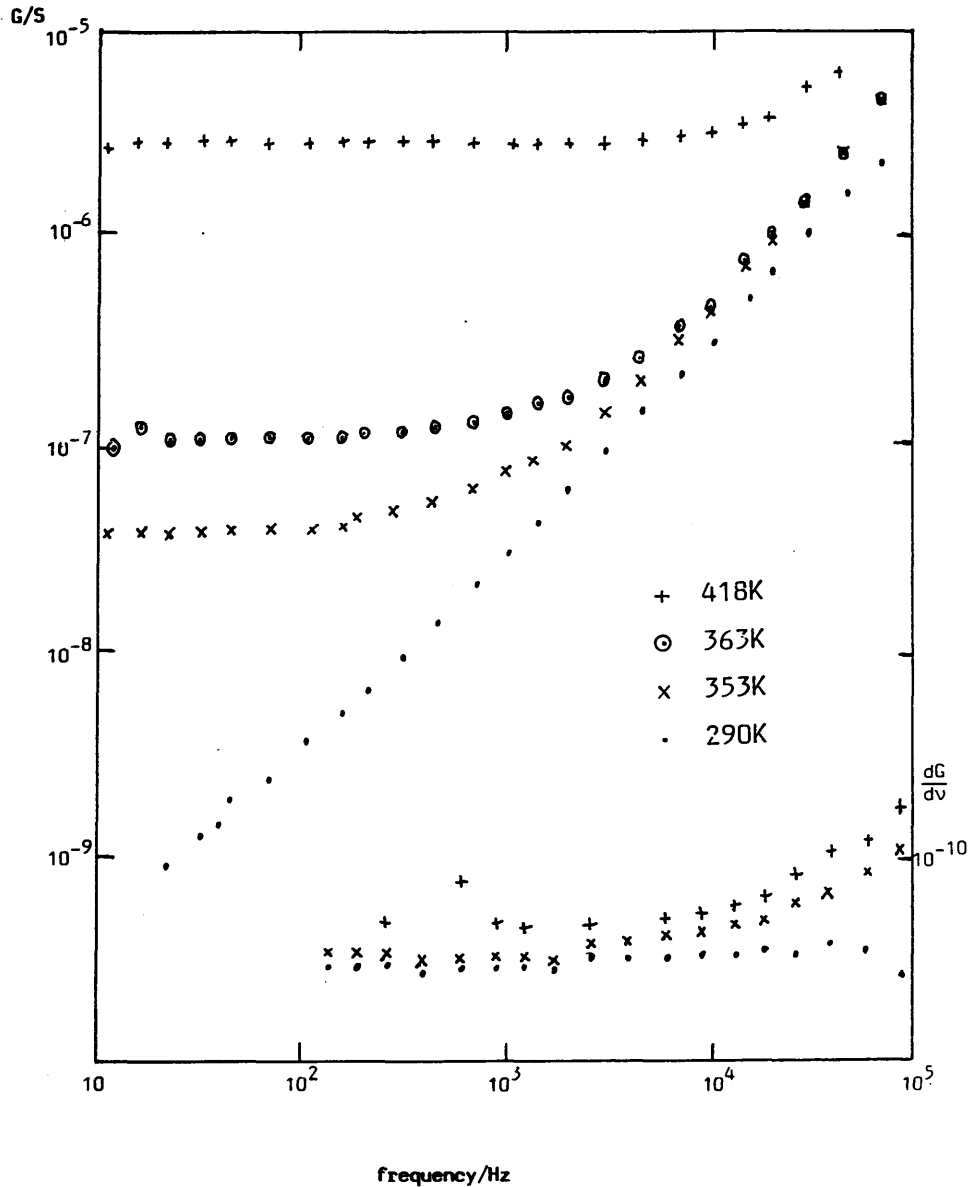
Sample	S2	S3	S5	K9	K11
$C_o \sigma_o$ (sm^{-1})	3.42×10^3	2.28	2.762	14.63	235
σ_o (sm^{-1})	1.125	0.741	2.4×10^{-3}	7.86×10^{-4}	0.010

Table showing values of $C_o \sigma_o$ and σ_o for various samples.



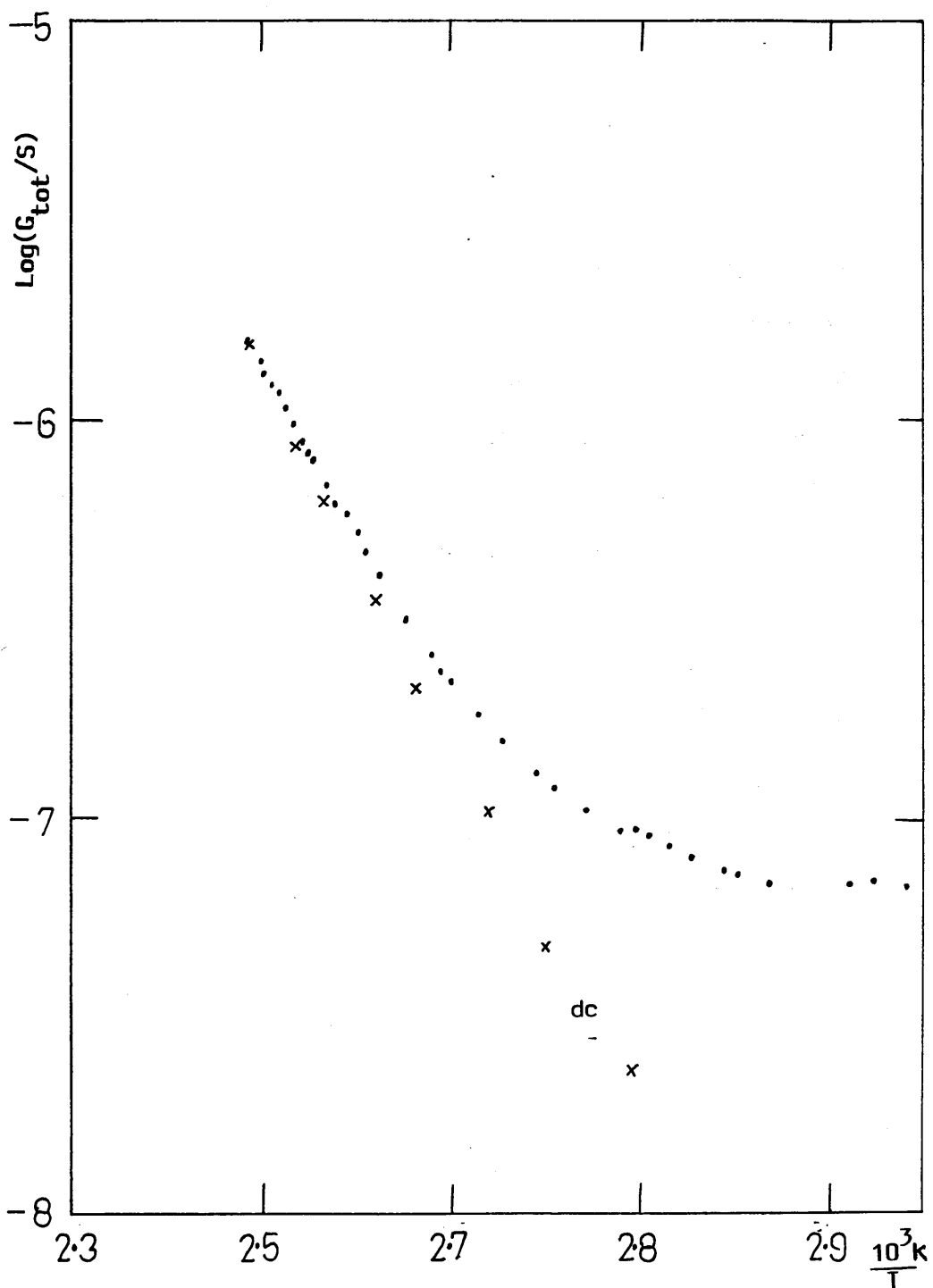
Graph 5.22

The variation of the total conductivity with temperature for an As_2Se_3 sample.



Graph 5.23

The frequency dependence of the total conductivity at a variety of temperatures for an As_2Se_3 sample. The inset shows the dependence of $\frac{dG}{dv}$ at three temperatures.



Graph 5.24

The high temperature dependence of the total and dc conductivities of the As_2Se_3 sample.

6.1 General Description of the Optical Response

6.1(a) Glow Discharge Material

The a-Si and a-Si:H films were illuminated through a semi-transparent electrode in the manner described in a previous section (Chapter 4). At low temperatures, usually from 1.2K up to 50K, a change in capacitance and conductance was observed when light was applied to the sample.

For illuminating intensities above $1\mu\text{W}/\text{cm}^2$ the optical response occurs within a few seconds. The increase in loss continues for about ten minutes until a saturation value is obtained. Both C and G show similar behaviour with the optical response superimposed on a background value. Further intensity changes, in steps up to a maximum of $\sim 100\mu\text{W}/\text{cm}^2$ cause C and G to increase and reach new equilibrium values for a particular illuminating intensity. The general form of the capacitance vs time graph for different illuminating intensities is shown in diagram 6.1. Lower intensities, less than $\sim 1\mu\text{W}/\text{cm}^2$ cause C and G to increase, but much more slowly. An integrating response, to a saturation value, is observed over a period of about 1 hour up to as long as 8 hours.

When the illumination is removed the capacitance (and conductance) falls. This fall consists of an initial fast decay (over several minutes) which becomes a slow decrease towards the dark values. At low temperatures (4K to 20K) the decay continues for many days. Higher temperatures (above 50K) cause the sample to return to the dark state much more quickly. On recooling, the sample can be seen to have returned to its low temperature dark state. This is a useful method of clearing the induced response.

Capacitance measurements taken by the computer controlled measuring system were found to be more accurate than conductance measurements.

This is due to small errors in the loss angle, $G/\omega C$, which contribute significantly to the conductance values. The measured conductance values are often close to the lowest limits detectable by the measuring system (see Chapter 4 for details of the accuracy of each measuring system). Capacitance data is also not as susceptible to dc photoinduced effects as conductance. All conductance values must be corrected for dc photoconductance to enable the optically induced change at 2KHz to be investigated. For these reasons, and the fact that C and G show similar behaviour regarding response and decay times, it was decided to concentrate on capacitance data throughout this chapter.

6.1(b) Sputtered Material

The magnetron sputtered a-Si sample, MA4, shows a similar capacitance and conductance response under illumination. The response times, however, are much shorter (seconds instead of minutes) and the magnitude of the change is larger. (See section 6.5.) Recombination times are also less and a typical decay to the dark state takes place over a period of around 8 hours, even at 1.2K, the lowest temperature investigated. The response and decay times, as well as the magnitude of the change at similar illuminating intensities, are consistent with those observed by Holland (Ph.D thesis 1987) for both conventionally and magnetron sputtered a-Si (see Chapter 7 for a more detailed comparison).

6.2 Preparation of the Dark State

The main problem is measuring the optically induced change in a-Si and a-Si:H is in defining the dark state. Even at a steady temperature of 12.5K, the dark conductance and capacitance values tend to fall over several days. The change is small (less than 0.01% for capacitance)

compared with the optical response and the rate of decrease is also extremely slow.

In order to minimize this problem a standard procedure was used. Initially a-Si:H samples were cooled from room temperature to low temperatures (usually 12.5K in CII Cryocooler) over a period of ~4 or 5 hrs. Illumination was then applied briefly (for ~15 to 20 min.) in order to check the response. After removal of the light the response was allowed to decay for a short time. The sample temperature was then raised to 50K for half an hour to 1 hour in the dark. On recooling the C and G values were often lower than the starting values at low temperature. The sample was then left at 12.5K overnight and the base values were recorded immediately before an optical run began. The temperature was always raised to 50K for at least half an hour after each overnight decay and allowed to cool before beginning a new run.

If a sample was held at 150K for several hours and then re-cooled the base values of C and G would fall even further below the starting values than they did when a sample was held at 50K and re-cooled although too high a temperature can thermally excite carriers. The dark state was defined as the initial values of C and G before the start of an optical run. Using this definition, after the preparation conditions described above, consistent results were obtained as detailed in the next sections.

6.3 Magnitude of Errors in Capacitance Measurements

The main source of errors in calculating errors on the $\log \Delta\epsilon_1$ vs $\log I$ plots is due to the uncertainty in estimating the base capacitance value. It is possible to measure capacitance to around $\pm 0.003\%$, if twenty points are averaged, between 100pF to 300pF at signal voltages of 100mV.

One contribution to the error in the dark base capacitance value occurs when a sample is left at a steady temperature for a period of time. At $\sim 12.5\text{K}$ (and at other low temperatures) the base capacitance value is found to decrease slowly with time at the rate of $\sim 0.02\text{pF}$ per day (estimated from the difference in dark capacitance values over 8 hours at 12.5K). Another error occurs when samples are re-cooled after being heated to a higher temperature ($\sim 50\text{K}$). It is found that the base capacitance, in the dark, on re-cooling is approximately 1% less than the dark base value before the sample was raised in temperature.

It is likely that two mechanisms are involved in producing the effects described above. The first, responsible for the slow continuous decrease in the dark, is probably due to residual carriers trapped in band-tail states. At low temperatures such trapped carriers will recombine very slowly (evidence is available from the decay tails seen in C vs time plots) thus leading to the slow decrease in capacitance in the dark.

This idea of residual charge trapped in band-tail states can also explain the decrease in capacitance when a sample is re-cooled after annealing at a higher temperature. At a greater temperature, carriers recombine more quickly (this is also observed in capacitance decays with time at 50K). On re-cooling, there will be less residual trapped charge and the capacitance will therefore be lower.

The second mechanism proposed to account for the decrease in the dark capacitance at low temperatures involves the states responsible for the background capacitance. These states are due to structural defects and occur deep within the band-gap. A change in these states, possibly due to structural or electronic relaxation processes, could cause the background capacitance to decrease slowly with time.

It is likely that a combination of these mechanisms is responsible for the effect which is observed. In order to find out how the optical results are affected the size of errors due to these processes is now considered.

The slow decrease of the dark capacitance at low temperature would produce a change of less than $10^{-3}\%$ over the period required to carry out an optical experiment. Such a change produces an error of less than 1% in the optically induced capacitance at the lowest intensities used.

The above error is negligible in comparison with the error due to subtracting the base capacitance from the illuminated capacitance values. The measured response under illumination can be in error by up to ~50% at the lowest intensities used. This is due to the optically induced charge being close to the lowest change which can be detected by the measuring equipment. As the light intensity increases the $\Delta\epsilon_1$ values increase meaning that the error due to subtracting the base value becomes less significant. For example, a typical low intensity change in $\Delta\epsilon_1/\epsilon_1$ is of the order of 0.05% (K11 at $I = 0.5\mu\text{Wcm}^{-2}$). An error of around 10% occurs in this case. As I increases to the maximum intensity ($\sim 100\mu\text{Wcm}^{-2}$ for K11) then the value of $\Delta\epsilon_1/\epsilon_1 = (0.25 \pm 2)\%$.

Data is also available, from D1, at 12.5K and mid-intensities, to show that the magnitude of the induced optical response is the same, to better than 2%, for 2 optical runs carried out under identical conditions. The sample was heated to 50K after the first run and recooled to 12.5K before beginning the second. The base value of capacitance decreased by 0.0447 pF on recoiling (equivalent to a $6 \times 10^{-3}\%$ decrease).

It was concluded that the procedure used for producing the dark

state was sufficiently good so as not to introduce significant experimental error, except at the lowest intensities of light which were applied to the samples. At such low intensities further errors are introduced due to the equilibrium value of the response not being reached, even after several hours. The errors are marked on the $\log \Delta\epsilon_1$ vs $\log I$ plots.

6.4 Intensity Dependence of $\Delta\epsilon$

6.4(a) Sputtered Material

The response, $\Delta\epsilon$, is non linear with increasing intensity at low temperature. The data, obtained from graph 6.1 and plotted on graph 6.2, shows high and low intensity regions. A weak intensity dependence, with a gradient of 0.24 is observed above $\sim 50 \text{ nW/cm}^2$ (surface intensity to sample) at 4.2K. This region corresponds to the " $I^{\frac{1}{4}}$ " region observed by Holland (1987) in a-Si and a-Si:H prepared by conventional and by magnetron sputtering. As the intensity decreases the gradient becomes larger and increases to about 0.48 at the lowest intensities used (the " $I^{\frac{1}{2}}$ " region). The change is not abrupt and a transition region is observed between the $I^{\frac{1}{2}}$ (see Holland Ph.D. thesis 1987) and the $I^{\frac{1}{4}}$ regions. This transition region occurs from around 10 nWcm^{-2} to 100 nWcm^{-2} .

The 1.2K data shows only a region with a gradient of 0.2. $\Delta\epsilon$ values at the highest intensities are close to those measured at 4.2K.

6.4(b) Glow Discharge Samples

All the types of sample studied (S, K and D) had similar $\log \Delta\epsilon_1$ vs $\log I$ characteristics. The following points apply to all the $\log \Delta\epsilon_1$ vs $\log I$ curves. (See graphs 6.14 to 6.18. The C vs time plots are shown in graphs 6.4 to 6.13.)

1. At low temperatures and at intensities above $\sim 10 \mu\text{Wcm}^{-2}$ the curves are linear implying that a power law applies. i.e. $\Delta\epsilon \propto I^\alpha$
2. A division into high and low intensity regions is observed in the $\log \Delta\epsilon_1$ vs $\log I$ plots. This division is not rigid and the two regions merge into one another.
3. Above $\sim 10 \mu\text{Wcm}^{-2}$, $\alpha \sim 0.25$ at low temperatures.
4. Below $\sim 10 \mu\text{Wcm}^{-2}$ the values of $\Delta\epsilon_1$ decrease at a faster rate than $I^{0.25}$. This is due to the integrating response observed at low intensities. Sample D1 was illuminated with low intensity light (at $\sim 17 \times 10^{-1} \mu\text{Wcm}^2$) and the response was measured over a period of around 8 hours. Even after this length of time the optically induced response was not fully saturated. Applying light for shorter times will therefore not cause the response to saturate at these intensities. The points taken in the integrating region are not the upper limits of the optically induced response and are denoted as † on $\log \Delta\epsilon_1$ vs $\log I$ curves.
5. A weak temperature dependence of the optical response is observed (graphs 6.14 to 6.18). At high temperatures ($\sim 50\text{K}$) the values of $\Delta\epsilon_1$ are generally lower than the values, at the same intensity, at 12.5K . The gradient α , can be observed to increase weakly with increasing temperature.

6.5 Magnitude of $\Delta\epsilon$

6.5(a) Dependence of $\Delta\epsilon$ on Sample Material

Three different types of sample were investigated in order to quantify the optical response. These were (a-Si, a-Si:H and a-As₂Se₃ prepared by the methods described in Chapter 4.

As₂Se₃ Sample

This sample was illuminated at high intensities (up to $10\mu\text{Wcm}^{-2}$) using both the He-Ne laser (at 633nm) and a white light source. The experiment was carried out in a standard He cryostat at 1.2K and at 4.2K. No change in capacitance or conductance was measured by the computer controlled system (implying an upper limit of $\Delta\epsilon/\epsilon = 0.0085\%$ which is the lowest detectable response which can be measured on this system) when the sample was illuminated for 5 or 6 hours. This is consistent with a similar experiment performed by Holland (Ph.D thesis 1987) on a sputtered As₂Se₃ film.

Magnetron Sputtered a-Si Sample

Optical experiments were performed at 4.2K and at 1.2K on MA4. Illumination was provided by a He-Ne laser, $\lambda = 633\text{nm}$, at intensities up to $1.8\mu\text{Wcm}^{-2}$ (after correcting for the transmittance and reflectance of the sample electrodes and for the a-Si film).

The low temperature response (at 1.2K) was found to be slightly greater (0.699% at 1.2K compared with 0.465% at 4.2K at an illuminating intensity of $1\mu\text{Wcm}^{-2}$) than the 4.2K response. This data is shown in graph 6.2. The response of the thick junction is seen to be less than that of the thin junction, at 4.2K. Values of $\Delta\epsilon/\epsilon$ are tabulated in diagram 6.3.

Glow Discharge Samples

All the glow discharge samples showed a smaller optical response when compared with sputtered samples. In order to obtain a 0.2% change in capacitance at the lowest temperatures it was necessary to illuminate the junction with an intensity of $\sim 50\mu\text{W/cm}^2$. To compare the various types of sample (i.e. S, K and D) a fixed value of

$I = 1.0 \text{ W/cm}^2$ was used. Values of $\Delta\epsilon_1/\epsilon_1$ were taken from the various graphs and are tabulated in diagram 6.20. At 12.5K, the D samples, D2 showed a large response (0.35% at 4.2K (D2)) and 0.16% at 12.5K (D1)). The K and S samples, with ITO/AL electrodes, showed a similar size of optical response (approximately 0.12% and 0.14% respectively). It can be seen that the response is lower than that observed in sputtered material, as equivalent changes are observed at a lower intensity ($10 \times 10^{-3} \text{ nW/cm}^2$) in sample MA4.

6.5(b) Effect of Electrode Material on $\Delta\epsilon_1$ for Glow Discharge Material

It was found that the electrode material had a significant effect on both the background loss (see section 5.9 for details) and on the optically induced loss. A number of experiments were performed on a-Si:H n^+ -i-Al samples (S2,S3) and on an a-Si:H n^+ -i- n^+ -ITO sample (K9). Initially, semi-transparent gold electrodes were evaporated onto S2 and an optical run was carried out at 12.5K, as was the practice for sputtered samples. No optical response could be measured using the general radio bridge, even at a maximum applied intensity of $10 \mu\text{W/cm}^2$. This implies that $\Delta\epsilon_1/\epsilon_1$ is less than 0.0085%.

A $\Delta\epsilon_1/\epsilon_1$ value of 0.3% was measured when evaporated Cu-Ni electrodes were deposited on S2. This is a factor of ~5.7 less than the 1.7% response recorded on the same sample when thin Al electrodes were used. and the response measured at the same intensity.

A null response was observed when chromium electrodes were evaporated onto K9 and light of $10 \mu\text{W/cm}^2$ was applied in a similar experiment.

The above results suggest that the recombination rates of excited carriers is being enhanced due to diffused metal atoms acting as recombination centres (see section 7.6(b) for further discussion on this subject).

The values of $\Delta\epsilon/\epsilon_1$ at an illuminating intensity of $10\mu\text{W}/\text{cm}^2$ on the sample, for different electrode materials on a number of samples are plotted on diagram 6.20, against the dark loss, at low temperature. It can be seen that the lowest loss and highest $\Delta\epsilon/\epsilon$ is found in S2 with top and bottom Al electrodes. Unfortunately, thin films of Al deteriorate after a few days, leading to non conducting electrodes with changed optical properties (see section 5.8). Al electrodes in a semi-transparent film are therefore not particularly suitable. If a less reactive metal such as Au or Cr is used, the dark loss is an order of magnitude greater and the optically induced loss is less than 0.01% for Au. Cr-ITO combinations range from less than 0.01% for K9 up to 0.09% for an S sample (S5). Cu-Ni electrodes were more successful, in terms of a high $\Delta\epsilon/\epsilon$ (0.1%), but these were also prone to deteriorate after a short time.

It was finally decided that a semi-transparent material, ITO, could be used. Samples with electrodes of this material were found to have a rather high dark loss (at 2KHz) than Al-a-Si:H-Al samples, but the $\Delta\epsilon/\epsilon$ values were reasonably high (~0.2% at $10\mu\text{W}/\text{cm}^2$)

6.6 Temperature Dependence of $\Delta\epsilon_1$

Measurements of the magnitude of $\Delta\epsilon_1$ show variations with temperature, to some extent, in all the silicon samples studied.

MA4 shows a slightly higher $\Delta\epsilon_1$ at 1.2K than at 4.2K at all intensities up to the highest applied $\sim 290\text{nW}/\text{cm}^2$, see diagram 6.3. The gradient of the $\log \Delta\epsilon$ vs $\log I$ plot is also lower at the lower temperature, which is similar to the results found by Holland (Ph.D. Thesis 1987). These experiments involved applying light of similar intensities at 633nm onto a-Si and a-Si:H sputtered onto room temperature substrates using orthodox and magnetron (one

a-Si sample) targets. Holland showed that the $\log \Delta\epsilon_1$ vs $\log I$ plots have gradients of ~ 0.45 at low intensities (up to $\sim 0.1 \text{ nWcm}^{-2}$). The gradient decreases (to ~ 0.25 above $\sim 10 \text{ nWcm}^{-2}$) at high intensities. At higher temperatures (up to 10K) and low intensities the gradient is larger than at 1.2K or 4.2K.

Undoped samples prepared using the glow discharge technique (S and K samples) also show a temperature dependent $\Delta\epsilon_1$. The largest changes in ϵ_1 under illumination are observed at the lowest temperatures. At $10 \mu\text{W/cm}^2$, the change observed at 12.5K is of the order of $(0.150 \pm 0.002)\%$ in K11. S5 shows a $\Delta\epsilon_1/\epsilon_1$ of $\sim (0.169 \pm 0.002)\%$ at the same intensity and temperatures. (See diagrams 6.4 and 6.10 for details.) As temperature increases to 50K, the magnitude of $\Delta\epsilon_1/\epsilon_1$, at the same I , decreases. K11 shows a $\Delta\epsilon_1/\epsilon_1$ value of $\sim (0.046 \pm 0.002)\%$ and S5 shows a $\Delta\epsilon/\epsilon$ of $(0.010 \pm 0.002)\%$ at $10 \mu\text{W/cm}^{-2}$ applied intensity.

The gradients of the $\log \Delta\epsilon$ vs $\log I$ plots are also temperature dependent. The gradients, α , have been calculated for the various samples studied. The values of α are all taken in the saturating response region above $\sim 10 \mu\text{Wcm}^{-2}$, unless otherwise stated. The gradients in S and K samples are generally around 0.2 and α increases weakly with increasing temperature.

The D-samples (doped a-Si:H), D1 and D2, are different halves of the same film. For a fixed I of $10 \mu\text{Wcm}^{-2}$ $\Delta\epsilon_1/\epsilon_1$ decreases with temperature, but less strongly than is seen in S and K samples. At high intensities ($> 30 \mu\text{W/cm}^2$) the $\Delta\epsilon_1/\epsilon_1$ values are very close at all temperatures up to 50K. As the intensity drops below $10 \mu\text{Wcm}^{-2}$ the $\Delta\epsilon_1/\epsilon_1$ values show a greater spread. The largest values are seen at 4.2K and the smallest at 50K.

Gradients in the D-samples range from 0.164 ± 0.005 at 4.2K, at all applied intensities, to 0.299 ± 0.005 at 40K (above $3.1 \mu\text{W}/\text{cm}^2$ illuminating intensity). Below $I = 2.1 \mu\text{W}/\text{cm}^2$, the gradients between 12.5 to 30K are very close and at 40K and 50K the slope increases to (0.452 ± 0.005) .

6.7 The Effect of Increasing Temperature at a Constant Level of Illumination in Glow Discharge Samples

In these experiments the sample was illuminated at 12.5K. The temperature was then raised in $\sim 10\text{K}$ steps, still with the sample under the same level of illumination, and the response measured.

In S and some K samples it was found that the total response increased and then a decay to an equilibrium value was reached after about 30 min (see diagrams 6.24, 6.25).

D1 and some K samples showed that the total capacitance, under illumination, increased to a steady value when the temperature was increased.

The explanation for the behaviour observed is dependent upon the value of the background capacitance at a particular temperature and upon the rate at which a higher temperature increases the recombination rate of carriers. This will be discussed further in section 7.2(e).

6.8 The Frequency Dependence of the Optical Response

The typical dark frequency dependence taken at low temperatures has been described in Chapter 5.

Dark frequency sweeps were taken on all the samples before applying light to the sample. The samples were then allowed to attain their equilibrium response at a particular intensity and further frequency sweeps were taken. Data for various experiments is plotted

in graphs 6.22 to 6.23

It can be seen (from diagram 5.12) that, in the dark, conductance values obey an ω^s law with $s \approx 1$.

Frequency sweeps taken when a sample is illuminated show decreased s values. As the intensity of light increases the value of s drops further (see graph 6.22). Both doped and undoped a-Si:H samples show similar behaviour.

Capacitance vs frequency curves (graph 6.8) are also influenced by light. The values of C rise with increasing level of illumination.

Both C and G vs ω curves show that light has the effect of increasing values of C and G . The values attained under illumination are comparable to those seen at higher temperatures in the dark. For example, in D1 the illuminated frequency sweeps under $19.4\mu\text{Wcm}^{-2}$ intensity and at 12.5K, are similar to a 70K sweep taken in the dark. The full significance and implications of this result will be discussed in Section 7.

6.9 The Decay to the Dark State

When the optical excitation is removed the conductance and capacitance values fall towards their dark values. The rate at which this takes place was found to be strongly dependent on temperature and on sample material.

6.9(a) Sputtered Samples

Sample MA4 showed an initial fast decay, with C falling to 0.4% above its dark value, after the light was removed. This took 8000sec to happen at 4.2K. A slower decay, of about 60000sec. followed, after which the dark values were recovered to within a measurement error of 0.01%. (See graph 6.1).

The 1.2K data shows a similar form of decay. In this case, the fast decay, to about 0.52% above the dark value, lasted for ~1000sec. The base values were attained after slow decay of ~60000sec.

6.9(b) Glow Discharge Material

The decay times in glow discharge samples were extremely long at 12.5K or below. In fact, the samples did not return to their dark states during measurement periods of several days at these temperatures.

S, K and D samples generally show a rapid decrease in C and G on removing the light. This is similar to the rapid decay observed in MA4 and takes place over several thousand seconds. A drop of 50% (S, K samples) to 70% (D samples) is seen in the induced capacitance values over this time.

The fast decay merges into a long decay region where the decay rate is slower with time. However, on a $\Delta\epsilon_1$ vs $\log t$ graph there is little difference in the decay rate, as the graph is close to being linear in S and K samples. The long decay takes place very slowly in all glow discharge samples at this temperature.

As the temperature increases, the decay rate increases and samples return to their dark states more quickly. At 20K or 30K decay rates increase slightly, but at 50K or greater a rapid fall is observed (see diagrams 6.4 to 6.13). This has been shown to be a useful method of clearing the induced response and returning samples to their dark states. If samples are left for around half an hour or more and recooled, the C and G values will return to their original low temperature values.

Decays have also been plotted on $\Delta\epsilon_1/\epsilon_1$ vs $\log t$ plots. The K9 decays show a $\log t$ behaviour at 12.5K, but other samples (e.g. K11, 12, D1,2, S samples) exhibit a degree of curvature in their decays.

This becomes more pronounced at higher temperatures. A detailed analysis of this data is presented in Chapter 7.

6.10 Contact Effects

Data analysis has been complicated in a number of optical runs by "jumps" in the capacitance and conductance vs time plots. In some cases it is straightforward to measure the magnitude of the displacement since it occurs when C is in equilibrium for an applied intensity. In this case the value of the offset has been subtracted to give the $\Delta\epsilon$ vs I plots. If the offset occurs at an intensity change it is more difficult to account for this in data analysis and an estimate must be made. This has been indicated on the graphs where this occurred and compared to the uncorrected data. The decay "tails" also sometimes show offsets.

The problem is due to the samples themselves rather than the measuring equipment. Measurements performed during samples over long periods are very stable (to better than 0.01%) at 2KHz.

The offset was traced to poor contact conditions. When contacts are evaporated in a poor vacuum gases may be trapped by the electrode material as it condenses on the silicon surface. In a good vacuum (better than 10^{-6} Torr) the contact effect was eliminated as the data for S5, K9, K11, 12 and D1, 2 shows.

6.11 The Thickness Dependence of the Response in Sputtered a-Si

Sample MA4 was a double thickness a-Si film. The junction thicknesses, measured by optical interference techniques (see section 4.14), were 9600\AA and 4750\AA and the junction areas were measured to be identical to within $\pm 3\%$.

One reason for performing the measurement on this double thickness sample was to determine whether the optical effect was dependent on

the bulk of the sample or on surface effects. Optical measurements were carried out at 1.2K and at 4.2K and the results can be seen in diagram 6.2. The intensity scale is corrected to account for the differences in junction position with respect to the fibre outlet and is corrected for the transmittance and reflectance of the Au electrodes and the a-Si film. Capacitance data was averaged over 20 points, under computer control, for the thin junction. Data was taken, at the same time, for the thick junction but was only averaged over 5 points, leading to a lower accuracy.

The graph of $\Delta\epsilon_1/\epsilon_1$ vs I at 4.2K lie on roughly the same lines for both the thick and the thin junctions. This is similar to the result found by Holland (Ph.D. thesis 1987). The 1.2K data for the thin junction is inconclusive due to "jumps" in the measurements.

It is possible that $\Delta\epsilon/\epsilon$ is not a bulk effect because <2% of light at 633nm is transmitted by the thin junction. This shows that more than half the thickness of the other junction will receive very little illumination and is therefore unlikely to be involved in the optically induced loss. This will be discussed more fully in Chapter 7.

6.12 Effect of Different Wavelengths on $\Delta\epsilon_1$

A small amount of data taken at different wavelengths of light is available for glow discharge material. Due to the low intensities of light output from the monochromator it was difficult to perform optical runs at varying intensities. Low intensity light with wavelengths of 500nm and 800nm was applied to D1 at 12.5K. The intensities were $0.06\mu\text{Wcm}^{-2}$ and $0.10\mu\text{Wcm}^{-2}$ respectively. Measurement errors are indicated on the intensity scale on graph 6.18. The response was allowed to integrate to a near equilibrium value over a period of

70000seconds, The $\log \Delta\epsilon_1$ values were plotted against $\log I$ on graph 6.18. Here the intensities are those absorbed by the a-Si:H film so that the data points at 500nm and 800nm can be compared with similarly corrected data at 633nm. Comparison shows that the values of $\Delta\epsilon_1$ at 500nm and 800nm are the same as those at 633nm to within a 10% measurement error at identical intensities.

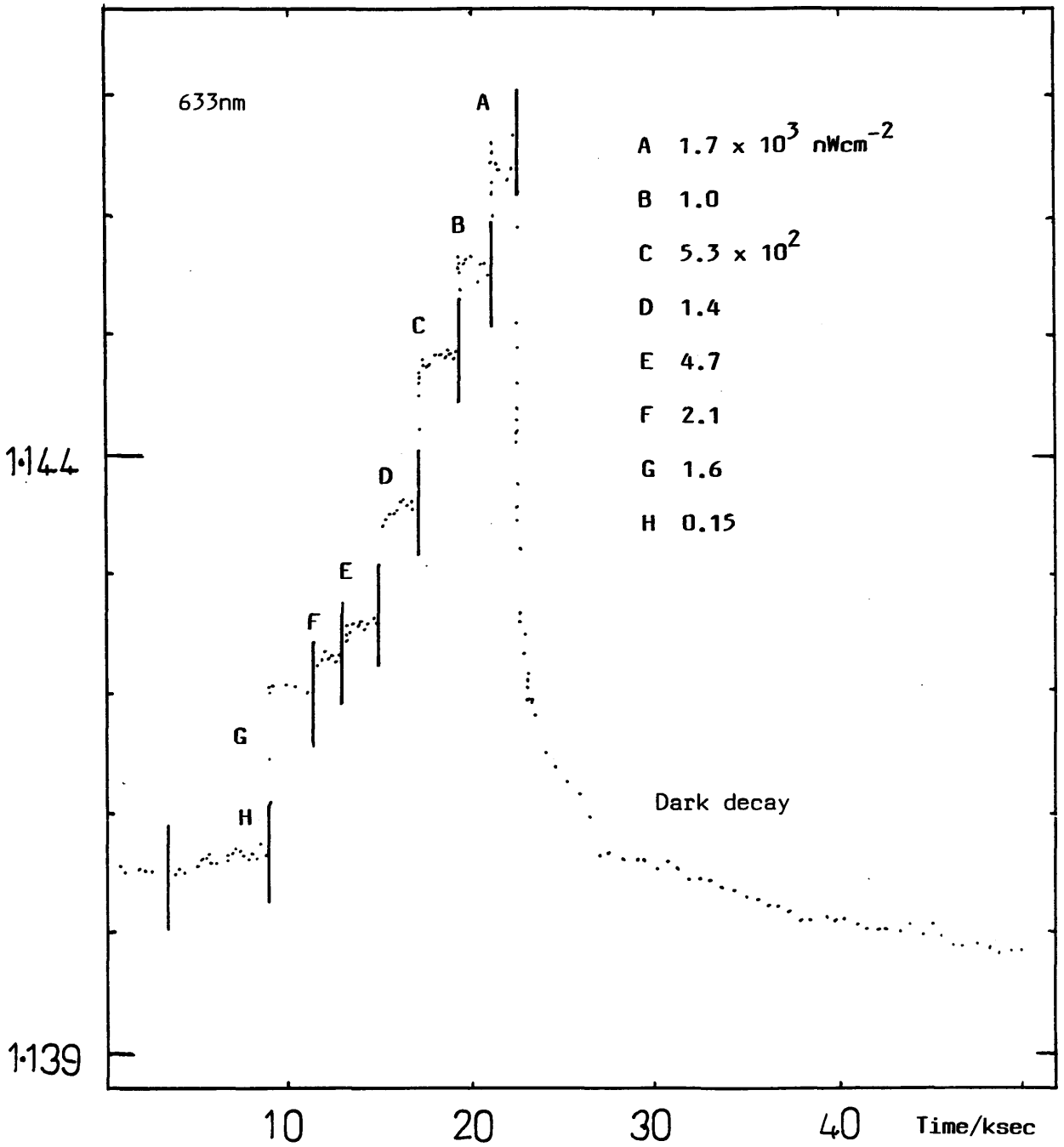
6.13 DC Photoconductivity

The DC photoconductivities of some of the samples were measured as a function of temperature. Results for K9 are plotted in diagram 5.8.

The graph is linear down to ~100K. Below this temperature the photoconductivity falls away rapidly until it is less than 10^{-11} S at 50K. At temperatures below 50K the other samples have shown that the photoconductivity is about two orders of magnitude less than the ac conductivity at the same temperatures. This is illustrated on graph 5.8.

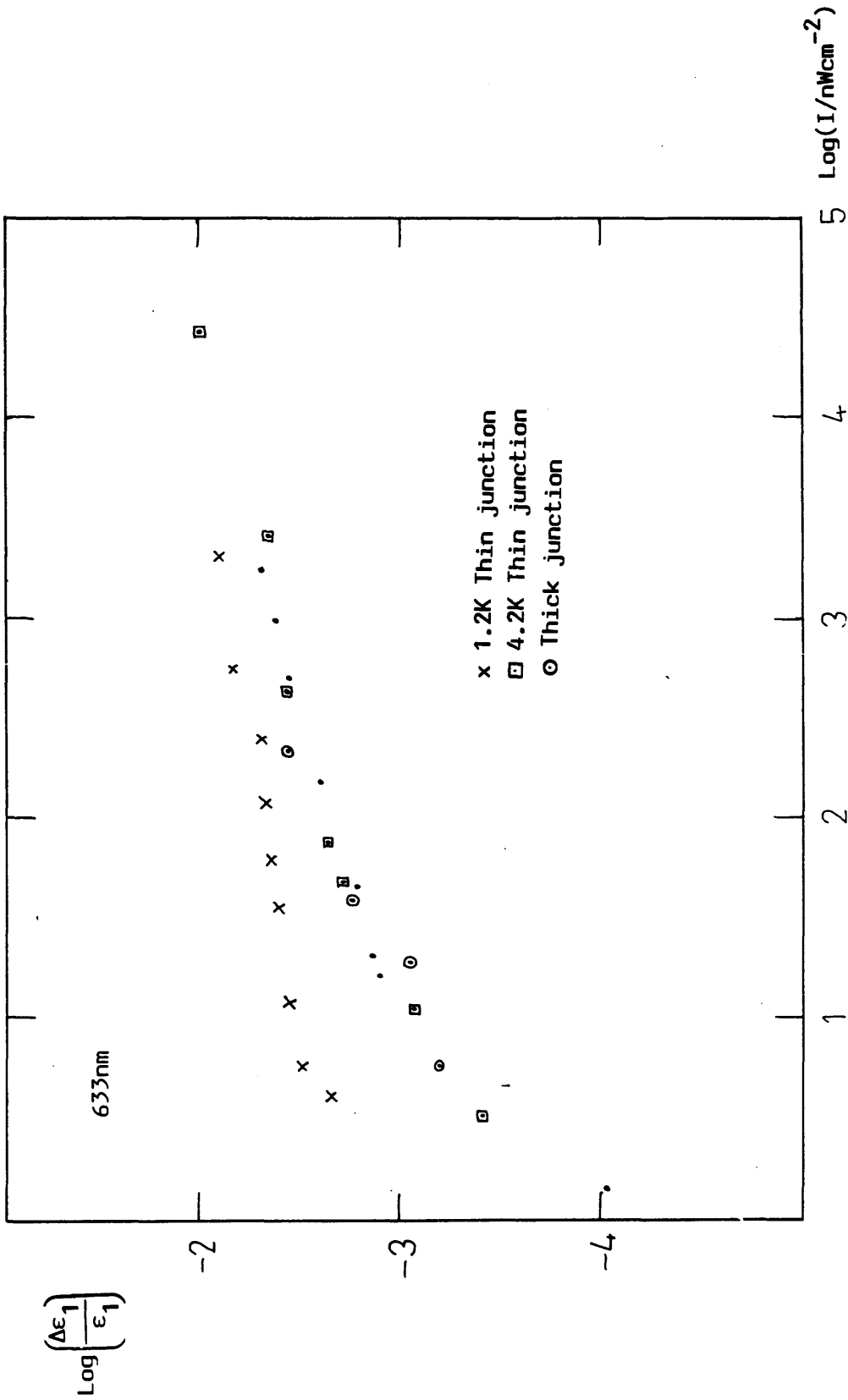
The photoconductivity was measured as a function of intensity and plotted as $\log G_{DC}$ vs $\log I$ on graph 6.29. It can be seen that part of this graph is linear and therefore $G_{DC} \propto I^\gamma$ where $\gamma = 0.818 \pm 10\%$.

Capacitance/nF



Graph 6.1

The capacitance of MA4 (magnetron sputtered pure a-Si) versus time at 4.2K.



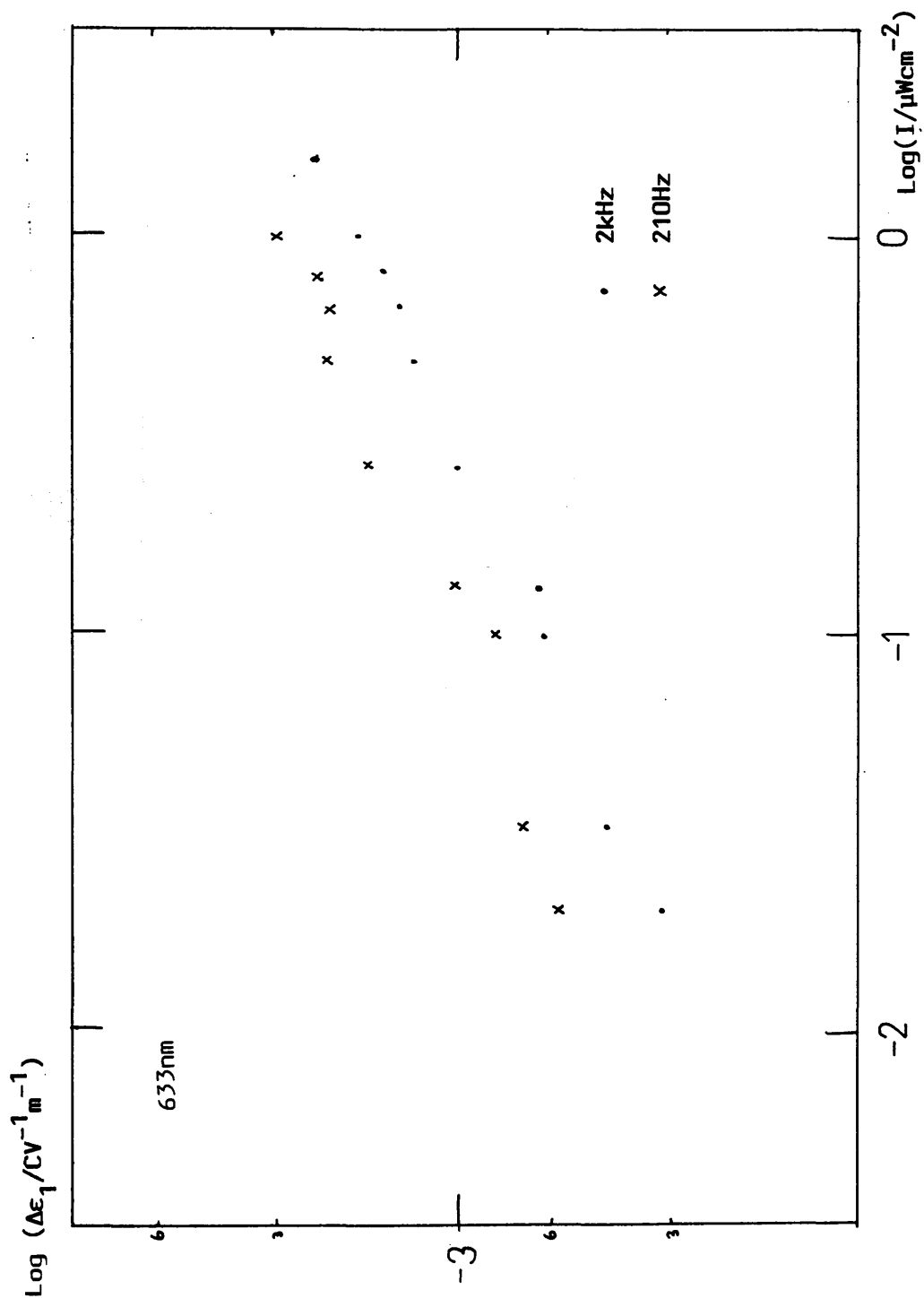
Graph 6.2

The change in the normalized permittivity plotted against the illuminating intensity on logarithmic scales for a magnetron sputtered pure a-Si sample (MA4)

Diagram 6.3

Sample	T(K)	C base (pF)	$\Delta\epsilon_1/\epsilon_1$ (%)
MA4	4.2	1140	0.465
		590	0.470
	1.2	115 5	0.699

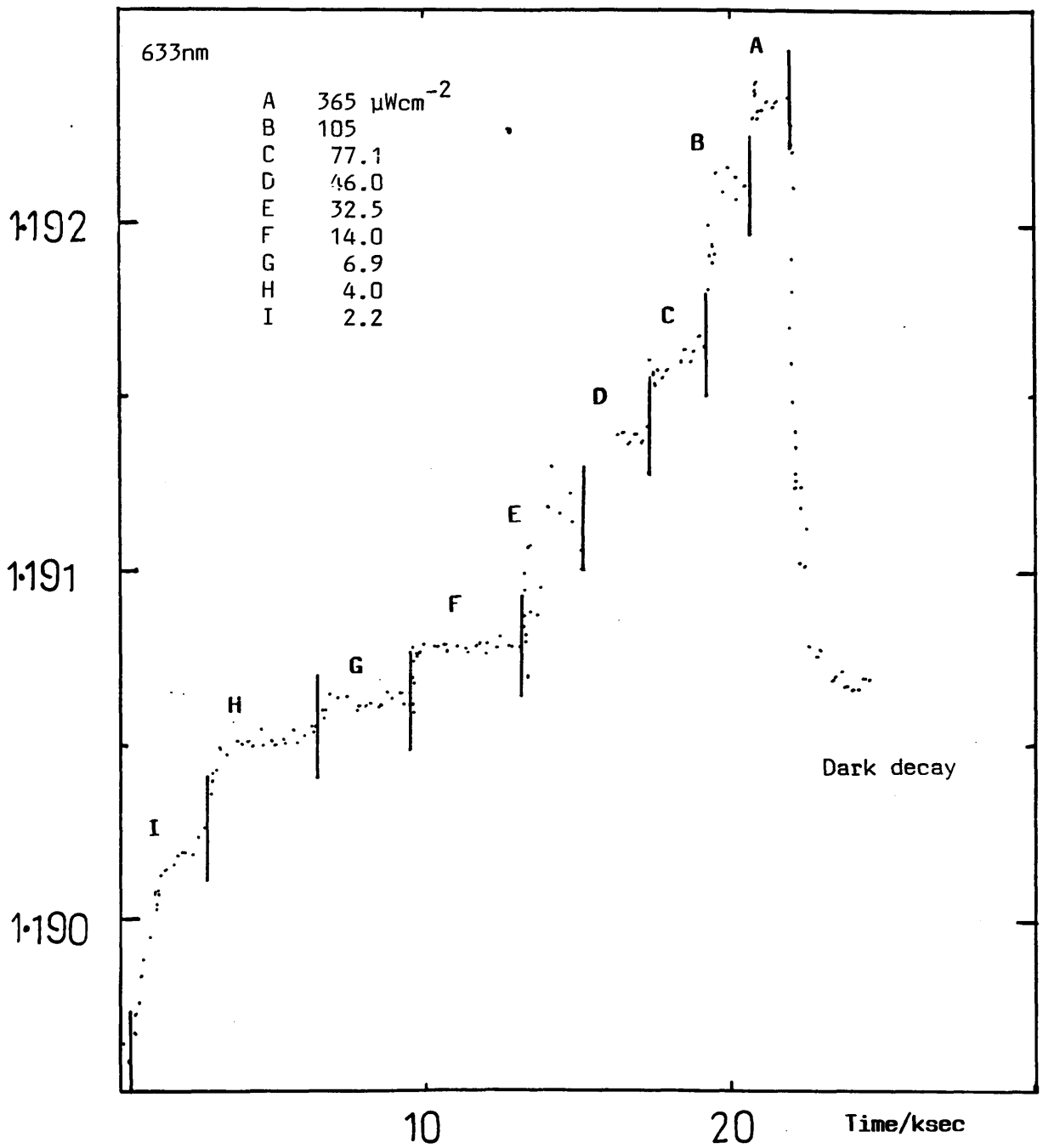
Table showing the base capacitance, in the dark, and the values of $\epsilon\Delta_1/\epsilon_1$ at the maximum illuminating intensities for MA4 at 4.2K and 1.2K.



Graph 6.4

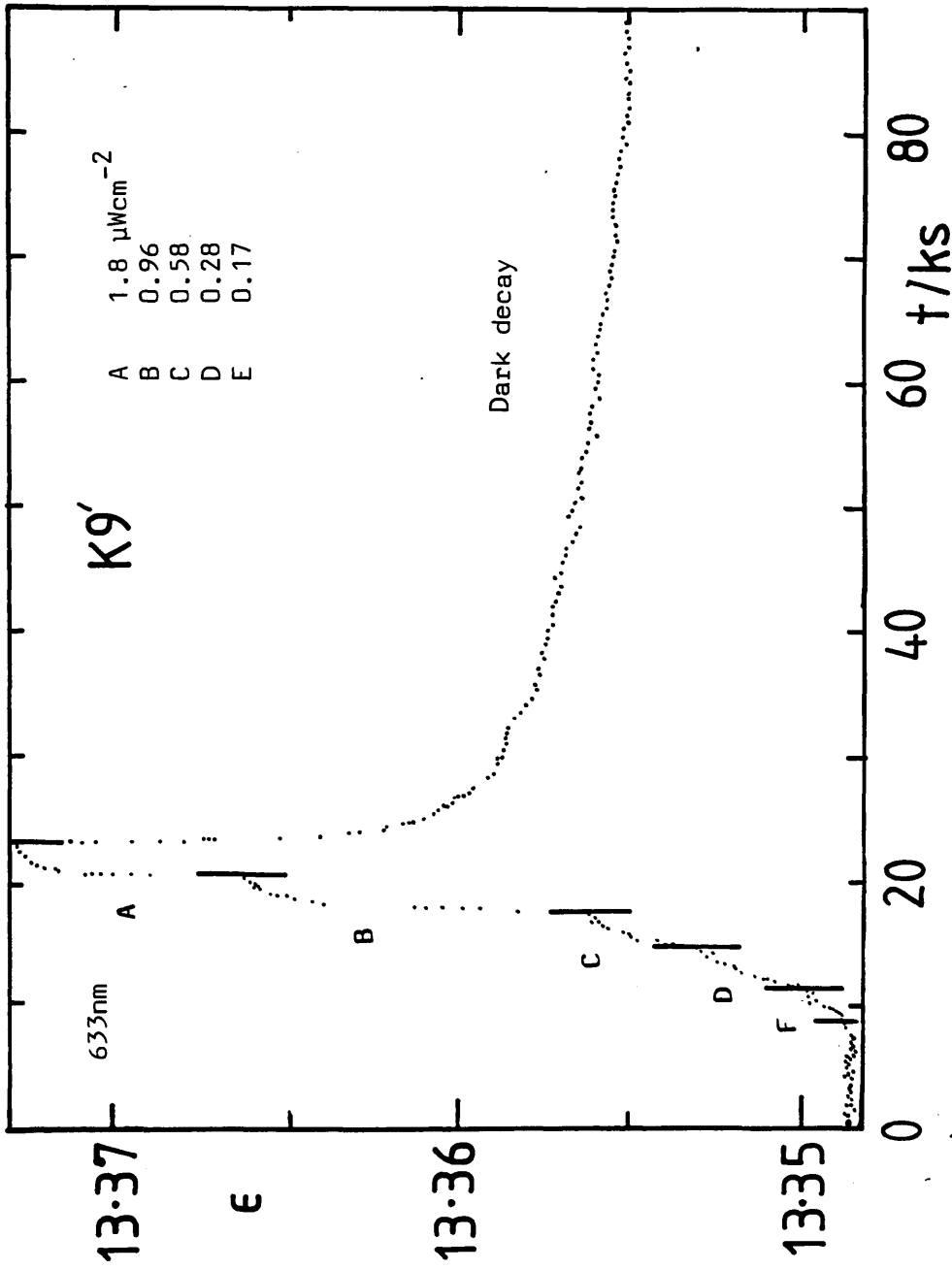
The logarithm of $\Delta\epsilon_1$ plotted against the logarithm of the applied illuminating intensity for an $n^+ - i$ sample, with Cu-Ni electrodes (S2)

Capacitance/($F \times 10^{-10}$)



Graph 6.4

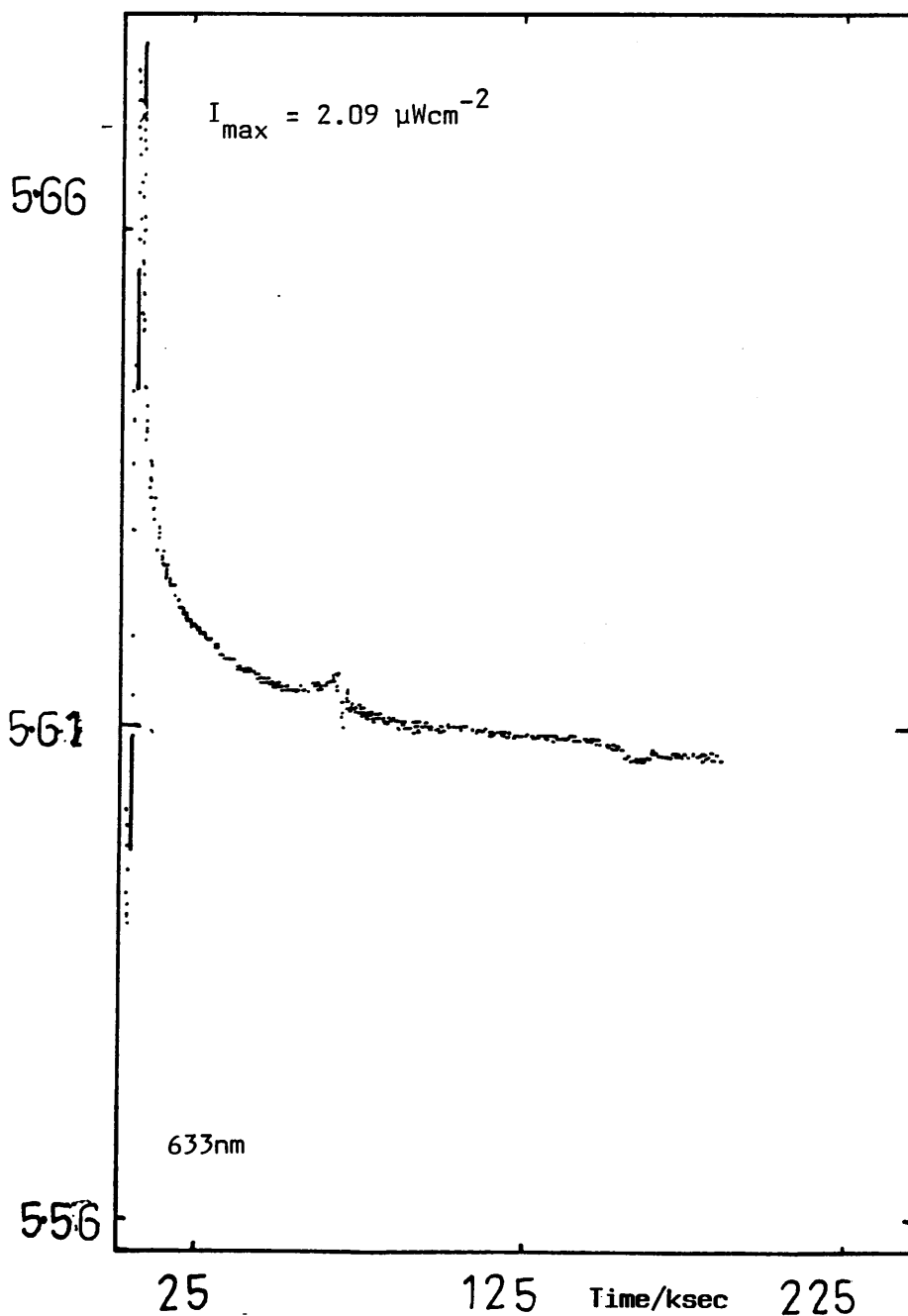
- (a) The variation of capacitance with time under different illumination intensities applied to an $n^+ - i$ sample (S5') at 30K.



Graph 6.5

The value of ϵ_1 versus time at varying applied illuminating intensities for an $n^+ - i - n^+$ sample (K9') at 4.2K.

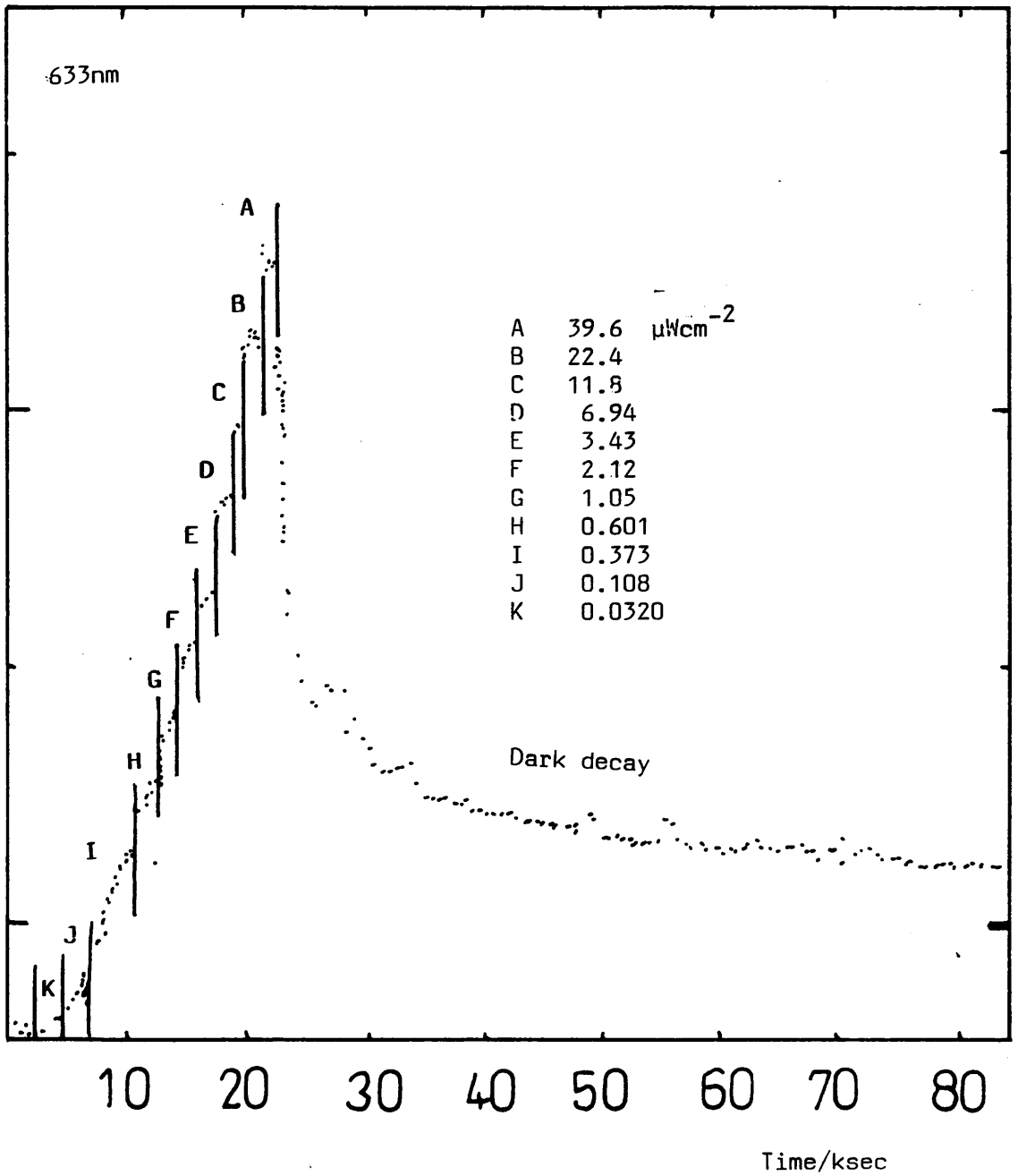
Capacitance/(F $\times 10^{-10}$)



Graph 6.6

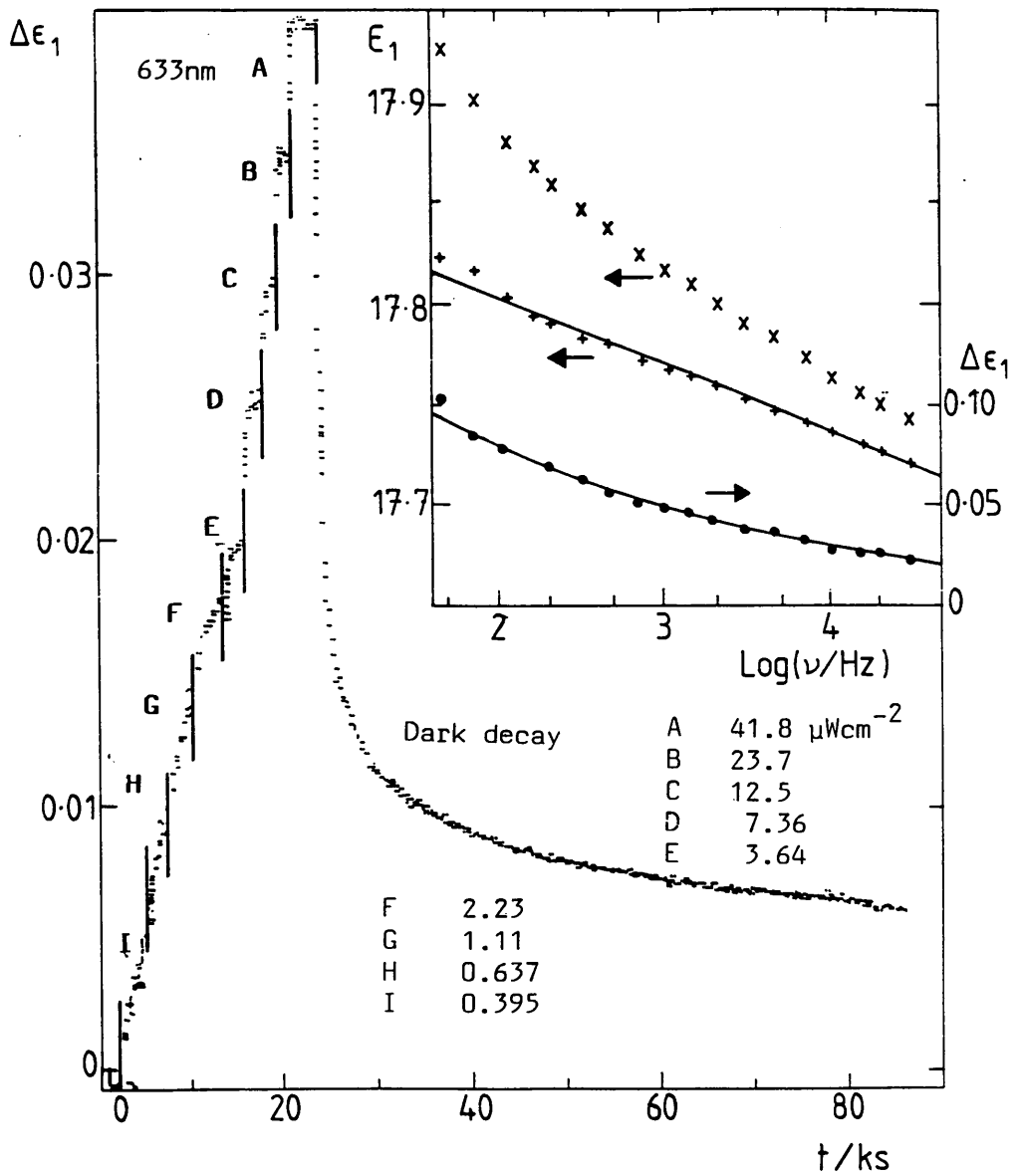
The capacitance of an $n^+ - i - n^+$ sample (K2') versus time at 4.2K. The dark decay is also shown.

Capacitance/(F $\times 10^{-10}$)



Graph 6.7

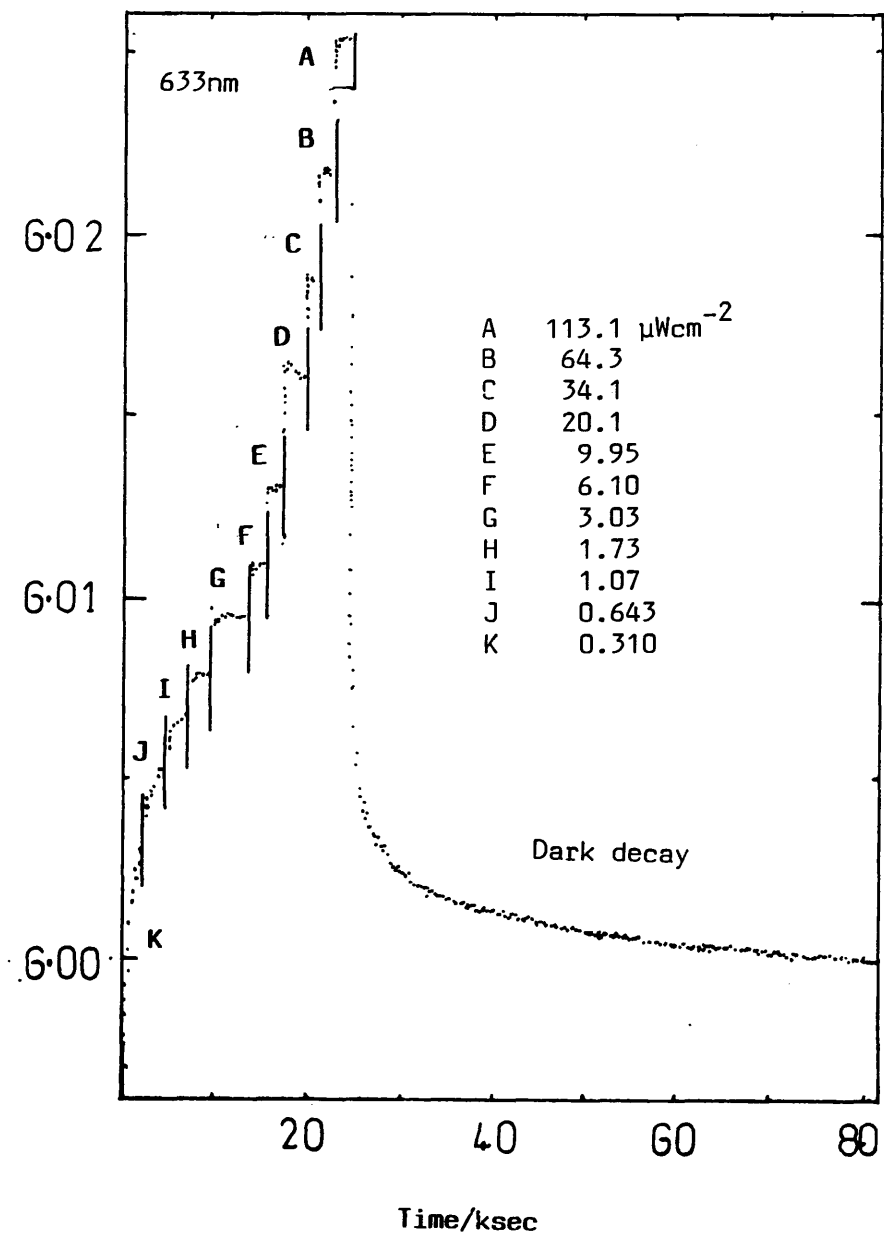
Capacitance against time for an $n^+ - i - n^+$ sample (K11') at 12.5K. The dark decay occurs after ~ 21000 seconds.



Graph 6.8

A plot of the value of $\Delta\epsilon_1$ against time for K11' at 30K. The inset shows the frequency dependence of the dark and illuminated values of the dielectric constant. The change, $\Delta\epsilon_1$ is also shown on the inset.

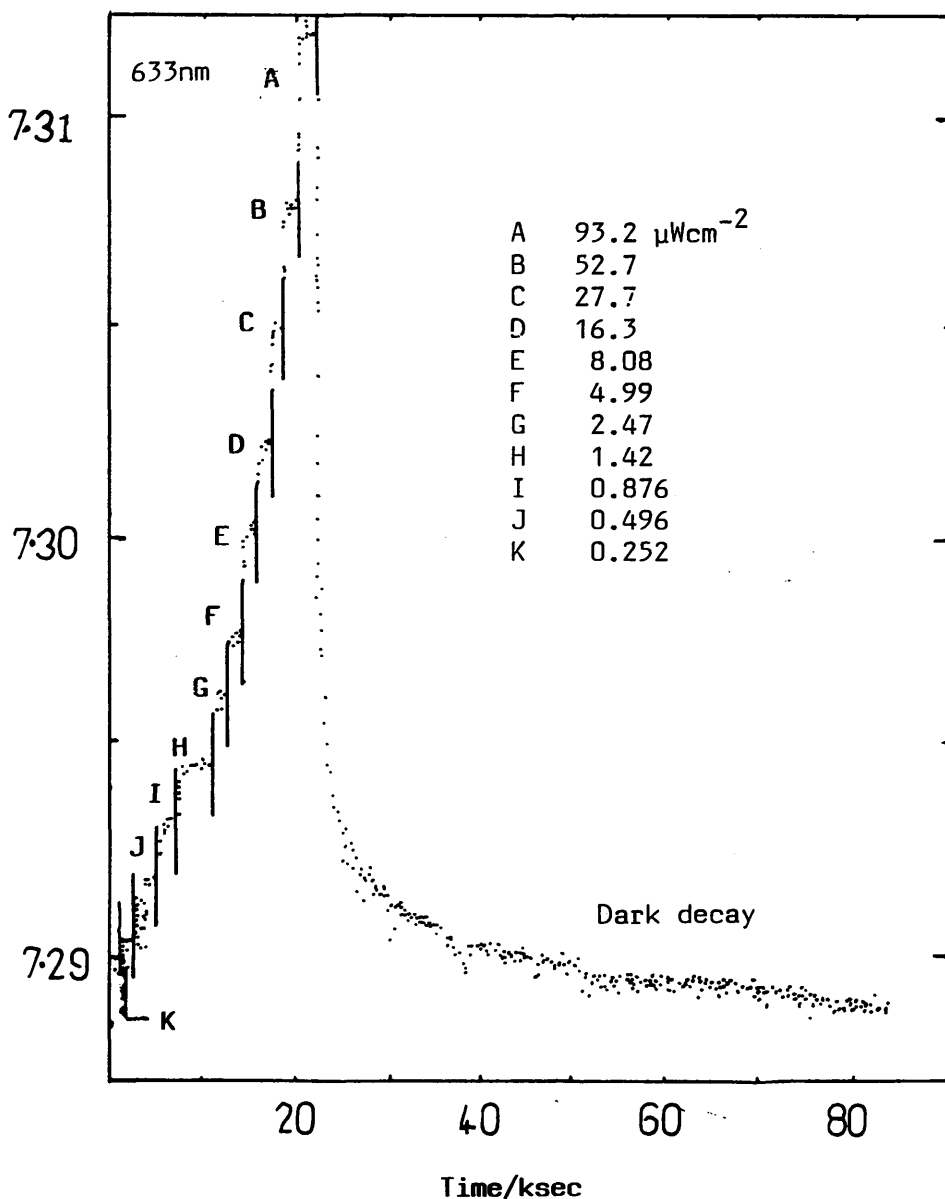
Capacitance/(F $\times 10^{-10}$)



Graph 6.9

The change in capacitance with time under different levels of applied constant illumination in an n^+ sample (D1) at 12.5K. The decay in the dark is also shown.

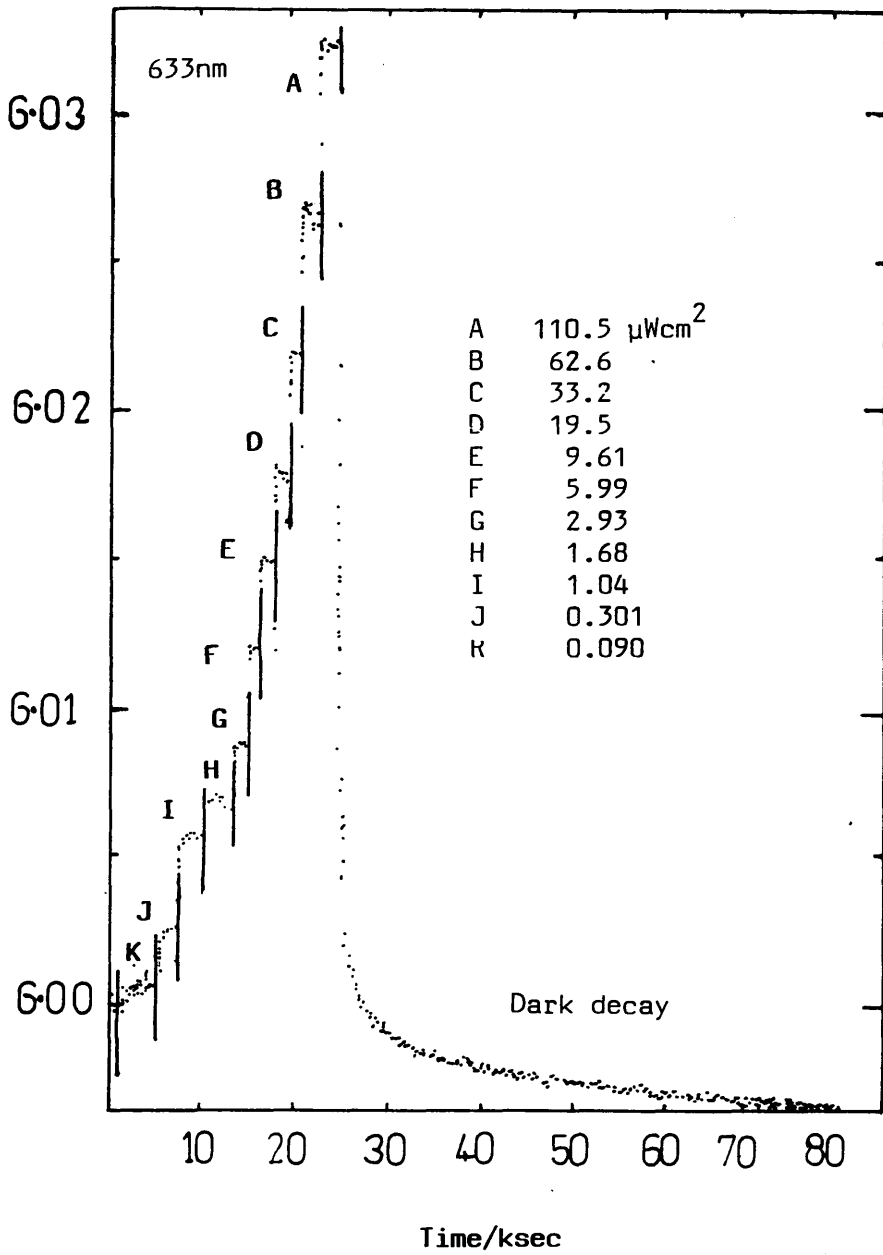
Capacitance/(F $\times 10^{-10}$)



Graph 6.10

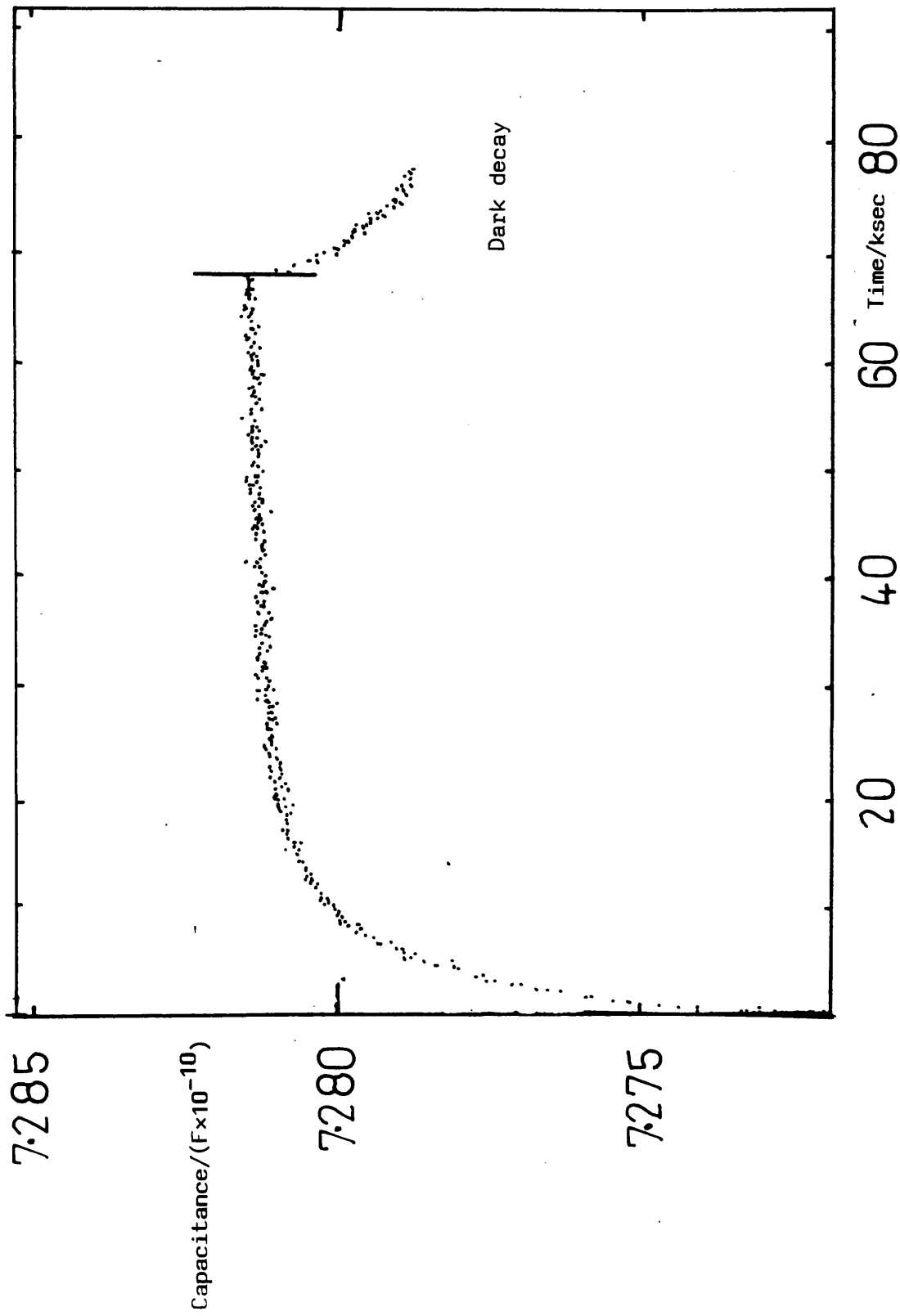
Capacitance versus time under varying applied intensities of light for D1 at 40K.

Capacitance/(F $\times 10^{-10}$)



Graph 6.11

The change in the capacitance versus time at a number of illuminating intensities for at 50K. The dark decay begins at ~29000 seconds.

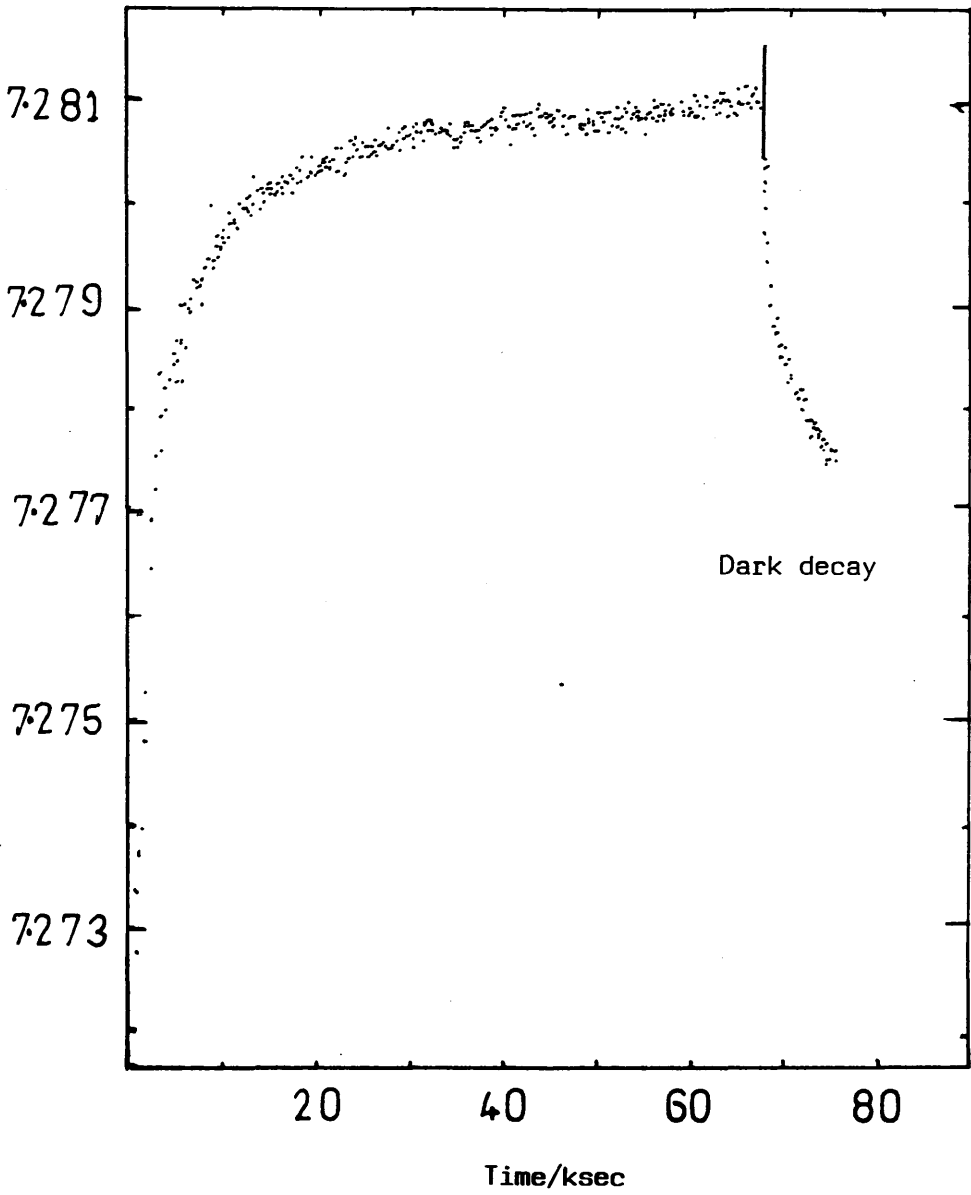


Graph 6.12

The integrating response of D1 at a wavelength of 500nm and at

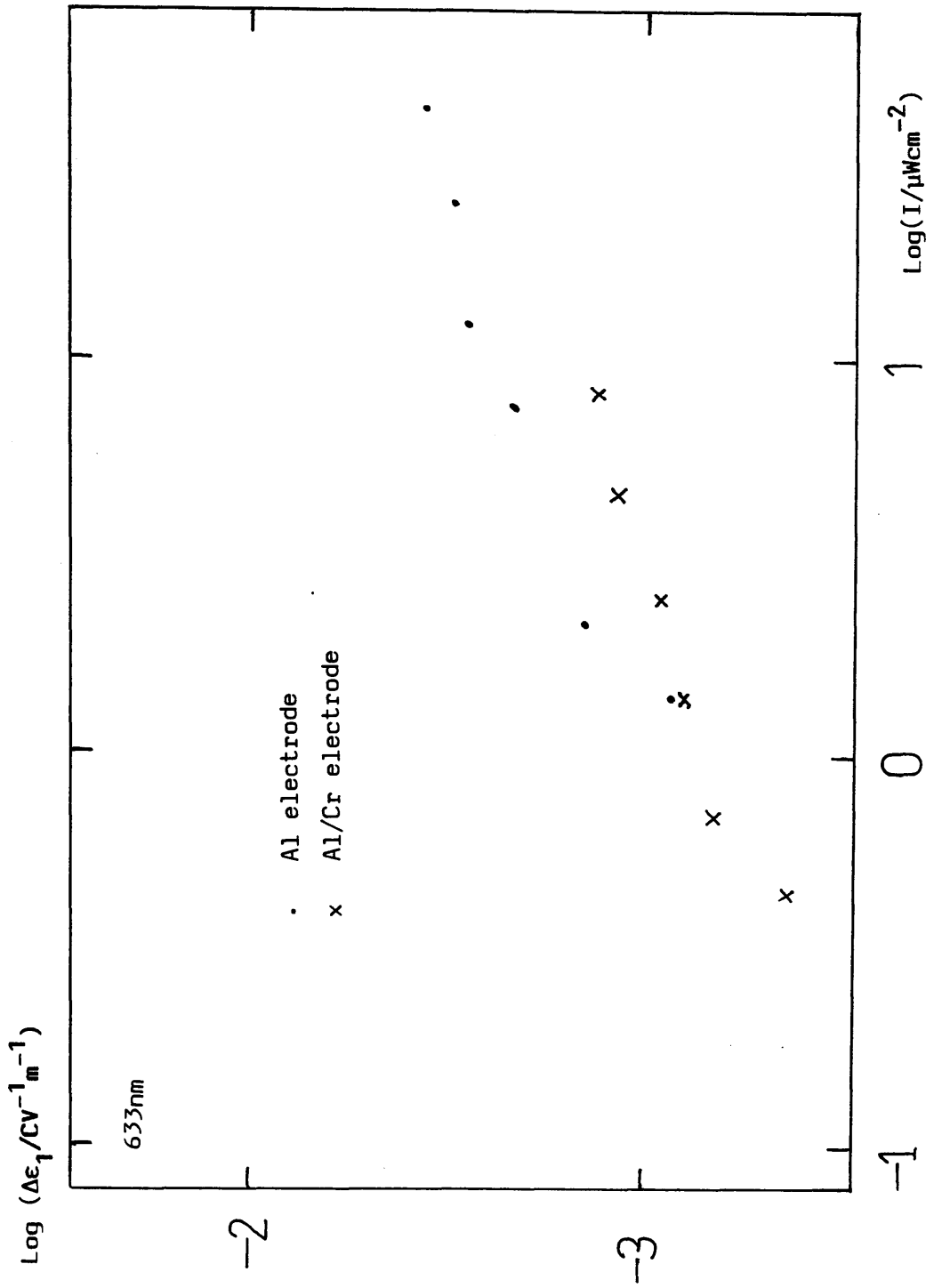
12.5K.

Capacitance/($F \times 10^{-10}$)



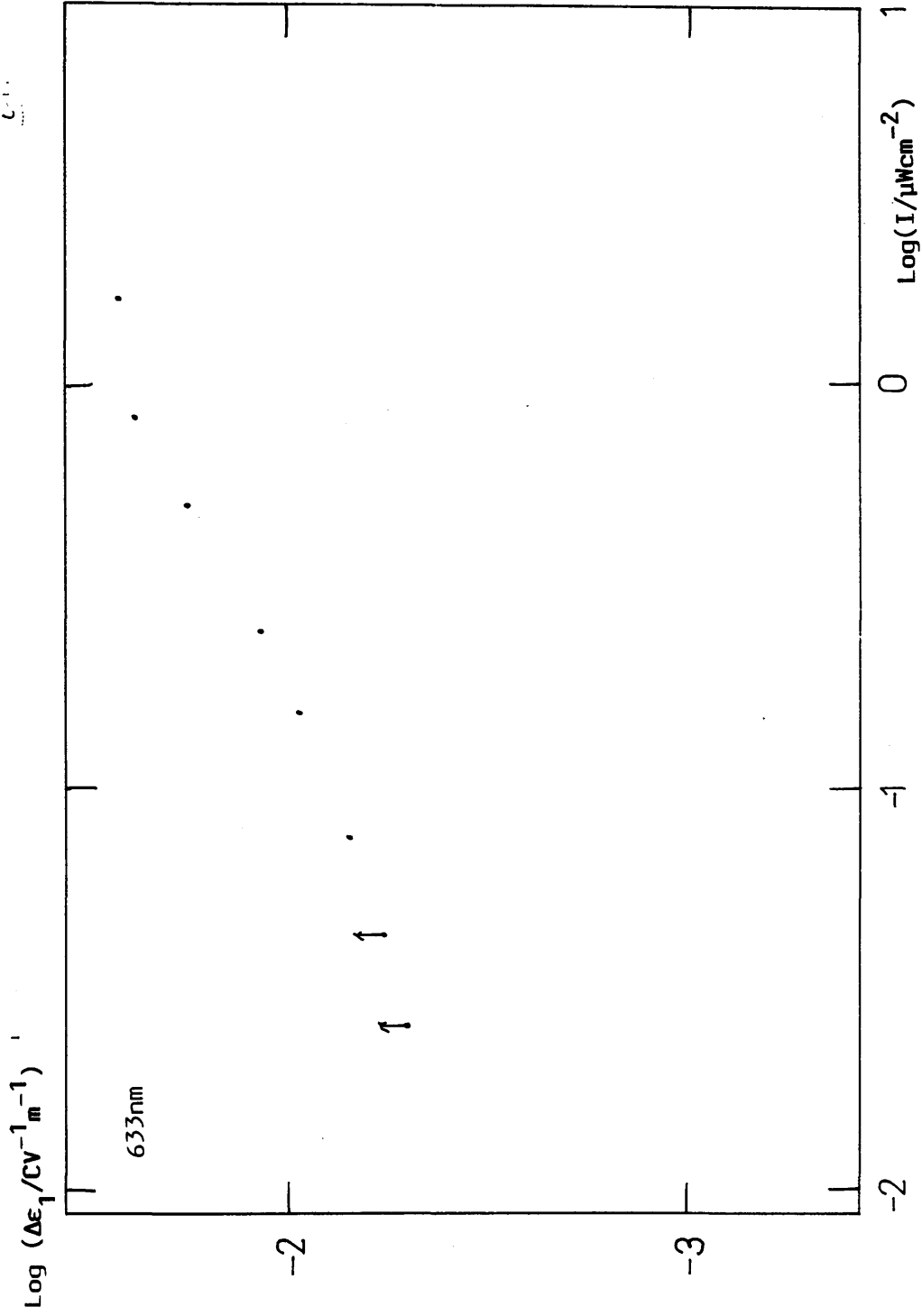
Graph 6.13

The integrating response at 12.5K for D1. The applied light had a wavelength of 800nm.



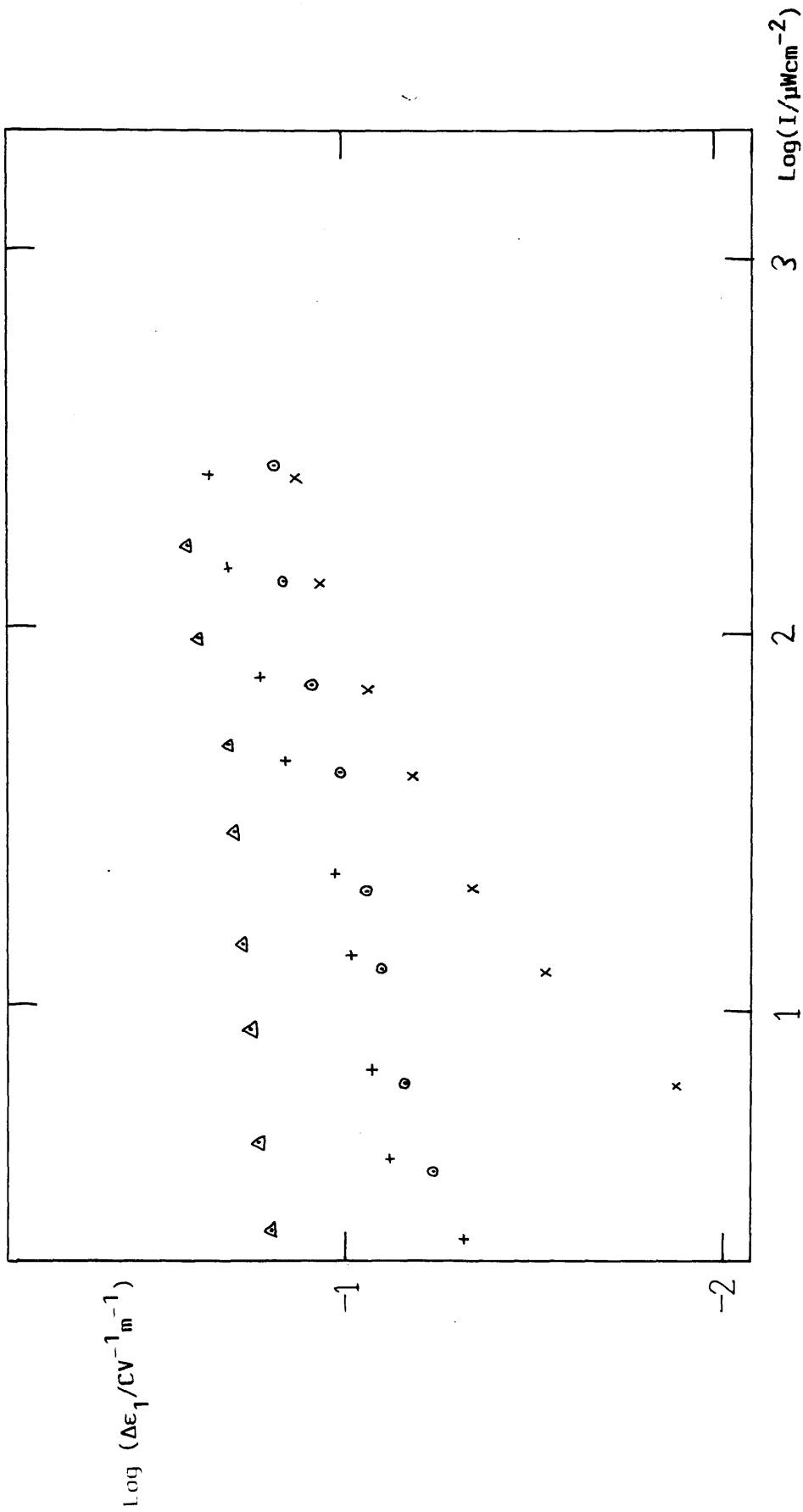
Log ($\Delta\epsilon_1/\text{CV}^{-1}\text{m}^{-1}$) versus $\log(I/\mu\text{Wcm}^{-2})$ for an n⁺-i sample (S3) with Al or Al/Cr top electrodes. A measuring frequency of 2kHz was used for the applied ac field and a temperature of 4.2K.

Graph 6.15



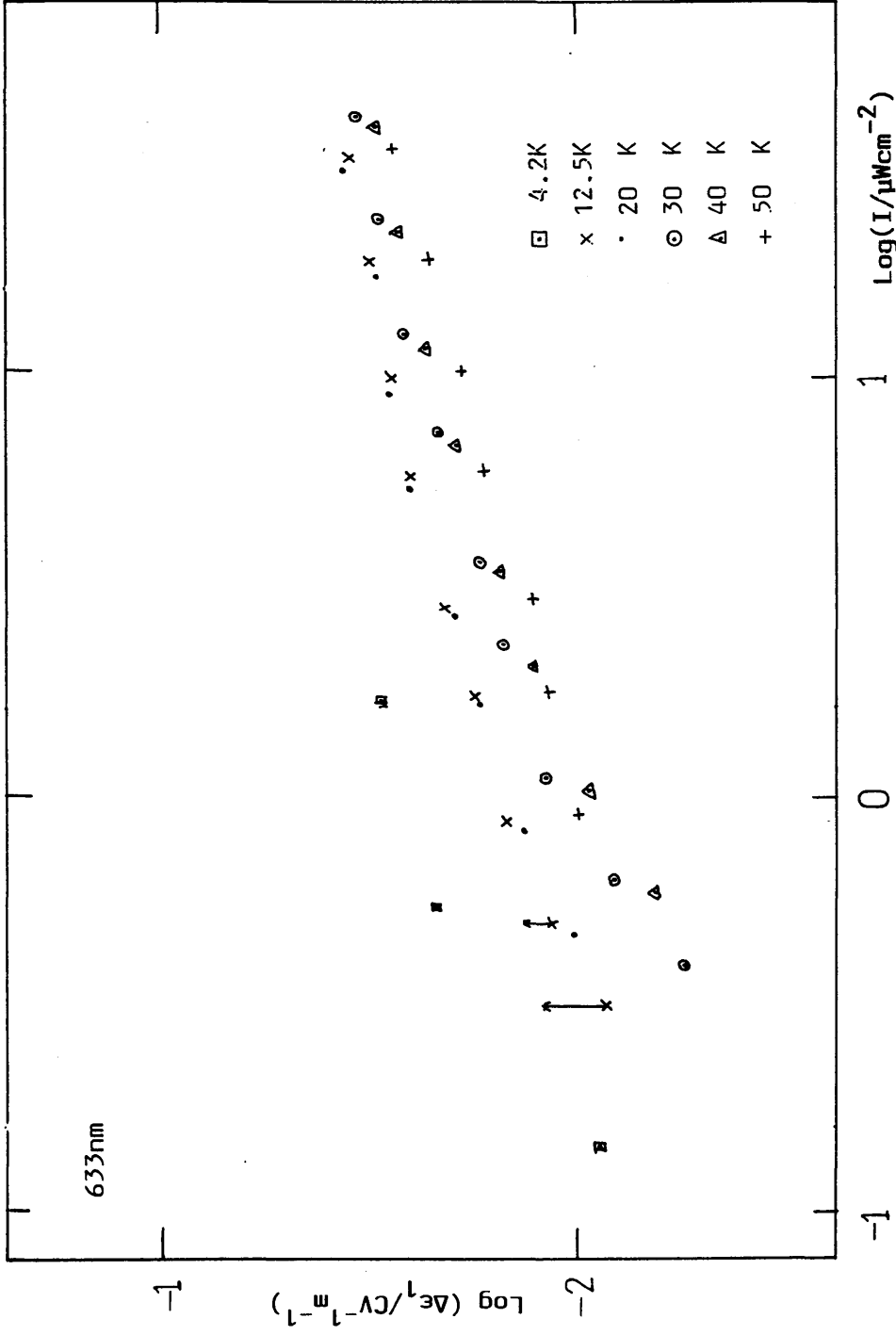
Graph 6.16

The change in relative permittivity versus I on logarithmic scales for an n⁺-i-n⁺ sample (K91) at 4.2K.



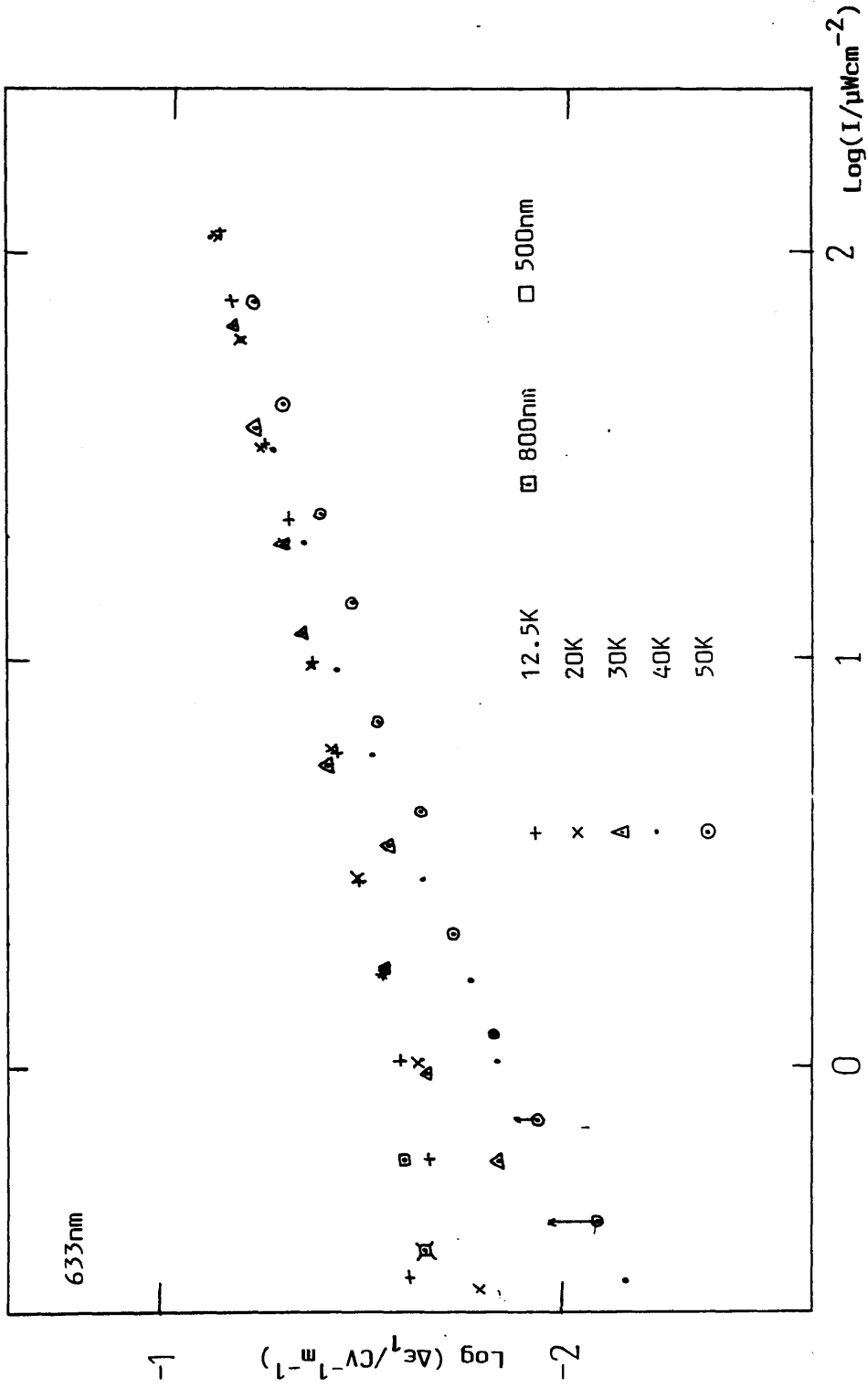
Graph 6.17

The intensity dependence of the change in the dielectric constant plotted at 50K (x), 40K (⊙), 20K (+) and 12.5K (Δ).



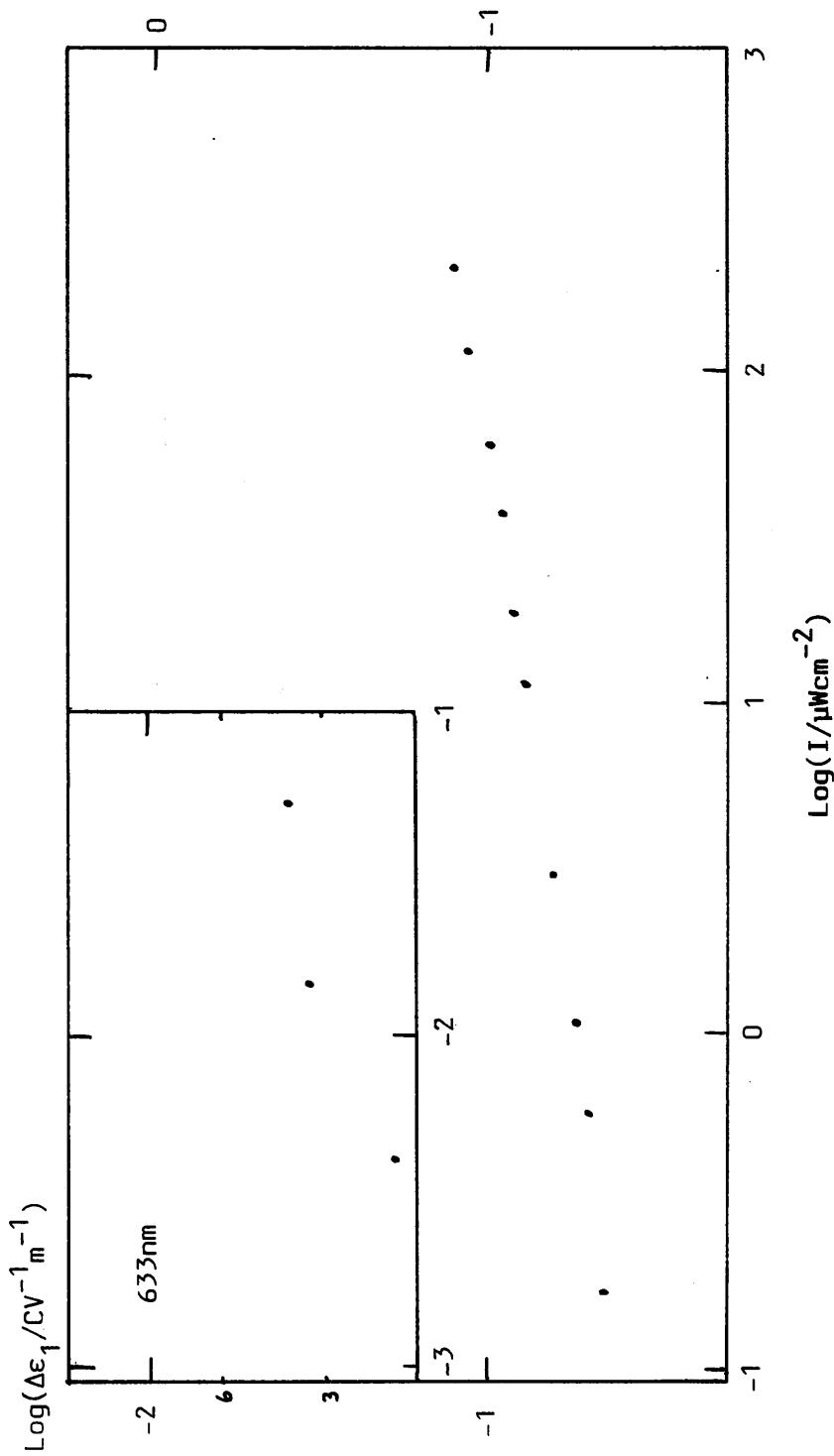
Graph 6.18

The effect of temperature on the $\log(\Delta\epsilon_1/CV^{-1}m^{-1})$ vs $\log(I/\mu Wcm^{-2})$ for samples K11 and K12 (n^+i-n^+ samples). The K12 data is only at 4.2K.



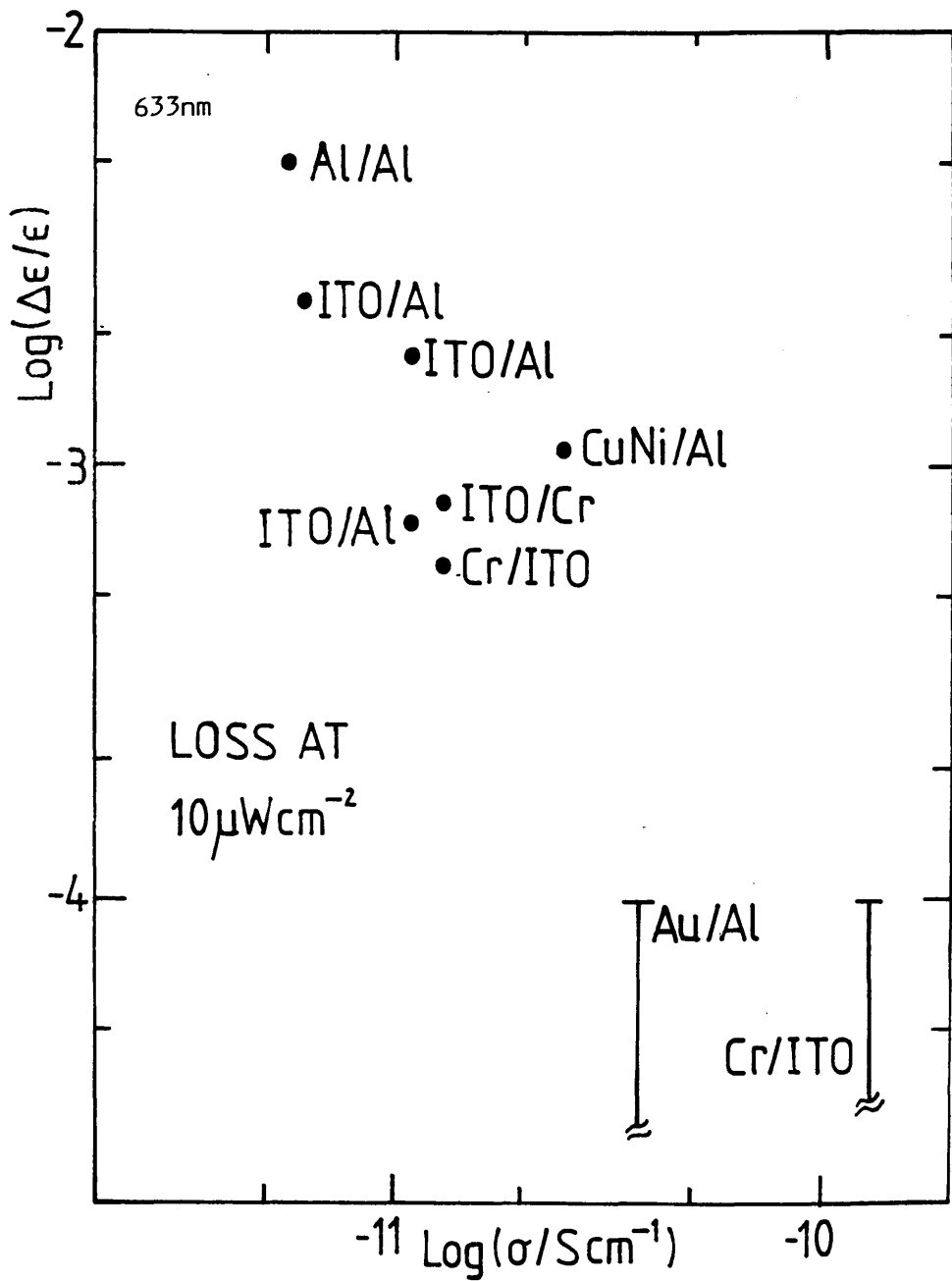
Graph 6.19(a)

The temperature dependence of the $\log(\Delta\epsilon_1/CV^{-1}m^{-1})$ vs $\log(I/\mu Wcm^{-1})$ for a doped sample (n^+ - sample, D1).



Graph 6.19(b)

The temperature dependence of the change in $\Delta\epsilon$, vs I on a logarithmic scale for D2 at 4.2K.



Graph 6.20

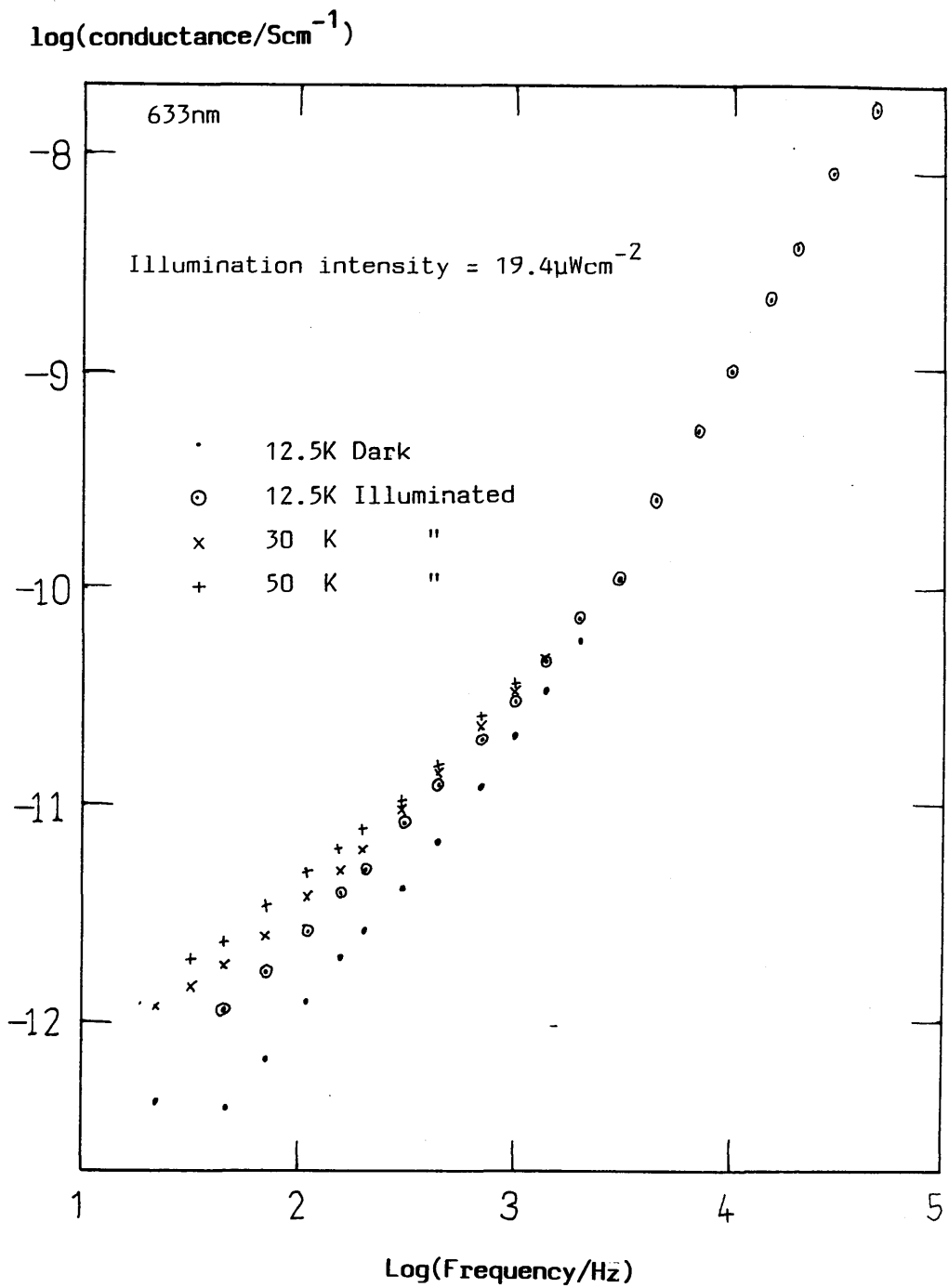
The values of $\Delta\epsilon_1/\epsilon_1$ vs σ at an intensity of $10\mu\text{Wcm}^{-2}$ dark incident on the sample.

$$I = 10\mu\text{Wcm}^{-2}$$

Sample	Temperature (K)	$\Delta\epsilon_1/\epsilon_1$ (%)
K9	12.5	$1.88 \times 10^{-3} \pm 10\%$
K11	12.5	1.21×10^{-3}
K12	4.2	1.44×10^{-3}
D1	12.5	1.57×10^{-3}
D2	4.2	3.52×10^{-3}
S5	12.5	1.4×10^{-3}

Table 6.21

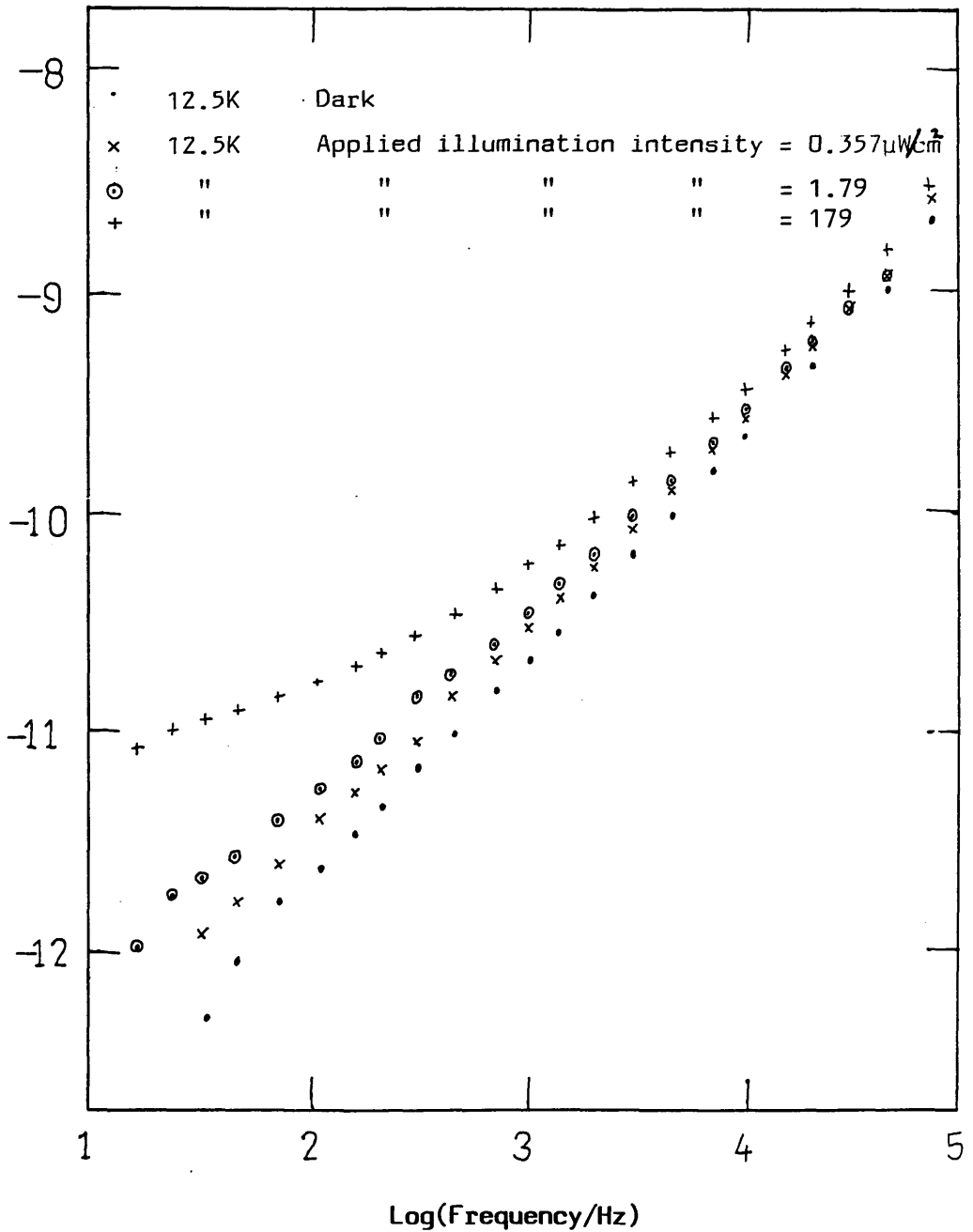
Table showing the values of $\Delta\epsilon_1/\epsilon_1$ for various samples at the indicated temperatures for an illuminating intensity of $1.0\mu\text{Wcm}^{-2}$



Graph 6.22

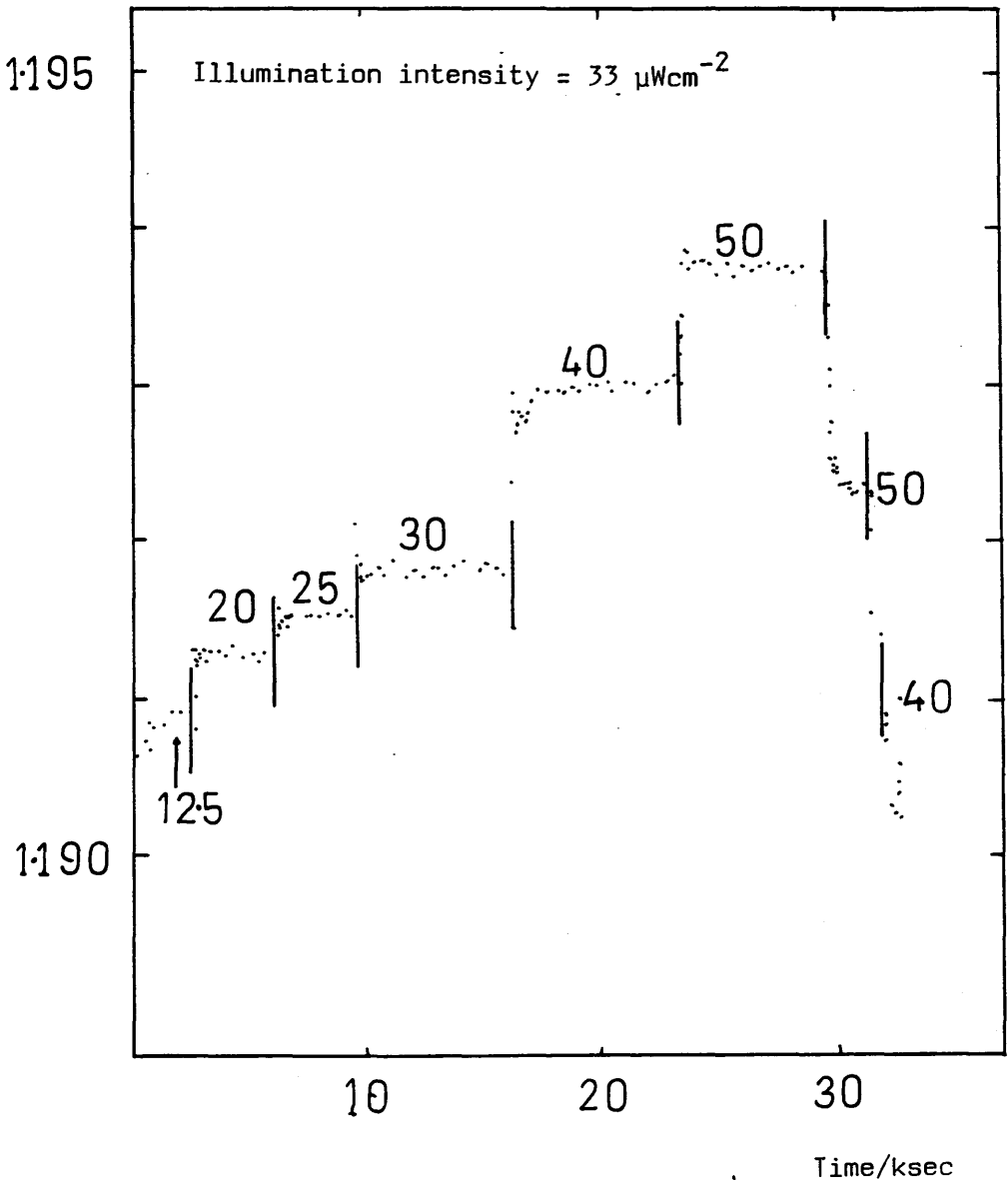
Frequency data for D1 under illumination ($\lambda = 633\text{nm}$) at varying temperatures.

$\log(\text{conductance}/\text{Scm}^{-1})$



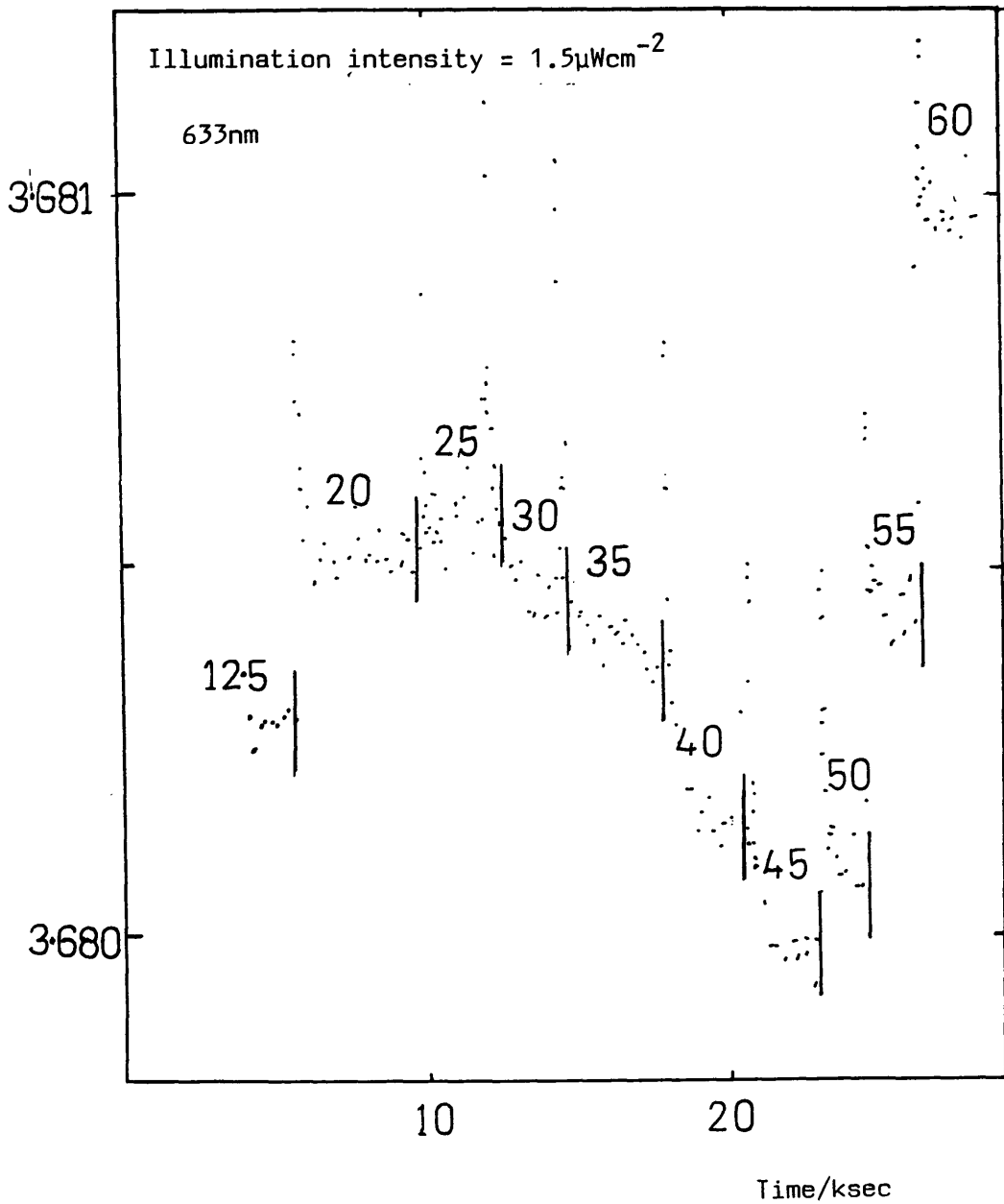
Graph 6.23

The frequency dependence of the total conductivity, for D2, under varying degrees of illumination ($\lambda = 633\text{nm}$).



Graph 6.24

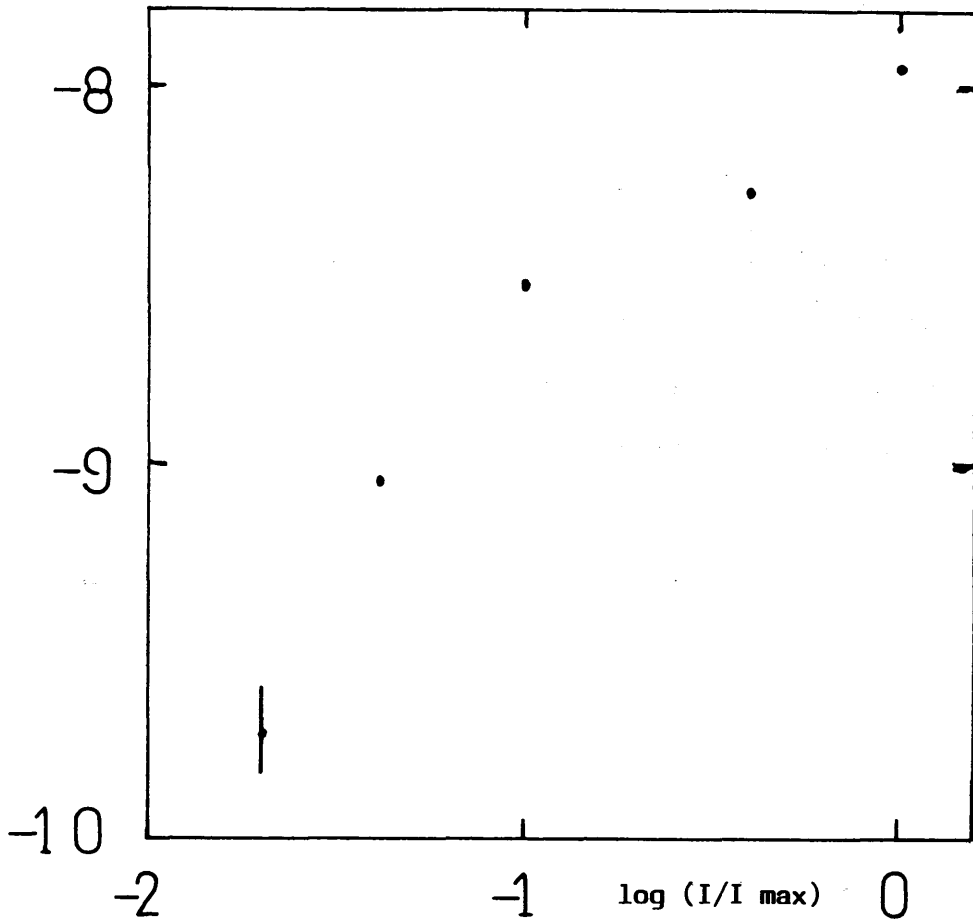
The charge in capacitance against time at a constant level of illumination. The temperature was varied and the values are shown in Kelvin. This graph shows an n^+i sample (S5).



Graph 6.25

The variation of capacitance with time under a constant illuminating intensity. The temperature was varied and the values are shown in Kelvin. This sample is an $n^+ - i - n^+$ sample (K9').

log(DC photoconductance/S)



Graph 6.29

DC photoconductance vs Intensity for sample D2 (n^+)
at 4.2K. The maximum intensity applied is $179\mu\text{Wcm}^{-2}$.

CHAPTER 7

7.1 General Mechanism for Optically Induced AC Loss in a-Si and a-Si:H

The changes, described in Chapter 6, in capacitance and conductance of the a-Si (or a-Si:H) samples under low intensity illumination are not due to temperature variations. In experiments where a-Si samples are cooled using liquid helium the temperature increase indicated by the values of ΔC or ΔG would be about 4K. The ac measuring equipment and the laser light supply power to the sample. Assuming that all this energy is converted to heat, we obtain, using known thermal conductances, a rise in temperature of ~ 1 mK due to these sources. The ac power is frequency dependent and at 2kHz it is greater than the power supplied by the light. A temperature rise of 1mK is obviously insufficient to account for the observed changes in ΔC and ΔG under illumination.

The decay observed when the light is removed lasts for several days in a-Si. If the induced change was due to a thermal effect then the decay should take place very quickly as the sample cools. For example, a temperature decrease from ~ 10 K down to 4.2K occurs within minutes, as shown by the germanium thermometer and by the change in a-Si samples or in the change in C in a-Si:H. The germanium thermometer is in good thermal contact with the sample so it will also be at 4.2K. The values of C and G stabilise to the new temperature within minutes.

In a-Si:H samples, prepared by glow discharge, the rise in C and G under illumination is again due to the light and not heating of the sample. To produce the measured values of ΔC and ΔG would require raising the sample to around 100K from ~ 12.5 K. Since the power supplied by the light and the measuring system are similar to those applied to

a-Si such a change in temperature cannot occur. Again, the decay in the dark occurs over a long period (weeks in the case of a-Si:H at $\sim 12.5\text{K}$) and cannot be attributed to a temperature change. An alternative model must therefore be found to explain the optically induced ac loss. A model suggested by Long and Holland (1985) involves the generation of free carriers by the incident light. These are rapidly trapped in gap states and respond to the applied ac field, enhancing the ac loss. Removing the light then allows these trapped carriers to recombine over a long time period, giving rise to the observed decays.

The remainder of this chapter will show how this general mechanism can be applied to different materials such as a-Si and a-Si:H. Firstly, previous work is reviewed and compared with current studies in a-Si. The results presented in Chapter 6 for a-Si are discussed and compared with a model proposed by Long and Holland (1985). In the next section a-Si:H is discussed and detailed mechanisms are presented to explain both the optical effects at high and low intensities and the dark decay. Finally other optically induced phenomena, such as LESR and photoconductivity are discussed. Other problems encountered, such as metallic diffusion, experimental and analysis problems, doped samples and As_2Se_3 samples are also discussed.

7.2 Sputtered a-Si and a-Si:H

(a) Holland (Ph.D. thesis 1987) found that the optically induced ac

loss was observed in sputtered a-Si and sputtered a-Si:H. These materials were prepared using both conventional and magnetron sputtering.

The non-linear $\log \Delta \epsilon_1$ vs $\log I$ graphs obtained by Holland are similar to those for MA4 (a sputtered a-Si sample used in this work). The magnitude of the response was also similar and decreased with increasing hydrogen content.

Long and Holland (1985) suggested that free electrons and holes are generated by the incident light. In the sputtered a-Si and a-Si:H studied these carriers are rapidly trapped in defect clusters close to the fermi level. The carriers trapped in the defects can then respond to the applied measuring field thus giving rise to an enhanced ac loss.

Long et al (1985) derived a rate equation to explain the results obtained for sputtered material (see also Holland, Ph.D thesis 1987). It is assumed that equal numbers of electrons and holes are created by the incident photon energy. Recombination occurs by tunnelling at the rate

$$\tau^{-1} \sim \tau_0^{-1} \exp(-2\alpha R) \quad (7.1)$$

where α^{-1} = the decay length of the wavefunction

and R = the electron-hole separation.

A random distribution of holes is assumed to exist around each electron so that the nearest-neighbour probability function is

$$P(R) = 4\pi R^2 \exp\left(-\frac{4}{3} \pi R^3\right) \quad (7.2)$$

where p = the number of excited holes per unit volume = the
 number of excited electrons per unit volume = n .

By calculating the average recombination rate, τ^{-1} it is found

$$\begin{aligned}\tau^{-1} &= \int_0^{\infty} \tau_0^{-1} \exp(-2\alpha R) 4\pi p R^2 \exp(-\frac{4}{3}\pi p R^3) dR \\ &= \frac{\pi p}{\tau_0 \alpha^3} = \frac{\pi n}{\tau_0 \alpha^3}\end{aligned}\quad (7.3)$$

if the defect density is low, i.e. $\alpha^{-1} \ll p^{-\frac{1}{3}}$.

Thus the rate equation is

$$\frac{dn}{dt} = g_0 - n\tau^{-1} = g_0 - An^2 \quad (7.4)$$

where $A = \frac{\pi}{\tau_0 \alpha^3}$.

g_0 is the generation rate and is equal to IEd , where I is the light intensity, E = the photon energy and d is the sample thickness. Here, it is also assumed that all the photogenerated carriers are trapped and contribute to the induced loss and recombination by luminescence or geminate thermal recombination can be neglected. A final assumption is that the optically induced loss is distinct from the dark loss. This is shown to be a valid assumption in section 7.3(d).

7.2(b) Applications of the Rate Equation in Sputtered Material

In order to determine under what conditions the rate equation is valid a series of calculations has been performed.

The rate equation gives rise to

$$n = \left(\frac{g_0}{A} \right)^{\frac{1}{2}} \quad (7.5)$$

when equilibrium conditions are reached.

$$\text{i.e. } \frac{dn}{dt} = 0. \quad (7.6)$$

When the illumination is removed the generation rate, g_0 , becomes zero, thus

$$n = \frac{1}{At} \quad . \quad (7.7)$$

It is assumed that the change in the dielectric constant is proportional to the number of excess carriers generated by the illumination,

$$\text{thus } \Delta\epsilon_1 = Kn. \quad (7.8)$$

A further assumption, which is reasonable at short and intermediate times, is that the distribution of trapped carriers is uniform (Holland, Ph.D thesis 1987).

The long decays in sputtered material and in the decays observed in glow discharge material do not follow a $1/t$ relation. A more detailed analysis is therefore required and is discussed in section 7.3(e).

Equations 7.7 and 7.8 give rise to

$$\Delta\epsilon_1 = \frac{1}{t} \frac{K}{A} = \left(\frac{K^2}{A} \frac{I}{Ed} \right)^{\frac{1}{2}} \quad . \quad (7.9)$$

This predicts that the change in capacitance with increasing intensity will follow an $I^{\frac{1}{2}}$ relation. This has been observed at low intensities (less than 100nWcm^{-2}) in sputtered material. This includes both pure a-Si and weakly hydrogenated material prepared by sputtering at room temperature. The a-Si:H samples prepared by the glow discharge decomposition of SiH_4 gas and deposited on heated substrates

are analysed in the next section.

The value of K can be found from the gradient of the $\log \Delta\epsilon_1$ vs $\log I$ plot and from a knowledge of K/A . This is found from the decay data at long times using 7.9 and graph 7.2 at 4.2K. Thus K is $1.096 \times 10^{-19} \text{ cm}^3$ and a value for A is 3.477×10^{-20} seconds. The density of excited electrons at the top of the $I^{\frac{1}{2}}$ region in graph 6.2 is then calculated, from K by using $n = \frac{\Delta\epsilon_1}{K}$. The value of $N(E_F)$ (for a 1eV distribution of defects) is then obtained and is $\sim 4.6 \times 10^{17} \text{ eV}^{-1} \text{ cm}^{-3}$. Holland (Ph.D thesis 1987) obtained similar values at 4.2K. For example figures of around $4.1 \times 10^{17} \text{ cm}^{-3}$ were obtained for pure a-Si (magnetron sputtered) at 4.2K. Samples containing hydrogen were found to have a lower density of excited electrons ($\sim 1.9 \times 10^{17} \text{ cm}^{-3}$ down to $3.2 \times 10^{16} \text{ cm}^{-3}$). These figures are consistent with the idea that hydrogen reduces the number of defect states by saturating dangling bonds within the a-Si:H structure.

7.2(c) Inadequacies of the Simple Model

The simple analysis described in the previous two sections (7.2(b) and 7.2(c)) is clearly inconsistent with some of the data obtained for sputtered material. Firstly, the $\log \Delta\epsilon_1$ vs $\log I$ plots show that the gradient changing from $I^{\frac{1}{2}}$ to $I^{\frac{1}{4}}$ as I increases over 5 orders of magnitude. Secondly, the decay only follows a $1/t$ relation for short times, as graph 7.2 clearly shows. Plotting the decay on a $\Delta\epsilon_1$ vs $\log(\text{time})$ graph gives a straight line.

The reason for the discrepancies between the experiment and theory is that the random distribution of trapped carriers is not preserved as time progresses. The more closely spaced a trapped carrier and holes recombine before more distantly separated pairs. The

recombination times of trapped carriers will now become greater as a result. This idea is developed in more detail in section 7.3(f) which deals with the decays in glow discharge material.

7.2(d) The Reduced Rate of Increase of $\Delta\epsilon$ with Increasing Intensity

Graph 6.2 shows that below $\sim 100 \text{ nW cm}^{-2}$ the gradient of the $\log(\Delta\epsilon_1/\Delta\epsilon)$ vs $\log I$ plot is around 0.5 in sputtered a-Si. As the light intensity rises to $4 \times 10^2 \text{ nW cm}^{-2}$ the gradient decreases until it follows an $I^{\frac{1}{4}}$ relation. A sharp change is not observed and the two regions merge into one another. Holland (Ph.D thesis 1987) attributed the $I^{\frac{1}{2}}$ behaviour to strongly self-trapped carriers. Defect states close to the Fermi level are filled by carriers excited at low intensities. As the light intensity increases states further from the Fermi level are filled. These are likely to be less strongly trapped leading to a decrease in recombination times. Shorter recombination times are evident in the quicker response times of ΔC . At the highest light intensities the excited states will possess a broad distribution of recombination times meaning that carriers trapped in shallow states will recombine more rapidly than those trapped in deep states.

Evidence for self-trapping is obtained by finding the α^{-1} values. These have been calculated by Holland (Ph.D thesis 1987) and are of the order of 8\AA to 12\AA for sputtered material.

The width of the $I^{\frac{1}{4}} \rightarrow I^{\frac{1}{2}}$ transition region can be explained by considering the light intensity absorbed, by the sample, at varying depths within the bulk.

As the 633nm light penetrates the a-Si, some will be absorbed. The surface illuminating intensity will therefore be greater than the intensity found in deeper regions of the sample. This means that the film surface will be receiving more light and will exhibit a greater

response, and change as $I^{\frac{1}{4}}$, than deeper regions. The response from the deeper regions will be masked by the response of surface states. As the maximum illuminating intensity drops, the surface states will begin to receive less light. This implies that a reduced response will be observed, and will approach $I^{\frac{1}{2}}$ behaviour, leading to the $I^{\frac{1}{4}} \rightarrow I^{\frac{1}{2}}$ transition region. As the intensity drops further towards the lowest intensities even the sample surface will be in the $I^{\frac{1}{2}}$ region.

7.2(e) The Temperature Dependence of $\Delta\epsilon_1/\epsilon_1$

Both sputtered and glow discharge material show a temperature dependent $\Delta\epsilon_1/\epsilon_1$. The dependence of $\Delta\epsilon_1/\epsilon_1$ is weak in sputtered material (between 1.2K and 4.2K) and is most obvious at low intensities (see graph 6.2). If recombination is by tunnelling (see section (7.3(d))) then the temperature effect can be explained. Electron self-trapping occurs due to interactions with the lattice. To excite these trapped carriers into recombining, energy must be supplied. At low temperatures this comes from the zero point energy of lattice vibrations and as the temperature increases energy is supplied by thermally excited phonons. This leads to a faster recombination rate. The effect of increasing the rate of recombination at a constant excitation (equal to g_0 which is proportional to the illuminating intensity) is to decrease the optically induced change. This is evident in the data for sample MA4 and in the sputtered material studied by Holland (Ph.D thesis 1987).

7.3 Glow Discharge a-Si:H

7.3(a) Comparison of the Optical Effect in Glow Discharge Material with the Response in Sputtered Samples

The optically induced response in a-Si:H prepared by the glow discharge decomposition of SiH_4 gas shows some similarities to that observed in sputtered material. At high intensities (i.e. above $\sim 1 \mu\text{Wcm}^{-2}$) the response saturates i.e. it increases until a constant value is reached. The saturation value of $\Delta\epsilon_1$ is found to vary as a low power of intensity. Removal of the light causes a return to the dark state. This differs from the decay in sputtered samples in that the decay lasts for a much longer time (e.g. days or longer, compared with less than one day for sample MA4, a pure a-Si sample). This indicates that the excited carriers remain trapped for longer.

The illuminated response persists to higher temperatures in low discharge a-Si:H (up to -50K or -60K) than in the sputtered material studied by Holland (Ph.D thesis 1987).

Other important differences found in the optical response of ϵ_1 and σ_1 in glow discharge samples include the integrating response at intensities below $\sim 1 \mu\text{Wcm}^{-2}$ and in the illuminated frequency response. These are discussed in greater detail in sections 7.3(b) and 7.3(c) respectively.

7.3(b) Mechanism Responsible for the Optically Induced Loss in Glow Discharge Material

This material has a lower density of defect states deep within the band-gap than sputtered material. ESR studies have shown that the spin density is less than 10^{16}cm^{-3} for a-Si:H (compare with a value of 10^{19}cm^{-3} in a-Si) prepared using the glow discharge technique. These

defects are responsible in sputtered a-Si or sputtered a-Si:H for trapping carriers which respond to the applied ac field. The contribution from these states i.e. a-Si:H, prepared by glow discharge, is likely to be small compared with a sputtered material but a strong induced signal is still found. Another trapping mechanism must therefore exist. We postulate that carriers are trapped in *band-tail states* where they can remain for a considerable length of time (~ several days or weeks at 12.5K) before recombination takes place.

The results presented in Chapter 6 showing the frequency dependence of the optically induced loss and the $\log \Delta\epsilon_1$ vs $\log I$ graphs are now used to confirm the above idea.

It has been assumed that the optically induced loss is independent of the background loss. We now show both experimentally and analytically that this is the case.

Experimentally the frequency dependence of the capacitance and conductance are considered.

The dark conductivity at 4.2K (see graph 5.12) obeys the following law

$$\sigma \propto \omega^s \text{ with } s \approx 1. \quad (7.10)$$

Under illumination, of varying degrees of intensity, it can be seen that s decreases from 0.90 to 0.70 when $I = 0.357 \mu\text{Wcm}^{-2}$ and $I = 1.70 \mu\text{Wcm}^{-2}$ respectively.

These curves are equivalent to the dark conductivity curves at higher temperatures as can be seen in graph 5.2.

A similar effect is observed in the capacitance data where the frequency dependence of the induced capacitance is similar to that observed at higher temperatures (see graph 6.8. It can therefore be concluded that the induced loss involves a different population of states, i.e. those in the band-tails, from the defect states responsible for the low temperature loss in glow discharge material. Analytically, Holland (Ph.D thesis 1987) and Long showed that the rate equation can be written as

$$\frac{dn}{dt} = g_o + g_{th} - An^p \quad (7.11)$$

where g_o = the generation rate due to illumination

g_{th} = the thermal generation rate of carriers

p = an integer

A = a constant.

The term An^p is the recombination term in equation 7.11. For dark equilibrium $g_{th} = An_o^p$

$n = \hat{n} + n_o$ where n_o = the number of carriers/unit volume which contribute to the dark loss and \hat{n} is the number of optically induced carriers contributing to the ac loss.

From 7.11, and setting $p=2$,

$$\begin{aligned} \frac{dn}{dt} &= g_o + An_o^2 - An_o^2 - 2A\hat{n}n_o \\ &= g_o - 2A\hat{n}n_o \end{aligned}$$

This equation predicts that, under equilibrium conditions, the light induced loss is linear i.e. $n \propto g_o$ and if $\Delta\epsilon \propto Kn$ then the plot of $\Delta\epsilon$ vs I will be linear. An exponential decay will also be observed on removal of the light since $n_i \sim \exp(-2An_o t)$. Such

results are not observed and the only assumption made is that $\Delta n \ll n_0$. The optically induced change in ΔG is found to be small so the above assumption is valid.

Other experiments also support the idea of carriers trapped in band-tail states. These concern LESR measurements, DC photoconductivity, low temperature drift mobility and transient photoconductivity measurements. These are discussed in greater detail in section 4.5

7.3(c) The Integrating Response at Low Intensities

The integrating response observed at intensities below $\sim 1 \mu\text{Wcm}^{-2}$ is due to the fact that the population of trapped carriers does not build up sufficiently fast in order for the recombination rate to be balanced by the generation rate. The speed of the increase in the optically induced signal is because $\sim 98\%$ of the charge lodged in the band-tails recombines via geminate channels e.g. luminescence.

As the illuminating intensity increases the generation rate of carriers also increases. This means that the population of trapped carriers can become greater until the recombination rate balances the rate at which these trapped carriers build-up. Equilibrium conditions will be achieved in this case.

The rate at which photo-excited carriers are trapped can be used to calculate the efficiency of the carrier trapping mechanism. It is assumed that a value of $\Delta\epsilon \approx 2 \times 10^{-2}$ is equivalent to around 10^{17} spins in the following calculation. $\Delta\epsilon_1/\Delta t$ can be obtained from the rise times in the integrating region and hence $\Delta n/\Delta t$ can be found. In a typical sample, K9, $\Delta n/\Delta t \approx 4.79 \times 10^{12} \text{ cm}^{-3} \text{ s}^{-1}$. An illuminating intensity of $\sim 2.9 \text{ nW}$ was used and hence the number of photons absorbed by the silicon can be calculated. A value of $\sim 0.58 \times 10^{15} \text{ photons cm}^{-3} \text{ s}^{-1}$ is obtained. Dividing the value of $\Delta n/\Delta t$ by this number gives a trapping efficiency, η , of $\sim 8.4 \times 10^{-3}$. This is of the order expected due to the fact that about 97% of carriers recombine very quickly by processes such as luminescence. Calculating η for other samples, in the integrating region, gives similar values, e.g. $\sim 6.0 \times 10^{-3}$ for K11 and $\eta \sim 3.4 \times 10^{-2}$ for D1 at similar illuminating intensities applied for similar times (see also table 7.14). It can be seen that η decreases as the saturation limit is approached. This is expected because of the recombination mechanisms which compete with the trapping of carriers as equilibrium conditions are reached.

7.3(d) Recombination

The model proposed by Dersch et al (1983) accounts for the recombination mechanisms involved in a-Si and a-Si:H samples. The only states within the band gap, in this model, are localized tail states and defect states. Initially, carriers are excited by the applied illumination (as shown in diagram 7.1). These thermalize to shallower states in the band-tails in the case of a-Si:H. They then remain trapped until recombination takes place via a defect state,

as shown in diagram 7.1. Electrons then recombine by diffusing to excess holes.

In a-Si, carriers are trapped in defect states until they recombine by tunnelling.

The above model is also discussed in Chapter 3 where it is applied to explain infra-red quenching of an optically induced ESR signal. The decay curves, plotted on a graph of $\Delta\epsilon_1(\text{time})/\Delta\epsilon_1(0)$ against $\log(\text{time})$ are close to being a straight line, or even a straight line in some samples studied. As in a-Si samples (see section 7.2(c)) this can be explained qualitatively by the more closely spaced electron-hole pairs recombining more quickly than more distantly spaced pairs. In the next two sections we develop a simple analytical model in which this idea is incorporated and apply it to our data.

7.2(e) Analysis of the Dark Decay

The decay of $\Delta\epsilon_1$ with time once the light has been removed is not linear. In some cases the data is linear on a $\Delta\epsilon_1$ vs $\log(\text{time})$ plot, but not in all samples at every temperature. In order to quantify the decay rates and the effect of temperature, or sample material the following model has been proposed.

The following assumptions are made in the model:

- (i) Equal numbers of electrons and holes are trapped (i.e. $n = p$) thus recombination is bimolecular.
- (ii) Holes are trapped and are immobile. Electrons diffuse to the trapped holes in order for recombination to occur. We estimate that the distance required for an electron to diffuse to a trapped hole is $\sim [n(t)]^{-1/3}$.

- (iii) The diffusion process which precedes recombination takes place by electrons tunnelling through band tail states (Monroe 1985).
- (iv) Diffusing electrons drop lower in energy as time progresses. No thermal energy is available to excite trapped carriers at the low temperatures involved. The separation of trapped electrons in the band-tail will increase as a result of diffusion leading to an increase in the time required for tunnelling. The diffusion coefficient $D(t)$ will therefore decrease as a result.
- (v) Movaghar et al (1986, 1986, 1987) calculated the diffusion coefficient for a pulse of injected carriers at low temperatures. It was found that $D(t) \sim A \left(\frac{t_0}{t}\right)^{1-\alpha}$. The recombination time can now be calculated i.e. recombination time $\sim n^{-2/3}/D$ where

l = the distance an electron diffuses

n = the number of electrons diffusing = p

t = time

A = a constant

t_0 = a scaling time

The diffusion rate is therefore $n^{2/3}D$ and the differential equation governing the recombination rate is

$$\frac{dn}{dt} = -D_0 n^{5/3} \left(\frac{t_0}{t}\right)^{1-\alpha} \quad (7.12)$$

Solving the differential equation and setting the initial conditions as $n = n_0$ when $t = 0$ it is found that

$$\frac{n}{n_0} = \frac{1}{\left[\left(\frac{t}{t_0} \right)^\alpha + 1 \right]^{3/2}} \quad (7.13)$$

$$\text{where } (t_0')^\alpha = \frac{3}{2} \frac{t_0^\alpha}{t_0} \frac{\alpha}{A n_0^{2/3}} \quad (7.14)$$

(vi) The final assumption is that $\Delta\epsilon_1 \propto n$ i.e. the optically induced loss is proportional to the number of trapped carriers assuming that the contribution to the loss due to each trapped carrier is equal.

7.3(f) Fitting Procedure

The decay curves were plotted on a $\Delta\epsilon_1/(\Delta\epsilon_1)_0$ vs log (time) plot. This enabled direct comparisons between the various graphs and theory to be made. Fitting the theoretical results obtained from equation 7.13 to the experimental data was accomplished by firstly, calculating the maximum gradient. From equation 7.13

$$-\frac{d}{d \ln t} \left(\frac{n}{n_0} \right) = \text{gradient.} \quad (7.15)$$

and rewriting 7.13 in a more general form as

$$\frac{\Delta\epsilon}{[\Delta\epsilon_1]_0} = \frac{n}{n_0} = \left(1 + \left(\frac{t}{t_0} \right)^\alpha \right)^{-3/2} = y \quad (7.16)$$

$$\text{it can be shown that } -\frac{dy}{d \ln t} = \frac{3}{2y} \left(\frac{y^{2/3} - 1}{y^{3/2}} \right). \quad (7.17)$$

The gradient has a maximum value when its derivative equals zero.

i.e. $y = \left(1 + \frac{2}{3}\right)^{3/2} \approx 2.152$.

The maximum value of the gradient is therefore approximately 0.465α . The value for the maximum gradient was then compared with the experimentally observed value and fitted to the curve. This enabled the parameters α and hence t'_0 to be determined.

Curves, obtained using equation 7.13, have been fitted to the decay data. These are plotted in diagrams 7.3 to 7.13. Graph 7.8 for K11, (an $n^+ - i - n^+$ sample) shows that the fitted curves are a similar shape. In the middle portions of the graphs the fit is reasonably close, but at short and very long times these deviate from the experimental data. The fitted curves can be seen to fall more rapidly as time progresses, and the initial values, at times less than 10 seconds, are slightly lower. When $n = n_0$, $D = D_0$ and assuming $n_0 \sim 10^{17} \text{ cm}^{-3}$ (from LESR studies) and taking $t_0 \sim 10^{-13}$ seconds, $D_0 = 5 \times 10^{-4} \text{ cm}^2 \text{ s}^{-1}$. This value does not differ significantly from those found by Gr \ddot{u} newald et al (1985).

7.3(g) The Detection of Carriers Trapped in the Band Tails

The trapped carriers responding to an applied ac field of $\sim 2 \text{ kHz}$ have relaxation times of $500 \mu\text{s}$. It is stated in previous sections, which describe and explain the mechanisms responsible for the low temperature ~~ac loss, that~~ carriers can move, in response to the ac field, within inhomogeneous regions. The decays, which last for $\sim 10^{-5} \text{ s}$ or longer, are due to the recombination of trapped carriers. These are trapped at a site and can respond to the measuring field. The length of the decay time is then due to the time taken for carriers to recombine via other sites which can be modelled by considering inhomogeneous regions within the band-tails (see Chapter 5 and Long

1989). The distribution of states in the band-tails may therefore not be random and clusters of states may be closely or distantly spaced.

7.4(a) The Temperature Dependence of $\Delta\epsilon_1$ in Glow Discharge Samples

The weak temperature dependence of $\Delta\epsilon_1$ in the glow discharge material can be explained by considering the variation of α and t'_0 with temperature. Both these parameters are weakly temperature dependent implying that recombination processes are activated by thermal energy. As this recombination process is competing with the generation of carriers by optical excitation the $\Delta\epsilon_1/\epsilon_1$ values, at a constant illuminating intensity, are observed to decrease with increasing temperature.

An important point to note is that the experimental evidence obtained predicts that $\alpha \sim 0.3$ and is weakly temperature dependent. This result disagrees with calculations by Movaghar et al (1985, 1986) who predicted that $\alpha \rightarrow 0$ at low temperature. It was expected by Movaghar et al that a "freezing" of carriers would occur at low temperatures leading to $\alpha \rightarrow 0$. (See Table 7.15.)

Experimental work was performed by Richert et al (1984) in order to study the time dependent diffusion of excitons in amorphous benzophenone. The time dependence of the decays were shown to have a form similar to 7.13. The dispersion parameter, α , was shown to be temperature dependent and varies from 0.23 to 0.55 between 4.2K and 90K.

7.4(b) The Effect of Increasing Temperature at a Constant Level of Illumination

The results presented in section 6.7 show the result of increasing the temperature at a constant illuminating intensity. The shape of the

$\Delta\epsilon_1$ vs t curve when the temperature is increased will depend upon the recombination rate of the optically induced carriers. In a sample, such as K9' the decay curves observed at each temperature step indicates a slow recombination. The rate at which the background capacitance reaches its equilibrium value at a particular temperature will also contribute to the shape of the curve. In K9 the two contributions (the optically induced capacitance will saturate very quickly (~ a few seconds) at the intensities used) are such that a curve is observed.

In other samples a decay is not seen (e.g. S5, D1) at each temperature step. This is because the background capacitance reaches its equilibrium value quickly and in the case of D1, the recombination rates of the carriers are faster than in K9' (see section 7.6(a)).

7.4(c) Other Analysis Problems

In section 6.3 it was explained that difficulties occurred in the estimation of the base capacitance value. If the base value is known to $\pm 0.02\text{pF}$, then a $\Delta\epsilon_1/[\Delta\epsilon_1]_0$ error is around 0.006%, which is insignificant. Above 50K, the difficulty in obtaining a base value increases. By holding a sample at 50K for ~90000 seconds, the trapped carriers are thermally excited and recombine more quickly, leading to a lower value of dark capacitance of a decay than before illumination began. This error can be as large as 0.2% leading to errors of ~0.2% in the $\Delta\epsilon_1/[\Delta\epsilon_1]_0$ axis. Such errors can be observed in the 40K decay plot of sample D1 (see diagram 6.10).

Other problems associated with fitting the curves to the data are due to starting transients. Since it is possible to estimate the time when the light is removed to within a second an error occurs in

the first decade on the time axis. This error can increase if the automatic bridge does not respond for a second after the light is removed. At longer times (greater than ten seconds) this error is not important.

7.5 Other Relevant Experiments

7.5(a) Comparisons with LESR Measurements

Street and Biegelson (1982) presented results showing the effect of light (at a wavelength of 649nm and at excitation intensities between $\sim 10^{-6}$ mW and 10^{-1} mW) ESR measurements. They discovered that a plot of the logarithm of the number of light induced spins against log intensity was close to being linear with a gradient of 0.20 at 30K. This result is comparable to the gradients obtained from the $\log (\Delta\epsilon_1/\epsilon_1)$ vs $\log (\text{Intensity})$ plots which generally have a gradients between 0.22 and 0.25. The magnitude of the LESR response was around 0.05% to 0.5% of the initial ESR values in the dark at the lowest and highest illuminating intensities. Decays of the number of induced spins with time, after the illumination was removed, were also measured by Street and Biegelsen. They discovered that up to 10^3 or 10^4 seconds elapsed before their samples returned to their equilibrium state. Although these results were obtained using pulses of light (of around 1 m sec duration at intensities between 0.07mW and 30mW) the time scales involved are comparable to those seen in the $\log (\Delta\epsilon_1/\epsilon_1)$ vs $\log (\text{time})$ plots shown in diagram 7.3.. The two experiments show similar shapes of decay curve which are linear with $\log (\text{time})$ over much of the range of $\log (\text{time})$.

Although such similarities exist between LESR and optically induced ac loss experiments there are some differences. The first is

the states which are responsible for the changes under illumination. ESR is dependent upon states which are paramagnetic, therefore LESR measurements will record the fraction of states which become paramagnetic under illumination. Such states consist of neutral dangling bonds and trapped majority carriers in doped samples. In undoped samples both types of band-tail carriers are recorded. The LESR technique does not therefore measure the total number of states which are occupied under illumination. AC loss measurements records the states which can respond to a particular measuring frequency. Dangling bond and tail-states which are not necessarily paramagnetic and are occupied, due to the illumination, can therefore be recorded.

7.5(b) DC Photoconductivity and Low Temperature Drift Mobility

Spear and Cloude (1988) investigated the low temperature drift mobility in a-Si:H. By subjecting barrier and junction samples to short ($\sim \mu$ sec) pulses of light it was possible to obtain the drift mobility of the carriers. This was done by applying a voltage pulse at the same time as the light and then measuring the transit time of the carriers. The mobility was then found from the $1/t$ vs Voltage plots.

The results obtained are interpreted in terms of excited carriers thermalising rapidly into a band in the lower regions of the tail states. Electron transport takes place in this region and is detected by the enhanced mobility of the carriers.

The experiment showed that thermalization through the upper tail states was extremely rapid and occurred too fast for detection. Thermalisation slows down as the electrons progress through the tail states as expected since the separation of states is increasing.

Information regarding the shape of the band-tail is also obtained from the results. Calculations by Speare and Cloude involving different tail state distributions and the time taken for thermalisation down to around 0.11eV to 0.13eV below E_c show that a purely exponential band tail cannot account for the results obtained, i.e. the rapid initial thermalisation followed by a slowing down of the rate. Distribution involving an initial shallow distribution of states of ~0.12eV in width followed by a more rapid decrease (close to exponential) account for the experimental results more satisfactorily.

These experiments show that the drift current is passed in states above the exponential band tail at low temperatures. The ac loss measurements refer to processes occurring below this region. The drift mobility experiments suggest that the dc photocurrent will be carried through states near the valence band at low temperature, but will be irrelevant to the ac loss because this occurs in different states.

7.5(c) Transient Photoconductivity

This work involves exposing amorphous films to a short pulse of light and then monitoring the decay of the photocurrent.

Analysis of these transient photoconductivity experiments was performed by Monroe (1985, 1987 and 1988) who used hopping arguments, and shows that the decays are close to being linear on a log (photocurrent) vs log (time) graphs. A mechanism where carriers "hop up" or "hop down" in energy was suggested. The hopping down mechanism is expected to dominate at low temperatures and the hopping up of carriers from deeper states to shallower band tail states before hopping to lower energies is the process expected to be dominant at high temperatures (i.e. above ~100K).

A hopping up mechanism is unlikely to be responsible for recombination in the optically induced ac loss decays since insufficient thermal energy is available at low temperatures. Such a mechanism would imply that as more thermal energy becomes available the decays will be much more rapid. The values of α obtained for the decays are weakly temperature dependent and do not support this idea. The model discussed in section 7.3(e) involving bimolecular recombination is more likely i.e. as recombination events take place, the remaining states will be further apart leading to longer recombination times.

7.6(a) D Sample

When the illumination was removed from the D samples (D1 and D2) an initial drop is seen in the $(\Delta\epsilon_1/\epsilon_1)$ vs log (time) plots. This drop is due to a fast recombination mechanism involving closely spaced light induced electrons and holes. After the initial rapid recombination (after ~10 seconds) has taken place, the remaining optically induced electron-hole pairs will be more distantly spaced, thus leading to a slower recombination rate. Fitting curves, using equation 7.13 gives reasonably good results for the decay after ~10 seconds. Another contributing mechanism must be introduced to account for the initial drop in $\Delta\epsilon_1/\epsilon_1$ with log (time). Such a mechanism could involve the rapid decay of carriers in the region of states at the top of the band-tails (c.f. Spear, see section 7.5(b)).

7.6(b) Metallic Diffusion in a-Si and a-Si:H Samples

The dark characteristics in a-Si:H, prepared by the glow discharge decomposition of silane were studied by Shimakawa et al (1987). The ac conductivity in samples with Au top electrodes have an ac conductance which is up to an order of magnitude greater than that in samples with

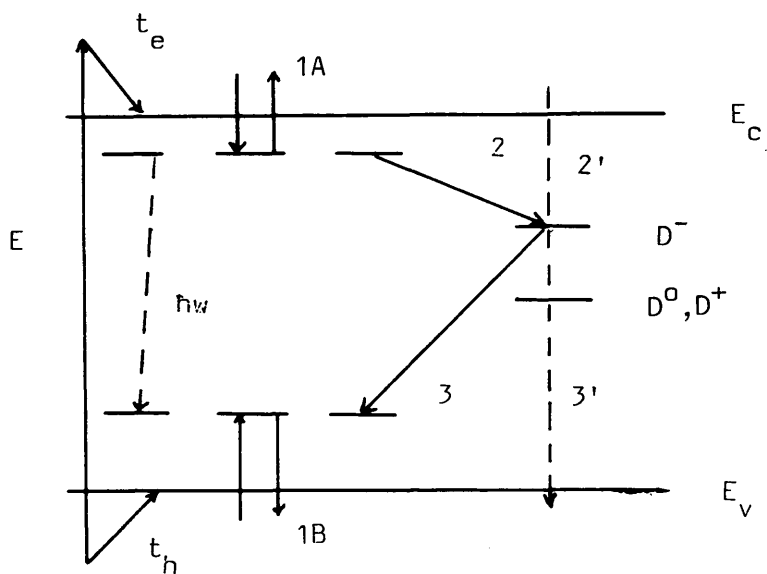
Al top electrodes at temperatures between ~20K and 200K. The temperature dependence of the dark conductivity shows that $G_{ac} \propto T$ where T ranges from 12.5K to ~150K (see graph 5.11). A mechanism described by Austin and Mott (1969) involves uncorrelated hopping between centres and predicts that $G_{ac} \propto T$. Hopping of carriers between diffused metallic impurities in the a-Si:H film accounts for the temperature dependence of the dark ac loss in these films.

Under illumination, at low temperatures, no detectable response was found in the samples with Au top electrodes. The diffused Au atoms may be acting either as recombination centres or could be facilitating hopping to other recombination centres thus accounting for the absence of an optically induced effect.

In sputtered material (e.g. sample MA4) an optically induced signal is observed even when Au top electrodes are used. Since the loss is attributed to carriers trapped in defect states and since this is greater in sputtered material (by ~2 or 3 orders of magnitude) recombination due to diffused metal atoms is likely to be insignificant when compared with glow discharge a-Si:H.

7.6(c) As₂Se₃ Sample

This material showed no optical response as described in section 6.5(a). This could be due to metallic diffusion since Au top and bottom electrodes were used on the sample. The observed dark loss was very much greater than in bulk As₂Se₃ glasses (Elliott 1987) and resembled the dark losses found in the a-Si:H samples with diffused Au electrodes.

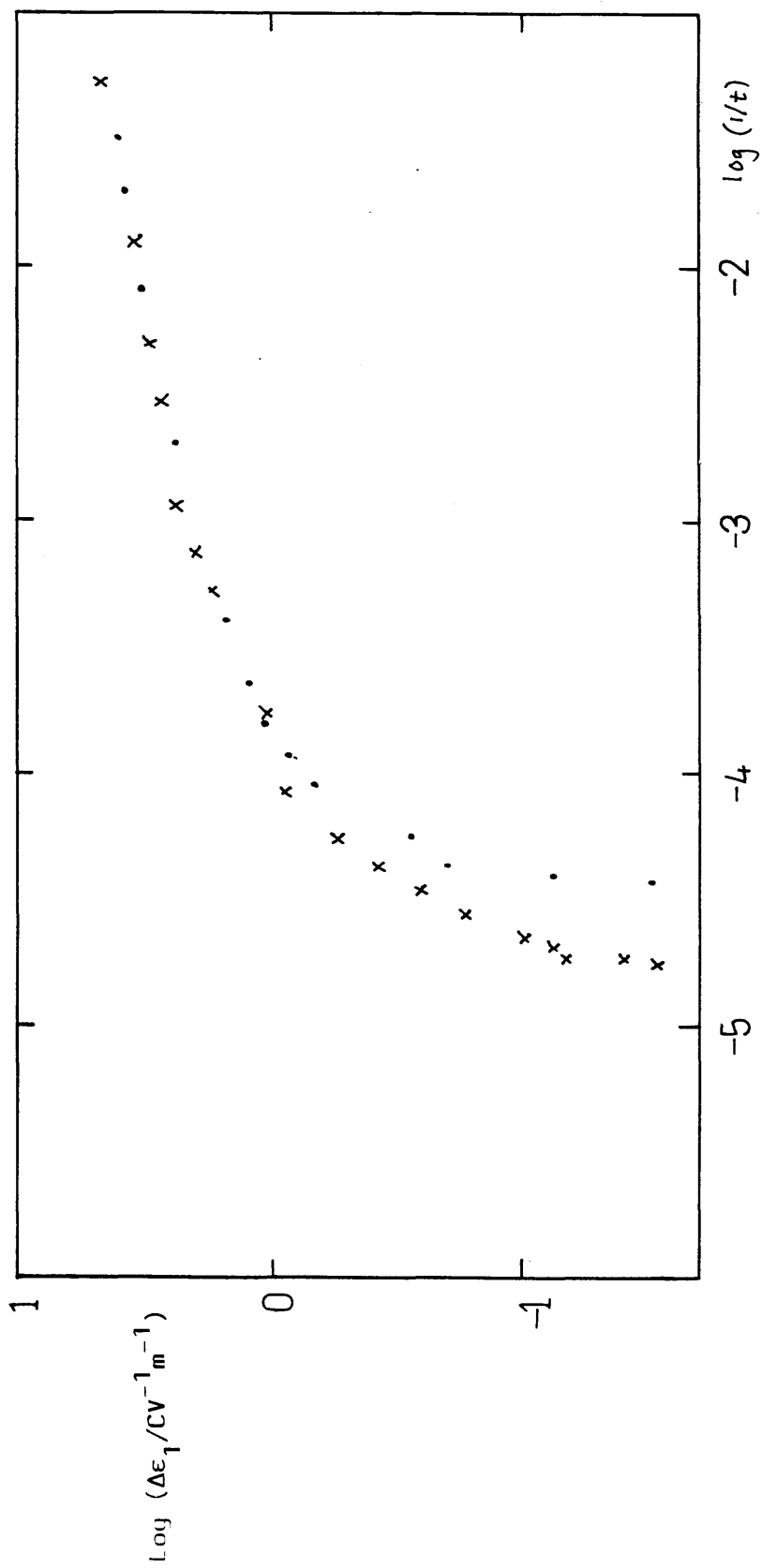


Key

D⁻, D⁰, D⁺ are the charge states in which dangling bonds can exist. E represents the energy required to create an electron hole pair. After thermalization (t_e and t_h) the carrier can be trapped or re-emitted (1A, 1B). Recombination can also take place via defect states (2, 3). Radiative (hw) and other non radiative transitions (2', 3') also account for recombination steps

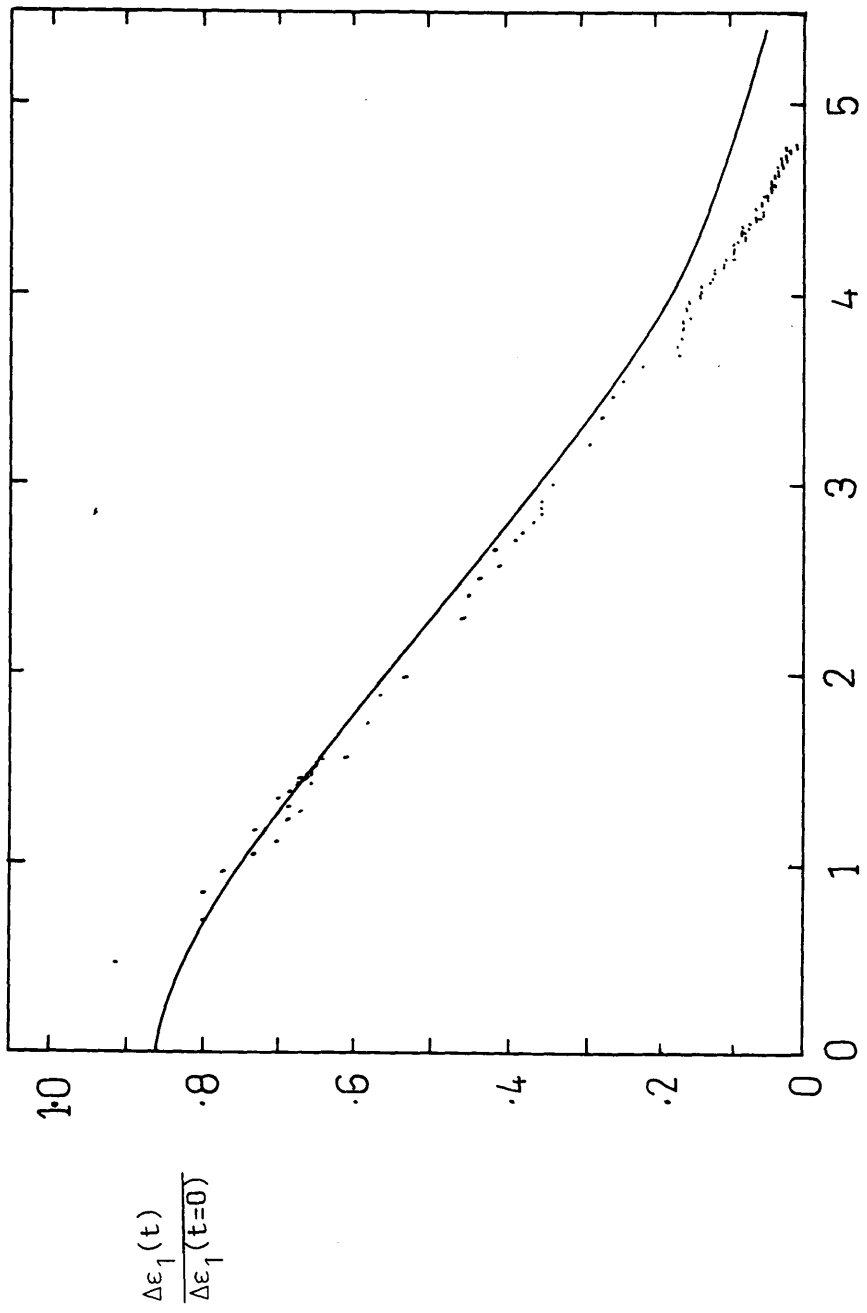
Diagram 7.1

The general mechanism used to explain the optical response and recombination (Dersch et al 1983). See text for details.



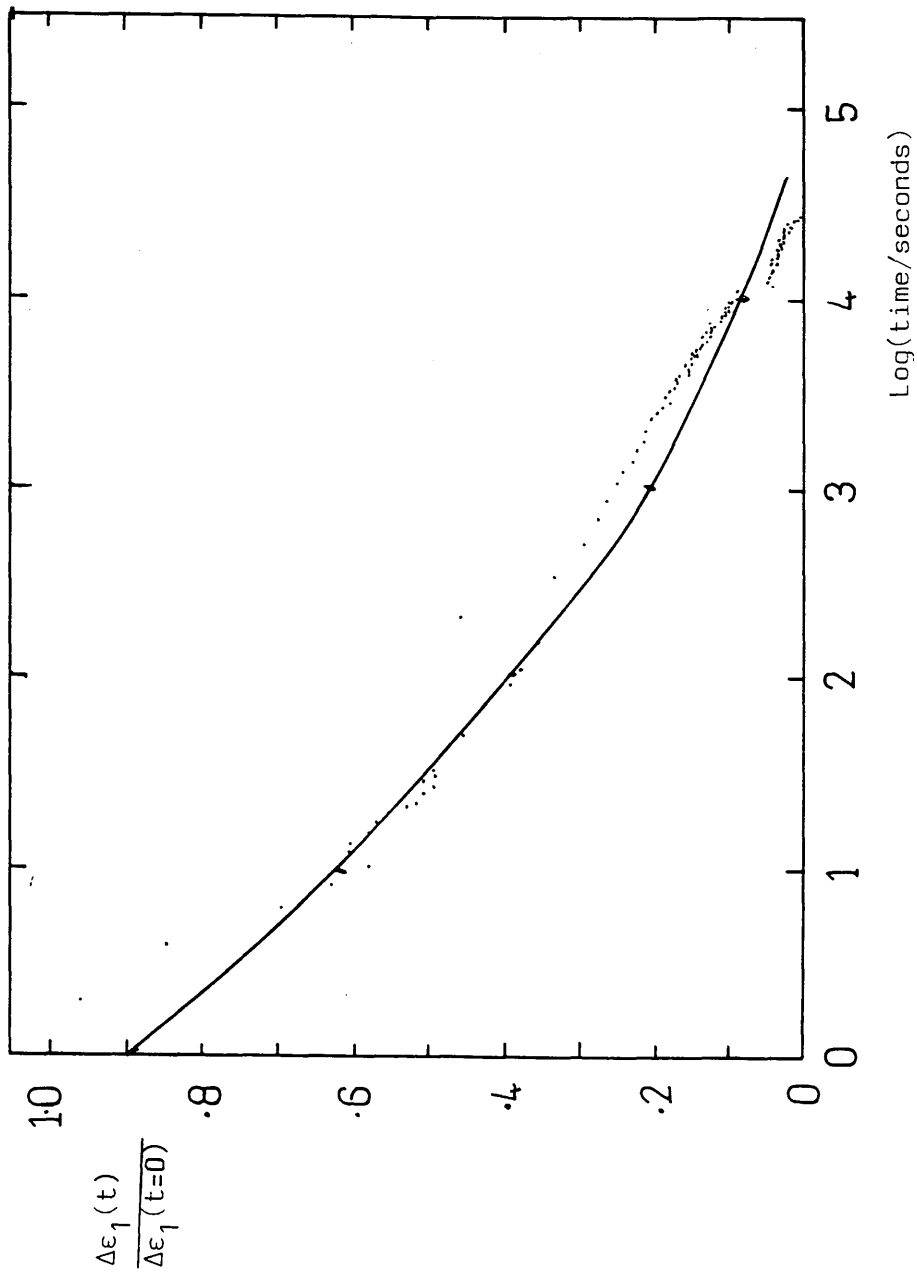
Graph 7.2

A $1/t$ fit the decay data presented in graph 6.1 for a magnetron sputtered pure a-Si sample (MA4).



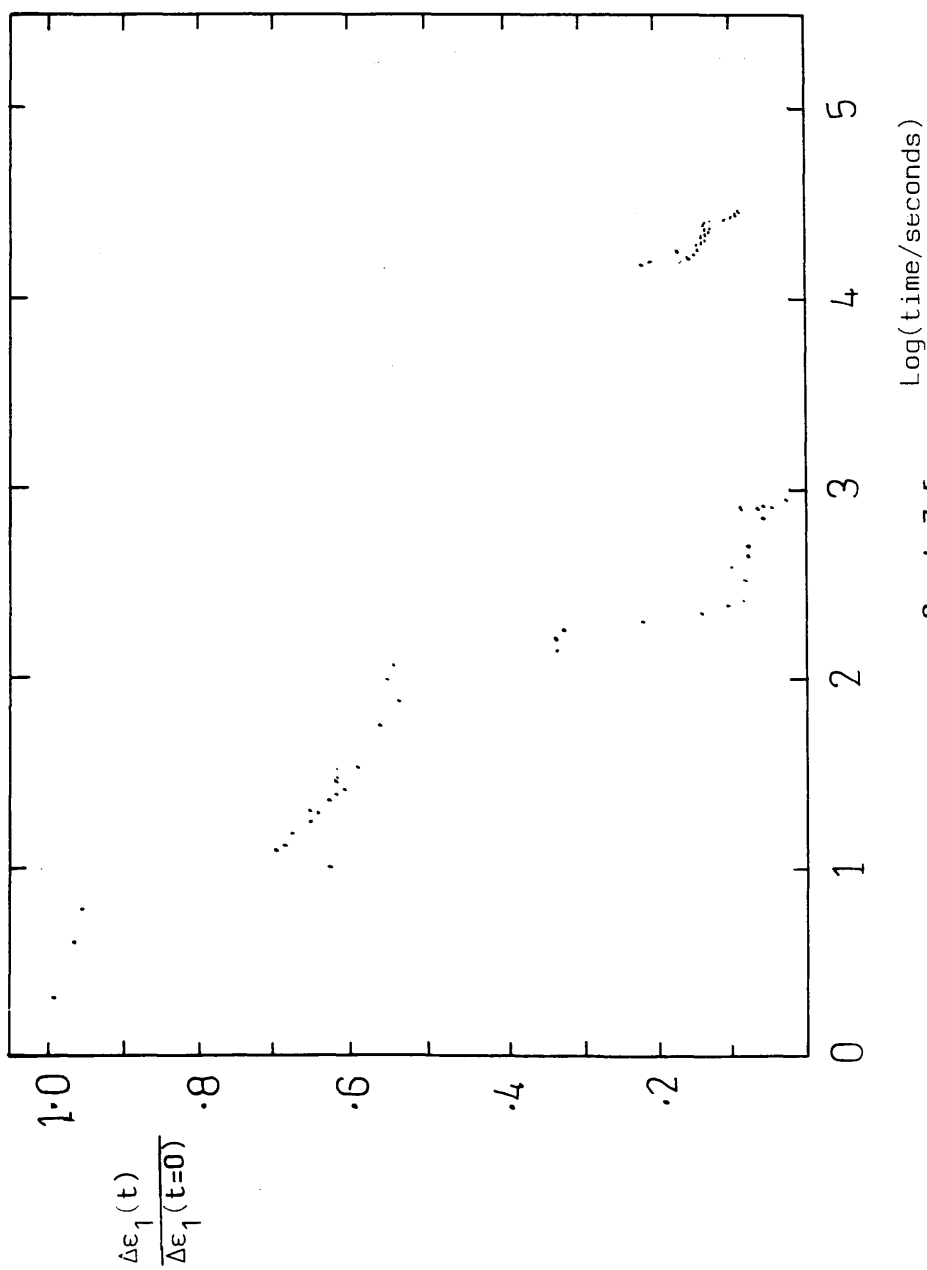
Graph 7.3 $\text{Log}(\text{time}/\text{seconds})$

The decay data for MA4, plotted against $\log(\text{time})$ at 4.2K. This is the 4750Å junction. A theoretical fit is also shown (see section 7.3(1)).



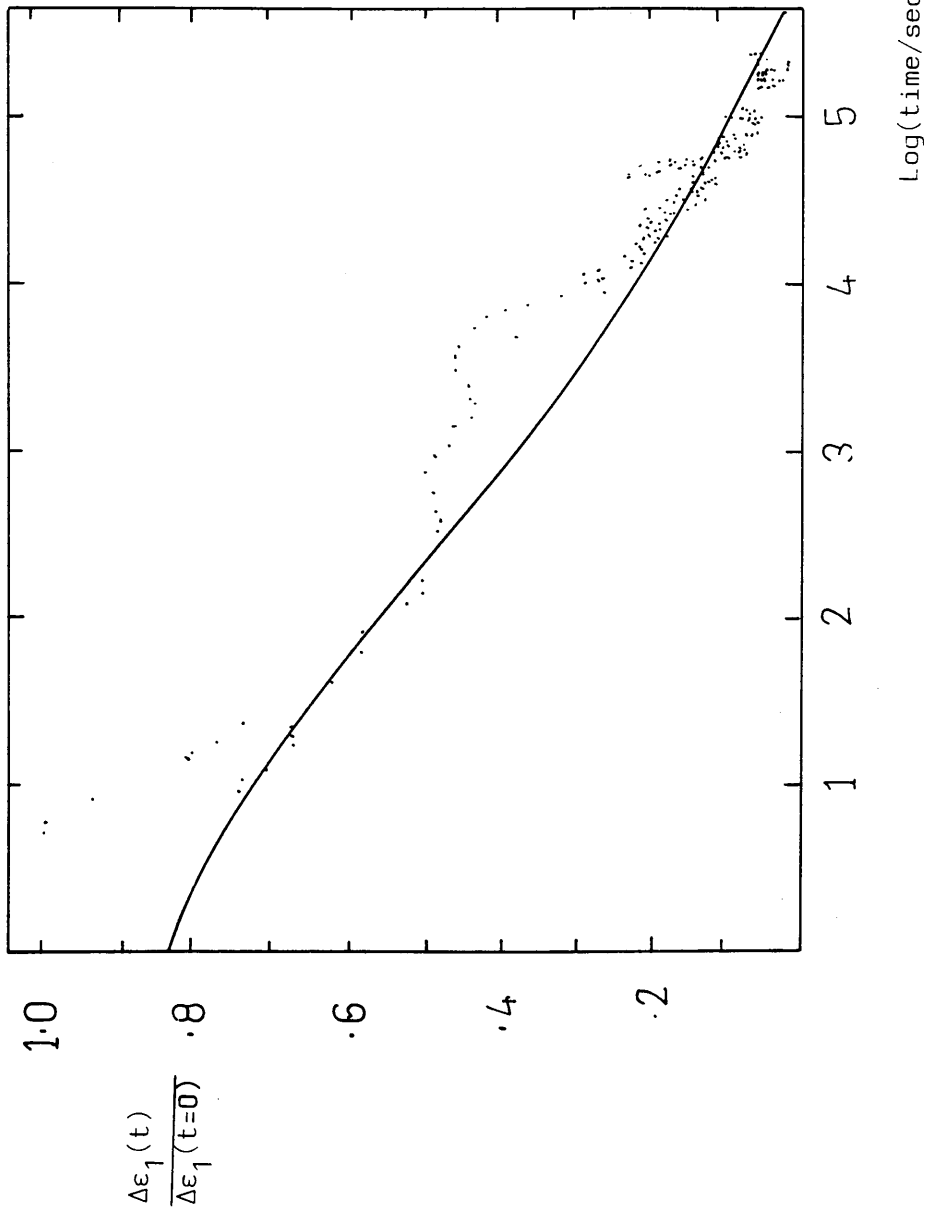
Graph 7.4

The decay data for MA4 at 1.2K. Again, this is the 4750Å junction.



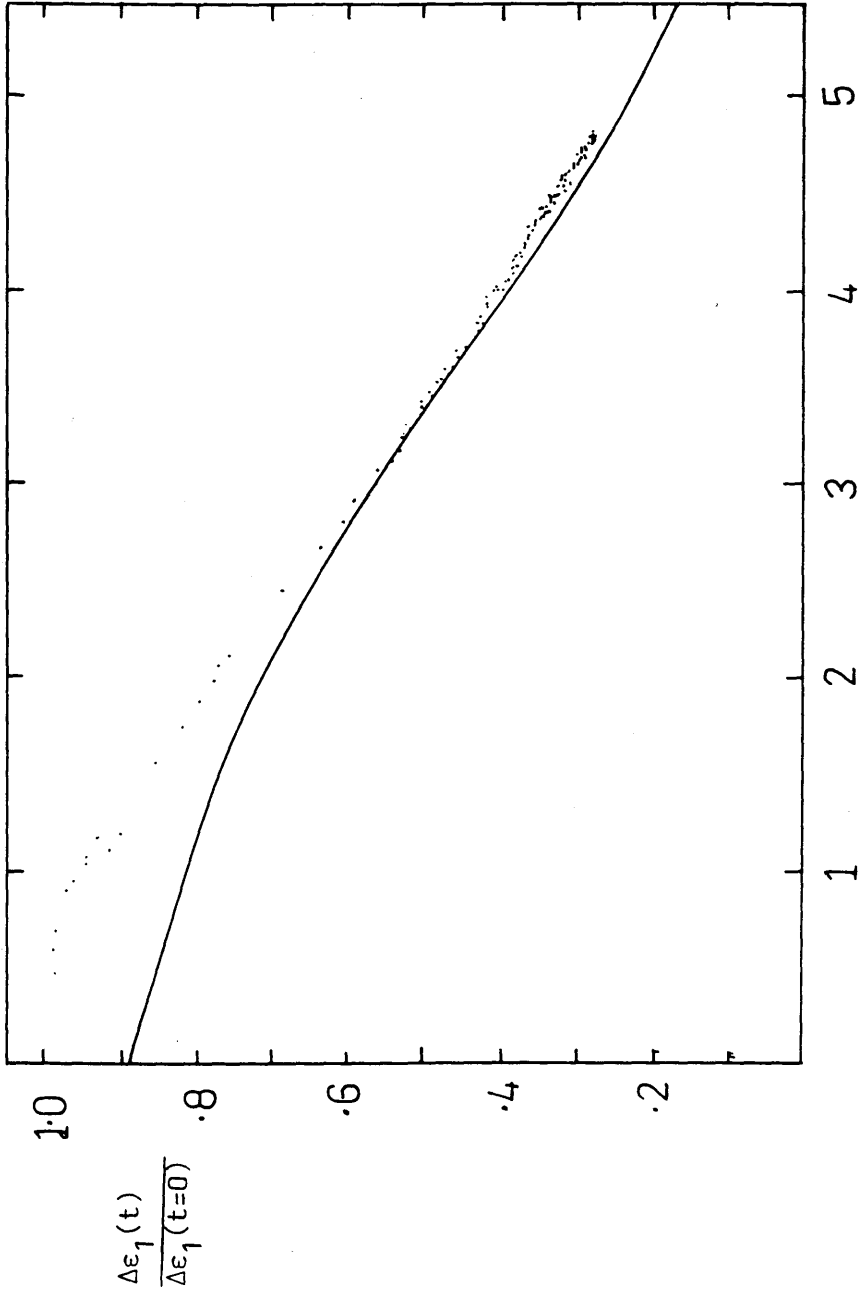
Graph 7.5

The 9600Å decay data for MA4 at 4.2K. Note the effect of contact problems (see Chapter 5).



Graph 7.6

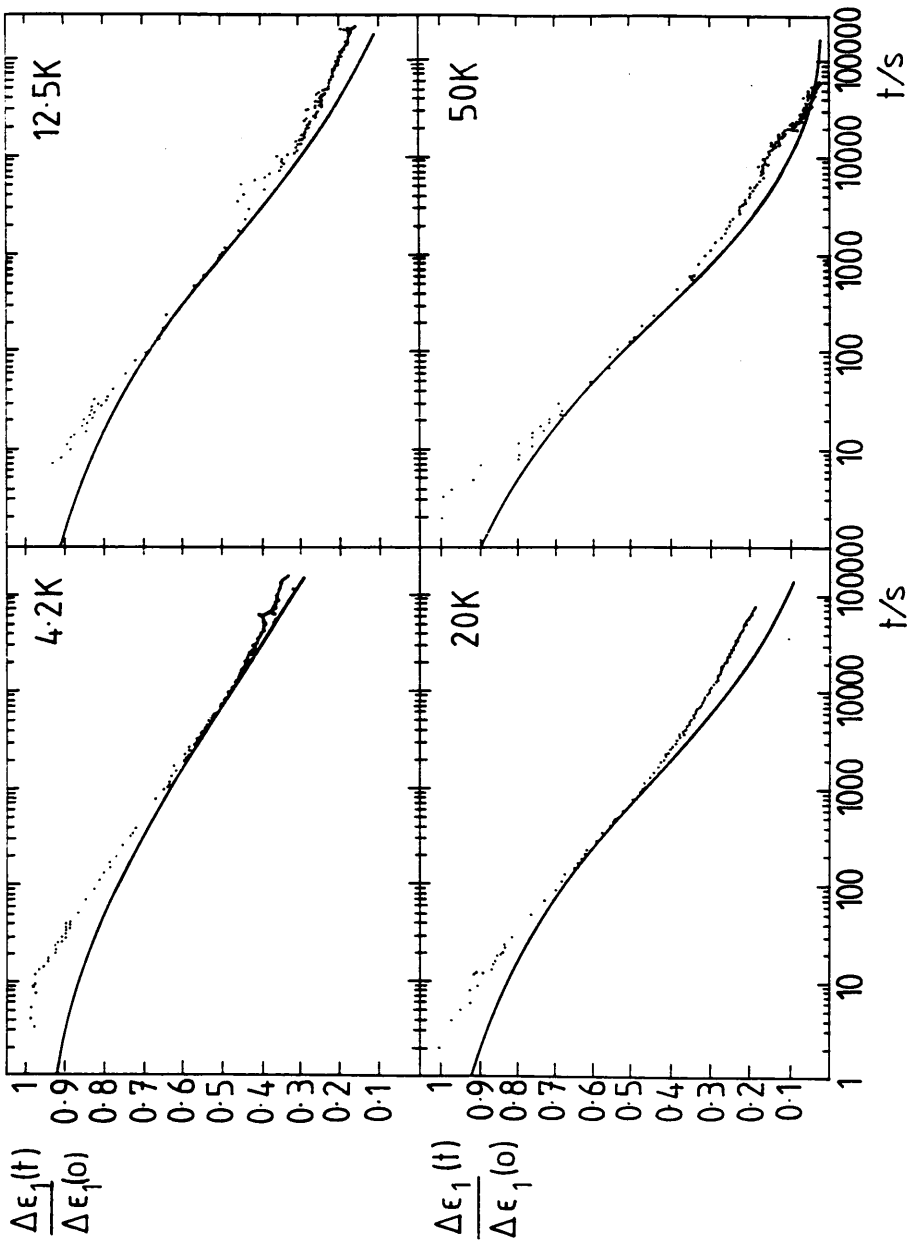
The decay data for an $n^+ - i$ sample (S5).



$\text{Log}(\text{time}/\text{seconds})$

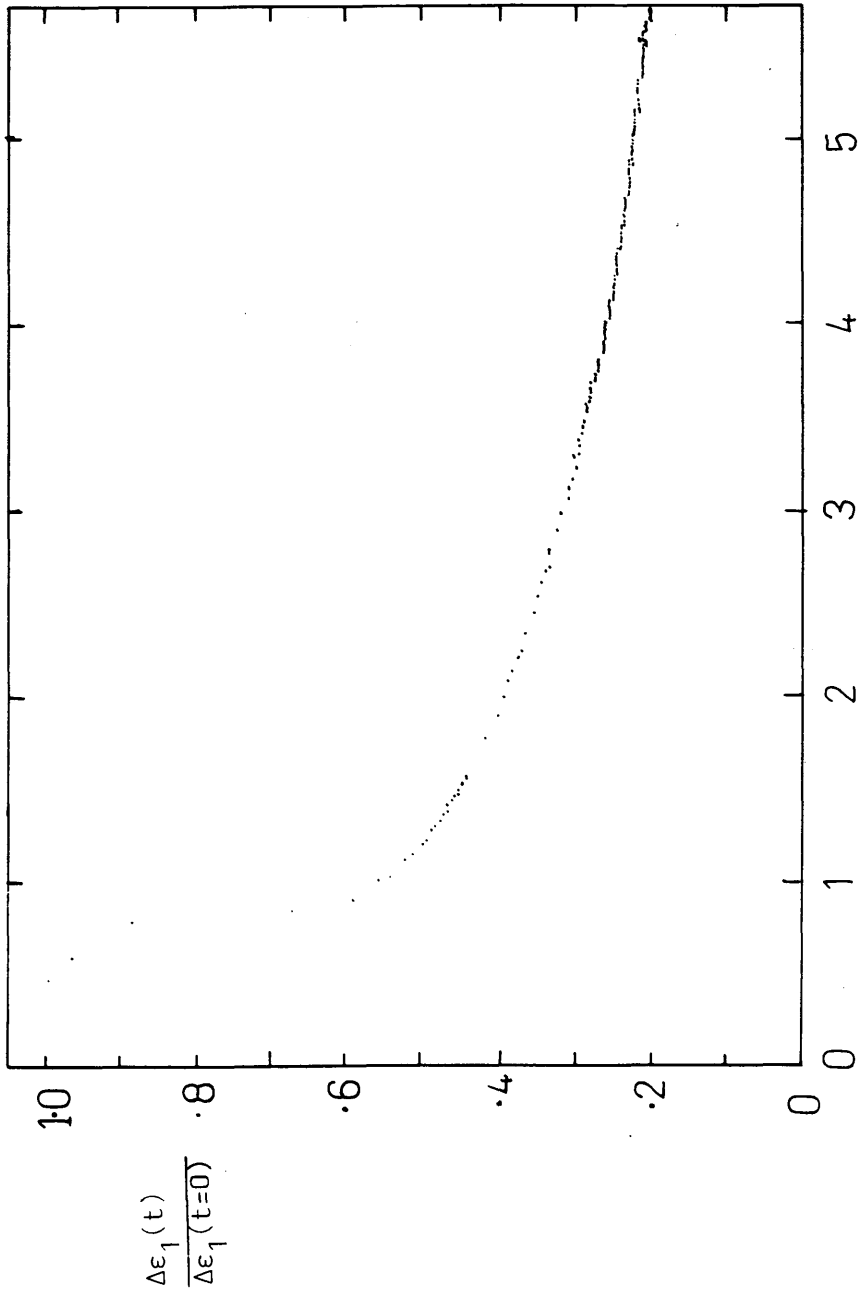
Graph 7.7

The capacitance decay for an $n^+ - i - n^+$ sample (K9') at 12.5K.



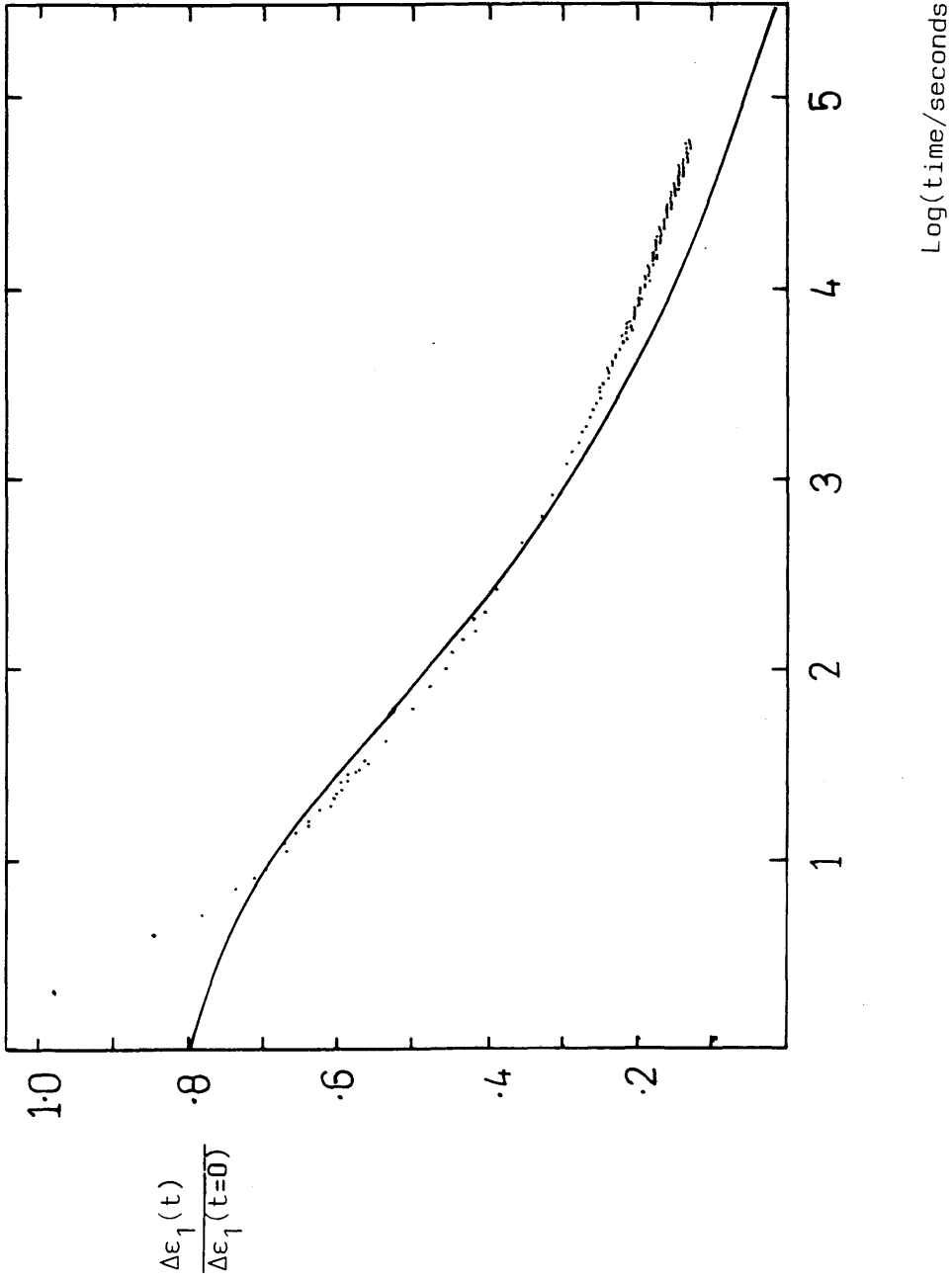
Graph 7.8

The decay data for an $n^+ - i - n^+$ sample K12' (at 4.2K) and for K'11' at 12.5K, 20K and 50K). A calculated curve is fitted to each graph.



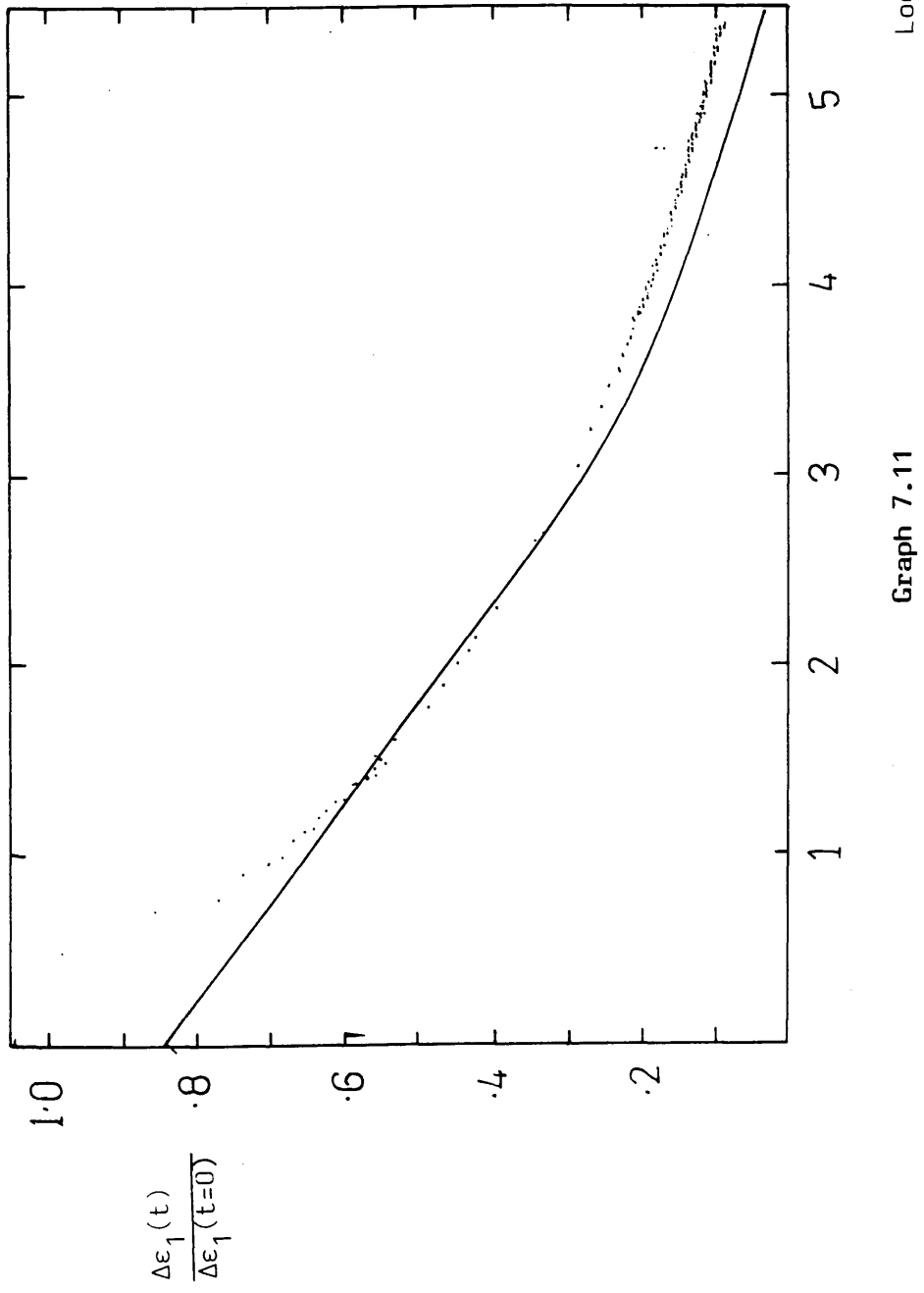
Graph 7.9

The dark decay in a doped (n^+) sample (D2) at 4.2K.



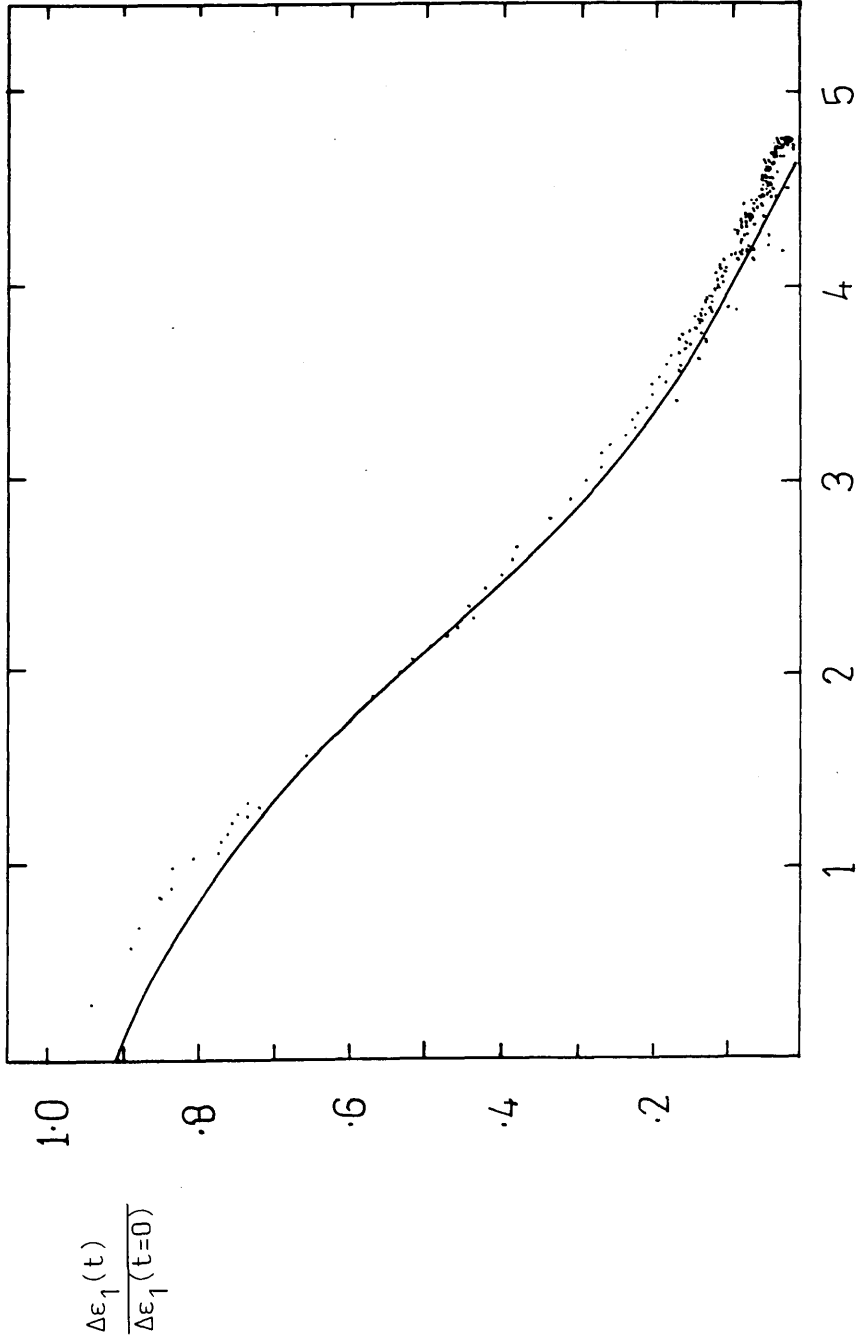
Graph 7.10

The decay data for an n^+ sample (D1) at 12.5K.



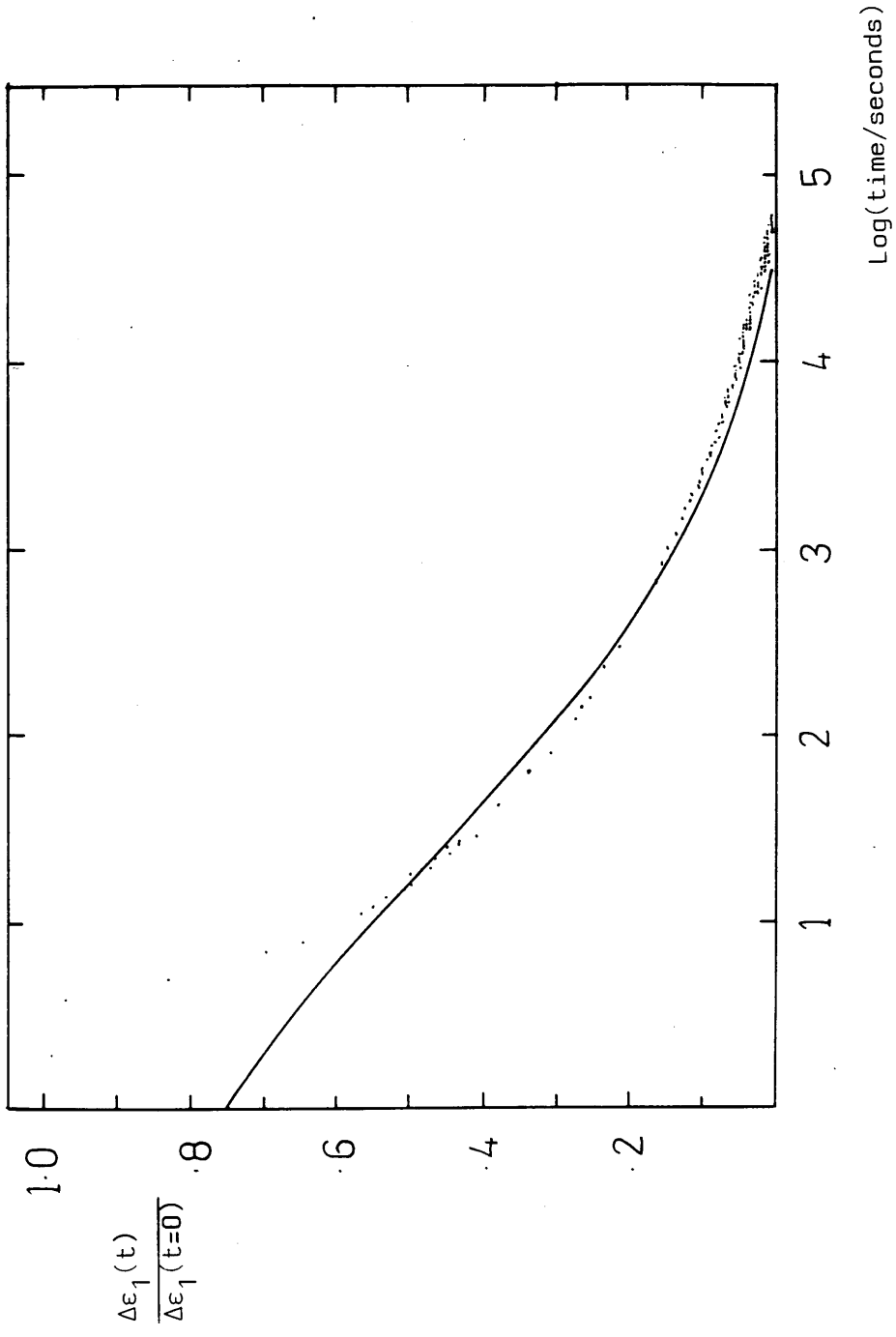
Graph 7.11

The experimental decay data for D1 at 20K. This has been compared with theoretical predictions, as has the data shown in the next three graphs.



Graph 7.12
Log(time/seconds)

The decay data at 40K for D1.



Graph 7.13

The decay data at 50K for D1.

Diagram 7.14

Sample	S2	S5	K9'	K11	D1
η	0.089	6.07×10^{-3}	8.4×10^{-3}	6.07×10^{-3}	0.034
T(K)	12.5	20	12.5	12.5	12.5

Table illustrating the efficiency of the trapping of carriers per photon of incident light.

Diagram 7.15

Sample.	K11'					K12
Junction.	640	640	660	660	640	
T	12.5K	20	30	40	50	4.2
α	0.322	0.349	0.361	0.422	0.418	0.258
t'_0	5219s	3330	2323	931.4	209.8	4.68×10^4

Sample.	D1			D2
Junction.	600	700	600	
T	12.5K	20	40	50
α	0.372	0.319	0.420	0.412
t'_0	460.0s	583.1	365.6	43.6

Sample.	S5	K9'
Junction,		
T	12.5K	40
α	0.28	0.38
t'_0	735.6s	8009

Tables showing the values of α and t'_0 at different temperatures for a variety of samples.

CHAPTER 8

Summary and Conclusions

The aim of this thesis was to present the data, results and analysis of a variety of experiments in which the properties of amorphous materials were studied. These properties included the ac and dc conductivity and capacitance studied in the dark and under illumination, generally at low temperatures. The results of these experiments were then compared with previous research on a-Ge, a-Si and a-Si:H prepared by RF sputtering.

The dark characteristics, i.e. conductance and capacitance changes with temperature, found in glow discharge a-Si:H are presented in Chapter 5. A variety of models, involving ac and dc transport mechanisms, and which are discussed in Chapter 2, are then applied to the data. The low temperature conductivity is attributed to electrons within deep states responding to the applied measuring field. At higher temperatures (i.e. above ~100K) the dark loss is due to transitions between states. A model using an effective medium method was developed by Long (1989) and successfully used to account for the high temperature ac conductivity in undoped glow discharge a-Si:H.

The major part of this thesis is concerned with the optically induced ac loss in amorphous materials. Previous experiments on sputtered silicon samples showed an increase in the capacitance and conductance of these materials when they are illuminated (Long and Holland 1985). The light induced ac loss in glow discharge a-Si:H was studied and the change in dielectric constant was found to obey a power law at high illuminating intensities i.e.

$$\Delta\epsilon_1 \propto I^A \quad (8.1)$$

where $A \sim 0.2$.

At lower illumination (less than $0.1\mu\text{Wcm}^{-2}$) intensities an integrating response is observed in which equilibrium conditions may still not be achieved after many hours. This region merges into the high intensity regime where saturation of the response occurs within minutes.

The frequency and temperature dependence of the light induced changes in the dielectric constant and conductance were studied and it was found that the major trapping and recombination mechanisms involved different states from those in sputtered samples. In sputtered material a high density of defect states exists within the band gap and these states are responsible for trapping carriers which respond to the measuring field and hence contribute to the optically induced ac loss. Evidence was found, from the frequency dependence of the ac conductivity and dielectric constant at different levels of illumination (see Chapter 6 for further details), to attribute the induced loss to trapping in band-tail states.

Removing the light caused the induced response to decay towards the dark values. The decay rate was found to be temperature dependent. For example, at 12.5K the decays would last many days and the dark value could still not be reached. At 50K the samples returned to their initial dark state after shorter times above a few hours. This temperature effect was attributed to the excitation of trapped band-tail carriers. At higher temperatures some of these trapped carriers could be excited and could then recombine with excess holes.

At lower temperatures less thermal energy is available and such a process will take place more slowly by tunnelling.

A model involving the diffusion of trapped carriers was used to describe the decays. Fitting this model to the decays showed that

$$\frac{n}{n_0} = \left(1 + \left(\frac{t}{t_0} \right)^\alpha \right)^{-3/2} \quad (8.2)$$

(where α and t_0 are weak functions of temperature) was a reasonable fit over several orders of magnitude.

The results of the optically induced ac loss experiments were then compared with the result of other experiments involving the effect of light on amorphous materials. These experiments are discussed in Chapter 3 and involve LESR measurements, transient photoconductivity, luminescence drift mobility, the Staebler Wronski effect and dc photoconductivity. The mechanism responsible for the Staebler Wronski effect involved photostructural changes rather than electronic excitation and the subsequent trapping of carriers and is therefore of less relevance than the other experiments. The LESR experiments show many similarities to the light induced ac loss experiments. Both show closely linear log (induced response) vs log (Intensity) plots with gradients of around 0.2. Long decays to the dark states are also observed. Since the LESR technique only detects paramagnetic states and the light induced ac loss technique only detects carriers which respond to an ac field the populations of states which are being measured will differ.

An important point in this work concerned the electrode material used in conjunction with the a-Si:H samples. It was found that

materials such as Au or Cr diffused into the a-Si:H and were responsible for an enhanced dark loss and a reduced optical response. This was explained, in Chapter 7, by considering that the diffused metal atoms acted as recombination centres or assisted recombination. No problems were observed with Au contacts or sputtered a-Si because the dark loss is higher to begin with than in glow discharge a-Si:H and any effect of the metallic impurities is not large enough to contribute to the measured ac loss.

The possibility of using either sputtered a-Si or glow discharge a-Si:H as an optical detector was also considered. An ideal detector should use a material which has a large (~ a few percent) and fast response to illumination. It must also be possible to clear the response easily and quickly. The glow discharge a-Si:H was found to have a reasonable magnitude of response which could be cleared by raising the temperature, to above 50K, but at low high intensities saturation values were often not reached for several hours. This limits the usefulness of this material for optical detection. Maximising the sensitivity and optimising the electrode areas and configurations and sample thicknesses and comparing different materials in detail could be the subject of further research.

Future work in this area could also involve promoting recombination by using sub-bandgap radiation (in the manner of Carius and Fuhs 1985. Here recombination was accelerated, in LESR experiments, by applying IR-radiation to a-Si:H. Trapped carriers were excited and subsequently recombined. This led to shorter decays to the dark state).

Other experiments involving doped samples, containing different concentrations of impurities could also be carried out. Further work

on the decays to equilibrium are also possible. This would involve illuminating samples at a fixed intensity and then removing the light. Different levels of illumination would be used and the decays compared. Such an experiment could provide information into the recombination mechanisms involved. By producing varying numbers of excess carriers it should be possible to determine whether closely spaced σ distant pairs are involved.

REFERENCE

- AMBEGAOKAR, V., HALPERIN, B.I., LANGER, J.S. (1971), Phys. Rev. B, 4, 2612.
- BALKAN, N., BUTCHER, P.N., HOGG, W.R., LONG, A.R., and SUMMERFIELD, S., (1985), Phil. Mag. B, 51, No. 1, L7-L12.
- BOULITROP, F., (1984), AIP Conf. Proc. 120, 178.
- BRODSKY, M.H., (1978), Thin Film Solids, 50, 57-67.
- BRUGGEMAN, D.A.G. (1936), Ann. Phys. (Leipzig), 24, 636.
- CARIUS, R. and FUHS, W., (1985) Journal of Non-Cryst. Solids, 77 and 78.
CRAVEN AJ, PATERSON AM, LONG AR, WILSON JLB (1985), Journ. Non-Cryst Solids, 77 & 78, 217.
- DERSCHE, H., SCHWEITZER, L. and STUKE, J., (1983), Phys. Rev. B 28, 467B.
- DYRE, J.C. (1985), Journal de Physique, C8-343.
- EFROS, A.L. (1981), Phil. Mag. B, 43, 829.
- ELLIOTT, S.R., (1983) "Physics of Amorphous Materials", (London:Longman).
- ELLIOTT, S.R. (1987), Adv. in Phys., 36, 135.
- FRITZSCHE, H., (1985), Journal of Non-Cryst. Solids 77 and 78, 273-280.
- FUHS, W., Milleville, M. and Stuke, J. (1978), Phys. Stat. Soc. (b) 89, 495.
- FUHS, W., (1985), Journal of Non-Cryst. Solids, 77 and 78.
- GRÜNEWALD, M., MOVAGHAR, B. POHLMANN, B., WÜRTZ, D. (1985), Phys. Rev. B, 32, No. 12.
- GRÜNEWALD, M., MOVAGHAR, B., (1987), Proceedings of 12th ICALS (Prague).
- HIRATA, K., KITAO, M. and YAMADA, S., (1983), J. Phys. Soc. Japan, 52, 1317.
- HOHEISEL, M., CARIUS, R. and FUHS, W., (1984), Journal of Non-Cryst. Solids, 313-319.
- HOLLAND, M. (1987), Ph.D. thesis.
- HUANG, C.Y., GUKA, S. and HUDGENS, S.J., (1982), Phys. Rev. B, 27, No. 12.
- KAPLAN, D., (1979), Inst. Phys. Ser. No. 43, Chapter 30.

- LE COMBER, P.G. and SPEAR, W.G., (1970), Phys. Rev. Letters, 25, 509.
- LONG, A.R., (1982), Advances in Physics, 31, No. 5, 553-637.
- LONG, A.R., HOGG, W.R. and BALKAN, N., (1983), Phil. Mag B, 48, No. 6, L55-L60.
- LONG, A.R. and McMILLAN, J., (1985), Journal of Non-Cryst. Solids, 77 and 78, 467-470.
- LONG, A.R. and HOLLAND, M.C. (1985), Journal of Non-Cryst. Solids, 77 and 78, 471-474.
- LONG, A.R., HOGG, W.R., HOLLAND, M.C. and BALKAN, N., (1985), Phil. Mag. B, 51, No. 1, 39-54.
- LONG, A.R., McMILLAN, J. BALKAN, N. and SUMMERFIELD, S. (1988), Phil. Mag. B, 58, No. 2, 153-169.
- LONG, A.R., ANDERSON, M.J., SHIMAKAWA, K. and IMAGAWA, O. (1988), J. Phys. C, 21, L1199-L1204.
- LONG, A.R. (1989), Phil. Mag. B, 59, No. 3, 377-386.
- LONG, A.R. (1989 to be published) Chapter in "Hopping Conduction in Solids" editors Pollak, M. and Shklovskii, B.I., Elsevier, Amsterdam.
- MAISSEL, L.I. and GLANG, R. (1970), "Handbook of Thin Film Technology", McGraw-Hill.
- MONROE, D., Phys. Rev. Letters (1985), 54, No. 2.
- MONROE, D., (1989 to be published), Chapter in "Hopping Conduction in Solids" editors Pollak, M. and Shklovskii, B.I., Elsevier, Amsterdam.
- MOTT, N.F. and DAVIS, E.A. (1979), "Electronic Processes in Non-Crystalline Materials" (Oxford Clarendon Press).
- MONROE, D., Phys. Rev. Letters, 1985, 54, No. 2.
- MOVAGHAR, B., GRÜNEWALD, M., RIES, B. and BÄSSLER, B., (1986), Phys. Rev. B, 33, 8.

- MOVAGHAR, B., RIES, B., GRÜNEWALD, M., 1986, Phys. Rev. B, 34, 8.
- RICHERT, R., RIES, B. and BÄSSLER, H., Phil. Mag. B, 1984, 49, No. 3, L25-30.
- RIES, B., SCHÖNHERR, G., BÄSSLER, H., Phil. Mag. b, 1984, 49, No. 3, 259-270.
- ORENSTEIN, J. and KASTNER, M., (1981), Phys. Rev. Letters, 46, 1421.
- OVERHOF, H., and BEYER, W., (1981), Phil. Mag. B, 43, 433.
- OVERHOF, H. and BEYER, W., (1983), Phil. Mag. B, 47, 377.
- OVERHOF, H. and THOMAS, P., "Electronic Transport in Hydrogenated Amorphous Materials", to be published in "Springer Tracts in Modern Physics".
- PIKE, G.E., (1972), Phys. Rev. B 6, 1572.
- POLLAK, M. and GEBALLE, T.H., (1961), Phys. Rev. 122, 1742.
- POLLAK, M., (1971), Phil. Mag. 23, 519.
- SHIMAKAWA, K., (1982), Phil. Mag. B, 46, 123.
- SHIMAKAWA, K., LONG, A.R. and IMAGAWA, O., (1987), Phil. Mag. Letters, 56, No. 2, 79-84.
- SHIMAKAWA, K., LONG, A.R., ANDERSON, M.J. and IMAGAWA, O., (1987), J. Non. Cryst. Solids, 97 and 98, 623.
- SPEAR, W.E. and CLOUDE, C.S., (1987), Phil. Mag. Letters, 55, No. 6, 271-276.
- SPEAR, W.E., CLOUDE, C., GOLDIE, D. and LeCOMBER, P., (1987), Journal of Non-Cryst. Solids 97 and 98, 15-22.
- SPEAR, W.E. and CLOUDE, C.S., (to be published).
- SPRINGETT, B.E., (1973), Phys. Rev. Letters, 31, 1463.
- STAEBLER, D.L. and WRONSKI, C.R., J. Appl. Phys., (1980), 51, (6).
- STREET, R.A. (1976), Advances in Physics, 25, 397.

- STREET, R.A., (1980), Solid State Comm. 34, 157.
- STREET, R.A., (1981), Phys. Rev. B 23, 861.
- STREET, R.A. and BIEGELSEN, D.K., (1982), Solid State Comm., 44, 501.
- SUMMERFIELD, S. and BUTCHER, P.N., (1982), J. Phys. C.
- SUMMERFIELD, S. and BUTCHER, P.N., (1983), J. Phys. C, Solid State
Physics, 16, 295.
- SUMMERFIELD, S., BUTCHER, P.N. and LONG, A.R., (1985), J. Non-Cryst.
Solids, 77 and 78, 475
- TSANG, C. and STREET, R.A., (1979), Phys. Rev. B, 19, No. 6.
- VARMAZIS, C., HIRSCH, M.D. and VANIER, P.E., (1984), AIP Conf. Proc.
120, 133.
- WHITE, G.K., (1968), "Experimental Techniques in Low Temperature
Physics", (Oxford : Clevedon Press).
- WINER, K. HIRABAYASHI, I. and LAY, L., (1988), Phys. Rev. Letters, 60,
No. 25.